MICROCOPY RESOLUTION TEST CHART

NATIONAL BUREAU OF STANDARDS-1963-A

Final Report

# THE USE OF SYNTHETIC APERTURE RADAR TO DETECT AND CHART SUBMERGED NAVIGATION HAZARDS

APRIL 1982

E.S. KASISCHKE
D.R. LYZENGA
R.A. SHUCHMAN
Y.S. TSENG
B.S. TERMAAT
B.A. BURNS
G.A. MEADOWS

Radar and Optics Division

DTIC
ELECTE
MAR 25 1983
A

ENVIRONMENTAL
RESEARCH INSTITUTE OF MICHIGAN

BOX 8618 ● ANN ARBOR ● MICHIGAN 48107

| REPORT DOCUMENTATION PAGE | READ INSTRUCTIONS BEFORE COMPLETING FORM |
|---|---|

| 1. REPORT NUMBER | 2. GOVT ACCESSION NO. AD-A126071 | 3. RECIPIENT'S CATALOG NUMBER |
|---|---|---|
| 4. TITLE (and Subtitle) THE USE OF SYNTHETIC APERTURE RADAR TO DETECT AND CHART SUBMERGED NAVIGATION HAZARDS | | 5. TYPE OF REPORT & PERIOD COVERED Final Report, April 1981 through April 1982 |
| | | 6. PERFORMING ORG REPORT NUMBER 155200-1-F |
| 7. AUTHOR(s) E.S. Kasischke, D.R. Lyzenga, R.A. Shuchman, Y.S. Tseng, B.S. Termaat, B.A. Burns, and G.A. Meadows | | 8. CONTRACT OR GRANT NUMBER(s) N00014-81-C-2254 |
| 9. PERFORMING ORGANIZATION NAME AND ADDRESS Environmental Research Institute of Michigan Radar and Optics Division, P.O. Box 8618 Ann Arbor, MI 48197 | | 10. PROGRAM ELEMENT, PROJECT TASK AREA & WORK UNIT NUMBERS |
| 11. CONTROLLING OFFICE NAME AND ADDRESS Naval Research Laboratory 4555 Overlook Avenue Washington, DC 20375 | | 12. REPORT DATE April 1982 |
| | | 13. NUMBER OF PAGES |
| 14. MONITORING AGENCY NAME AND ADDRESS (if different from Controlling Office) | | 15. SECURITY CLASS (of this report) UNCLASSIFIED |
| | | 15a. DECLASSIFICATION/DOWNGRADING SCHEDULE |

16. DISTRIBUTION STATEMENT (of this Report)

Approved for public release; distribution unlimited.

17. DISTRIBUTION STATEMENT (of the abstract entered in Block 20. if different from Report)

18. SUPPLEMENTARY NOTES

The Technical Monitor for this project was Mr. Peter A. Mitchell.

19. KEY WORDS (Continue on reverse side if necessary and identify by block number)

| | |
|---|---|
| Synthetic aperture radar | Bathymetry |
| Seasat | Oceanography |
| Bottom features | |

20. ABSTRACT (Continue on reverse side if necessary and identify by block number)

This report discusses the utility of synthetic aperture radar (SAR) data collected by the Seasat satellite for the detection and charting of bottom features which might be hazardous to navigation. Data from 35 Seasat orbits were used to examine nine test sites. These test sites included: the Tongue of the Ocean, Bermuda, Haiti, Sula Sgier, Cook Inlet (Alaska), the Mississippi River Delta, the English Channel, the Nantucket Shoals, and the northeast
(continued)

Atlantic Ocean.  The northeast Atlantic test site actually contained 17 distinct bottom features such as seamounts, submarine ridges, banks, and the edges of continental shelfs.

Three distinct techniques were used to examine the Seasat SAR imagery: broad survey studies, multi-temporal analyses, and multisensor analyses.  This study continued to document the utility of Seasat SAR imagery for locating and identifying bottom features in both shallow and deep water portions of the world's oceans.  By correlating the SAR data with ancillary environmental data (such as wind, wave, and tidal current information) the causes of many of the bottom-related surface patterns on the SAR imagery have been identified, an important step for defining the limitations of SAR data for bottom feature detection.

This report also contains three appendices.  Appendix A presents a survey of the different types of oceanographic phenomena which have been detected on Seasat SAR imagery.  Appendix B contains the details of an examination of Seasat SAR imagery for navigation buoys and ship-wrecks.  Finally, Appendix C describes the radiometric and geometric correction algorithms used to digitally process Seasat SAR data.

## PREFACE

The work described in this report was conducted by the Radar and Optics Division of the Environmental Research Institute of Michigan (ERIM). This work was supported by the Naval Research Laboratory under Contract Number N00014-81-C-2254. The technical monitor for this contract was Mr. Peter A. Mitchell. Mr. James C. Hammack of the Defence Mapping Agency also provied guidance during this study.

The Principal Investigators for this project were Dr. Robert A. Shuchman and Mr. Eric A. Kasischke. Dr. David R. Lyzenga performed the multi-sensor analysis and was responsible for developing the geometric and radiometric algorithms used to process the Seasat SAR data. Mr. Y.S. Tseng conducted the analysis of the Seasat data from the JASIN test site, while Ms. Barbara S. Termaat assisted in the analysis of Seasat data collected over the Tongue of the Ocean. Dr. Barbara A. Burns conducted the English Channel shipwrecks and buoy detection analysis. Finally, Dr. Guy A. Meadows contributed the background section on SAR detection of bottom features.

iii

## ACKNOWLEDGMENTS

Special thanks go to Amanda Blake of the Marine Information Advisory Service who was particularly helpful in coordinating our data requests from the various British agencies.

Finally, the authors appreciate the efforts of Richard Larson and Jack Walker of ERIM, Peter Mitchell of NRL and James Hammack of DMA in reviewing the preliminary version of this report and for providing comments for the final version.

CONTENTS

## LIST OF ILLUSTRATIONS

LIST OF ILLUSTRATIONS (Continued)

LIST OF ILLUSTRATIONS (Continued)

LIST OF ILLUSTRATIONS (Continued)

LIST OF ILLUSTRATIONS (Continued)

# LIST OF ILLUSTRATIONS (Concluded)

## LIST OF TABLES

LIST OF TABLES (Continued)

THE USE OF SYNTHETIC APERTURE RADAR TO DETECT AND CHART
SUBMERGED NAVIGATION HAZARDS

1
INTRODUCTION

This report presents the results of a continuation of a previous study conducted for the Defense Mapping Agency (Kasischke, et al., 1980). The purpose of this study was to evaluate in greater detail the usefulness of information obtainable from synthetic aperture radar (SAR) data as it relates to locating and mapping features in coastal and deep water areas which might be hazardous to ship navigation. The study was carried out through an examination of data collected by the Seasat satellite over oceanic areas where potential submerged hazards exist.

The Seasat SAR operates at a radar wavelength (23.5 cm) that does not significantly penetrate the water surface. Thus, the subsurface-related patterns recorded on the SAR image are the result of a hydrodynamic interaction between a variety of oceanic processes (currents, waves, tides, etc.), atmospheric processes (wind, rain, etc.), bottom features (topographic irregularities), and man-made structures (ships and buoys), that perturbs the surface gravity wave fields and particularly the small scale ocean ultra-gravity waves.

This investigation supports the goals of the Defense Mapping Agency with respect to the utilization of remotely sensed data. Their goals are threefold: (1) to identify submerged features which are potentially hazardous to surface navigation; (2) to accurately locate these hazardous submerged features on either a relative or absolute coordinate system; and (3) to update the depth soundings on existing hydrographic charts. The last goal requires a basic research commitment and is beyond the scope of the present investigation.

In order to fulfill the objectives of this study, the investigation was divided into three primary research activities. These three reseach activities included: (1) a broad survey of Seasat imagery to identify depth-related SAR image features, (2) a multitemporal study involving multiple date data acquisitions over the same geographical area, and (3) a multi-sensor study involving a comparison of Seasat with other remote sensor data. These three research activities are presented as chapters in this report. Additional sub-tasks were carried out to support these investigations, including the acquisition of ancillary environmental data and the development of techniques for the radiometric and geometric correction of Seasat SAR data.

This report is organized into seven chapters including this introduction, an executive summary, and a background section containing an overview of SAR-observed subsurface and surface oceanographic phenomena as well as basic SAR sensor theory. Chapters 4, 5, and 6 describe the three main research activities conducted during this investigation as outlined above, and the final chapter presents the conclusions of this study and recommendations for further investigations.

2
EXECUTIVE SUMMARY

A variety of remote sensing techniques have been studied over the past decade to calculate their potential for providing information for updating navigation charts. The present study considered data collected by the Seasat imaging synthetic aperture radar for this purpose. A synthetic aperture radar (SAR) differs from optical remote sensors (i.e., photographic systems and multispectral scanners) in that it provides its own source of illumination in the microwave region of the electromagnetic spectrum. Imaging synthetic aperture radars today typically operate at wavelengths between 1 cm and 24 cm.

The electromagnetic energy emitted by a SAR does not penetrate appreciably into the water surface, thus the surface expressions of bathymetric features observed on the SAR are caused by a hydrodynamic interaction between the bottom feature and short wavelength, wind driven surface waves. The bathymetric related phenomena observed by a SAR can be classified into five categories:

1. A change in direction and wavelength of ocean swell as it enters shallow coastal regions;

2. A change in radar backscatter that is associated with a current flowing over a shallow water (<50 m) bottom feature;

3. A change in radar backscatter that is associated with an ocean swell propagating over a distinct depth discontinuity:

4. Classic internal wave patterns occurring over continental shelf regions; and

5. Anomalous SAR backscatter signatures found in deep (>200 m) ocean regions over topographic features (such as guyots and submarine ridges) on the ocean floor.

The first case (the change in direction and wavelength of ocean swell) was not within the scope of this study, but has been extensively analyzed elsewhere (e.g., Kasischke, et al., 1981). As gravity waves enter shallow coastal waters, the wavelengths and directions of the waves begin to change due to interactions with the bottom. The amount the wavelength and direction changes is proportional to the depth of the water at a given point: therefore, by measuring the change in wavelength and/or direction from SAR imagery, an indirect measure of water depth can be obtained. Figure 1 shows a plot of water depths calculated using estimates of wavelength obtained from Seasat SAR imagery versus water depths obtained from a hydrographic survey (after Kasischke, et al., 1981).

Figure 2 illustrates the case where a current is flowing over a shallow water bottom feature. In this example, a strong current (in excess of 2 knots) is flowing from north to south over the sand banks in the center of the English Channel. The sand banks in this area are approximately 30 meters high and extend to within 10 meters of the water surface.

Figure 3 presents an example where a change in radar backscatter is associated with an ocean swell propagating over a distinct depth discontinuity (the barrier reef surrounding the islands of Bermuda). The exact cause of this particular type of surface anomaly has yet to be determined. The prevailing theory to explain this phenomenon is based on a non-linear interaction between the gravity wave and the small capillary waves as the gravity wave propagates onto an abruptly changing bottom. In the above example, there exists a bottom morphology with a very abrupt change in water depth.

An example of internal waves observed on Seasat SAR imagery over a continental shelf area is presented in Figure 4. The cause of these internal waves has been attributed to tidal forcing. As a
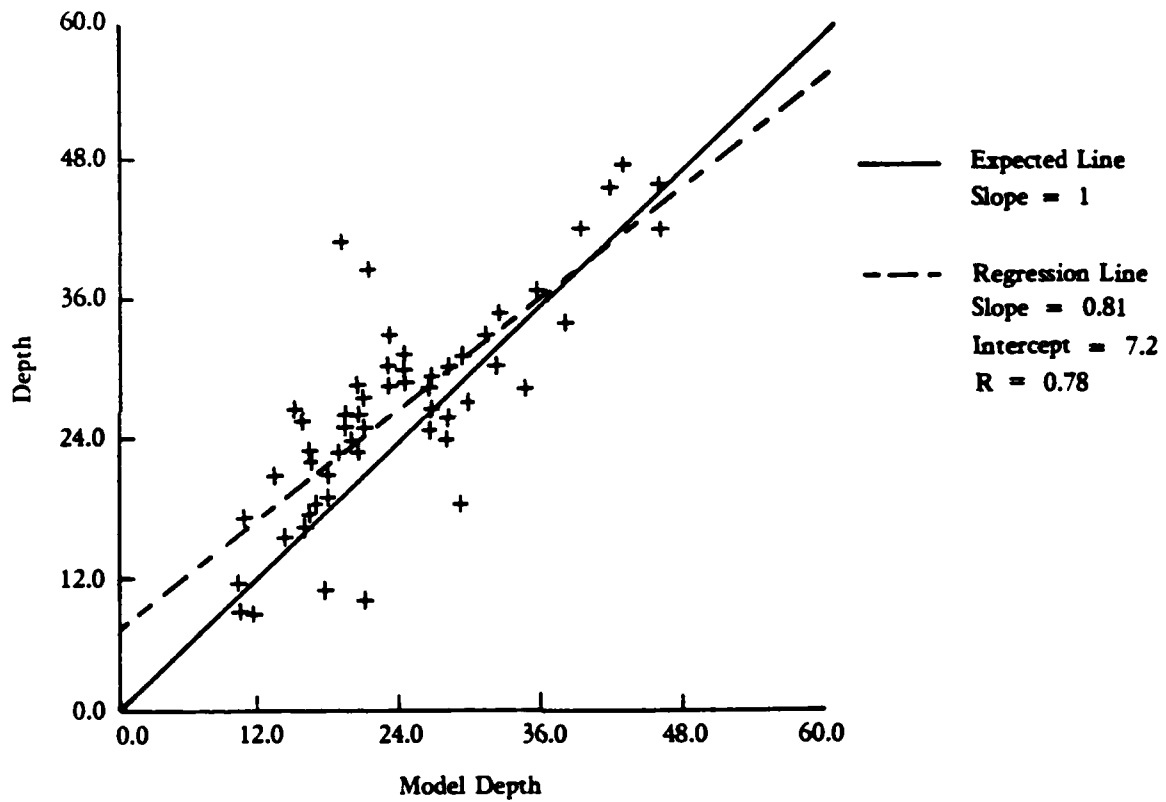
FIGURE 1. PLOT OF WATER DEPTHS CALCULATED USING INVERTED AIRY WAVE
THEORY WITH CHANGES OF WAVELENGTH EXTRACTED FROM SEASAT
SAR IMAGERY VERSUS DEPTHS OBTAINED FROM U.S. NATIONAL
OCEAN SURVEYS.

RADAR LOOK DIRECTION →

← SPACECRAFT FLIGHT DIRECTION
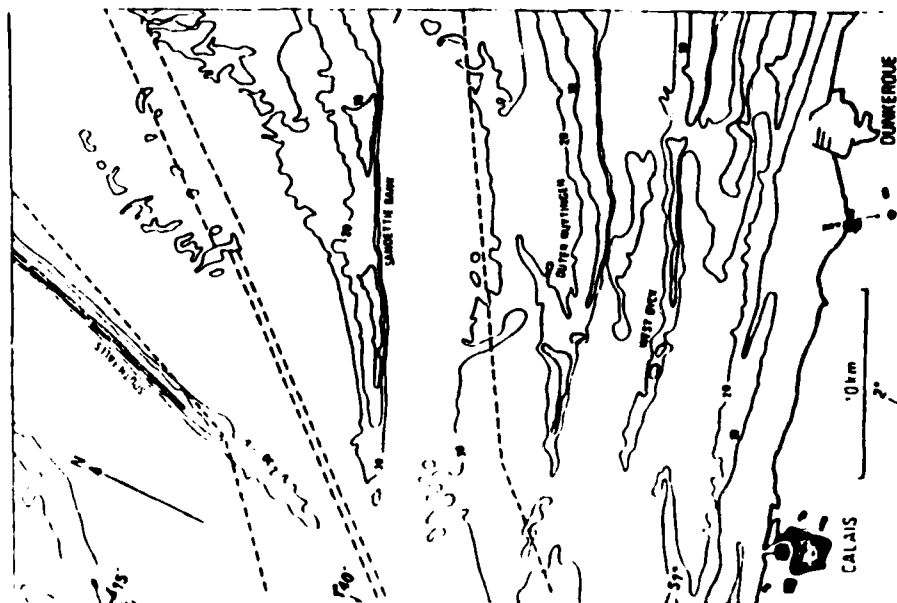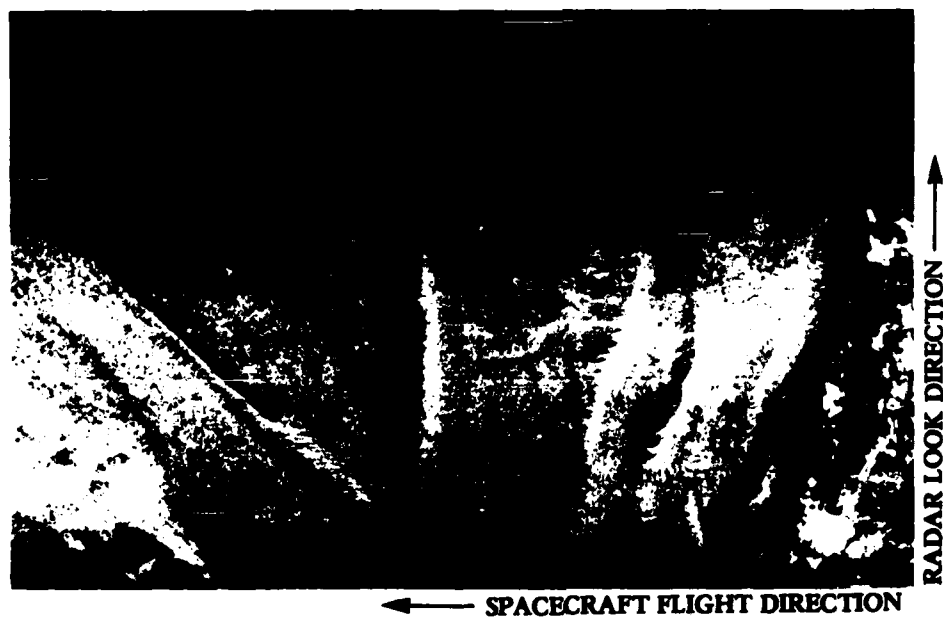
(The dashed lines in the figure are recommended ship routes.)

FIGURE 2.  EXAMPLE OF CURRENT-INDUCED, BOTTOM-RELATED PATTERNS ON SEASAT SAR IMAGERY COLLECTED OVER THE ENGLISH CHANNEL.  (Seasat Rev. 762, 19 August 1978, ERIM Optically Processed Imagery.)

SPACECRAFT FLIGHT DIRECTION ⟶

RADAR LOOK DIRECTION ⟶

⊢ 10 km ⊣

N ⟶
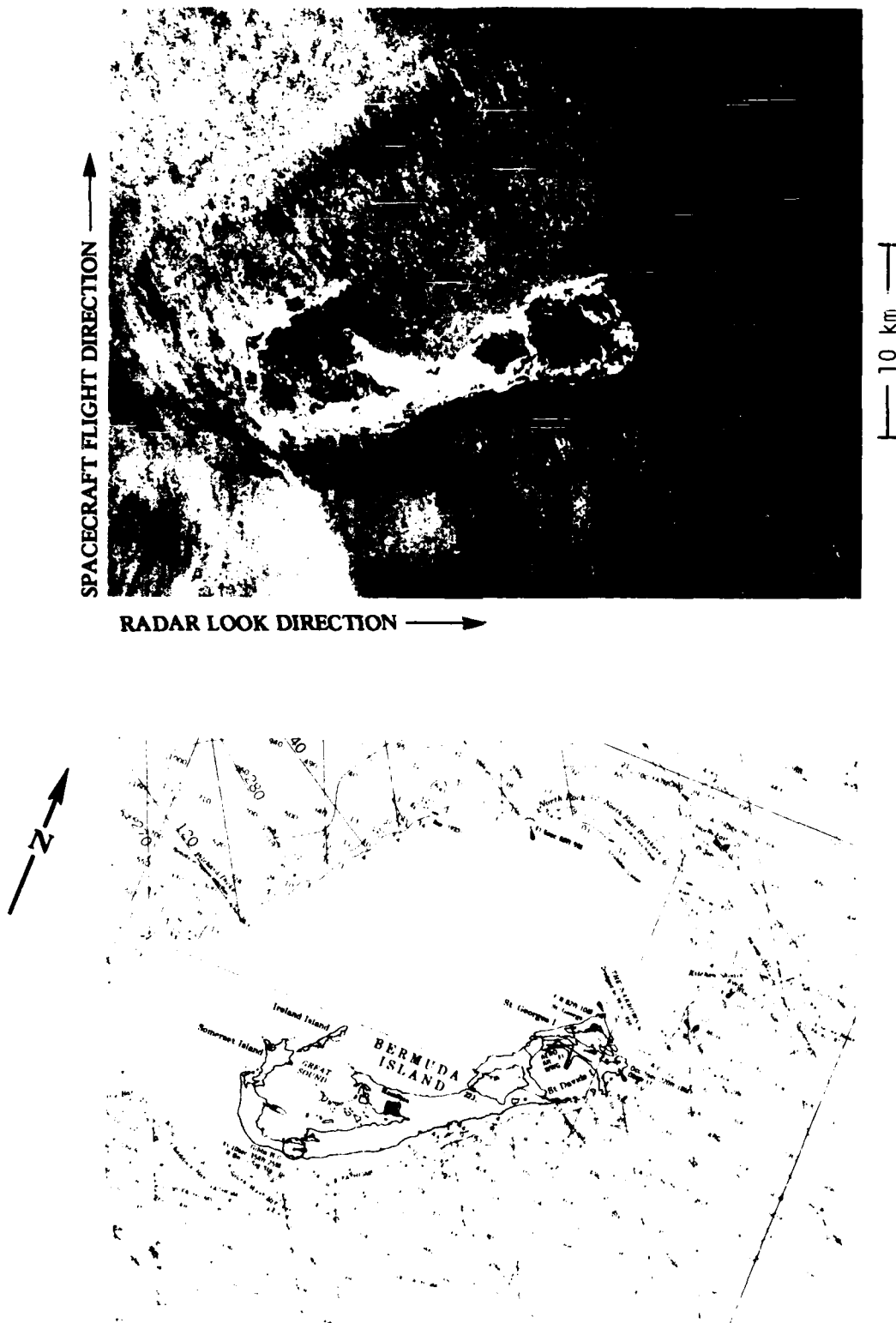
FIGURE 3.   EXAMPLE OF BOTTOM-RELATED PATTERN OF A SHOAL AREA SURROUNDING BERMUDA ISLAND. (Seasat Rev. 1267, 23 September 1978. Image Generated from JPL Digitally Processed Data.)

**ΣERIM**

## SEASAT SAR



**HUDSON CANYON AREA**
(OIL PLATFORMS)
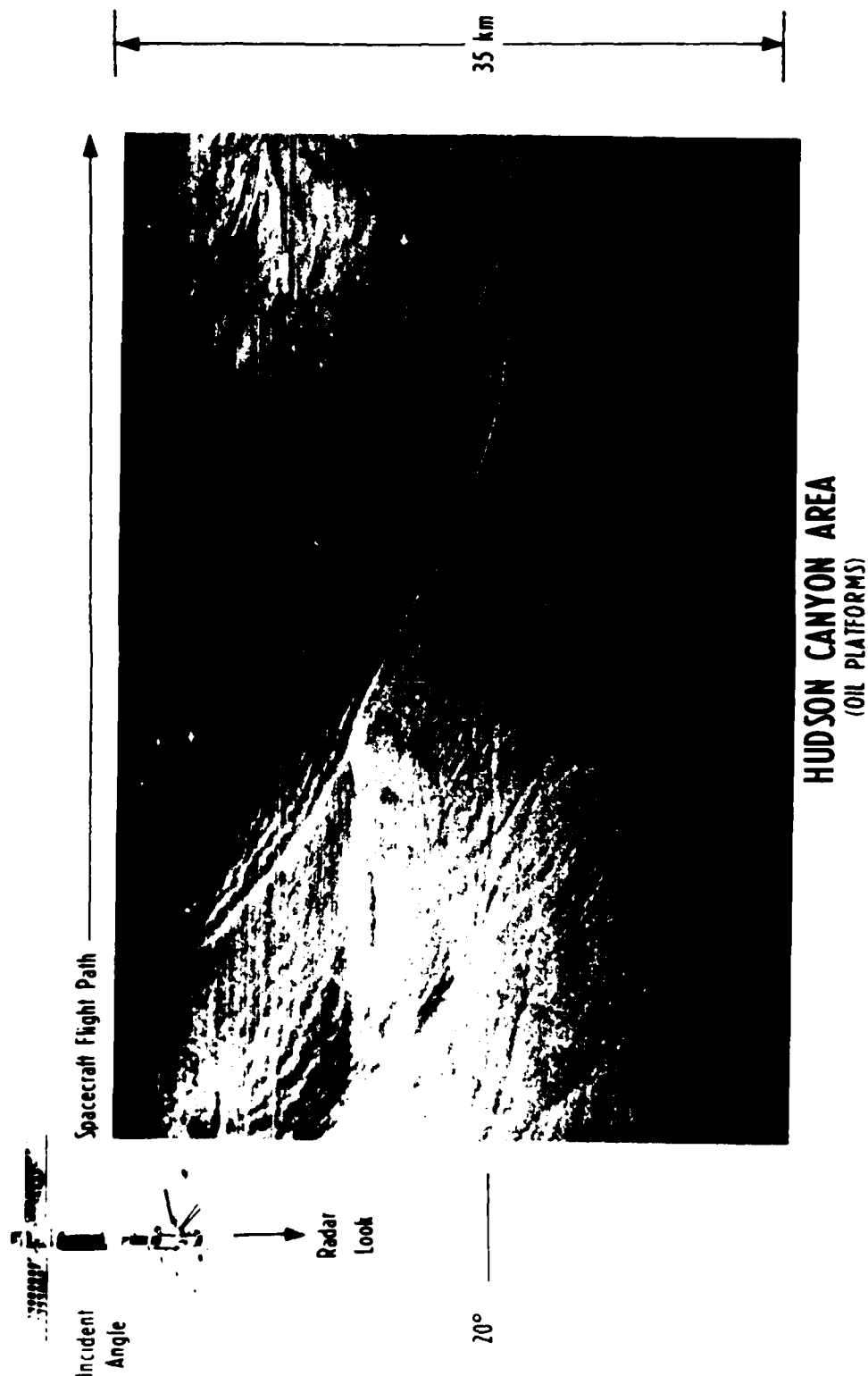
FIGURE 4.    INTERNAL WAVE PACKETS OBSERVED OFF EASTERN COAST OF U.S.    (Seasat Rev. 1232,
21 September 1978.    ERIM Optically Processed Image.)

tide flows on or off the continental shelf, an internal wave may be generated along the thermocline. The exact reason for their appearance on SAR imagery has yet to be determined, but it appears to be related to either the formation of a surface slick which dampens the small scale surface capillary waves or a non-linear interaction between the short period capillary waves and the long period internal waves resulting in a change in surface roughness.

An example of an anomalous SAR backscatter signature found in a deep-water region is presented in Figure 5. This "internal wavelike" structure occurred over the Wyville-Thomson Ridge, which rises to 600 meters in height above the surrounding 1200 meter deep ocean floor and is located northwest of Scotland in the North Atlantic. These deep-water signatures are not always internal wave-like, but can also resemble a frontal boundary. Figure 6 presents an example of an apparent frontal boundary observed on Seasat SAR imagery collected during Revolution 762 on 19 August 1978 at approximately 06:40 GMT. The curved, dark line beginning at A4 and continuing to B9 is believed to be a surface pattern caused by a frontal boundary. Its location appears to be in an area where the bottom is rising from the Faeroe Bank Channel to the Faeroe Shelf, over an area with a water depth between 600 and 1000 meters.

The suspected cause of these deep-water signatures is an interaction between a tidal driven current and large topographic features (such as underwater seamounts, ridges, and the edges of continental shelfs). The deep-water flow over these features may cause a variety of perturbations of the upper ocean layer, including deformation of the thermocline, the generation and propagation of Lee waves, and the formation of Taylor column type flows.

It is generally accepted that the scattering of microwave energy is a Bragg resonance phenomenon, thus making the received radar image particularly sensitive to capillary and short ultra-gravity surface waves. It is the alteration of these short surface aves which
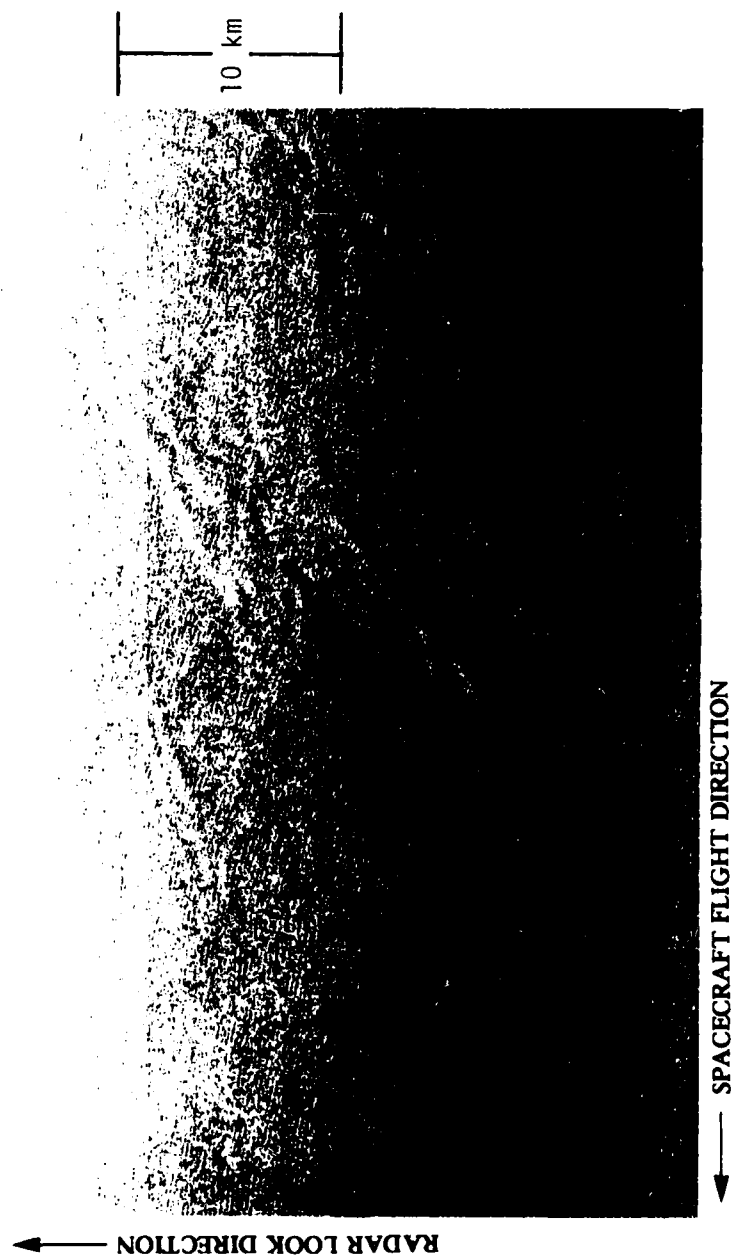
FIGURE 5.  INTERNAL WAVE-LIKE FEATURES OBSERVED OVER THE WYVILLE-THOMSON RIDGE. (Seasat Rev. 762, 19 August 1978.  ERIM Optically Processed Image.)

SPACECRAFT FLIGHT DIRECTION

RADAR LOOK DIRECTION

10 km
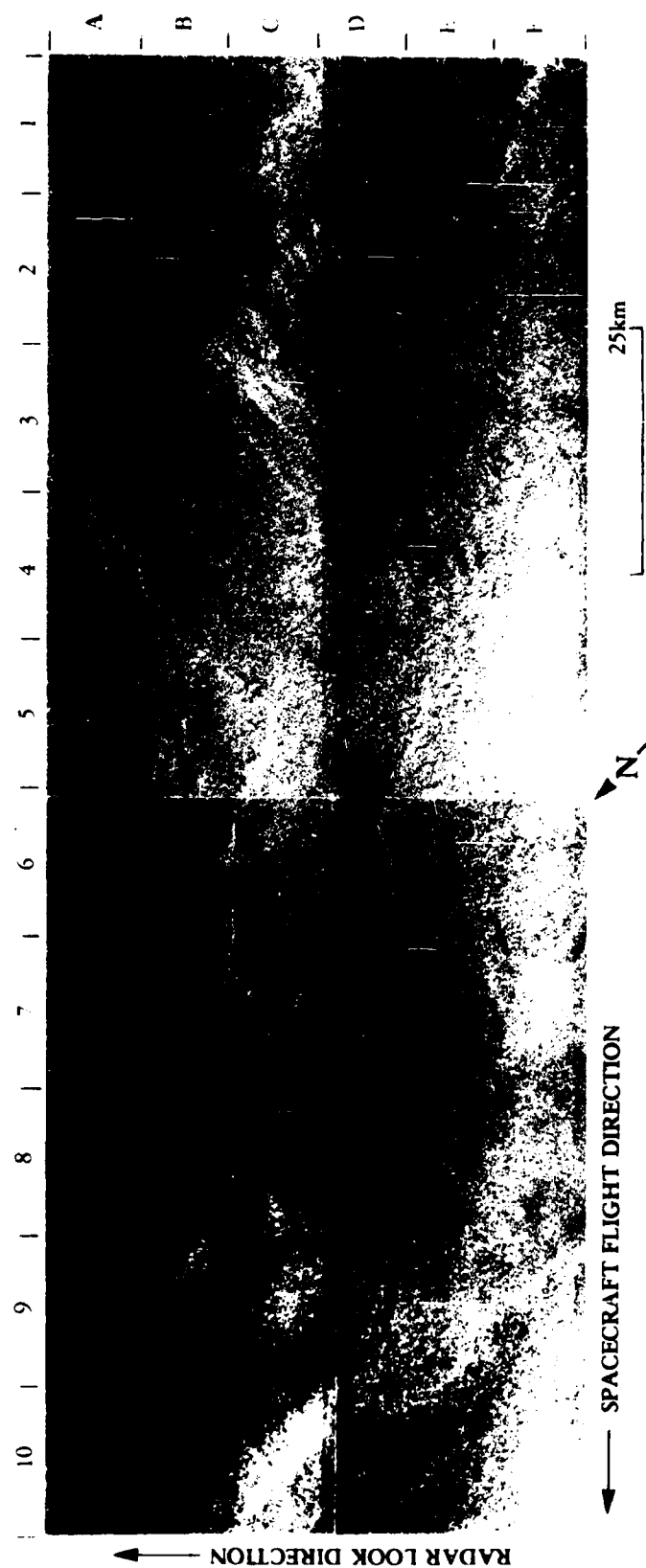
FIGURE 6. SEASAT SAR IMAGERY OF AN APPARENT FRONTAL BOUNDARY COLLECTED OVER THE FAEROE RIDGE. (Rev. 762, 19 August 1978. Optically Processed Image Courtesy of JPL.)

allows the SAR to detect surface manifestations of physical oceanic processes. To illustrate this concept, an example will be presented.

Figure 7 presents a scenario where a tidal driven current is flowing over a shallow-water bottom feature. Whether or not the SAR will "detect" the bottom feature and what type of SAR signature it will be (i.e., a decrease or increase in radar backscatter) depends on several factors, which include the depth of the feature, the current speed and direction, and the wind speed and direction, as well as the radar geometry. Figure 7 illustrates a situation where the surface capillary waves and current are traveling in the same direction. In this case, the increase in current velocity over the bottom feature causes a "stretching out" of the surface capillary waves, resulting in a decrease in radar backscatter due to the decrease in the amplitude of the Bragg scatterers in this region. If there is a large enough wind component in the same direction, the waves may be regenerated in this region and the wave amplitude "overshoot" in the convergence zone behind the bottom feature. This results in a banded appearance with a dark region on one side of the feature and a bright region on the other side. Essentially the same pattern results if the wind and waves are in the opposite direction to the current. Waves approaching from the left in Figure 7 are increased in amplitude in the convergence zone, decay toward their equilibrium state, and fall below their equilibrium amplitude in the divergence zone to the right of the bottom features.

During the present study, a total of nine test sites were examined using Seasat SAR imagery collected during 35 separate orbits. Of the nine test sites, eight were shallow-water test sites and one was a deep-water test site. The deep-water test site, located in the northeast Atlantic, actually contained seventeen distinct bottom topographic features.

gray    bright    dark              gray        RADAR IMAGE INTENSITY

wind
waves

current

bottom
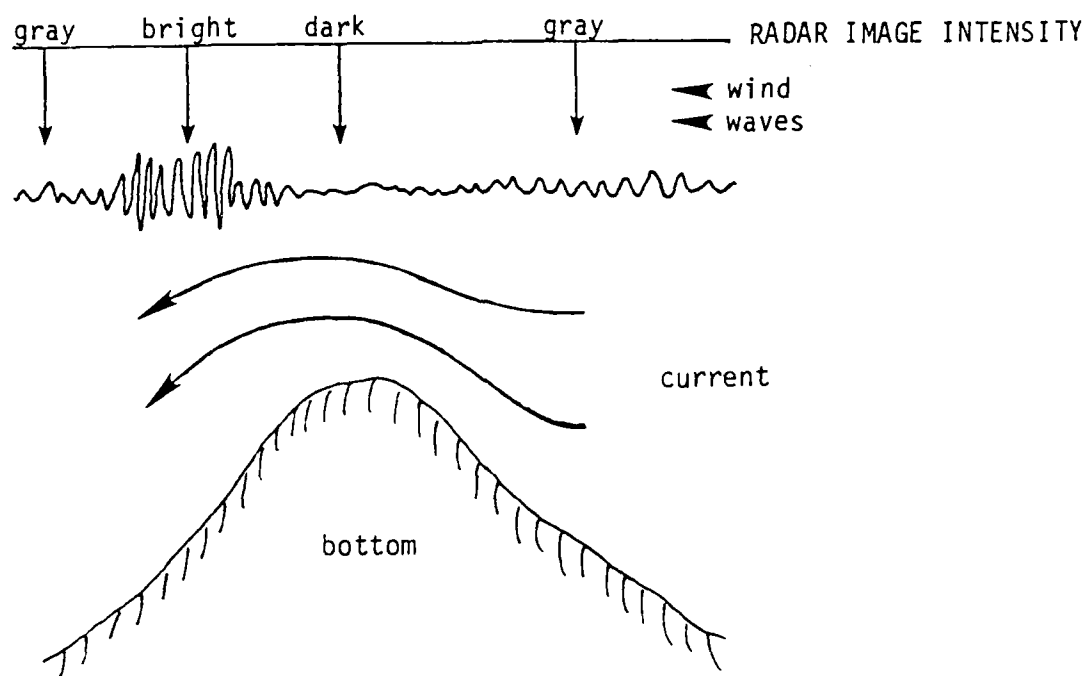
FIGURE 7.   SCHEMATIC DIAGRAM OF CURRENT, WIND, AND CAPILLARY WAVE
            INTERACTIONS

The selected test sites were examined using three techniques: (1) broad survey studies; (2) multi-temporal analyses; and (3) multi-sensor analyses. The broad survey studies were conducted to further document the occurrence of bottom-related surface patterns on Seasat SAR imagery. The multi-temporal analyses were intended to determine how often bottom-related surface signatures appeared on Seasat SAR imagery in a given area and also, when coupled with ancillary environmental data, to begin to define the limitations of using space-borne SAR imagery to detect bottom features. Finally, a multi-sensor analysis was conducted to compare the relative utility of Seasat SAR imagery to Landsat and Skylab imagery.

The broad survey studies continued to document the occurrence of bottom-related surface signatures. Of the six new, shallow-water test sites, five contained bottom-related surface signatures (Bermuda, Cook Inlet (Alaska), Haiti, Sula Sgeir and the Tongue of the Ocean) and one contained a false alarm (Mississippi River Delta). In addition, an assessment of the Seasat SAR's ability to detect shipwrecks and buoys in the English Channel was conducted. The broad survey of the deep-water test site revealed numerous examples of bottom-related surface signatures. These signatures were of two types: internal waves and frontal boundaries.

Multi-temporal analyses were conducted on three test sites: The English Channel, the Tongue of the Ocean and the JASIN test area in the northeast Atlantic Ocean.

The analysis of four different sets of Seasat imagery collected over the English Channel showed that a distinct surface pattern occurred 50 percent of the time over the two major sand banks in this area. The smaller banks and sand ridges in this area were imaged only 25 percent of the time. Comparison of the Seasat SAR imagery to ancillary environmental data indicates the appearance of the SAR signatures is dependent on the water depth above the feature, the current speed, and the wind velocity. Implementation of a

hydrodynamic/electromagnetic model developed earlier (Shuchman, 1982) was verified using the English Channel Seasat data.

The analysis of twelve different sets of Seasat imagery collected over the Tongue of the Ocean (TOTO) showed that a distinct, bottom-related surface pattern occurred over the tidal bar belts in this area 90 percent of the time. The edge of the Great Bahama Bank was imaged between 50 and 80 percent of the time, depending on location. The degree of detectability of these features was shown to be related to water depth and tidal current velocity. The tonal patterns associated with these features were shown to be dependent on the tidal current direction (i.e., ebb or flow).

Seasat SAR imagery collected on fifteen different occasions over seventeen distinct deep-water bottom features in the two northeast Atlantic were examined during the present study. Internal wave patterns appeared 63 percent of the time the Seasat SAR passed over or near a deep-water feature. In the northeast Atlantic, at no time did an internal wave pattern occur over a deep water basin. A frontal boundary occurred 38 percent of the time the Seasat SAR passed over or near a deep-water feature. The frontal boundaries did not appear to be as closely associated with the bottom features as the internal waves. Each of the seventeen deep-water bottom features were "detected" at least once, during the fifteen Seasat orbits, by an internal wave pattern.

In the shallow-water test sites studied, the appearance of surface patterns on SAR imagery over the same bottom feature is usually quite similar and in the same location on different Seasat passes, and thus can be used to map the location of these bottom features. For sand banks and ridges, SAR imagery can often be used to map the small scale structure of these features.

Although internal wave and frontal boundary patterns in deep water areas indicate the presence of a bottom feature, at this time they cannot be used to indicate what that feature is or determine the exact shape or location of that feature. The probability of such a pattern being present on two successive passes is high for certain features (such as seamounts, ridges and shelfs), but the chances are low that these patterns will be in exactly the same location or that they will have the same appearance.

A multi-sensor study was also carried out, in which data from Seasat, Landsat, and Skylab were compared with digital depth data (obtained from the National Ocean Survey) for the Nantucket Shoals area. Seasat and Landsat data were co-registered with the depth data and detailed statistical comparisons were made to determine the positional accuracy of the depth-related image features, and the degree of correlation between the water depth and the image brightness. The result of this comparison was that for relatively large features, the Seasat and Landsat data are both highly correlated with the depth on a local basis, if allowance is made for a horizontal shift between the images and the depth data. The rms shift between the point of minimum depth and the location of maximum signal on both the Seasat and Landsat data was found to be approximately 500 meters.

The higher spatial resolution of Seasat allows the imaging of small-scale bottom features, such as transverse sand waves, which are not imaged by Landsat. Examination of Skylab photography also shows that the appearance of depth-related surface features in visible imagery is highly dependent on the look direction relative to the solar azimuth. Essentially, the Skylab data appear to indicate that the view azimuth and solar azimuth must be within about 45° of each other in order to observe the surface patterns with a visible sensor. Thus, a fortuitous combination of sun angles and orbital paths are required for these features to be imaged by Landsat.

# 3
# BACKGROUND

This chapter presents a description of the Seasat SAR system, reviews the basic principles involved in SAR imaging of the ocean surface, and summarizes the mechanisms responsible for the appearance of bathymetric-related features in the SAR imagery.

## 3.1 SEASAT SAR BACKGROUND

The data to be presented in this report were collected by the Seasat satellite. Among the instrumentation carried by Seasat, which was launched during June of 1978, was a synthetic aperture radar (SAR). This satellite collected over 500 passes of SAR data before suffering a catastrophic power loss in October of 1978. The SAR on-board Seasat was an L-band (23.5 cm wavelength) radar. It collected 25 x 25 meter resolution imagery with a ground swath-width of 100 km and a length of up to 4000 km, and viewed the surface of the earth with an average incident angle of 20°. For a detailed discussion of the Seasat SAR, see Jordan (1980).

An imaging radar such as the Seasat SAR is an active device that senses the environment with short wavelength electromagnetic waves. As an active sensor, the Seasat SAR provided its own illumination in the microwave region of the electromagnetic spectrum and thus was not affected by diurnal changes in emitted or reflected radiation from the earth's surface.

Side-looking radars such as the Seasat SAR use pulse ranging, whereby the radar antenna attached to a moving platform illuminates a section of the ground and the amplitude, and the phase and polarization of the returned echoes are processed to determine the distance to the scene and to obtain the measure of relative strength of the return ($\sigma_0$). In real-aperture systems, the resolution in azimuth is limited by the beamwidth (i.e., the physical length) of the

antenna. Since resolution decreases with range for such systems, operation at spacecraft altitudes is not possible with real-aperture radars.

Synthetic aperture radar is a coherent radar that uses the motion of a moderately broad physical antenna beam to synthesize a very narrow beam, thus providing fine azimuthal (along-track) resolution (Brown and Porcello, 1969; Harger, 1970). Fine range (cross-track) resolution is achieved by transmitting either very short pulses or longer coded pulses which are compressed by matched-filtering techniques into equivalent short pulses. Usually, the coded pulse is a waveform linearly modulated in frequency.

Historically, in SAR systems, the phase history of a scattering point in the scene is recorded on photographic film as an anamorphic (astigmatic) Fresnel zone plate. The parameters of the zone plate are set in the azimuth direction by the Doppler frequencies produced by the relative motion between the sensor and the point scatterer, and in the range direction by the structure of the transmitted pulses. The film image is a collection of superimposed zone plates representing the collection of point scatterers in the scene. This film is used by a coherent optical processor (a set of spherical and cylindrical Fourier transform lenses) which focuses the anamorphic zone plates into the points which produced the microwave scatter of the scene (Kozma, et al., 1972).

Recently, SAR systems have employed digital techniques to both record and process the data. Digital processing typically uses matched filtering techniques to "dechirp" the signal in range, while Fast Fourier Transform (FFT) techniques achieve the required azimuthal compression of the SAR Doppler history (Ausherman, 1980). After appropriate system corrections, digital data have better geometric and radiometric fidelity than optical data and are subject to fewer image processing artifacts such as noise streaks. Additionally, digital data recorded in square root mode can store 40 dB

worth of information. In contrast, an optical SAR image has only an 18 dB dynamic range. A disadvantage of digital SAR data is that processing algorithms are quite slow, particularly when one-look (full resolution) data are required. Due to long processing times (originally, 8 hours for a 100 x 100 km Seasat scene, which has now been reduced to 2 to 3 hours), a limited amount of digital Seasat SAR data exists. The optical processing time for a 100 x 100 km scene is approximately one minute, excluding set-up or film development.

The Seasat SAR's 99 day mission and sensor description is best summarized by Beal, et al. (1981). Specific parameters of the Seasat SAR system are presented in Table 1, and the discussion at present will be confined only to pertinent parameters of the Seasat SAR that affect the detection of submerged hazards. The wavelength at which the Seasat SAR system operates, 23.5 cm, does not penetrate more than a few centimeters into the water surface. Therefore, the recorded signal is primarily reflected from the water's surface and is a function of the surface roughness, slope, and motion of the scatterers. The 23.5 cm wavelength will also determine the ocean wavelength (Bragg wave) to which the SAR is most sensitive. The Bragg ocean wavelength for resonance for the Seasat SAR parameters is approximately 36 cm. Later in this discussion, the equation to predict this value from the radar wavelength and viewing angle (incident angle) will be presented. The bandwidth and incident angle, given in Table 1, determine the ground range resolution. The range to target, velocity, azimuth resolution and antenna dimensions are information that can be utilized to determine the synthetic aperture length. Thus, this information indicates that in order to achieve an azimuth resolution of 6.25 m on the ground, a synthetic aperture length of approximately 16 km is required. Seasat (operating at an 800 km altitude) had an orbital speed of 7.8 km/s, and therefore required about two seconds to synthesize the required aperture (see Jordan, 1980).

TABLE 1
RADAR PARAMETERS OF THE SEASAT SYNTHETIC APERTURE RADAR (SAR)

| | |
|---|---|
| Frequency | 1274.8 MHz |
| Wavelength | 23.5 cm (L-band) |
| Transmitted Bandwidth | 19 MHz |
| Pulse Duration | 33.8 μsec |
| Pulse Time-Bandwidth Product | 642 |
| Transmitter RF Power | 800 W Peak – 46 W Average |
| Transmitter Type | Solid-State Bipolar Transmitter |
| PRF | 1647 Hz |
| Satellite Altitude | ~800 km |
| Nominal Range (20°) | ~850 km |
| Antenna Beamwidth, Elevation | ~6° |
| Antenna Beamwidth, Azimuth | ~1° |
| Antenna Pointing Angle | 19-25° off nadir, right side |
| Surface Resolution | 25 m x 25 m (4 look data) |
|    Slant Range Resolution | 8 m |
|    Azimuth Resolution (one look) | 6.25 m |
| Integration Time: | 0.5 to 2.5 sec depending on resolution |
| Image Swath Width | 100 km |
| Image Length | 250 to 4000 km |
| Sensor Power | 60 W, nominal operation |
| Satellite Velocity | ~7800 m/sec |

20

## 3.2  SAR IMAGING MECHANISM - AN INTRODUCTION

The principle in imaging any ocean surface with a radar is that the backscatter of microwave energy (echo) received by the radar contains information on the roughness characteristics (shapes, dimensions and orientations) of the reflecting area. Parameters that influence the SAR image of the ocean surface include the motion of the scattering surfaces, the so-called speckle effect, system resolution and non-coherent integration as well as primary contributions attributable to the effect of wind, waves, surface currents and surface tension. In addition, the orientation of ocean waves and the bottom topographic feature with respect to the radar look direction are influencing factors. When attempting to understand the SAR ocean-surface imaging mechanism, one must also consider factors pertaining to wave orbital velocity, Bragg scatter velocity, long wave (greater than 100 m) phase velocity and surface current velocity (Teleki, et al., 1978).

Several scattering models exist that attempt to explain ocean surface image formation with synthetic aperture radars. These models are of two types: static models that depend on instantaneous surface features, and dynamic models that employ surface scatterer velocities. Considerable debate exists on the limitations and applicability of either model.

Three static models have been suggested to describe the radar scattering of energy from large areas on the ocean surface. These three scattering models include: (1) the quasi-specular model which is most appropriate for small incident angles, (2) the Bragg-Rice scattering model, which correlates well with experimental data for incident angles between 20° amd 60°, and (3) a Rayleigh scattering model which is often used in terrestrial earth scattering calculations. There is general consensus within the radio-oceanography scientific community that a Bragg-Rice scattering theory best explained the Seasat SAR observed backscatter values obtained from the

ocean surface. The Bragg-Rice scattering model is based on a well known phenomena in the study of crystals, grating, and periodic structures. If one considers the random ocean surface to be represented by a combination of periodic surfaces (i.e., spectrum), then the spectrum region which satisfies the backscatter phase matching condition will be the main contributor to the backscatter cross section. Sometimes in the literature, this phase matching of the small ocean Bragg waves with the radar electromagnetic energy is termed a resonance phenomenon; more correctly stated, it should be termed a constructive interference between the electromagnetic and ocean waves.

Pioneering theoretical and experimental work by Wright (1966) at the Naval Research Laboratory (NRL) demonstrated the general validity of a Bragg scattering model for an ocean surface imaged by radar. In a series of wave tank measurements using 3 and 25 cm wavelength continuous wave (CW) Doppler radars, Wright (1966) demonstrated that transmitted radar energy with wave number K interacts in a resonant or interference fashion with ocean surface waves with wave number $K_W$ such that

$$K_W = 2K \sin \theta, \tag{1}$$

where $K_W = 2\pi/L$ and $K = 2\pi/\lambda$, L and $\lambda$ are the wavelengths of the surface waves and the radar, respectively, and $\theta$ is the incident angle. Shuchman, et al. (1981) showed that a Bragg scattering equation also satisfactorily explained the radar backscatter return from SAR using data collected during the Marineland experiment (Shemdin, et al., 1980). It should be noted that radar data of large ocean areas (1 x 1 km) were averaged in that analysis. Thus (based on the above), the principal radar reflectivity mechanism of imaging ocean surfaces is via the capillary and small gravity waves which produce Bragg scattering (Raney and Shuchman, 1978).

Changes in the amplitude of the Bragg waves result in a variety of surface patterns on Seasat and airborne SAR imagery. Many of these patterns are bathymetry-related, but a significant number appear to have no relationship to the bathymetry. Examples of such image features are presented in Appendix A. In order to effectively separate the bottom related anomalies from the others, one must first understand the dynamics of what causes the surface perturbations and then infer why the SAR is imaging them. A discussion of the interactions causing these perturbations is contained in the following section.

## 3.3 EVIDENCE OF BOTTOM-RELATED SURFACE SIGNATURES OBSERVED ON SAR IMAGERY

Recent studies at the Environmental Research Institute of Michigan (Kasischke, et al., 1980; Shuchman and Kasischke, 1979; Shuchman, et al., 1979; and Shuchman, 1982) have demonstrated the potential of using SAR data in providing bathymetric information. The goals of these initial investigations were to evaluate the potential of SARs to provide data for improving nautical chart products, primarily through the detection and location of submerged features hazardous to navigation. As a result of these investigations, five different physical oceanographic phenomena were identified as the agents responsible for the appearance of depth-related features on SAR imagery.

The first type of regularly observed topographically related ocean feature is that associated with changes in wavelength and direction of ocean swell entering coastal regions. Analytical models which incorporate these topographically induced changes in ocean surface gravity wave propagation characteristics can be used to gain an estimate of water depths in coastal regions. When a gravity wave enters a shallow-water region from deep water, its wavelength and direction change in direct proportion to the water depth. By measuring the change in wavelength and/or direction, an estimate of the

water depth can be obtained. Since a SAR can measure both ocean wavelength and direction, this information can be used in a wave re-fraction model to solve for depth to a first order (assuming no strong non-linear interactions; see Arthur, et al., 1952; Wiegal, 1964,). This procedure was successfully demonstrated in studies by Shuchman, et al. (1979); Shuchman and Kasischke (1981); and Kasischke, et al. (1981).

Utilizing linear wave theory and applying Snell's Law, relative changes in wave phase speed are successively calculated relative to a bathymetric grid. Hence, topographically induced changes in both surface wavelength and direction are available at each grid location as a function of water depth. The inverse mathematical problem can then be solved utilizing these observed changes in surface wave prop-agation characteristics and solving for the local water depth.

The second type of observed change in radar backscatter is asso-ciated with an ocean swell propagating over a distinct topographic irregularity in the sea bottom (see Figure 3). Rudimentary SAR/ oceanographic scattering theory indicates that the microwave energy from the  lar is being reflected by the small capillary and ultra-gravity waves present at the ocean's surface. Capillary and ultra-gravity waves have wavelengths between one and fifty centimeters and their generating source is the wind. Any change in this small wave structure will alter the radar backscatter being received by the SAR. When a gravity wave field crosses a sharp depth discontinuity, such as a coral reef surrounding an island, tne structure of the gravity wave is changed. The interaction between the changing gravity wave field and the small capillary/ultra-gravity wave field is sufficient to alter the small wave structure, and hence change the radar back-scatter. Such a phenomenon was noted on SAR imagery of an island area studied by Kasischke, et al. (1980).

The proposed hydrodynamic mechanism responsible for producing the observed change in the small scale ocean surface roughness is as follows. As the ocean gravity wave encounters an abrupt change in the total water depth, the wave begins a transition from a deep to eventually a shallow water wave. As this transformation proceeds, the mass transport and horizontal particle velocity at the surface increases thus straining the small scale surface roughness field and producing a corresponding change in the received electromagnetic backscatter by the radar.

A third class of SAR-sensed surface signatures is produced by a distinct change in radar backscatter which is associated with a strong current flowing over a bottom feature (see Figure 2). Tidal currents flowing over bottom features are often visible on SAR imagery, as the increasing and decreasing of the current velocity influences the surface small wave structure. This hydrodynamic interaction is another means by which bottom hypsographic information can be obtained from SAR data. Since its velocity and internal structure is regulated by the bottom topography, the tidal current will alter the ocean surface Bragg wave amplitude to which the SAR is sensitive. The current's modulation of the ocean Bragg wave amplitude enables successful SAR imaging of ocean bottom features in shallow water.

Several researchers have reported surface signatures on radar imagery which are the result of a current flowing over a bottom feature. DeLoor and Brunsvelt Van Hulten (1978) first described this phenomenon using real aperture radar imagery collected over the North Sea. Using Seasat SAR imagery, Kenyon, et al. (1979) and Kasischke, et al. (1980) have reported detecting sand waves in the southeast corner of the North Sea. McLeish, et al. (1981) reported on sand waves detected on real aperture radar imagery collected off the Dutch coast. Finally, Kasischke, et al. (1980) reported detecting sand waves and ridges in the Nantucket Shoals region off the Massachusetts

coast. Current-induced features were studied in detail during the present study using data over the English Channel, the Nantucket Shoals, and the Tongue of the Ocean.

The fourth type of oceanographic phenomena observed on SAR imagery are classic internal wave patterns over continental shelf regions (see Figure 4). Internal wave packets propagating either shoreward or seaward over a continental shelf or slope region also provide a mechanism permitting SAR detection of changes in bottom topography. The internal wave energy field alters the small capillary and ultra-gravity waves sufficiently so that the internal waves are visible on SAR imagery (Shuchman and Kasischke, 1979).

Since typical length and time scales of internal wave motions are generally very long compared with those of gravity waves, deeper oceanic topographic features can potentially influence the internal wave propagation characteristics. Changes in the velocity field associated with the passage of internal waves over a bottom feature tend to produce strong interactions with the small scale surface roughness. These in turn can result in ocean surface conditions that produce strong radar echoes. These strong wave/wave interactions result because the small capillary and ultra-gravity waves (small scale roughness) tend to possess characteristic group velocities comparable to the phase velocities of the internal waves.

The fifth and final form of bottom related radar signatures have been termed anomalous SAR backscatter patterns (Figures 5 and 6). These signatures are found in deep ocean regions over topographic "bumps" in the bottom. These surface anomalies are of two types. The first type is similar to an internal wave (but not as well structured into wave packets) and has been noticed on SAR images in deep-water areas between major continental shelf boundaries (Shuchman and Kasischke, 1979). The second type is a frontal boundary believed to be the result of deep-water upwelling. One interesting aspect of these surface anomalies is that in large part, they occur over major submarine ridges or seamounts.

It appears that the hydrographic mechanism responsible for the generation of an ocean surface velocity field of sufficient magnitude to perturb the small scale surface roughness must result from a complex interaction and combination of ocean dynamics throughout the water column. In many deep ocean regions, tidal induced motions can be the major cause of water movement. The disturbance of this flow or any other deep ocean flow by large topographic features such as submarine ridges or seamounts may cause a variety of perturbations to the upper level of the water column. These perturbations include deformation of the thermocline, the generation and propagation of Lee waves, and the formation of Taylor column type flows. These disturbances may then interact with the dynamics of the upper ocean. Hence, it appears reasonable to assume that in the vicinity of these deep ocean features, the small scale ocean surface roughness may be altered. The deviation in roughness away from the mean (undisturbed) state, if sufficient in magnitude, will produce a corresponding variation in the recorded radar return.

4
# SURVEY OF SEASAT SAR IMAGERY
(Examples of Bottom Features and Navigation
Hazards Detectable on Seasat SAR Imagery)

The purpose of the analyses presented in this chapter is to fur-
ther document the occurrence of bottom-related surface signatures on
Seasat SAR imagery. The first section (4.1) of this chapter reviews
the data sets utilized throughout the remainder of the report. The
second section (4.2) discusses the analysis procedures utilized in
the broad surveys. Section 4.3 presents surveys of seven shallow-
water test sites and Section 4.4 presents surveys of five areas with-
in the deep-water test site.

## 4.1 DATA SETS

The primary data source for this analysis was radar backscatter
intensities recorded on Seasat SAR data. The data were of two types:
(1) optically processed imagery: and (2) digitally processed imagery.
To better understand the difference between these two data types, a
review of how data from the Seasat SAR system are processed will be
presented. During the collection of SAR data, the Seasat system was
activated by a signal transmitted from a ground receiving station.
Once turned on, the Seasat SAR imaged a ground swath with a width of
100 kilometers and a length up to 4000 kilometers. Because of the
data storage constraints onboard the Seasat satellite, the received
radar echo data from a given pass were transmitted via a dedicated
20 MHz analog data link to the ground for recording on high density
digital tapes. Since the SAR was only operated in view of five re-
cording stations (ULA-Alaska; MIL-Florida; GDS-California; UKO-
England; and SNF-Newfoundland, Canada), the radar imagery coverage
was restricted to those corresponding areas in the Northern Hemi-
sphere. The data on these tapes were processed in one of two ways.
In one type the data on the tapes were re-recorded on a

photographic film. This "signal" film was then optically processed to produce a SAR image. The second method used was to digitally process the data from the high density tape.

The output products from optically processing the SAR signal histories consist of four 70-mm wide film transparencies which contain the entire length of the pass. Each of the four sub-swaths of the SAR imagery contains a 30 kilometer wide swath of data. There are two sources for optically processed imagery, both of which were used as a data source for this study. The Jet Propulsion Laboratory (JPL) produces Seasat SAR imagery with a scale factor of 1:500,000 and a ground resolution of approximately 40 meters. ERIM produces Seasat SAR imagery which has a scale factor of 1:700,000 with a ground resolution of 25 meters. Both of these optically processed output images have been geometrically corrected.

There are several sources for digitally processed Seasat SAR imagery. JPL; MacDonald, Dettwiler and Associates, of Richmond, B.C. (Canada); DFVLR (West Germany); and the Royal Air Force Establishment (United Kingdom). JPL digitally processed data were used in this study. The JPL digital data are available on computer compatible tapes (CCTs). Each CCT contains a single 100 by 100 kilometer scene of data. The data are processed to a 25 meter (4-look) resolution but have not been geometrically corrected. In the analysis discussed in this chapter, film transparencies generated from the CCTs were used. For a further discussion of the advantages and disadvantages of Seasat SAR data products, the reader is referred to Kasischke, et al. (1980).

For the various analyses (i.e., broad survey, multi-temporal, and multi-sensor) performed under this contract, nine different test sites were considered using SAR imagery from 35 different Seasat orbits. The test sites are presented in Figure 8 and Table 2. Summarized in Table 2 are: each test site, its location, the Seasat

TEST SITES

A - TONGUE OF THE OCEAN
B - BERMUDA
C - HAITI
D - SULA SGEIR
E - COOK INLET
F - MISSISSIPPI RIVER DELTA
G - ENGLISH CHANNEL
H - JASIN TEST AREA
I - NANTUCKET SHOALS
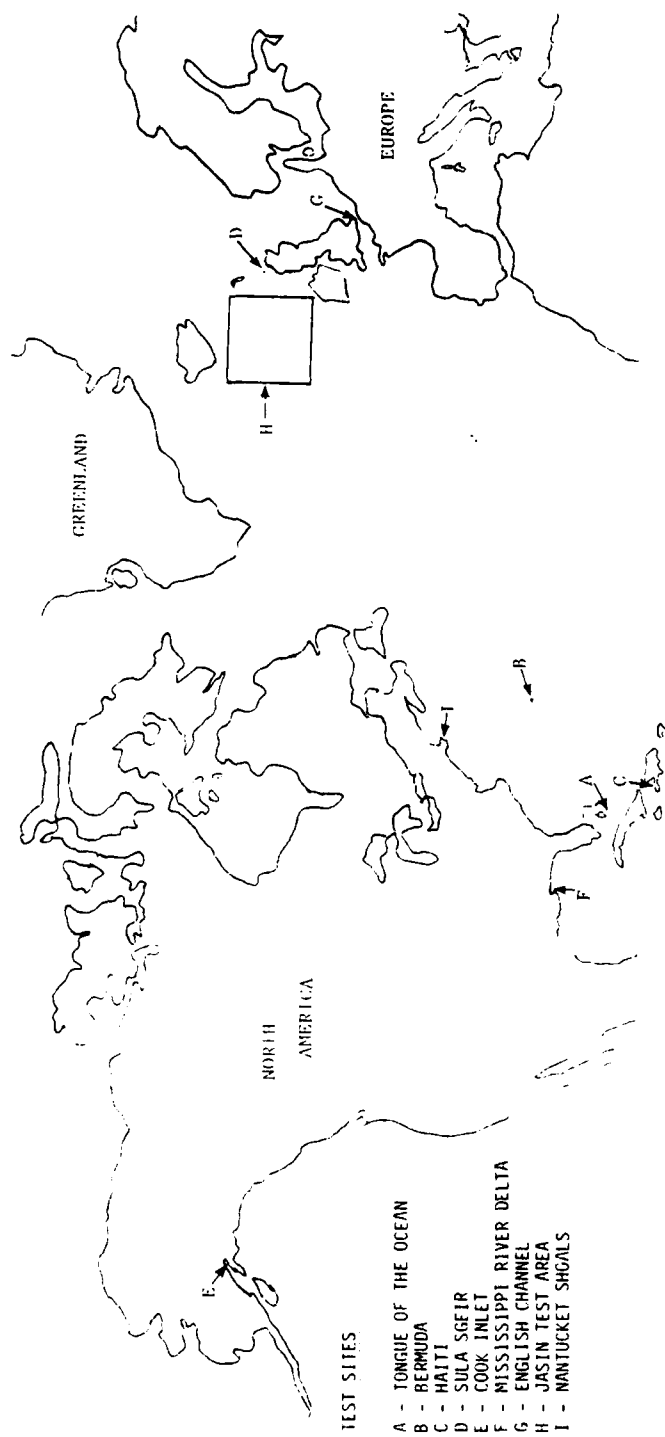
FIGURE 8. LOCATION OF TEST SITES

31

TABLE 2
SUMMARY OF TEST SITES USED DURING EXAMINATION OF SEASAT SAR IMAGERY FOR BOTTOM TOPOGRAPHIC FEATURES

| Test Site | Location | Seasat Revolution | Date | Time (GMT) | Satellite Heading (T) | Bottom Feature* | Analysis Technique** | Report Section or Chapter |
|---|---|---|---|---|---|---|---|---|
| A | Tongue of the Ocean | 450 | 28 July 1978 | 06:23 | 335 | EG, SR | MT | 5.2 |
| | | 529 | 02 August 1978 | 18:37 | 210 | EG, SR | MT | 5.2 |
| | | 694 | 14 August 1978 | 07:37 | 335 | CR, EG, SR | SM, MT | 4.3, 5.2 |
| | | 1024 | 06 September 1978 | 09:18 | 335 | EG, SR | MT | 5.2 |
| | | 1110 | 02 September 1978 | 09:43 | 335 | EG, SR | MT | 5.2 |
| | | 1153 | 15 September 1978 | 09:56 | 335 | EG, SR | MT | 5.2 |
| | | 1196 | 18 September 1978 | 10:09 | 335 | EB, SR | MT | 5.2 |
| | | 1239 | 21 September 1978 | 10:21 | 335 | EG, SR | MT | 5.2 |
| | | 1282 | 24 September 1978 | 10:34 | 335 | EG, SR | MT | 5.2 |
| | | 1325 | 27 September 1978 | 10:47 | 335 | EG, SR | MT | 5.2 |
| | | 1368 | 30 September 1978 | 11:?0 | 335 | EG, SR | MT | 5.2 |
| | | 1411 | 03 October 1978 | 11:12 | 335 | EG, SR | SM, MT | 4.3 |
| B | Bermuda | 1267 | 23 September 1978 | 14:20 | 331 | IS | SW | 4.1 |
| C | Haiti | 493 | 31 July 1978 | 11:28 | 337 | IS, FA | SM, FA | 4.3 |
| D | Sula Sgeir | 762 | 19 August 1978 | 06:41 | 336 | FA | FA | 4.5 |
| E | Cook Inlet | 289 | 17 July 1978 | 05:47 | 227 | SR, MB | SW | 4.5 |
| F | Mississippi River Delta | 393 | 24 July 1978 | 11:50 | 330 | FA | FA | 4.5 |
| G | English Channel | 762 | 19 August 1978 | 06:30 | 330 | SMB, SR | SMB, MT | 4.3, 5.1 |
| | | 957 | 01 September 1978 | 21:40 | 208 | SR | MT | 5.1 |
| | | 1430 | 04 October 1978 | 20:42 | 208 | SR | MT | 5.1 |
| | | 1473 | 08 October 1978 | 00:15 | 208 | SR | MT | 5.1 |

*Bottom Feature Key
CR: Coral Reefs
DWF: Deep-Water Feature
EG: Edge of the Great Bahama Banks
FA: False Alarm
IS: Shoal Area Surrounding an Island
MB: Mud Bank
SR: Sand Banks and Ridges
SMB: Shipwrecks and Buoys

**Analysis Technique Key
DW: Deep Water Survey
FA: False Alarm Analysis
MS: Multi sensor Analysis
MT: Multi temporal Analysis
SW: Shallow Water Survey
SWB: Shipwreck and Buoy Survey

TABLE 2

SUMMARY OF TEST SITES USED DURING EXAMINATION OF SEASAT SAR IMAGERY FOR BOTTOM TOPOGRAPHIC FEATURES (Continued)

| Test Site | Location | Seasat Revolution | Date | Time (GMT) | Satellite Heading (T) | Bottom Feature* | Analysis Technique** | Report Section or Chapter |
|---|---|---|---|---|---|---|---|---|
| H | Jasin Test Area | 547 | 04 August 1978 | 06:15 | 321 | DWF | MT | 5.3 |
| | | 556 | 04 August 1978 | 21:35 | 216 | DWF | MT | 5.3 |
| | | 599 | 07 August 1978 | 21:43 | 215 | DWF | DW, MT | 4.4, 5.3 |
| | | 633 | 10 August 1978 | 06:29 | 323 | DWF | MT | 5.3 |
| | | 642 | 10 August 1978 | 21:50 | 214 | DWF | MT | 5.3 |
| | | 719 | 16 August 1978 | 06:43 | 323 | DWF | MT | 5.3 |
| | | 757 | 18 August 1978 | 22:40 | 215 | DWF | MT | 5.3 |
| | | 762 | 19 August 1978 | 06:41 | 324 | DWF | DW, MT | 4.4, 5.3 |
| | | 791 | 21 August 1978 | 07:24 | 325 | DWF | DW, MT | 4.4, 5.3 |
| | | 834 | 24 August 1978 | 07:30 | 324 | DWF | MT | 5.3 |
| | | 958 | 01 September 1978 | 23:54 | 215 | DWF | DW, MT | 4.4, 5.3 |
| | | 1006 | 05 September 1978 | 08:15 | 322 | DWF | MT | 5.3 |
| | | 1044 | 08 September 1978 | 00:18 | 220 | DWF | MT | 5.3 |
| | | 1049 | 08 September 1978 | 08:27 | 323 | DWF | MT | 5.3 |
| | | 1087 | 11 September 1978 | 00:30 | 221 | DWF | MT | 5.3 |
| I | Nantucket Shoals | 880 | 27 August 1978 | 12:25 | 326 | SR | MS | 6.0 |

*Bottom Feature Key

CR:   Coral Reefs
DWF:   Deep-Water Feature
EG:   Edge of the Great Bahama Banks
FA:   False Alarm
IS:   Shoal Area Surrounding an Island
MB:   Mud Bank
SR:   Sand Banks and Ridges
SWR:   Shipwrecks and Bunys

**Analysis Technique Key

DW:   Deep Water Survey
FA:   False Alarm Analysis
MS:   Multi sensor Analysis
MT:   Multi temporal Analysis
SW:   Shallow Water Survey
SWR:   Shipwreck and Buoy Survey

33

orbit(s) which covered that test site (and were used in this study), the date, time and heading of each orbit, the bottom feature being considered in each orbit, the type of analysis performed for each orbit, and the section of the report where that analysis is presented.

Other remotely sensed data presented in this report include data collected by Landsat and Skylab. Digital Landsat data obtained from the EROS data center were used during the multi-sensor analysis (Chapter 6). Also used during this analysis was Skylab photography.

For each of the test sites considered, hydrographic charts were obtained to determine the bottom topography. It is realized that hydrographic charts do not always give a totally accurate portrayal of the der h soundings in an area, but it is felt they are sufficient for the purposes of the preliminary surveys being conducted for this portion of the analysis. During further analysis of selected test areas, where relative radar backscatter measurements are correlated to depth readings, more accurate depth readincs were obtained. The hydrographic charts used throughout this report were obtained from the U.S. Defense Mapping Agency and the Institute of Oceanic Sciences (United Kingdom).

The physical oceanic processes present at the time of a given overpass were determined by compiling and analyzing all available meteorological and oceanographic data from the area of interest. These data were included in ship reports, tide tables, tidal current charts, meteorological records, and tide gauge records, and were typically obtained in summary form. The actual sources for these data were numerous and will be identified at the time the data are presented.

## 4.2 ANALYSIS PROCEDURE FOR BROAD SURVEY

To select the study sites presented in this chapter, two data sources were reviewed. The first of these was Seasat SAR imagery

processed by and archived at ERIM. The second source was the JPL digital and optical data archived at NOAA's Environmental Data and Information Service. After a review of the Seasat SAR imagery contained at each data library, nine test sites were selected for further examination.

For each test site, photographs were generated from the SAR image transparencies. From the hydrographic charts of the test sites, clear cell reproductions, to the same scale as the photographs, were generated. By placing these clear cell overlays on the image, it could be determined if the anomalous signature on the SAR image occurred over or near a distinct bottom feature or navigation hazard.

Once a correlation had been established between a bottom feature and a SAR signature, an attempt was made to determine the cause. This was done by compiling a set of ancillary environmental data including tide stage, tidal currents, wind speed and direction, wave conditions and general meteorological conditions. By reconstructing the physical oceanic conditions present in the study area at the time of the Seasat overpass, the cause of the anomalous surface signature present on the SAR image could often be determined.

## 4.3  SHALLOW-WATER TEST SITES

The shallow-water test sites discussed in this section of the report include: the Tongue of the Ocean, Bermuda, Haiti, Cook Inlet (Alaska), Sula Sgeir, the English Channel and the Mississippi River Delta. The English Channel sand banks, as well as the Tongue of the Ocean data, will be further discussed with respect to detection of bathymetric features in Chapter 5, which presents the multi-temporal analysis. The Nantucket Shoal test area, also a shallow water site, will be presented in Chapter 6, which discusses the multi-sensor analysis.

In the remainder of this section, we have placed the SAR imagery and the bathymetry from the same location on facing pages for each test site presented (with the exception of the English Channel ship wrecks data). For each image, the location of the bottom-related surface patterns will be pointed out and the correlating bottom feature identified. Then, all known ancillary environmental data will be summarized, and the responsible oceanic process causing the patterns discussed.

EXAMPLES OF SEASAT SAR

DETECTED SHALLOW WATER BOTTOM FEATURES
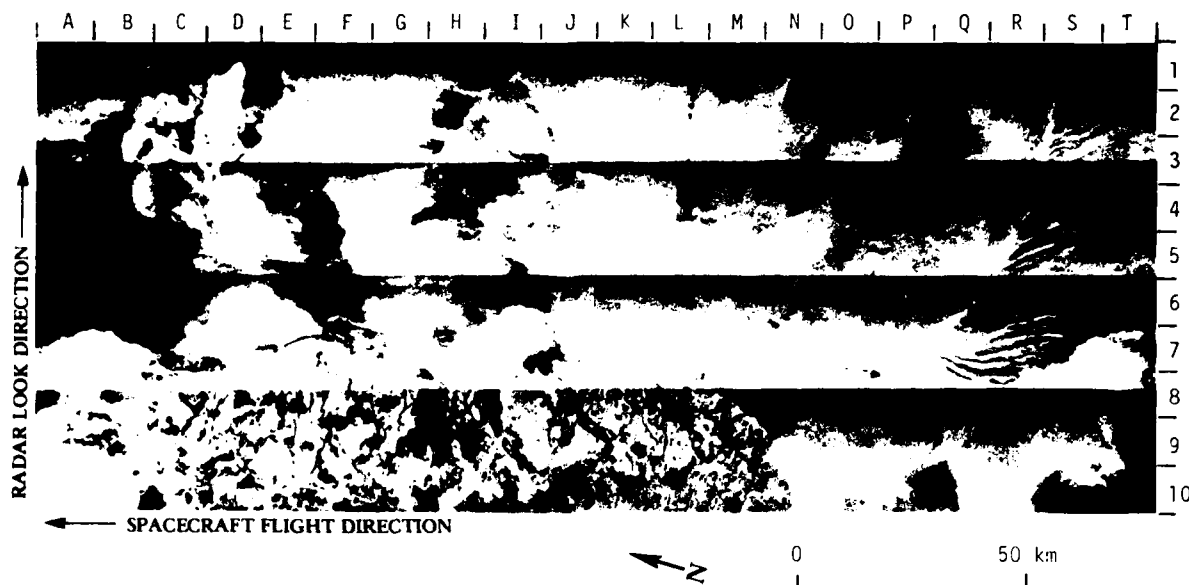
FIGURE 9. SEASAT SAR IMAGE OF TONGUE OF THE OCEAN. (Rev. 1411. Optically Processed Image Courtesy of JPL.)

The Tongue of the Ocean (TOTO) is a large (approximately 30 by 120 km) steep-walled channel within the Great Bahama Bank. The Tongue of the Ocean has a depth of well over 1300 meters, whereas the Great Bahama Bank is generally no deeper than 6 meters. The Seasat SAR imaged this part of the Caribbean on fifteen separate occasions. An example of this imagery is presented in Figure 9 (Revolution 1411, collected on 3 October 1978), and the hydrographic information for this area is presented in Figure 10.

Two bottom features are clearly in evidence on the SAR image. The edge of the Great Bahama Bank (O7 to R1, N1 to N4, and L4 to D4) is delineated by a continuous bright line in Figure 9, and the position of this feature corresponds to the 200 meter contour in Figure 10. The tidal bar belts which border the southern edge of the TOTO (indicated by the 6 meter contour in Figure 10) are clearly reflected on the SAR image (R7 to S1). The SAR surface patterns associated with the tidal bar belts in Figure 9 have a banded appearance, with a bright radar return along their western edge and a dark return along their eastern edge. These tidal bar belts are sand ridges which have one to two meters of water over their crests and are seven to nine meters deep in their troughs.
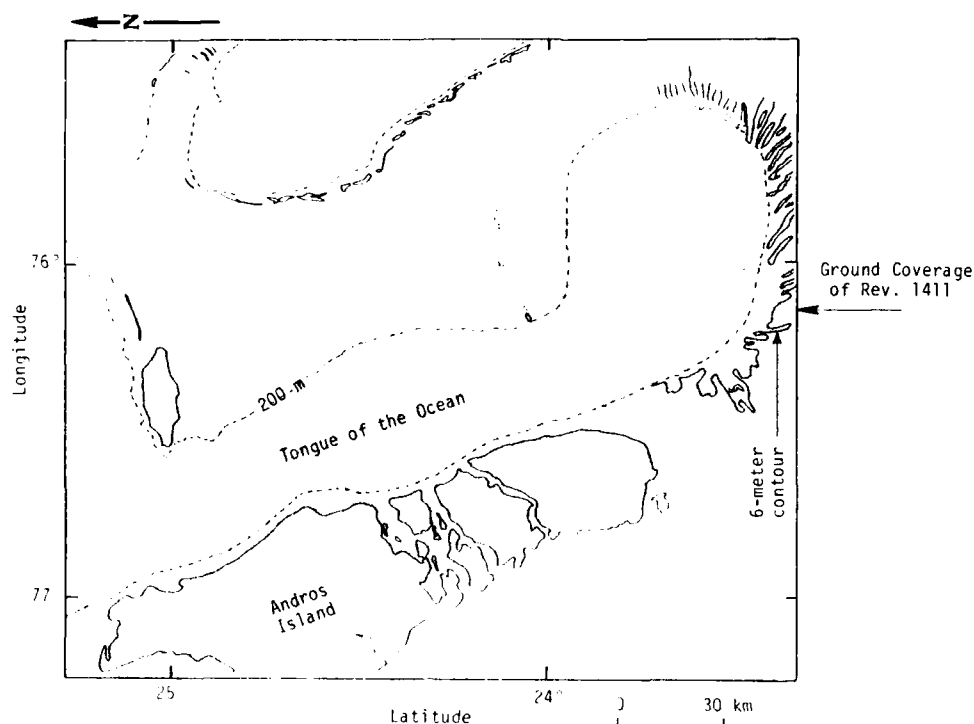
FIGURE 10.  MAJOR BOTTOM FEATURES OF THE TONGUE OF THE OCEAN
AND SAR GROUND TRACK OF SEASAT REV. 1411.  (After
DMA Chart No. 26300.)

Weather records for this date indicate a light wind (2.5 m/s) from the north.  Tide tables (Kline, 1978) indicate the tidal stage was three hours before low water, resulting in a tidal current flowing off the Great Bahama Bank into the TOTO.

Of the possible physical oceanographic mechanisms responsible for generating ocean surface expressions visible on spaceborne SAR imagery, the following appear most plausible for the patterns present in Figure 9:  (1) the strong tidal-driven flow of water over the tidal bar belts and off the Great Bahama Bank over the sharp bottom discontinuity of the edge of the TOTO may sufficiently disturb the small scale surface roughness structure (i.e., capillary and ultra-gravity waves) present with the light wind reported to cause a corresponding change in backscatter; and (2) although not reflected in the weather records, a remnant sea or short-period swell may also have been incident on the edge of the Great Bahama Bank.  The interaction of this surface gravity wave field with the tidal current flowing over the tidal bar belts or off the bank, or with the sharp depth discontinuity of the edge of the bank itself, may have produced the SAR-observed surface expressions.
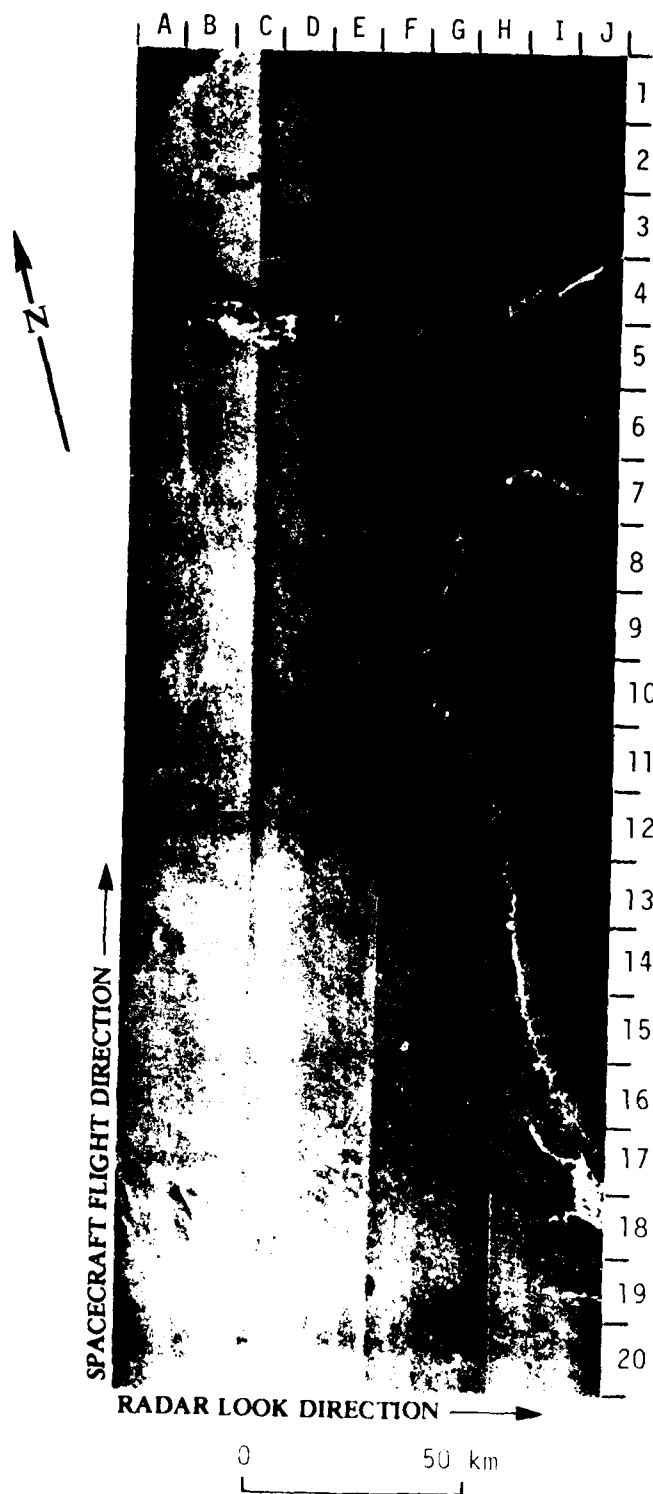
FIGURE 11.    SEASAT SAR IMAGE ILLUSTRATING EDGE OF GREAT
BAHAMA BANK.   Rev. 694.   Optically Processed
Image Courtesy of JPL.)

40
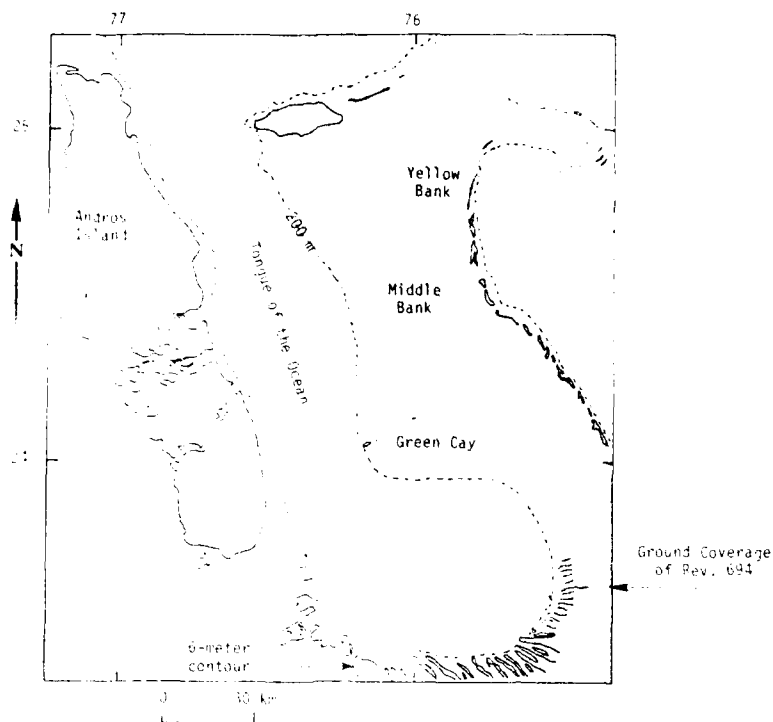
FIGURE 12.   MAJOR BOTTOM FEATURES OF THE TONGUE OF THE OCEAN
             AND SAR GROUND TRACK OF SEASAT REV. 694.   (After DMA
             Chart No. 26300.)

Seasat images collected over the TOTO were also examined to determine whether or not large patches of coral reefs could be detected using SAR data. The eastern portion of the Great Bahama Bank contains three areas of extensive coral reefs:  the Yellow Bank and Middle Ground areas southeast of New Providence Island (G6 to H6 on Figure 11); the area just west of Norman Island (E9): and the area east of Green Cay (B12 to C12).   Each of these areas contains numerous coral reefs (as indicated on DMA Chart No. 26300 and by Kline, 1978) in three to four meters of water.  Figure 11 is SAR imagery collected during Rev. 694 (14 August 1978).  The ground track of this pass is presented in Figure 12.   In Figure 11, the eastern edge of the Great Bahama Bank (A/B4 to A/B11) and the tidal bar belts (A18 to F17) can be inferred via the presence of bottom related surface patterns.  Examination of Figure 11 reveals no detectable surface pattern at the reported position of the reefs.   Imagery from twelve Seasat passes collected over this region was examined.   In no instance did surface patterns appear over the three areas containing reefs.

It appears that both insufficient water flow over the reef structures of the Great Bahama Bank, as well as insufficient surface gravity wave motion, existed to produce the necessary interaction with the subsurface reef structure to produce a visible surface expression.  From previous experience with Seasat SAR imaging of topographic features, it has been documented that, in general, either a strong current (on the order of 0.4 m/s) or a well-developed gravity wave field are required to produce a well correlated bottom topographic signature on the image film.  Ths absence of these two requirements is consistent with the conditions present in large, shallow reef regions.

41

**SPACECRAFT FLIGHT DIRECTION**

**RADAR LOOK DIRECTION ⟶**

N

A

A

0          10 km
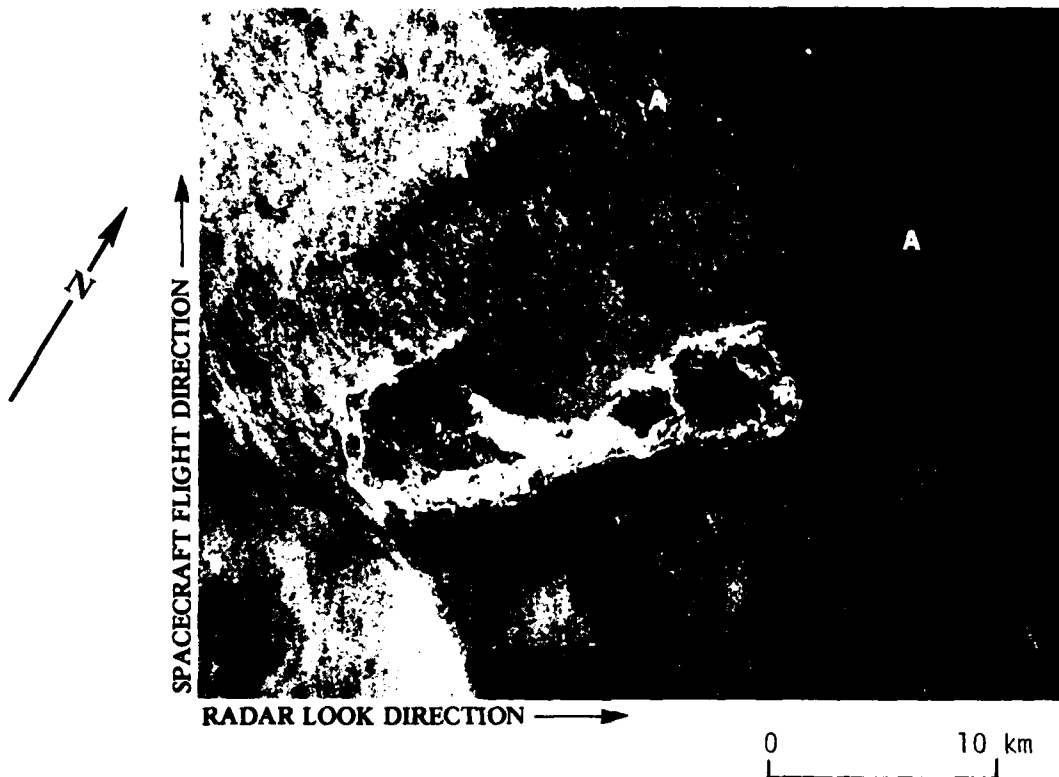
FIGURE 13.    SEASAT SAR IMAGE OF BERMUDA ISLAND COLLECTED DURING
              REV. 1267.   (Image Generated from JPL Digitally
              Processed Data.)

Seasat imaged the island of Bermuda during Revolution 1267 (23
September 1978).  The image produced from JPL-digitally processed
SAR data is presented in Figure 13 and the corresponding hydrographic
chart is presented in Figure 14.

The island of Bermuda and the shoal waters surrounding it were
originally a seamount which had undergone extensive weathering and
then were covered by 35 m of carbonate sediment (Rice, et al., 1980).
The top, horizontal plane of the seamount now has a concave shape in
that its edges are higher, and have shallower water depths, than its
center.  The southern border of the seamount contains the island of
Bermuda while the other borders contain a 3 to 5 km wide rock and
coral shoal.  The water over this shoal ranges from 0.3 to 3.5 m in
depth.  The deeper center of the seamount has a water depth between
6 and 15 m.  Within six kilometers of the island and the outer edge
of the shoal, water depths of greater than 200 m are reached, indi-
cating the steep drop-off of the seamount.

42
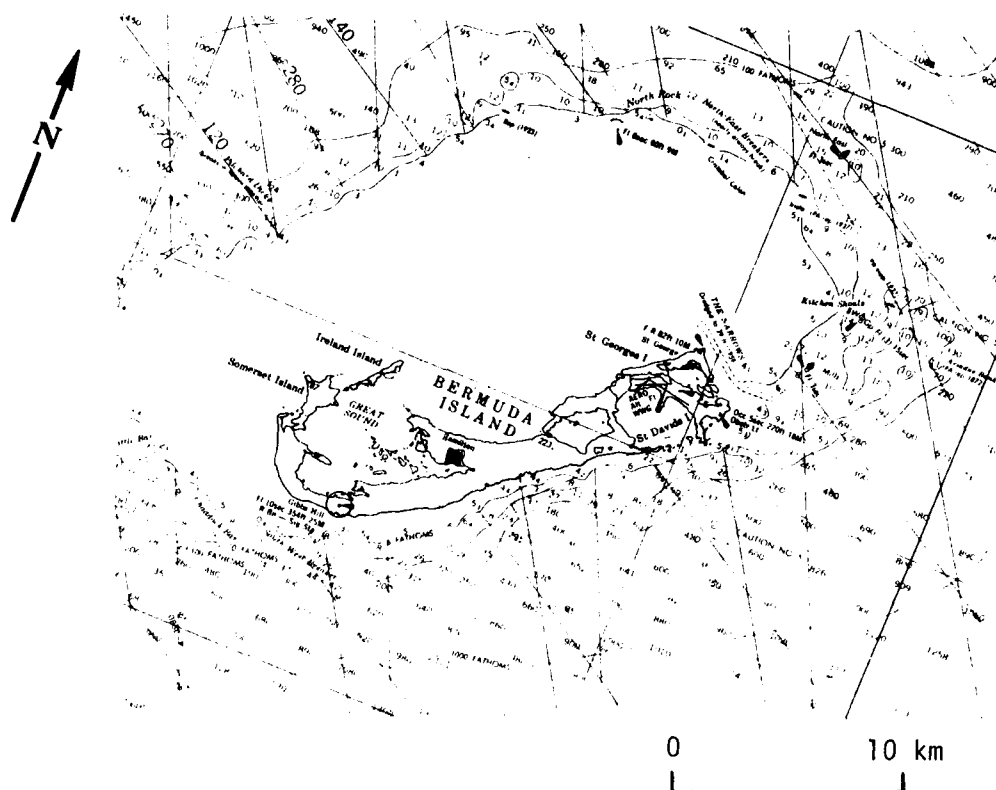
FIGURE 14.    HYDROGRAPHIC CHART OF BERMUDA ISLAND.    (After DMA
              Chart No. 26300, depths in fathoms.)


The position of 0.3 to 3.5 m deep shoal bordering the Bermuda Island seamount coincides with the narrow, dark, oval shaped band which encircles Bermuda (the feature marked A on Figure 13).

Ancillary environmental data were provided by several sources, including the Bermuda Weather Station, Bermuda Harbor Radio, the U.S. Naval Air Station, and U.S. Department of Commerce Tide Tables (NOS, 1978).  These data indicate there was a relatively calm wind (3 m/s from the north) and sea conditions (swell less than 0.5 m in height) present at the Seasat SAR overflight, with the tide in an ebb flow.

Since the surface disturbance is confined to a narrow, oval band encircling the shoal region, it appears that the incident swell is being rapidly dissipated on the outer boundary and damping the capillary/ultra-gravity wave structure created by the light wind.
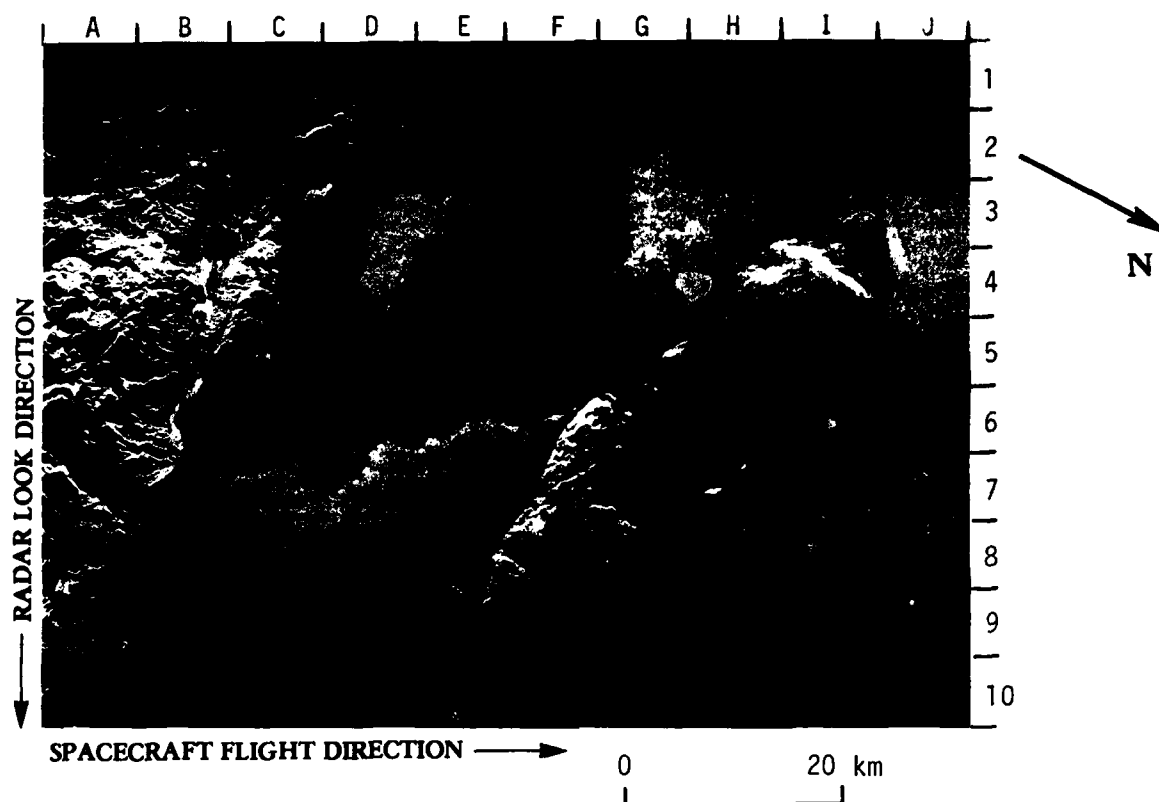
FIGURE 15.  SEASAT SAR IMAGE OF CANAL DU SUD AND GONAVE ISLAND,
HAITI, COLLECTED DURING REV. 493.  (ERIM Optically
Processed Image.)

The western portion of Haiti was imaged by Seasat during Rev. 493
(31 July 1978).  The ERIM optically-processed SAR image of this area
is presented in Figure 15, and the bathymetry of the study area is
presented in Figure 16 (reproduced from DMA chart number 26181,
"Canal De Saint-Marc to Baie Des Baraderes").

There are three distinct surface patterns present in Figure 15:

1.  A distinct boundary between a light and dark area running
    between Gonave Island south to the Haitian mainland (G5 to
    B6),

2.  A distinct S-shaped boundary (between dark and light areas)
    just south of the western tip of Gonave Island (F4 to H1),

3.  An oblong feature half-way between the western tip of Gonave
    Island and the mainland (F3 to F2).

Comparison of the location of these patterns with the hydro-
graphic chart reveals that the first two patterns (1 and 2) do not
appear to be related to any bottom feature, while the third pattern
is related to a bottom feature.
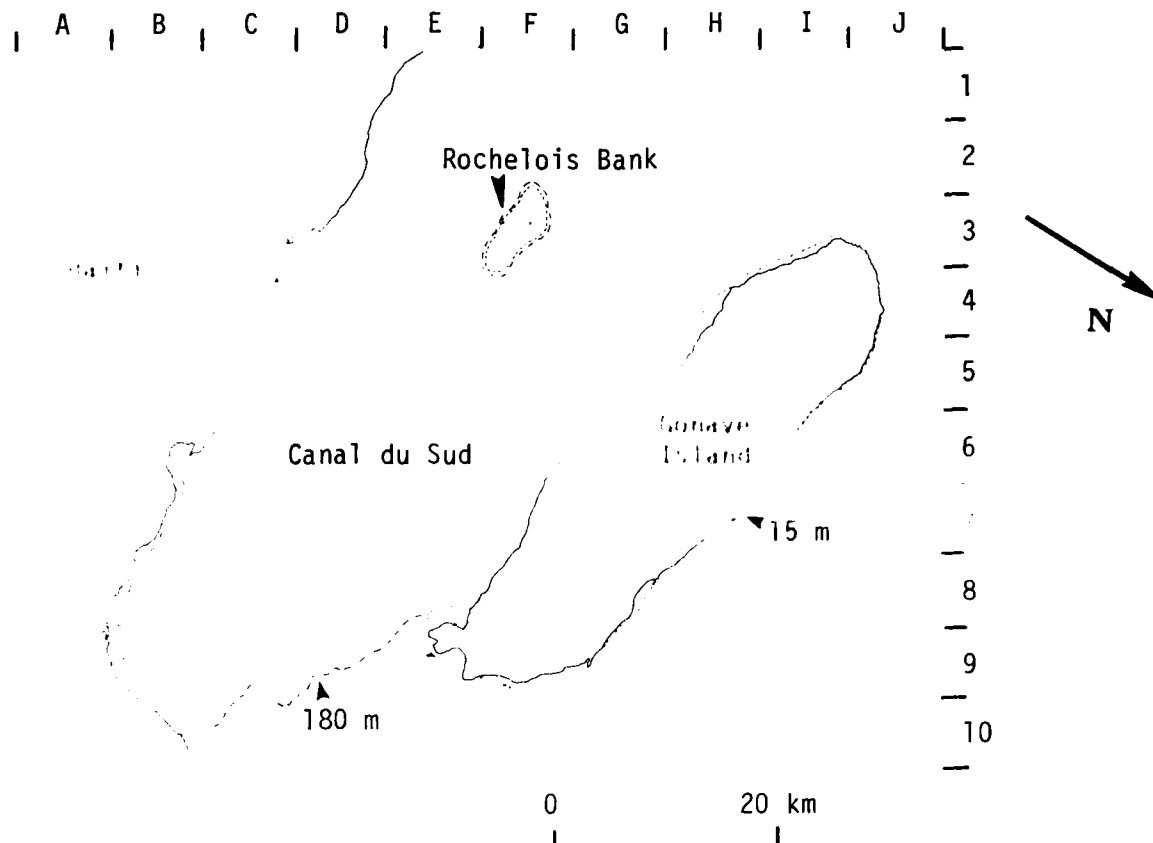
FIGURE 16.   BATHYMETRIC CHART OF CANAL DU SUD AND GONAVE ISLAND
             AND SURROUNDING WATER.   (After DMA Chart No. 26181.)

The location of the oblong feature (F2 to F3) in Figure 15 cor-
responds to the location of the Rochelois Bank (see Figure 16).   This
bank is in the center of the Canal Du Sud and rises from a water
depth of over 2000 meters to within 6 meters of the water's surface.
The boundary of this bank is delineated on the SAR image by a narrow
line, which is lighter than the surrounding water on its south, east
and west sides and darker on the north side (see Figure 15).

Efforts to contact the Haitian government to obtain meteoro-
logical and oceanographic data for this region were not successful.
Therefore, it is difficult to speculate about the exact causes of
the surface pattern over the Rochelois Bank.   The overall appearance
of the surface pattern is quite similar to the pattern observed on
Rev. 762 imagery over the shoal area around North Rona Rock
(Kasischke, et al., 1980), suggesting a gravity wave interaction with
the bottom.   The narrow, dark streak over the northern edge of the
bank is quite similar to the tidal current-induced pattern which was
observed on SAR imagery collected over the edge of the Great Bahama
Bank (see Figure 9).   The data in Figure 15 represents an area for
further research, if sufficient surface truth data can be obtained.

45
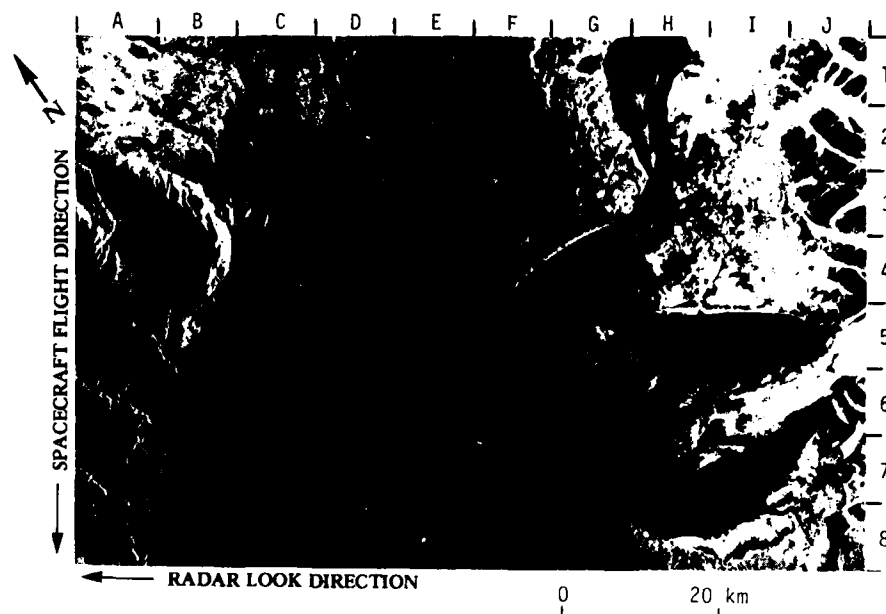
SEASAT SAR IMAGE OF COOK INLET, ALASKA.  (Collected
Rev. 289.   Image Generated from JPL Digitally

Seasat imaged the Cook Inlet region of Alaska during Rev. 289
(17 July 1978).  Figure 17 is a SAR image from Rev. 289 showing the
Cook Inlet.  This image was generated from the digital data.  Figure
18 presents the hydrographic chart of the Cook Inlet.  This figure
was generated from National Ocean Survey Chart Number ("Cook
Inlet, Northern Part; 21st Edition, October, 1980").  Weather conditions
at the time of the Seasat overflight (obtained from the Arctic En
vironmental Data Center, Anchorage) indicate a 6 m/s wind from
160°(T) with gusts up to 10 m/s was present.  The tide tables (NOS,
1978a) for this area indicate that the tide stage was one hour after
high tide (i.e., ebb flow) with a height of 3.5 meters above mean
low water.

Four areas were identified on Figure 17 where surface patterns
occurred on the SAR imagery which were believed to be related to a
bottom feature.  In the Cook Inlet there is a shoal which extends 30
kilometers southwest of Fire Island.  This shoal is clearly visible
on the Seasat SAR image as an area of lighter tone than the sur-
rounding deeper water (F6 to E8).  The shallowest portion of this
shoal is in 4 meters of water, while the rest of the shoal is in
approximately 14 meters of water using the tidal stage predicted from
the tide tables.  The surrounding deeper water has a depth of approx-
imately 30 meters.

The arcuate shaped, bright return just south of Fire Island (G6/
G7) correlates with a shoal in 8 meters of water, which is surrounded
by water 21 meters deep.

46
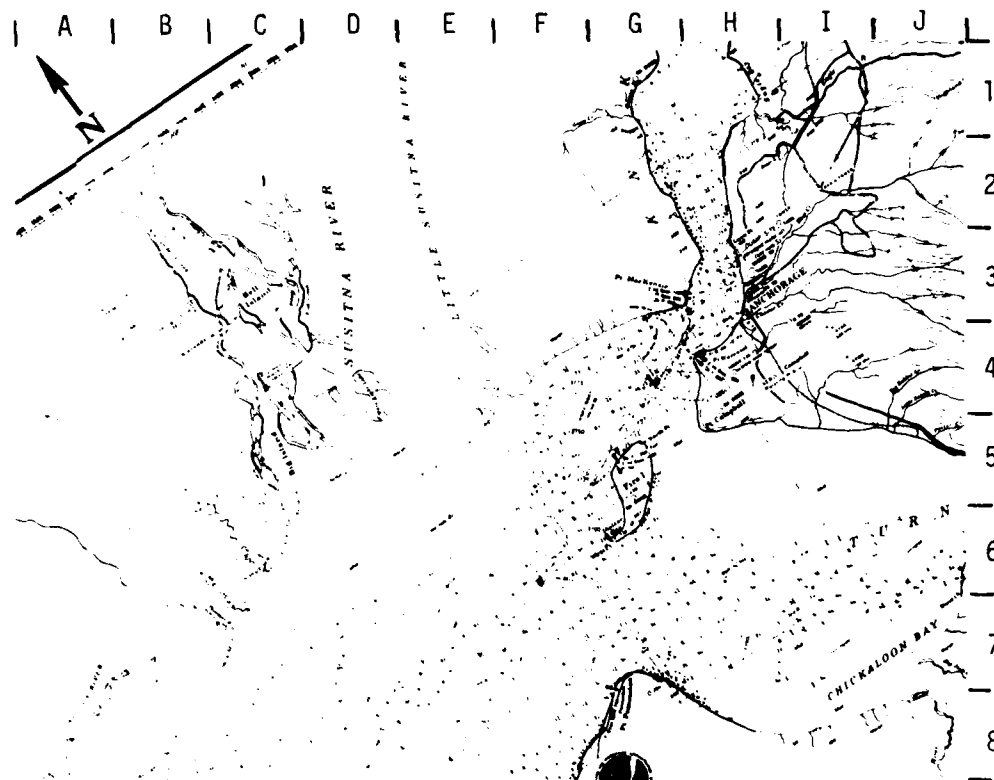
FIGURE 18.   HYDROGRAPHIC CHART OF COOK INLET.  (After National Ocean Survey Chart No. 16660, depths in fathoms.)

The shoal west of Fire Island (F5 to F6) is the subject of special Cautionary Note "C" on NOS Chart Number 16660: "The shoal charted at 61°08'45", 150°22'30", has shifted 650 yards in a south-easterly direction. Mariners should exercise caution when navigating in this area as the 5-fathom depth contour is now approximately 150 yards from the center line of the Pt. Mackenzie Range." This shoal is clearly visible on the SAR image and has a banded appearance, being bright on the north side and dark on the south. The shoal it-self is in about four meters of water, while the surrounding deep water is about 20 meters deep.

The banks of the Susitna River Delta (F4 to C7) are the sub-ject of Note "B" on NOS Chart Number 16660: "Area is sub-ject to continual change. Caution should be exercised when navigating." A darker area bounded by a bright return occurs in the image and serves to delinate the edge of the mud banks off the Susitna. These topographic/sea surface interactions appear to have been documented by Shuchman (1982) and others in the literature. Regions such as these which are subject to extreme tidal current irregularities provide sufficient disturbance to the surface of these features to cause straining of the surface, capillary and gravity wave structure. In turn, this modification of the SAR return by the small scale structure produces tonal variations in the SAR image.
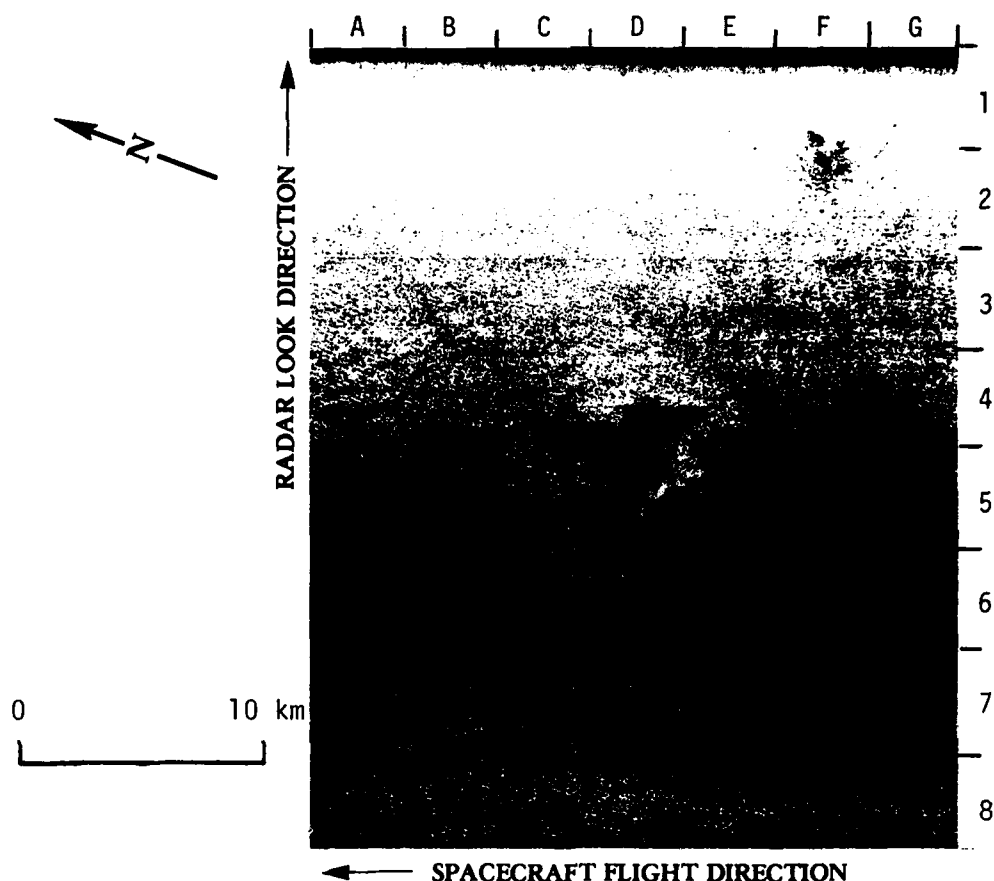
FIGURE 19.   SEASAT SAR IMAGE OF THE ISLAND OF SULA SGEIR AND THE
             SULISKER BANK COLLECTED DURING REV. 762.  (ERIM
             optically processed image.)

The SAR image presented in Figure 19 was collected by Seasat during Revolution 762 (19 August 1978) as the satellite passed over the islands of Sula Sgeir (D5) and North Rona Rock (F1/F2). These islands are located approximately 75 kilometers northwest of Cape Wrath, Scotland, approximately 50 kilometers southeast of the edge of the continental shelf. The corresponding hydrographic chart for this region is presented in Figure 20, which was reproduced from DMA Chart Number 35200 ("Butt of Lewis to Thurso Bay").

The L-shaped feature north of Sula Sgeir (C4 to D5) extends out to approximately the 50 fathom line, but no distinct bottom feature is shown on Figure 20 in this area. The Sulisker Bank extends about 15 kilometers south of Sula Sgeir. It rises to a depth of less than 25 fathoms (45 meters) from a surrounding deep water area of over 40 fathoms (75 meters). Careful examination of Figure 19 in this area (D/E6 to D/E8) reveals the existence of a very subtle tonal variation on the SAR image, which is slightly lighter over the reported position of the Sulisker Bank.
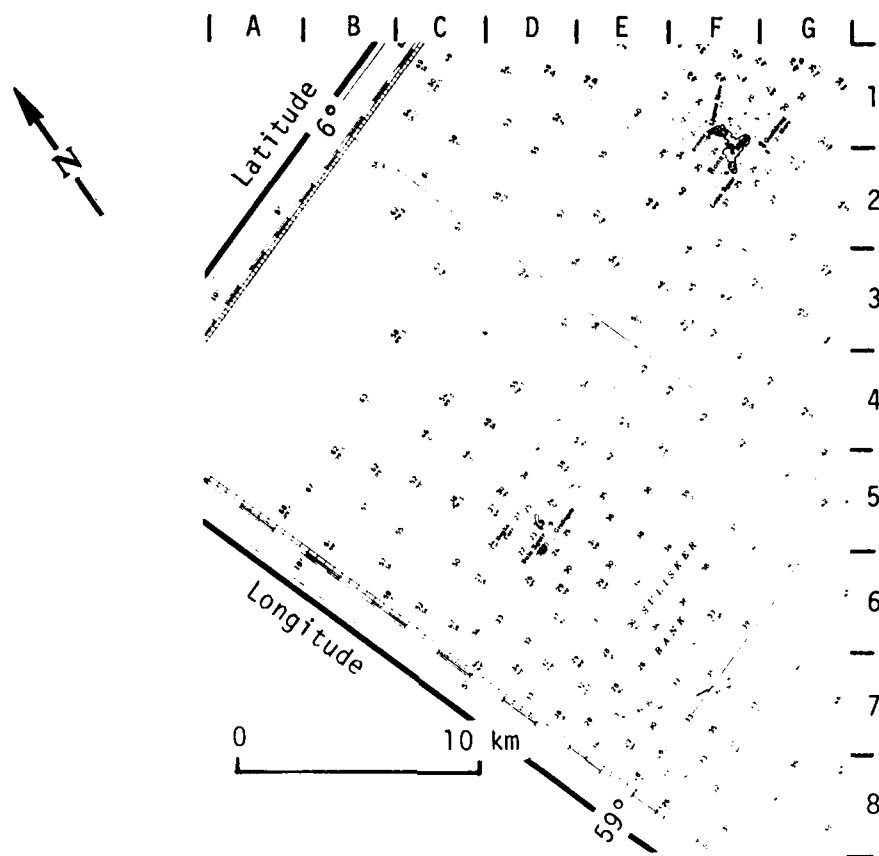
FIGURE 20.  HYDROGRAPHIC CHART OF SULA SGEIR AND THE
SULISKER BANK.  (After DMA Chart No. 35200,
depths in fathoms)


Surface observations made at the same time as the Seasat over-
flight indicate there was a strong wind (>10 m/s) from the south and
a wave field with a significant wave height of greater than five
meters, a dominant wavelength of 210 meters, and a direction of pro-
pagation of 60° (T).

Previous investigations (Kasischke, et al., 1980) revealed the
existence of a distinct tonal variation over the bank surrounding
North Rona Rock (which has approximately the same depth as the
Sulisker Bank), on imagery collected during Rev. 762.  Why a distinct
pattern is present in one case, and not the other, is not yet well
understood.  These two areas certainly represent an area for future
research.
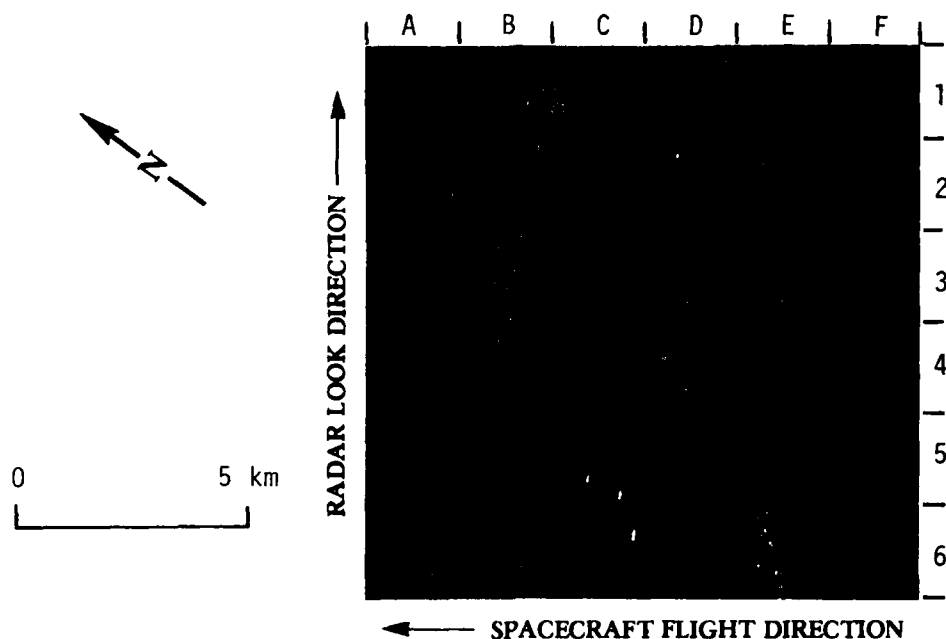
FIGURE 21.   SEASAT SAR IMAGE OF A SHIP WAKE COLLECTED DURING
             REV. 762 OVER THE ENGLISH CHANNEL.  (JPL digitally
             processed data, geometrically and radiometrically
             corrected at ERIM.)

Throughout the examination of Seasat SAR imagery of ocean
regions, numerous examples of ships and their wakes have been noted.
Figure 21 presents an example (D2 to D3) of a ship and its wake col-
lected during Revolution 762 (19 August 1978).   The bright Kelvin
(V-shaped) wake is visible, as is the long, dark turbulent wake be-
hind the ship.   Note how the image of the ship is displaced to the
right of the wake.   This happens because the ship's radial velocity
causes a shift in its signal histories, when recorded by the SAR,
relative to the more stationary water surface.   Theoretically, moored
navigation buoys that are in a current could also produce wakes which
might then be detected on SAR imagery.   Similarly, a current flowing
over or around a shipwreck might also be detectable.

An extensive analysis of Seasat SAR imagery collected during Rev.
762 over the Southern Bight of the North Sea was conducted to deter-
mine if shipwrecks and buoys could be detected on Seasat SAR imagery.
This area was selected because it has been extensively studied for
other portions of the DMA effort (see Section 5.1) and therefore
sufficient ancillary information exists, and also because this area
contains numerous charted buoys and shipwrecks.   The complete analy-
sis conducted for this study is presented in Appendix B.

Figure 22 presents an example of two surface patterns which are
believed to be surface signatures of buoy wakes (B5/B6).   These ex-
tremely subtle striations occur at the reported positions of two
buoys.   A sample of 32 buoys and 91 shipwrecks were randomly selected
from the study site.   The positions of these buoys and shipwrecks
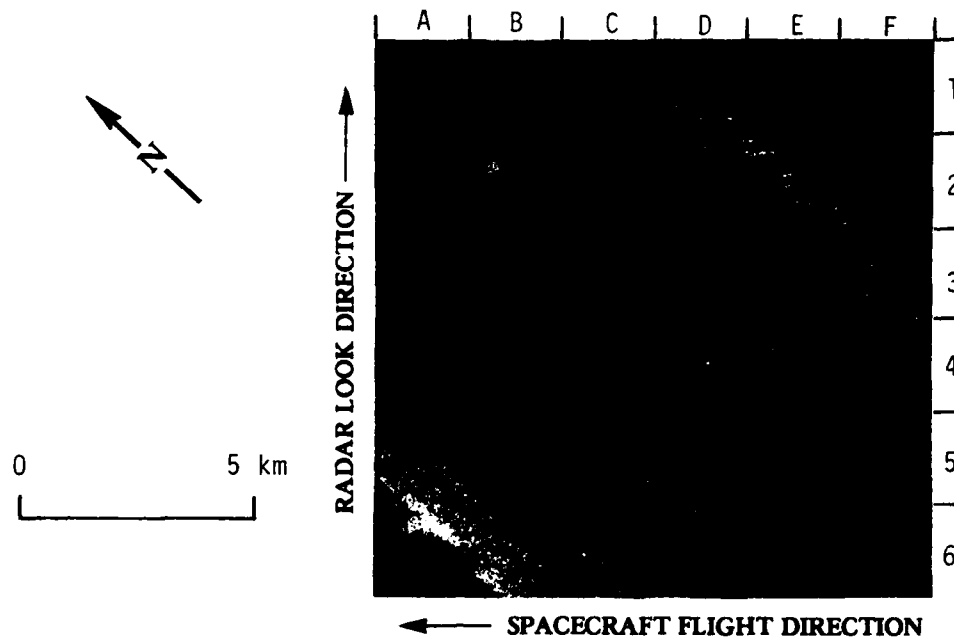
FIGURE 22. SEASAT SAR IMAGE OF BUOY WAKES IN THE ENGLISH CHANNEL COLLECTED DURING REV. 762. (JPL digitally processed data, geometrically and radiometrically corrected at ERIM.)

were marked onto a clear-cell overlay which was then placed over the Seasat SAR image. This composite was then examined to determine if any anomalous surface pattern existed at or near the marked positions.

The study revealed that only 19 percent of the buoys and 16 percent of the shipwrecks were detected on the SAR imagery. Several trends in the ancillary data were noted. As expected, the probability of detection of both buoys and shipwrecks increased with an increase in current velocity and also increased for submerged shipwrecks with a decrease in water level over the wrecks.

Although the Seasat SAR had a relatively low detection rate for shipwrecks and buoys in the English Channel, it is difficult to draw any definitive conclusion from the analysis of this data because it is unknown at this time what types of shipwrecks and classes of buoys were being examined. In order to do a more definitive analysis, it is necessary to know the exact position of the buoys and also what type of buoys are being used. The type of buoy will definitely influence the nature of both the SAR reflection from the buoy itself and the size of the wake the buoy is generating. It is also necessary to more clearly determine the types and extents of the shipwrecks being examined. For example, a submerged shipwreck can be anything from the wreck of a fifty foot long vessel covered by sand to a 200 foot ship which is not covered. A clearer identification of the characteristics of the shipwrecks being examined should lead to a better understanding of SAR's ability to detect them.
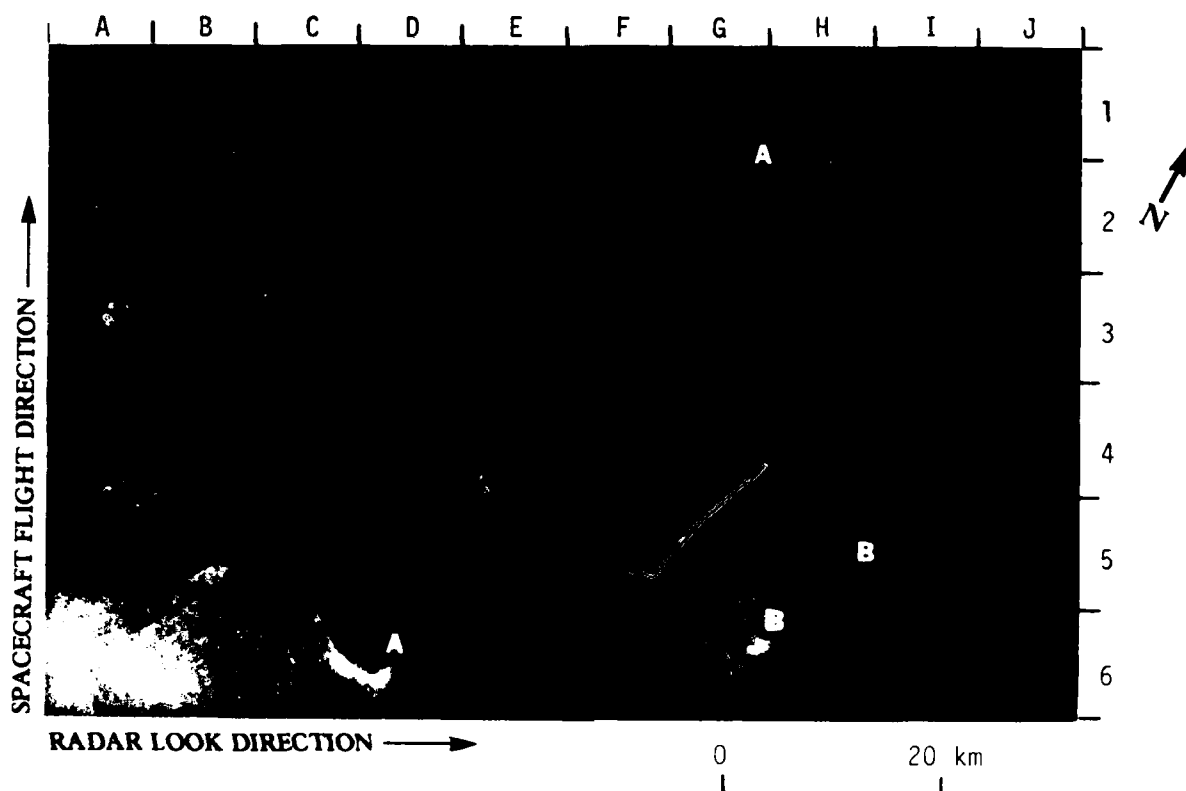
FIGURE 23. SEASAT SAR IMAGE OF THE MISSISSIPPI RIVER DELTA COLLECTED DURING SEASAT REV. 393. (Image generated from JPL digitally processed data.)

The image in Figure 23 was collected as Seasat passed over the Mississippi River Delta during Revolution 393 (24 July 1978). The hydrographic chart for this area is presented in Figure 24. In Figure 23, the positions of frontal boundaries found off of river mouths are marked "A". The bright point returns are believed to be oil platforms. The striped, finger-like signatures, marked "B" on Figure 23, are quite similar to bottom-related signatures found in past studies over sand banks and shoals. A comparison of the positions of these features to the bathymetry in Figure 24 indicates no significant bottom feature occurs near the SAR signatures, and perhaps represent frontal boundaries between Gulf of Mexico water and fresh water outflow from the Mississipi River Delta.
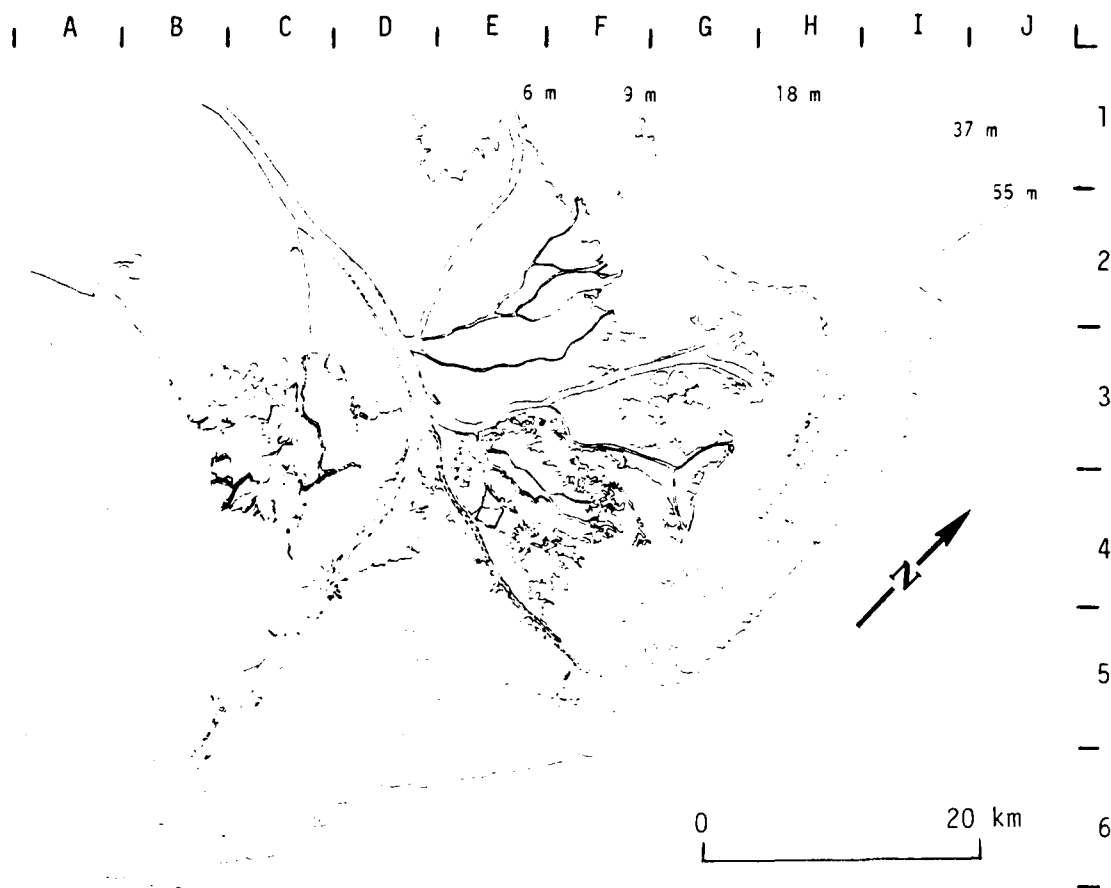
FIGURE 24.   HYDROGRAPHIC CHART OF THE MISSISSIPPI RIVER DELTA.
(After National Ocean Survey Chart No. 1272)


The features marked "B" on Figure 23 represent examples of false-alarms.  A false-alarm is defined as a pattern on a SAR image that was first thought to be related to a bottom topographic feature, but when the existing hydrographic chart for that area was consulted, were found to have no correlation to the existing bathymetry.  Other false alarms found during the survey of Seasat imagery include the L-shaped pattern north of the Sula Sgeir on Figure 19, and several patterns  on the Haiti Imagry (Figure 15).

In summary, the survey of shallow-water test sites continued to document the occurrence of bottom-related surface signatures on Seasat SAR imagery. These surveys substantiated the conclusions of previous studies (Kasischke, et al., 1980) in that additional bottom-related surface patterns were found on Seasat SAR imagery collected from a wide variety of locations.

It should also be noted that no new type of bottom-related surface pattern was found during the present study, and all the patterns observed can be explained in the terms of one of the five categories discussed in Chapter 3.

During the survey of shallow-water test sites, three examples of false-alarms were documented. During the previous study, no false alarms were documented. A false alarm is a surface pattern on SAR imagery which is first identified as being bottom-related, but when compared to the bathymetry of the area, is found not to be related to depth.

## 4.4 DEEP-WATER TEST SITES

During the early examination of Seasat SAR imagery, Shuchman and Kasischke (1979) reported detecting deep-water (>200 meters) internal wave-like signatures which occurred over or near significant bottom features such as seamounts, guyots and submarine ridges. During the present DMA study, a careful examination of SAR imagery collected during the Joint Air/Sea Interaction (JASIN) experiment (Allan and Guymer, 1980) was conducted to further examine the relationship between bottom-related surface signatures in deep-water regions. The JASIN experiment was a multi-national, oceanographic study which occurred in the North Atlantic coincident with the Seasat mission. Extensive sea truth measurements were collected during this period. The location of the oceanographic intensive array, where many of the surface truth measurements were collected during JASIN, is presented in Figure 25.
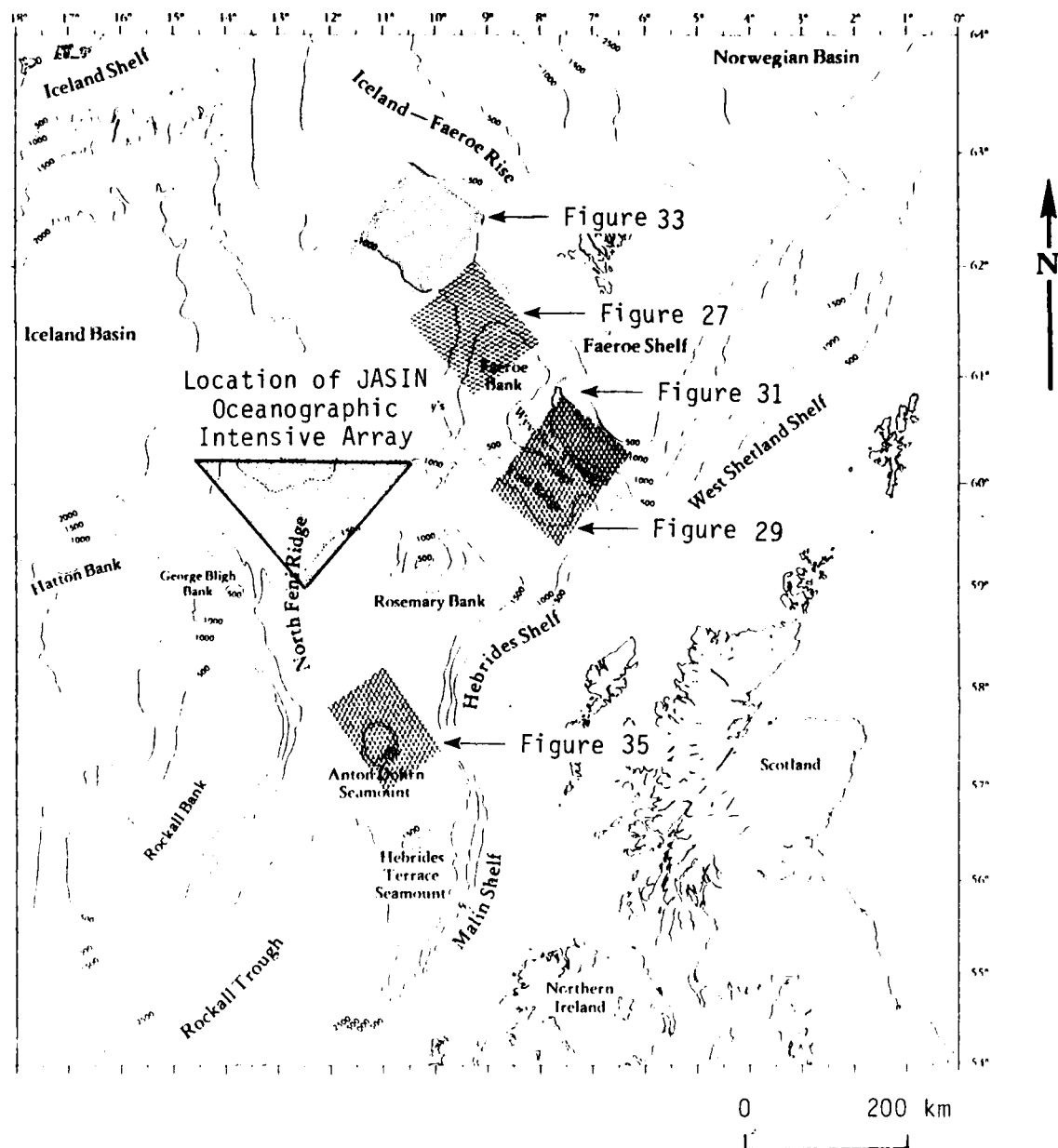
FIGURE 25. LOCATIONS OF JASIN TEST AREA AND AREAS EXAMINED
DURING DEEP-WATER SURVEY. (After Institute of
Oceanic Sciences Chart No. C6567, depths in
meters.)

The purpose of the data presented in this section is to give examples of SAR signatures which occurred in deep-water regions over topographic features. In all, there are 17 distinct bottom topographic features in the JASIN test area. A more complete discussion of the JASIN SAR imagery will be presented in Section 5.3. This later discussion will also include reasons why the internal wave-like and other anomalous surface patterns are thought to occur in deep water regions. The areas presented in this section are the Faeroe Bank, the Faeroe Ridge, the Faeroe Bank Channel, the Wyville-Thomson Ridge, the Iceland-Faeroe Rise, and the Anton Dohrn Seamount. The positions of the SAR images presented in this section are given in Figure 25.

In the following examples, Figures 27, 29, 31, 33, and 35 were reproduced from the Institute of Oceanic Sciences Chart number C6567 ("Bathymetry of the North Atlantic - sheet 2 - Continental Margin Around the British Isles"). The presentation of the deep-water examples will follow the same format as the shallow-water examples.

EXAMPLES OF SEASAT SAR

OBSERVED DEEP WATER BOTTOM FEATURES
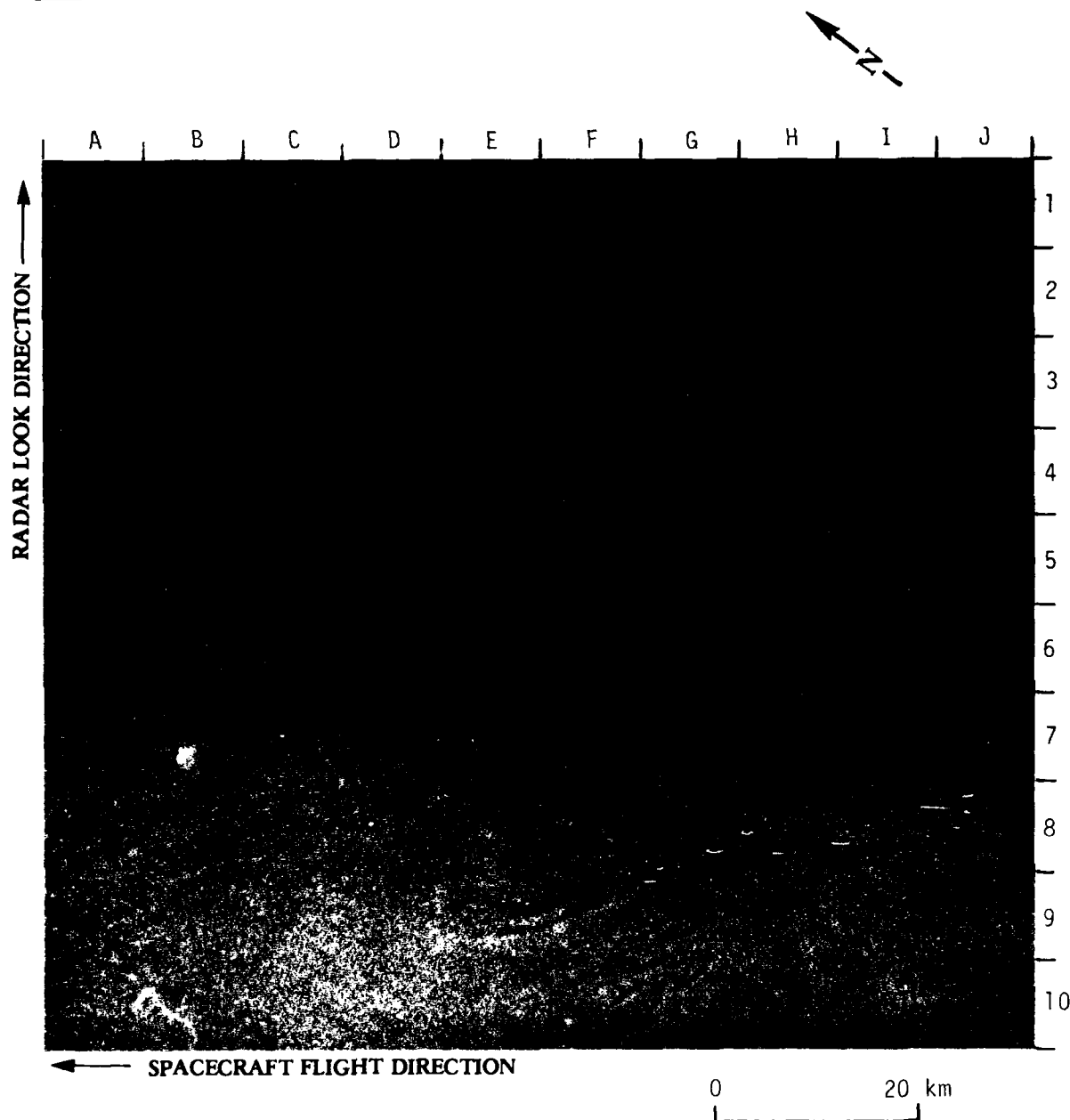
FIGURE 26.   SEASAT SAR IMAGE COLLECTED OVER THE FAEROE BANK DURING REV.
762.   (Image generated from JPL digitally processed data.)

The image presented in Figure 26 was produced from JPL-digitally
processed Seasat SAR data.   These data were collected during Revo-
lution 762 (19 August 1978) as Seasat passed over a portion of the
Faeroe Bank and Faeroe Shelf (see Figure 27).   The numerous "internal
wave-like" patterns in this image appear to be associated with the
Faeroe Bank, the Faeroe Bank Channel and the Faeroe Shelf.
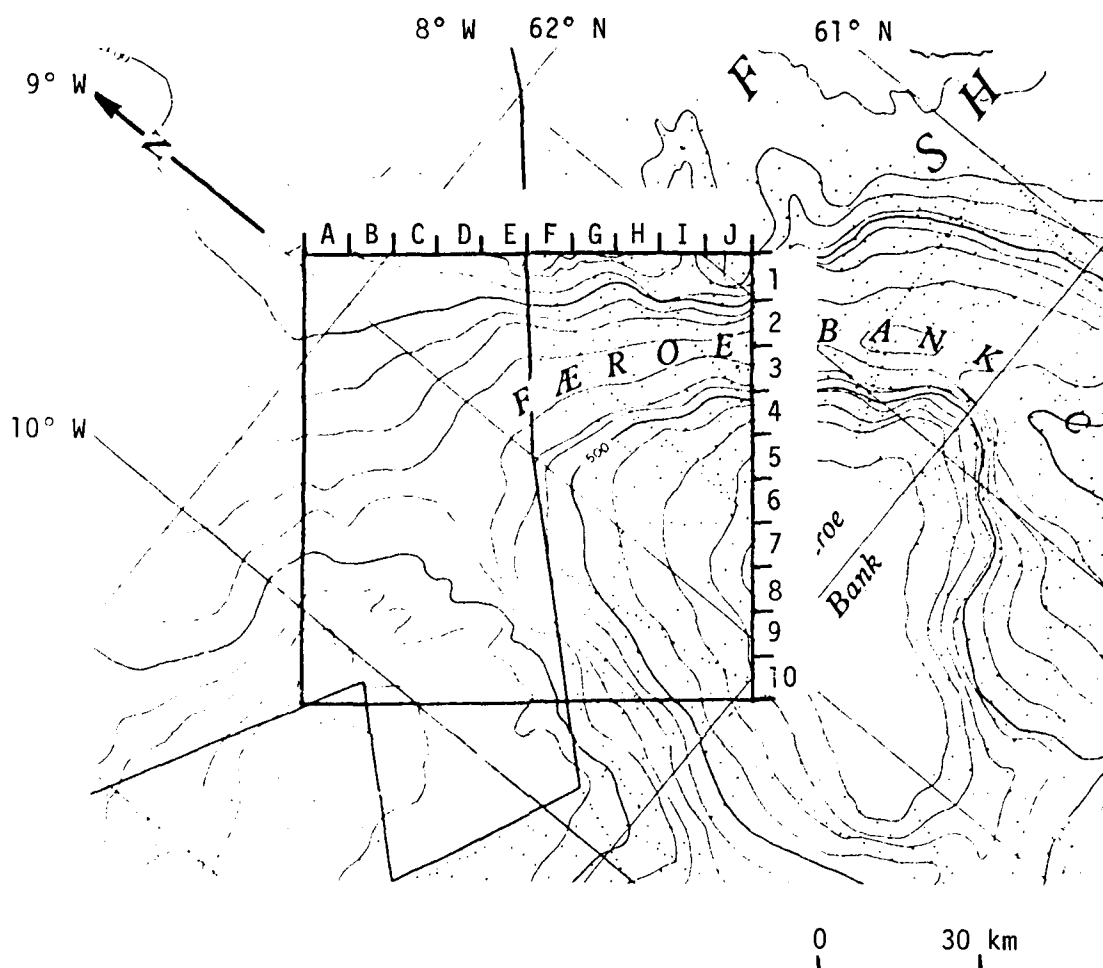
FIGURE 27. GROUND COVERAGE OF SEASAT REV. 762 OVER THE FAEROE BANK.
(After IOS Chart No. C6567, Contour intervals in 100-meter
increments.)

Surface measurements made coincident with the Seasat overpass at
the JASIN test site indicate there was a strong wind (12.5 m/s) from
the south and a swell with a significant wave height of 5.5 meters
and a wavelength of 210 meters, propagating towards $60°$(T).

It appears that topographically induced internal waves propagat-
ing at or near the thermocline (approximately 100 m depth) are inter-
acting with the surface gravity wave field through a kinematic inter-
action similar to that proposed by Phillips (1981). The dark regions
of the "internal wave-like" structures appear to be areas of de-
pressed surface roughness, and hence low radar return.

59

FIGURE 28.  SEASAT SAR IMAGERY COLLECTED OVER THE WYVILLE-THOMSON
RIDGE DURING REV. 599.  (Optically processed imagery
courtesy of JPL.)

60
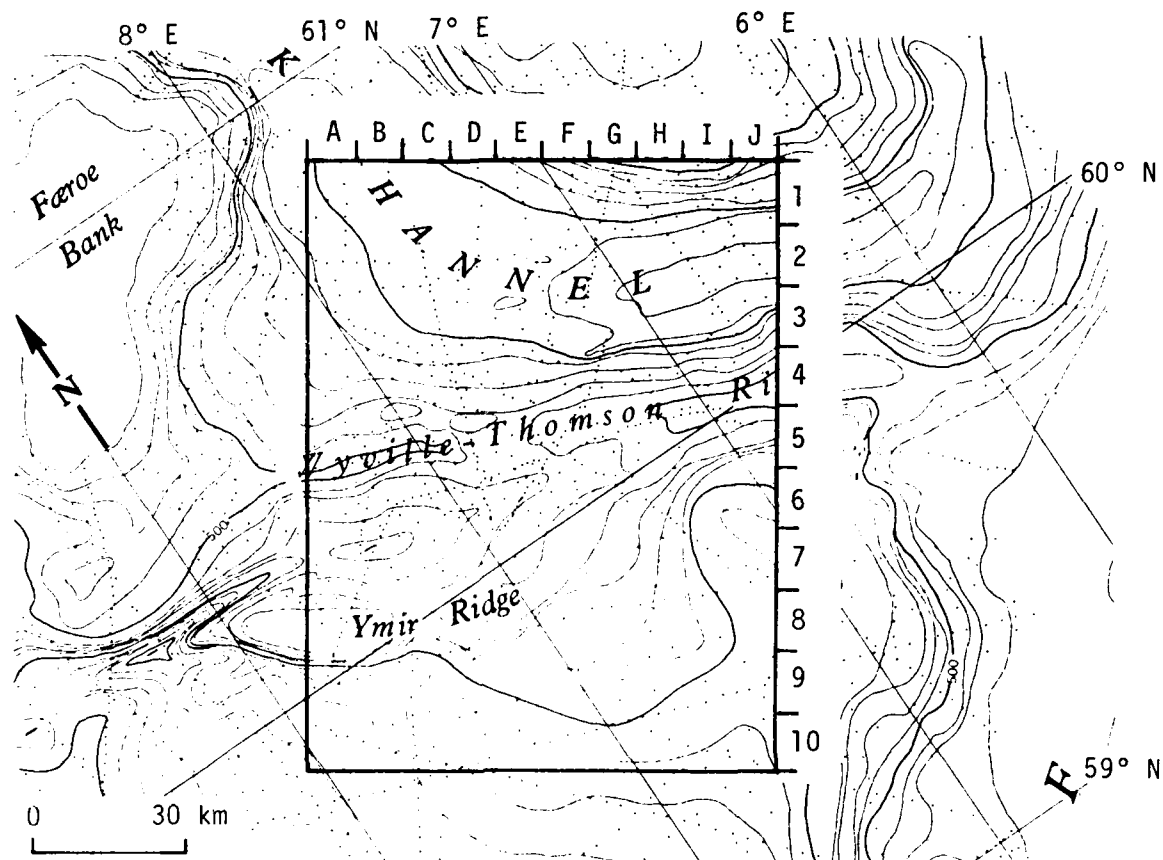
FIGURE 29. GROUND COVERAGE CORRESPONDING TO SEASAT SAR REV. 599. (After
IOS Chart No. C6567, contour intervals in 100-meter incre-
ments)

The JPL-optically processed SAR imagery presented in Figure 28
was collected during Rev. 599 (7 August 1978) as Seasat passed over
the Wyville-Thomson Ridge. The corresponding bathymetric chart for
this coverage is presented in Figure 29. From Figure 28, it can be
seen that there are numerous internal wave signatures. Note on the
SAR image that the internal waves are both range (e.g., C/D1 to C/D2)
and azimuth (e.g., A9 to D9) traveling. The internal waves in the
lower left corner of the SAR image appear to occur over the Ymir
Ridge; the internal waves in the middle of the image appear over the
Wyville-Thompson Ridge; and those at the to of the image occur over
the Faeroe Bank Channel.

Surface measurements collected at the time of the Seasat overpass
indicate a wind of 6.9 m/s from the north, and a wave field with a
significant wave height of 1.1 meters, and a dominant wavelength of
71 meters propagating towards 200°(T).
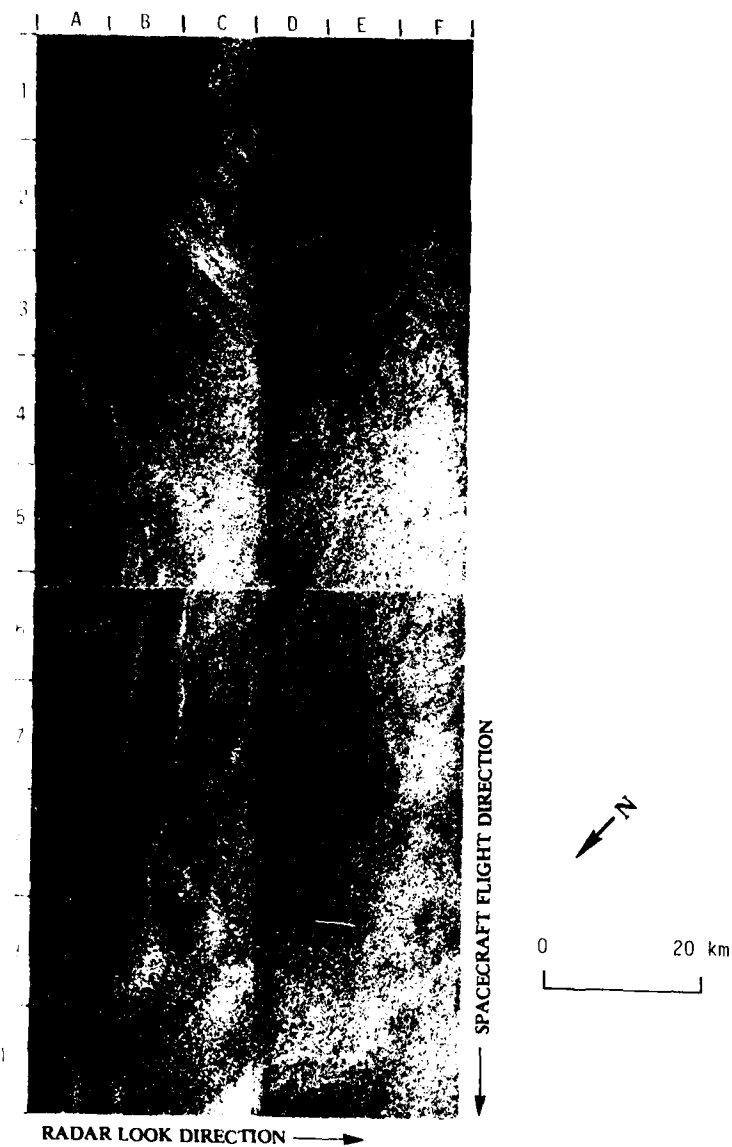
FIGURE 30. SEASAT SAR IMAGE OF A FRONTAL BOUNDARY COLLECTED OVER FAEROE BANK CHANNEL AND FAEROE RIDGE, REV. 762. (Image courtesy of JPL.)
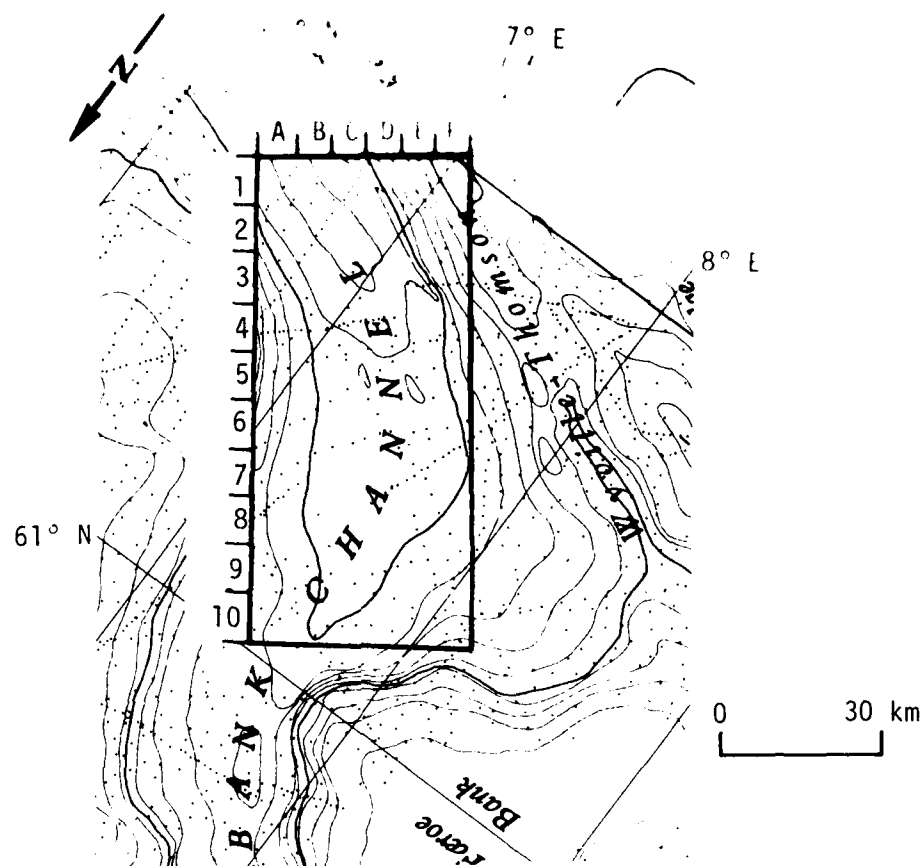
FIGURE 31.    GROUND COVERAGE OF SEASAT SAR REV. 762 OVER
              WYVILLE-THOMSON RIDGE.  (After IOS Chart No.
              C6567, depth contours in 100-meter increments.)


     The  JPL-optically  processed  image  presented  in  Figure  30  was
collected as Seasat passed over the Faeroe Bank Channel and the edge
of the Faeroe Shelf during Rev. 762.   The corresponding bathymetric
chart for this area is presented in Figure 31.   The curved, dark line
beginning  at  A4  and  continuing  to  B9  is  believed  to  be  a  surface
pattern  caused  by  a  frontal  boundary.    Its  location  appears  to  be
over the edge of the Faeroe Shelf, an area with a water depth between
600 and 1000 meters.

FIGURE 32.    SEASAT SAR IMAGERY COLLECTED OVER ICELAND-FAEROE RISE
             DURING REV. 958.   (Optically processed imagery courtesy
             of JPL.)
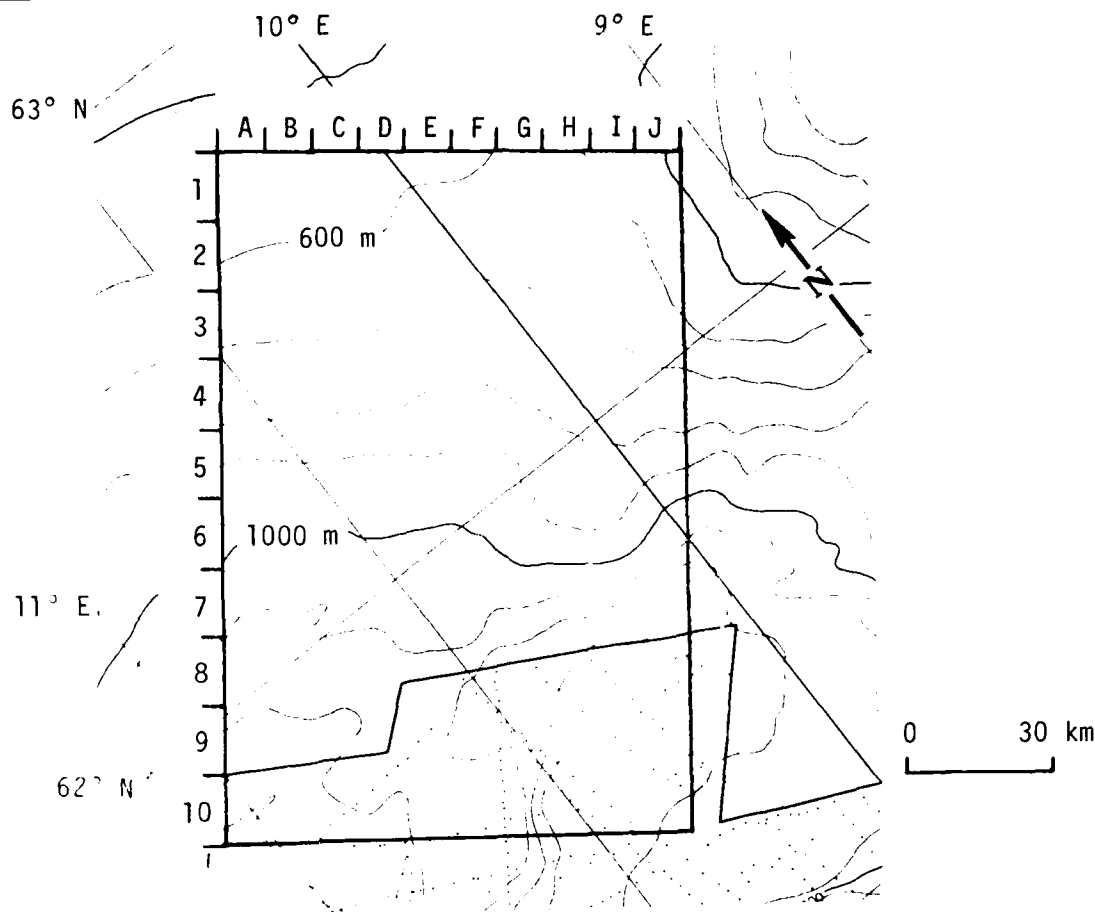
~ 'ND COVERAGE OF SEASAT REV. 958 OVER ICELAND-FAEROE
            ∴'ter IOS Chart No. C6567, depth contours in
                    ⋅ ⋅⋅⋅ents.⸗

      The ⸗AR  ⋅⋅⋅⋅⋅⋅             ∴⋅  ⸗llected during
Revolution 958  ⸗ ⸗eptember⸗ ⋅  ⋅         ⸗⋅ ⸗he Iceland-
Faeroe Rise.  The correspond⸗⋅⋅⋅ ⸗⋅⸗⋅        ⸗⋅ ⸗⸗⋅⋅ ⸗⸗
presented in Figure 33.  The intern⸗⸗ ⸗⸗⋅⸗                ⋅
of Figure 32 occur in an area where the w⸗t⸗⋅ ⸗⋅
and 1000 meters.  It is in an area where the ⸗⸗⸗⸗⋅ ⸗
from the deep (>2500 m) Iceland Basin to the rel⸗t⸗v⸗⸗⋅ ⸗⸗⸗  ⸗
m) Iceland-Faeroe Rise.  The dark areas of Figure 32 (⸗⸗6 and ⸗⸗⸗ ⸗⸗⸗
believed to be atmospheric events.

      Surface measurements obtained at the JASIN test area indicates
the gravity wave field present at the time of Revolution 958 had a
significant wave height of 1.4 meters, a dominant wavelength of 147
meters and was propagating towards 176°(⸗ .   Surface winds had a
speed of 7.2 m/s, but no direction was given.

RADAR LOOK DIRECTION ⟶
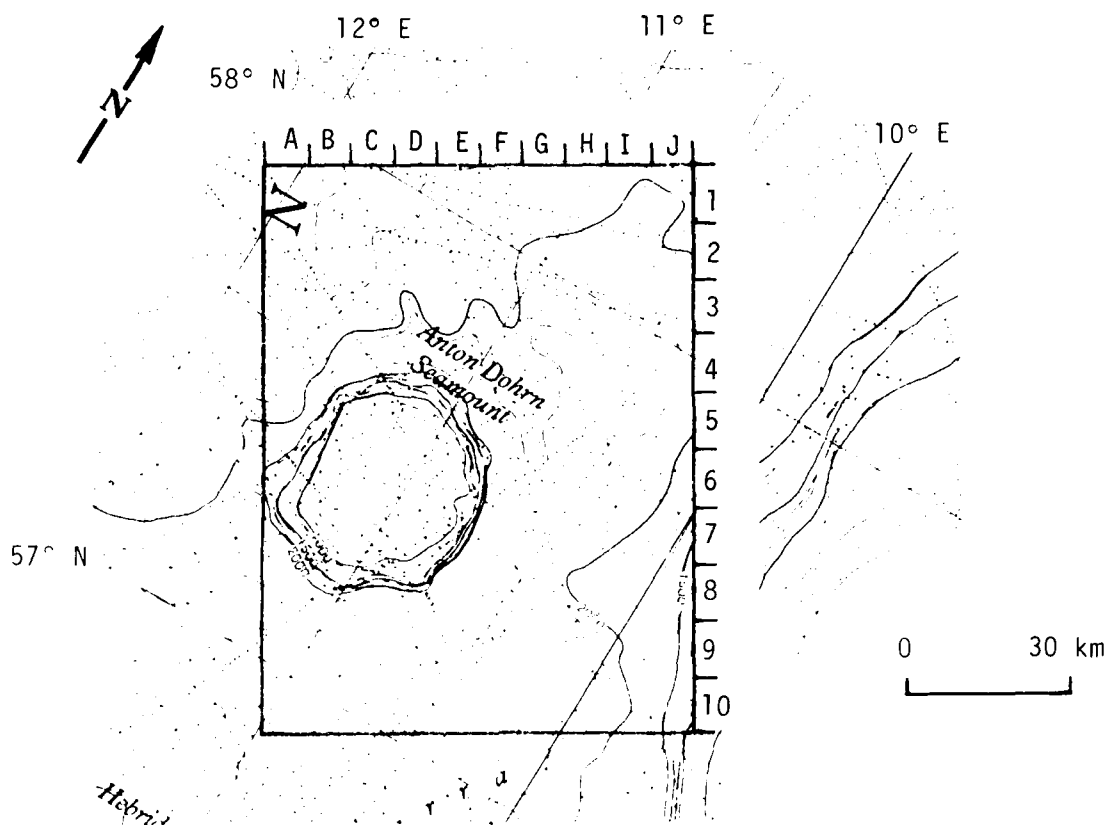
FIGURE 35.   GROUND COVERAGE OF REV. 791 OVER ANTON DOHRN SEAMOUNT.
(After IOS Chart No. C6567, depth contours in 100-meter
increments.)

Not all surface signatures believed to be related to deep-water,
bottom topographic features are as clear and distinct as the examples
presented previously.   Figure 34 was collected by Seasat during
Rev. 791 (21 August 1978) as it passed over the Anton Dohrn Seamount.
The corresponding bathymetry for this imagery is presented in
Figure 35.

The internal wave signatures collected over the Anton Dohrn Sea-
mount are quite subtle.   Three groups of internal waves (B6 to C6,
D/E6 to D/E8, and A8) occur over this seamount , which is quite steep
sided, as can be seen by the narrow spacing of the contour lines in
Figure 35.

The sea truth collected at the JASIN test area indicates the
winds were quite strong, with a speed of 13 m/s from the southwest.
The surface gravity wave field had a significant wave height of 3.1
m, a dominant wavelength of 151 m and was propagating towards 45°(T).

In summary, during the survey of deep-water test sites, Seasat SAR imagery collected during the JASIN experiment over the northeast Atlantic was examined. Two anomolous patterns (an anomolous pattern being one which could not be categorized as being caused by any known oceanic, meteorologic or man-made process) appeared over and over on this imagery: internal "wave-like" patterns and patterns similar to oceanic fronts. A comparison (presented in detail in the next chapter) between the locations of these anomolous patterns and the locations of major bottom topographic features (such as seamounts, submarine ridges, and shelfs) in the area revealed a distinct correlation between the two.

The purpose of the imagery and charts discussed in this section was two-fold: 1) to present examples of the different types of anomolous patterns which appear on Seasat SAR imagery collected in deep-wat er regions, and 2) to illustrate the correlation between the location of these patterns and the deep-water topographic features in the area. Through the analysis of these patterns it has been shown that bottom-related surface patterns exist in deep-water as well as shallow-water regions.

# 5
## MULTI-TEMPORAL ANALYSIS

As evidenced by the examples presented in this report and else-
where, presently there is little doubt that a significant portion of
the surface patterns present on SAR imagery can be correlated to a
bottom topographic feature.  However, before SAR imagery can become
an effective tool for updating hydrographic charts, the limitations
of this remotely sensed data base must be further defined.

This chapter contains a description of the methods used and the
results obtained from a detailed analysis of Seasat SAR imagery col-
lected over the same test sites at different times under different
imaging geometry and environmental conditions.  This concept is re-
ferred to as a multi-temporal analysis.

Perhaps the most important question surrounding the use of SAR
imagery to identify and locate hazardous features is how frequently
will a SAR image a surface pattern related to the bottom topography
in a given area   This question can be simply addressed by collecting
a set of SAR imagery over a known bottom feature and tabulating the
number of times a surface pattern occurs.  However, to accurately
predict how frequently a pattern will be imaged by a SAR, it is
necessary to determine what caused that pattern to appear, and then
predict how many times these conditions will occur at a given area.
This necessitates not only collecting a set of SAR imagery over a
given test site, but collecting a set of ancillary environmental
parameters and relating these parameters to the hydrodynamic inter-
actions between the water and the bottom feature.

Another important question which can be addressed through a
multi-temporal analysis is how the geographical position of surface
signature relates to the geographical position of a bottom feature,
and if it does change, what causes the variation.

A mu'ti-temporal analysis was conducted on three test sites imaged by the Seasat SAR: (1) the Southern Bight of the North Sea, (Engl' h Channel): (2) the Tongue of the Ocean, and (3) the JASIN test area.

The methods used during the multi-temporal analyses were much the same as those used to examine individual sites, as outlined in Section 4.1. Additional observations made were the number of times a SAR surface pattern occurred over or near a given bottom topographic feature and also statistical comparisons were made between the various ancillary data and the appearance of bottom-related SAR patterns.

The results of these analyses are presented in the rest of this chapter. Section 5.1 presents the results of the English Channel study, 5.2 the results of the Tongue of the Ocean study and 5.3 the results of the JASIN study. Finally, Section 5.4 discusses the results of these analyses.

## 5.1 SOUTHERN BIGHT OF THE NORTH SEA (ENGLISH CHANNEL)

The bottom-related signatures on Seasat SAR imagery collected over the Southern Bight of the North Sea (or the northern portion of the English Channel) during Rev. 762 have been intensively examined by several authors (see Kasischke, et al., 1980; Kenyon, 1981: Shuchman, 1982). In this section, an examination of Seasat SAR imagery from three additional dates is presented.

Four Seasat revolutions provide SAR coverage of the Southern Bight region of the North Sea and English Channel (see Figure 36). The SAR swaths (100 km wide) are indicated as rectangles on the figure. The SAR passes used in the study are Revolutions 762, 957, 1430, and 1473. As indicated on Table 2, the satellite overpasses span the time from August 19 to October 8, 1978, representing late summer conditions in the Channel. Note from Table 2 and Figure 36
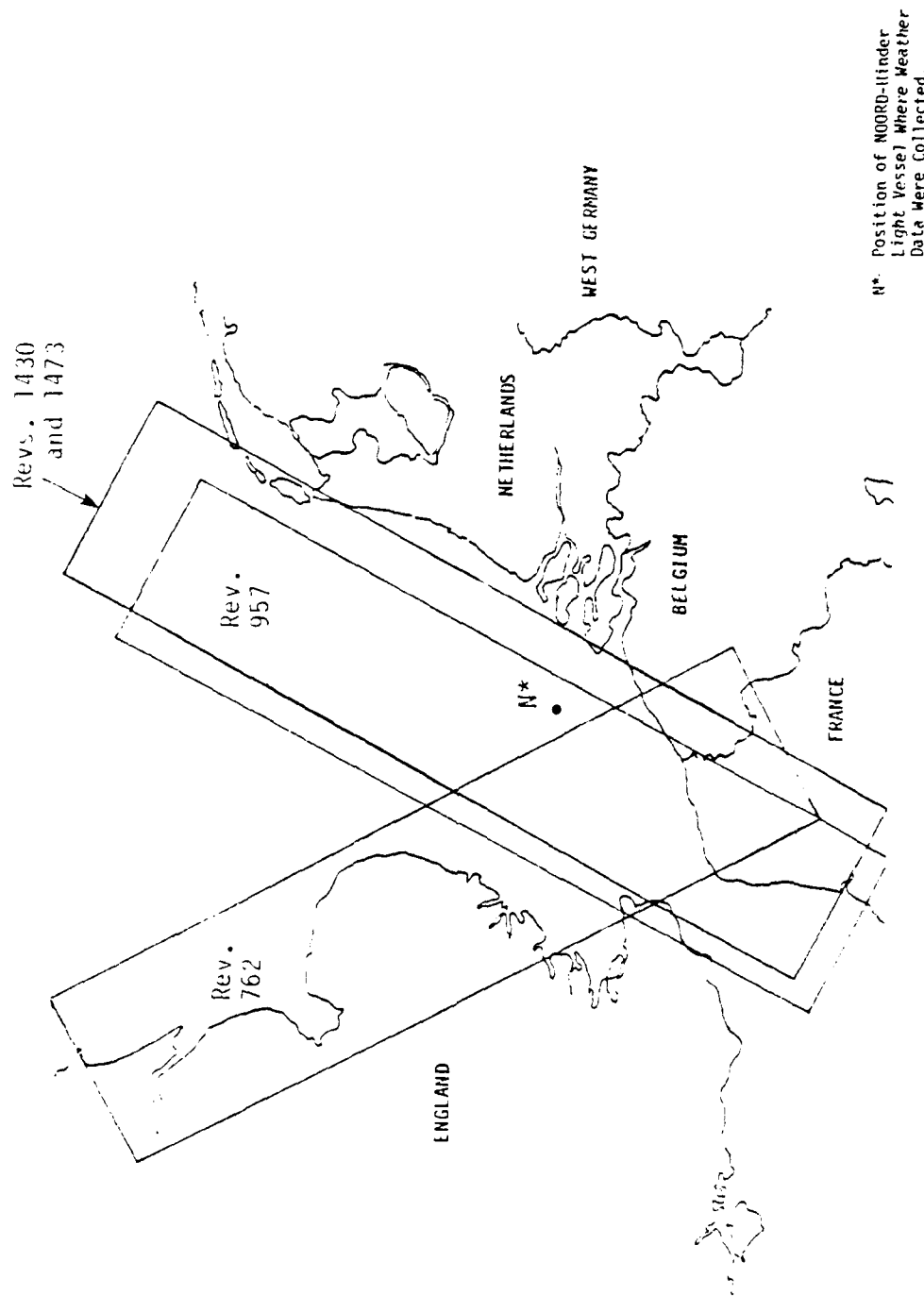
FIGURE 36. GROUND COVERAGE OF SEASAT REVOLUTIONS USED FOR ENGLISH CHANNEL ANALYSIS

that Revolutions 957, 1430, and 1473 have generally the same orientation (i.e., radar look direction with respect to the Channel), while Revolution 762 represents the nearly orthogonal look direction.

The English Channel test site is characterized by a series of longitudinal sand banks and transverse sand waves which are situated in water depth varying from approximately 3 to 50 meters. Bathymetric contour charts of the southern and northern ends of the study site are presented in Figures 37 and 38 respectively. The sand waves are clearly identifiable as elongated arcuate features with closely spaced contours contours indicating rapid depth changes surrounding the features.

Figure 39 is the Seasat digital image of the English Channel test site obtained during Revolution 762. The image, processed at the Jet Propulsion Laboratory, represents a 100 x 100 km scene with a resolution of 25 x 25 meters. This image has been radiometrically and geometrically corrected using procedures described in Appendix C. Figure 40 is a comparison of the radar image and the bathymetric chart of the bottom in the test area for Revolution 762. From Figure 40, it can be noted that the sand waves are visible with stronger radar returns resulting on the down current side of their crest lines. The transverse sand waves are predominantly on the gentler slope of the asymmetrical longitudinal sand waves (or banks) and their crest lines bend around to trend increasingly more parallel to the longitudinal sand wave axis. Kenyon (1981) reports that at the time of this image collection, a current of 1-2 m/s was flowing 20° obliquely to the longitudinal sand waves and parallel to the orthogonal of the transverse waves. Kenyon (1981) further noted that analysis of sidescan sonar records from near South Falls (Caston, 1979) has revealed additional transverse sand waves which are not seen on the image.

ΣERIM
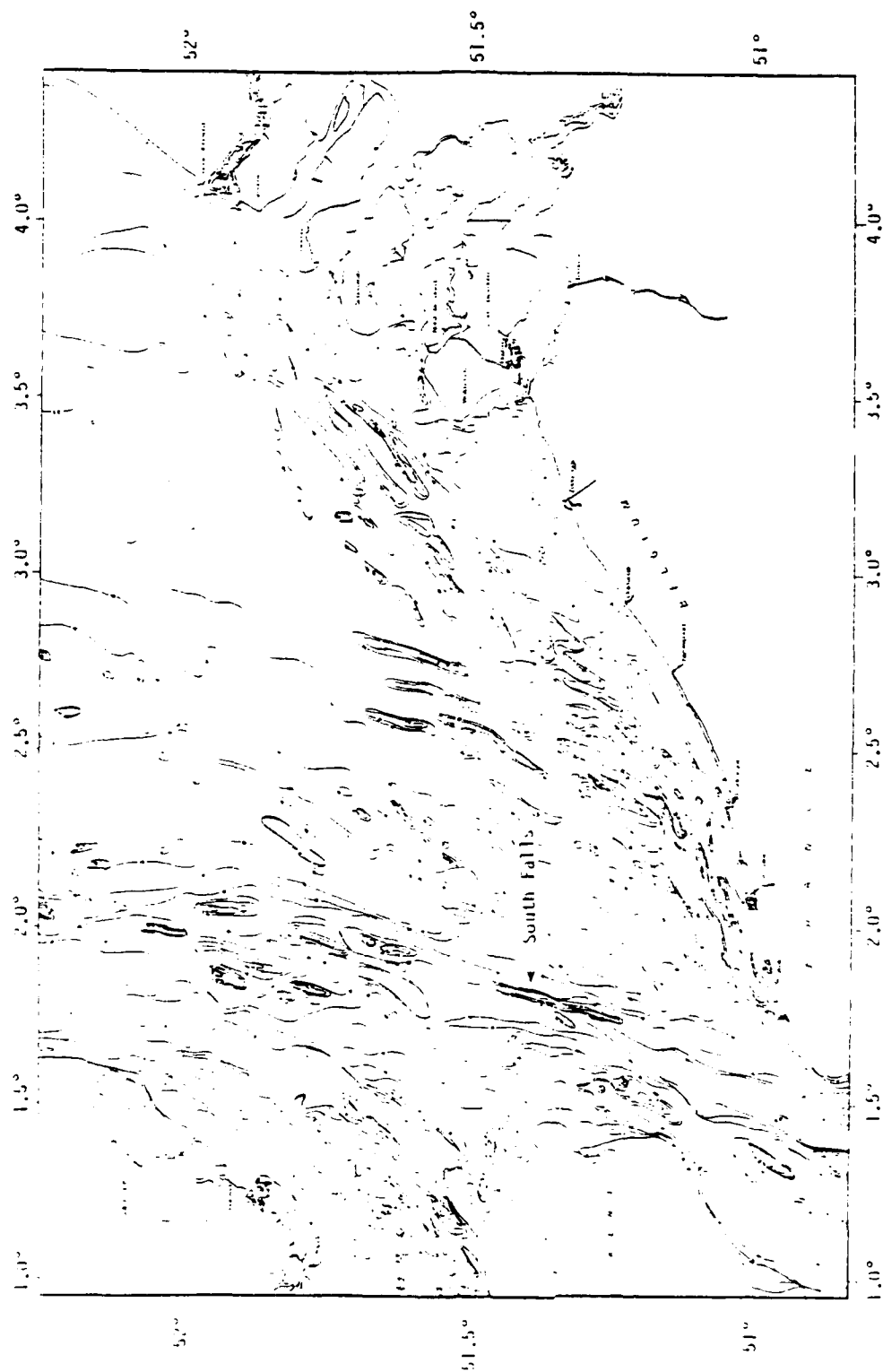


FIGURE 37. BATHYMETRIC CHART OF THE SOUTHERN END OF THE STUDY SITE. (Reconstructed from British Admiralty Chart 1406.)
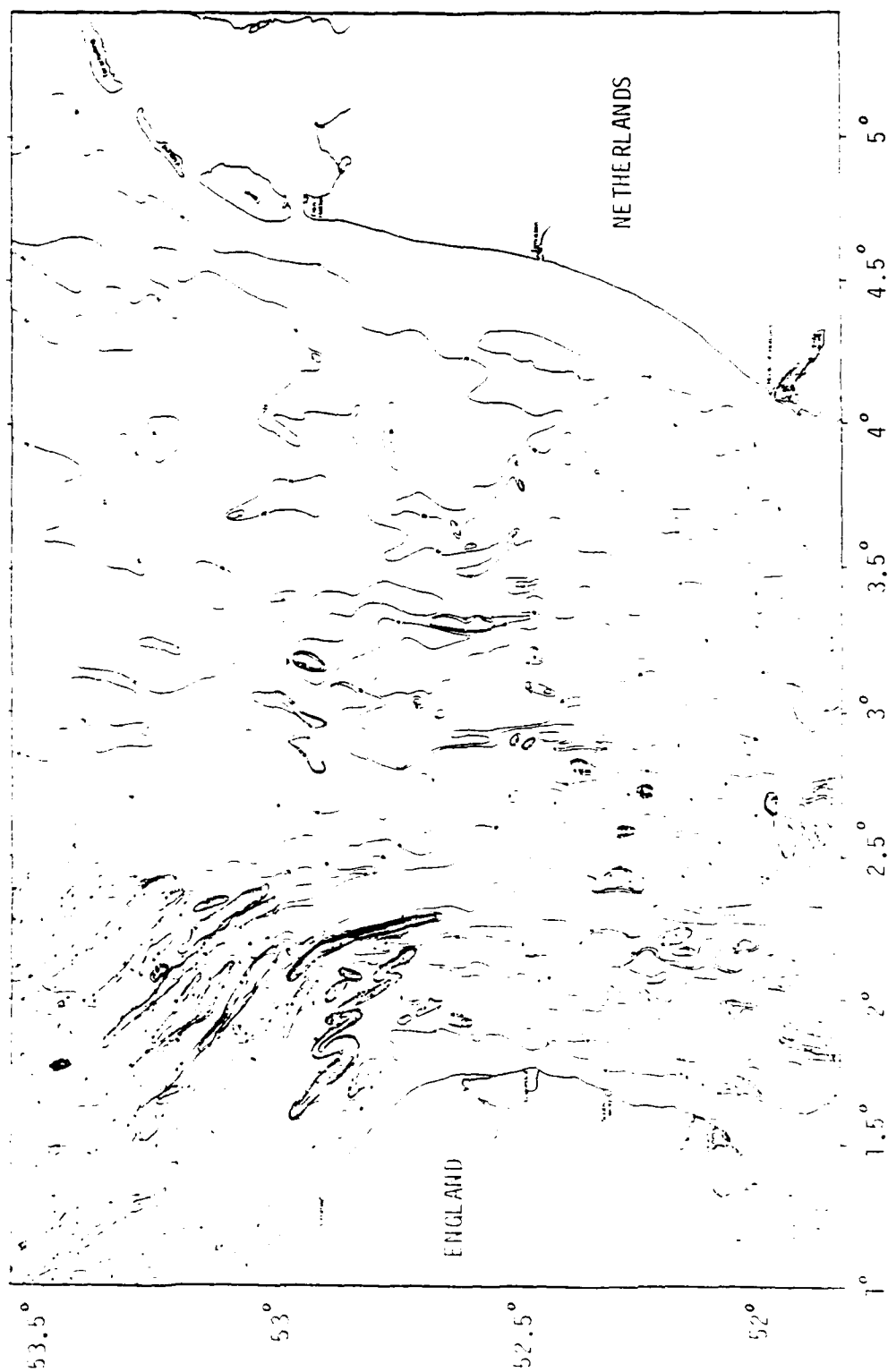
FIGURE 38. BATHYMETRIC CHART OF THE NORTHERN END OF THE STUDY SITE. (Reconstructed from British Admiralty Chart 37160.)
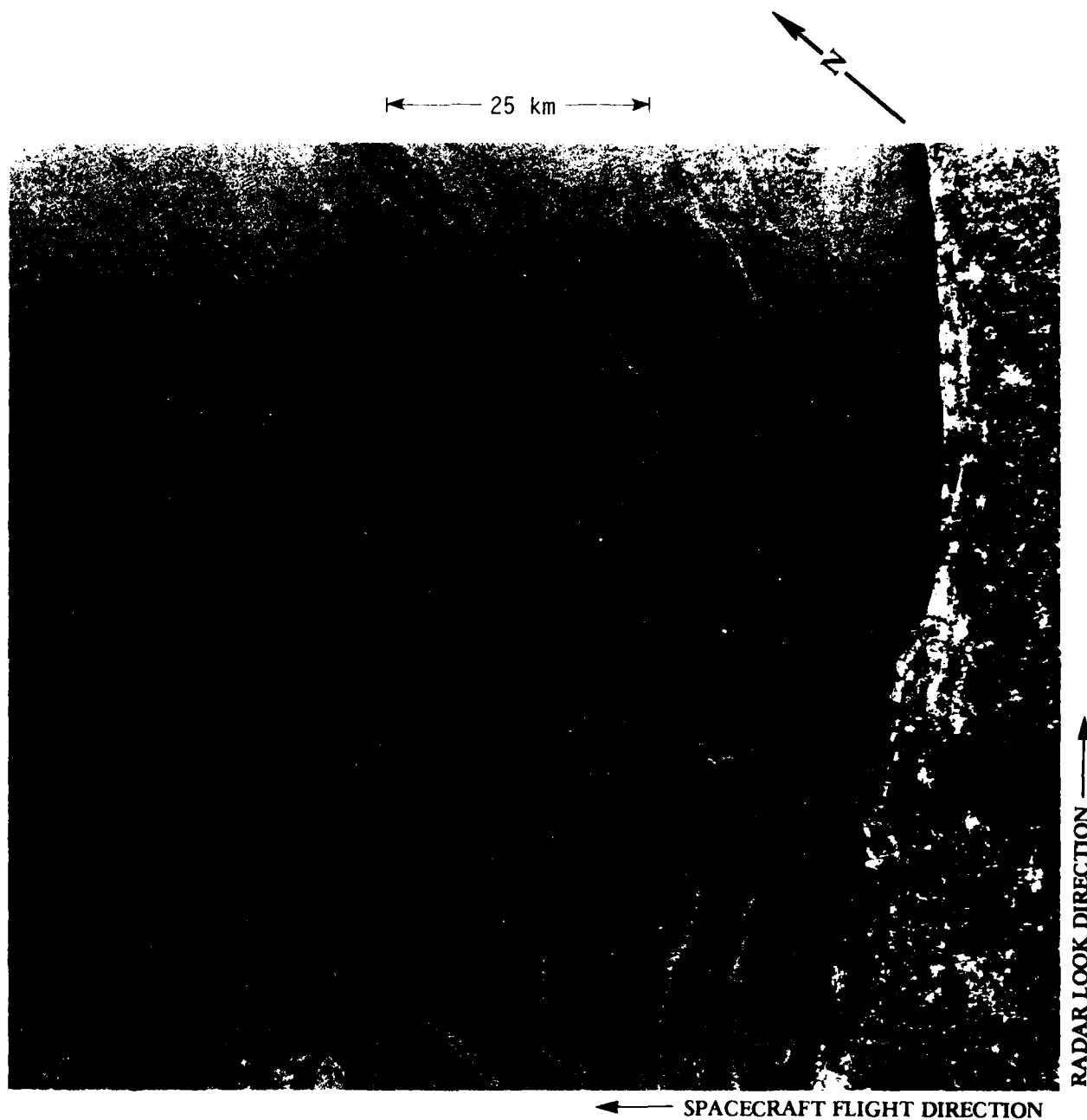
FIGURE 39.  JPL DIGITALLY PROCESSED IMAGE OF SEASAT REV. 762,
19 August 1978.  (Geometrically and radiometrically
corrected at ERIM.)

RADAR LOOK DIRECTION ⟶

⟵ SPACECRAFT FLIGHT DIRECTION
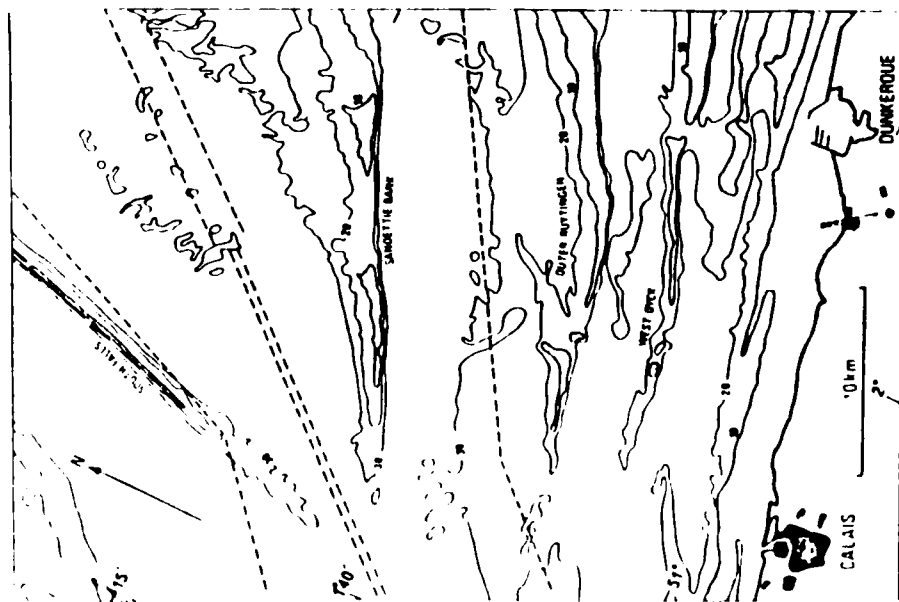
(The dashed lines in the figure are recommended ship routes.)

FIGURE 40. EXAMPLE OF CURRENT INDUCED, BOTTOM-RELATED PATTERNS ON SEASAT SAR IMAGERY COLLECTED OVER THE ENGLISH CHANNEL. (Rev. 762, ERIM Optically Processed Imagery)

The longitudinal sand banks are modern tidal built sand banks and are one of the two main depositional faces of the offshore tidal environment in the English Channel, the other being the offshore sand sheet faces (Kenyon, et al., 1979). The longitudinal sand banks are the largest bed forms of shallow, strongly tidal seas, and can in extreme cases be as much as 120 km long and 30 km wide. These sand banks tend to occur in groups, either well away from the coast or in estuaries, or are found as solitary near-coastal banner banks in the lee of headlands, islands or submerged rock shoals. Tidal currents passing over these modern sand banks are usually very strong, running between 1-2 m/sec at peak flow.

The modern tidal sand banks observed in the English Channel are not quite longitudinal bed forms, but are aligned obliquely to the regional direction of peak tidal flow and to the resulting net transport direction by as much as 20°, with an average value of approximately 10°. Figure 41 (from Kenyon, et al., 1979) indicates the offshore tidal sand banks and net transport direction in the test site. The steeper sides of the sand banks are indicated with a tick mark. It is noted with interest that Kenyon used Seasat SAR data in conjunction with standard oceanographic data to prepare this figure.

The transverse sand waves also found within the English Channel data are large flow-transverse bed forms coupled to oscillatory boundary-layer currents of tidal origin (Allan, 1980). These transverse sand waves are considered giant ripples with heights up to an average of 10-15 meters and with wavelengths of several hundreds of meters (Lohmann, 1976).

Previous examinations of the Seasat SAR imagery collected during Rev. 762 (see Figures 39 and 40) revealed that the surface patterns correlated almost one to one with bottom-topographic features (Kasischke, et al., 1980; Kenyon, 1981; Shuchman, 1982). For the purposes of the inter-comparison of data collected by the four Seasat
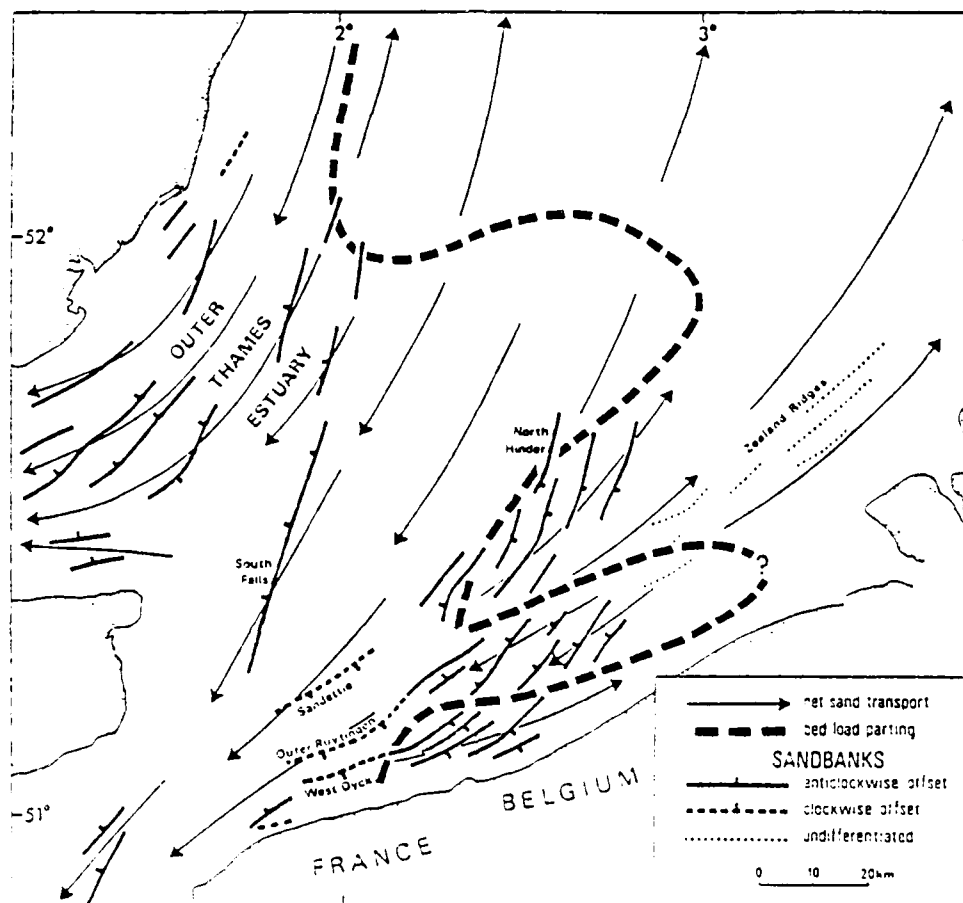
FIGURE 41. MAP SHOWING THE OFFSHORE TIDAL SAND BANKS AND NET SAND TRANSPORT DIRECTION OF THE NORTH SEA. (The steeper sides of the sand banks are indicated with a tick. From Kenyon, et al., 1979.)

passes, we will concentrate on the area around the Sandettie Bank and South Falls (see Figure 40). SAR imagery for this area from the four passes is presented in Figure 42. From these images, it can be seen that the surface patterns are quite distinct on the Rev. 762 imagery, moderately distinct on Rev. 1473 imagery, and very faint on the imagery from Revs. 957 and 1430.

The environmental conditions at the times of the four English Channel orbits are listed in Table 3. The conditions present are also summarized in Figure 43.

From the analysis of the data, it was determined that the following conditions must be met before bottom topographic features can be detected on SAR imagery over the English Channel:

1.  There must be a tidal current on the order of 0.4 m/s (0.8 knots) or more, depending on the depth of the bottom feature; and

2.  There must be a wind sufficient to generate surface waves at the Bragg wave number in the region surrounding the bottom feature (i.e., 1 m/s or 2 knots). Recall that the radar is sensitive to Bragg waves traveling in the range direction, so there must be some component of the wind in this direction in order to generate these waves.

Both of these conditions are met for Revolutions 762 and 1473, with tidal currents between 0.6 and 0.7 m/s (1.2 and 1.4 knots) and winds between 2 and 5.5 m/s (4 and 11 knots). For Revolution 957, the tidal current is less than 0.1 m/s (0.2 knots) which is insufficient to produce the necessary modulation or straining of the Bragg waves. For Revolution 1430, the tidal current is adequate (0.65 m/s (1.3 knots)), but the wind speed is so large (10.5 m/s (21 knots)) that the effects of the current variations across the ridge are quickly "erased" by the wind.

RADAR LOOK DIRECTION

REV. 762

REV. 957

RADAR LOOK DIRECTION

RADAR LOOK DIRECTION

20 km
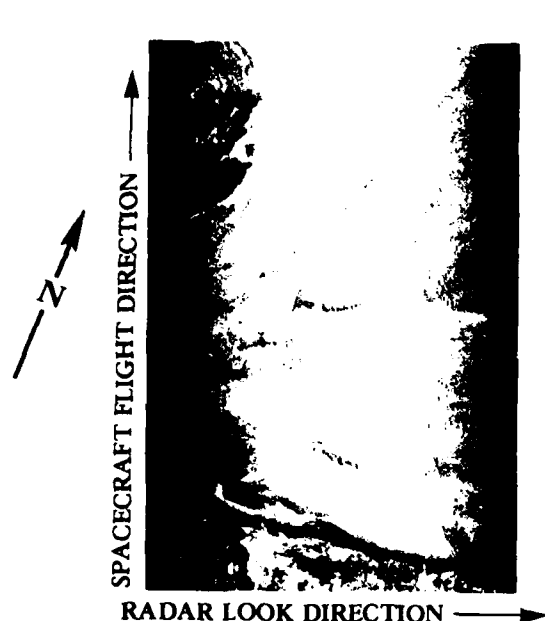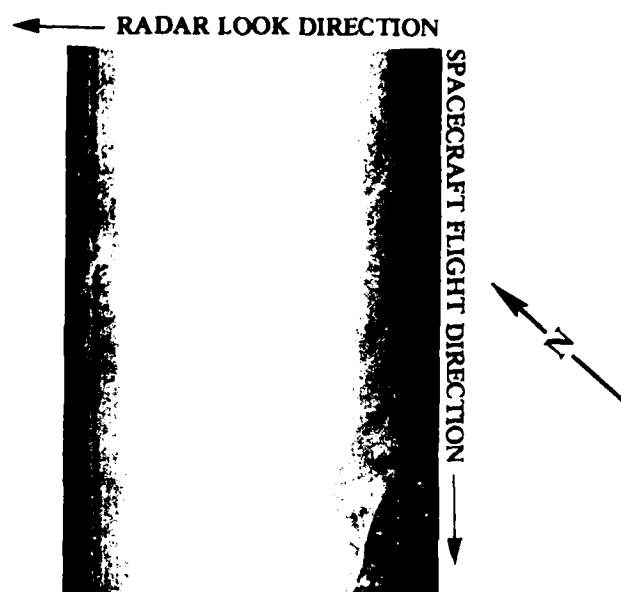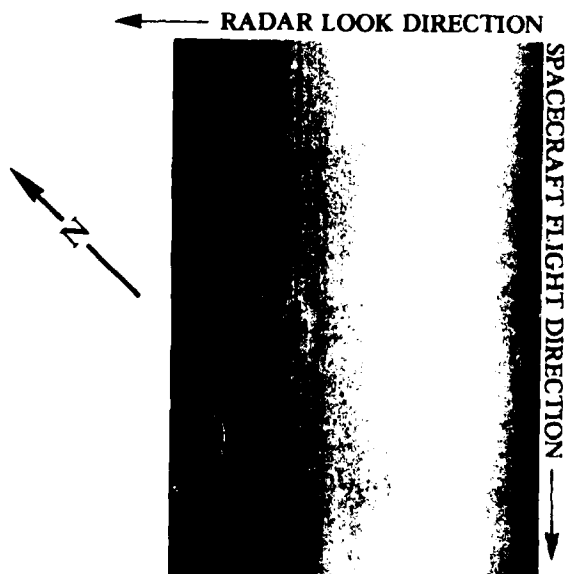
REV. 1430
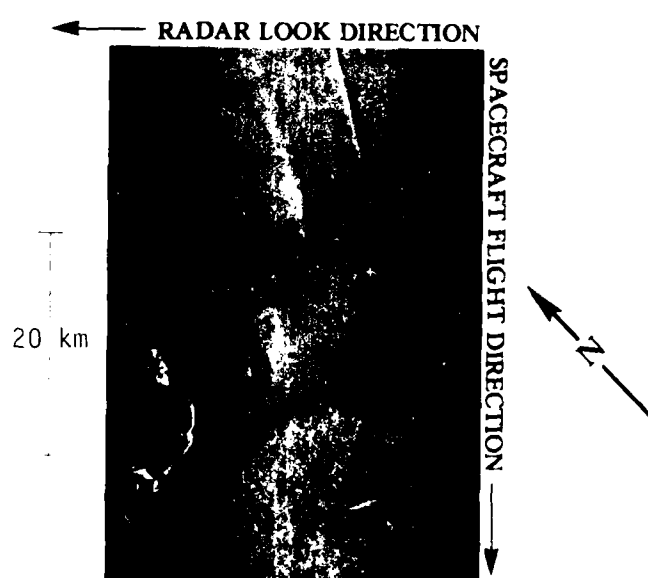
REV. 1473

Figure 42.   SEASAT SAR IMAGERY COLLECTED OVER SOUTH FALLS, SANDETTIE
             RIDGE AND GOODWIN SANDS.  (ERIM optically processed
             imagery.)

## TABLE 3
### ENVIRONMENTAL DATA RECORDED AT THE TIME OF SATELLITE OVERPASS FOR ENGLISH CHANNEL TEST SITES

| Seasat Revolution | Wind[1] Speed and Direction | Water Temp. | Air Temp. | Wave Ht. | Period of Waves | Current[2] Speed and Direction | Current[3] Speed and Direction | A Typical Water Depth at Feature |
|---|---|---|---|---|---|---|---|---|
| 762 | 4.0 Kn 146°(T) | 16.4°(C) | 17°(C) | 0.5 m | 1 s | 1.4 Kn 210°(T) | 1.6 Kn 224°(T) | 7.6 m |
| 957 | 20.0 Kn 326°(T) | 16.5°(C) | 15°(C) | 1.0 m | 4 s | 0.2 Kn 210°(T) | 0.2 Kn 174°(T) | 12.1 m |
| 1430 | 21.0 Kn 315°(T) | 15.5°(C) | 11°(C) | 1.0 m | 4 s | 1.3 Kn 30°(T) | 1.9 Kn 45°(T) | 13.1 m |
| 1473 | 11.0 Kn 15°(T) | 15.3°(C) | 15°(C) | 0.5 m | 3 s | 1.2 Kn 210°(T) | 0.7 Kn 218°(T) | 10.8 m |

1 Kn = 0.51 m/s

[1]Standard meteorological convention (i.e., direction from).

[2]Direction current is flowing towards (value is near South Falls sand bank).

[3]Average current value for test area.

NOTE: In all cases, the water column was unstratified, and no rainfall or ocean sw present.
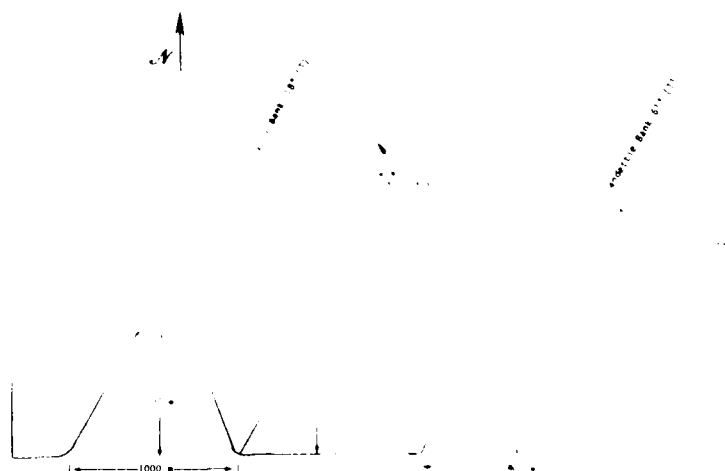
REV. 762
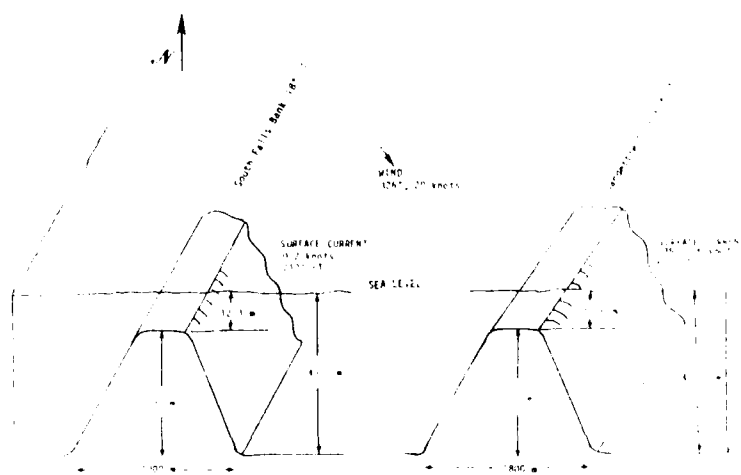


REV. 957

FIGURE 43a.  SUMMARY OF ENVIRONMENTAL CONDITIONS AND
CROSS-SECTION OF SOUTH FALLS AND SAND
AT THE TIME OF THE SEASAT OVERPASS
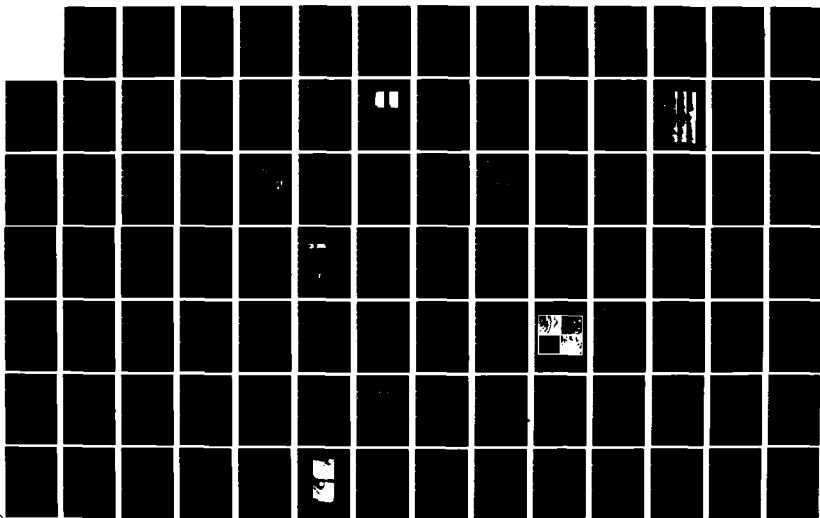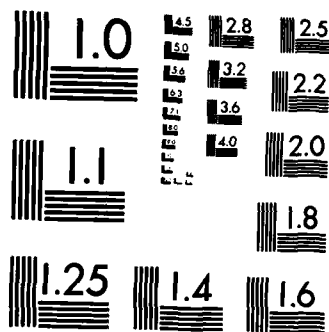
MICROCOPY RESOLUTION TEST CHART

NATIONAL BUREAU OF STANDARDS-1963-A
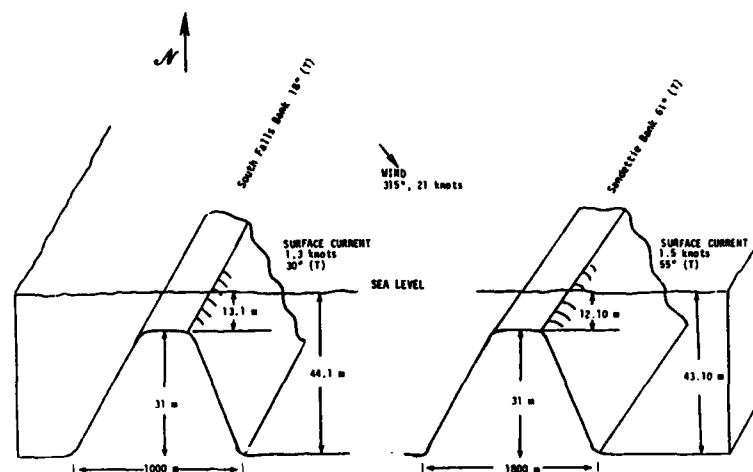
REV. 1430
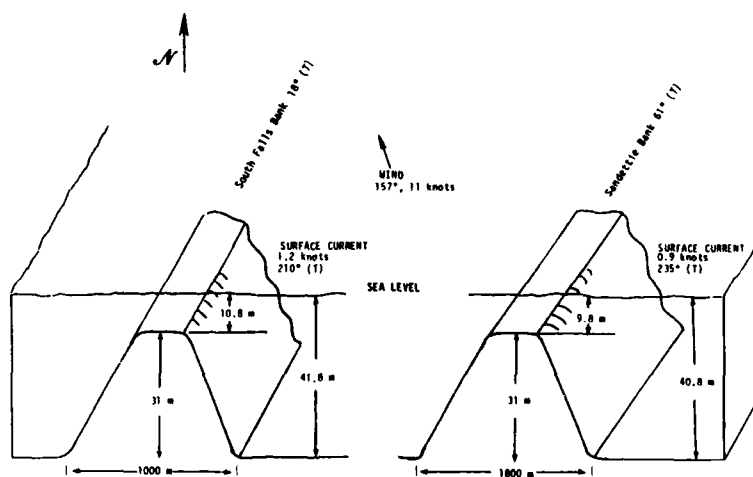


REV. 1473

FIGURE 43b. SUMMARY OF ENVIRONMENTAL CONDITIONS AND IDEALIZED
CROSS-SECTION OF SOUTH FALLS AND SANDETTIE BANKS
AT THE TIME OF THE SEASAT OVERPASSES

The observed dependence of the SAR image contrast on the current and wind conditions is explained by a hydrodynamic/electromagnetic model developed by Shuchman (1982). The hydrodynamic part of this model calculates the change in the current velocity as the current flows over a long linear bottom feature such as South Falls or Sandettie Bank. The interaction of the short surface waves with this variable current is then calculated using the kinematic conservation equation and the wave action equation (Phillips, 1981), including the regenerative effects of the wind. The result of this part of the model is the amplitude of the waves satisfying the Bragg criterion as expressed in Eq. (1); i.e., those with wavenumber

$$K_W = 2K \sin \theta \tag{1}$$

where K is the radar wavenumber and $\theta$ is the incidence angle, at each point in the scene. These results are then fed into the electromagnetic part of the model which calculates the radar cross section ($\sigma_0$) at each point in the scene. A random signal is added to simulate the effects of system noise and the total signal is displayed in the form of a two-dimensional gray map or a one-dimensional plot of the radar signal along a line through the feature.

An example of the two-dimensional output of this model is shown in Figure 44. This simulated image was generated using the environmental conditions for Rev. 762 as listed in Table 3. The image is very similar to the actual Seasat image for Rev. 762 (Figure 40) near the center of South Falls. A one-dimensional plot of the simulated signal through the South Falls feature is compared with the actual signal from Rev. 762 in Figure 45a. Similar agreement was obtained for t$^{\sim}$ transverse sand waves along Sandetti Ridge as shown in Figure 45b.

This model was exercised for the conditions occurring during Revs. 957 and 1430 and resulted in a predicted signal change of less than 1 dB across South Falls. This agrees with the observation that
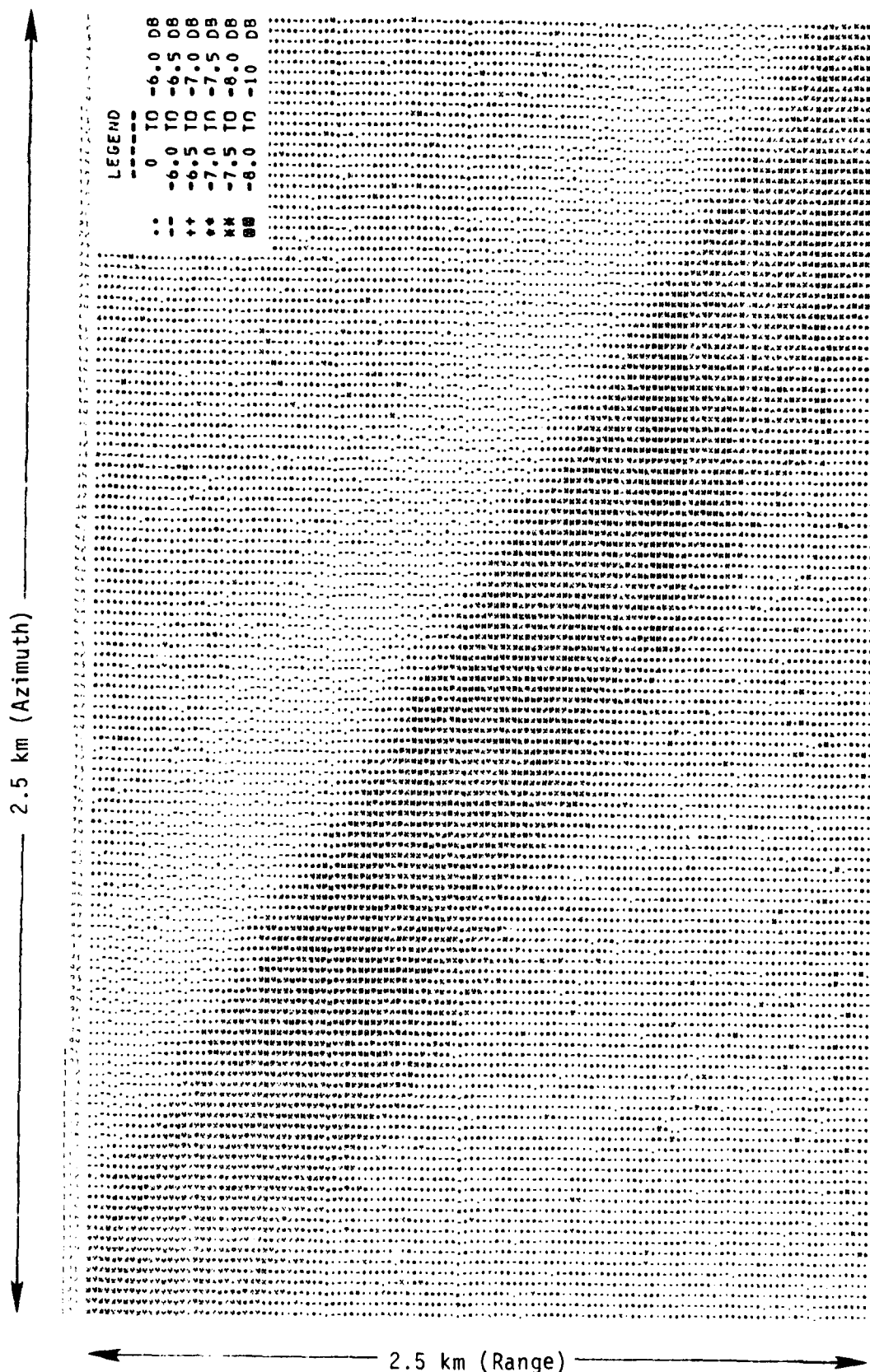
FIGURE 44.   MODELED BACKSCATTER MAP FOR REV. 762 SHOWING GOOD VISIBILITY OF SOUTH FALLS

2.5 km (Azimuth)

2.5 km (Range)

--- actual SAR values

—— model results

(a) SOUTH FALLS
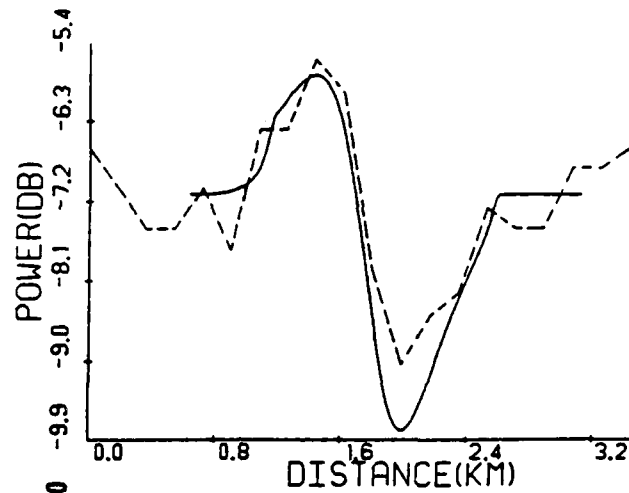


(b) TRANSVERSE
SAND
WAVES
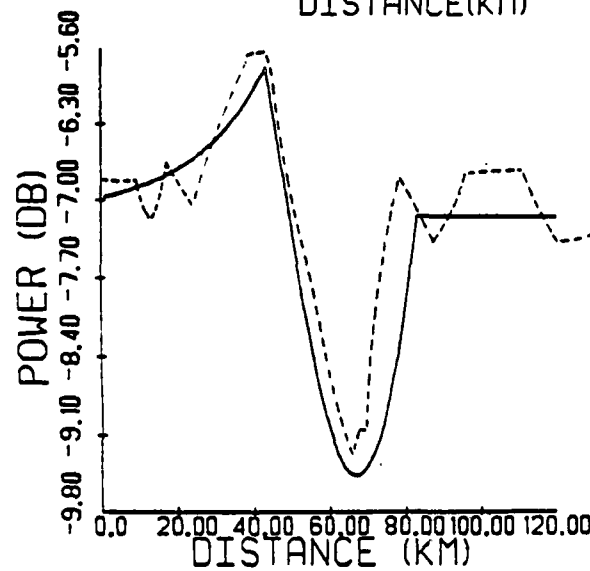


Note:  The model predicts
no backscatter change for
Sandettie Sand Bank.

FIGURE 45.  MODEL VS. ACTUAL BACKSCATTER CROSS-SECTION
FOR REV. 762 SOUTH FALLS AND TRANSVERSE
SAND WAVES CASE.

no image features corresponding to South Falls were visible on these passes. For Rev. 1473, the predicted signal change was 1.1 dB which is somewhat smaller than the observed change but is in qualitative agreement with the observation that the features are visible although less distinct than those in the Rev. 762 data.

As a result of this modeling effort, it is felt that the current/ bottom interaction mechanism is fairly well understood, at least in principle. The presently developed model is not applicable to all geometries and all types of bottom features, but in the cases for which it is applicable, the results are in good agreement with observations. Further exercise of this model could help to define the limitations of a given SAR system for detecting bottom features. Additional model development could also extend the range of applicability of the model and possibly begin to address the question of whether quantitative depths can be extracted from the SAR data.

5.2  TONGUE OF THE OCEAN

Twelve Seasat revolutions (of the fifteen collected) form the data base for the multi-temporal analysis of the Tongue of the Ocean (TOTO) area. From Table 2, it can be seen that Seasat was on an ascending orbit, with a satellite heading of approximately 335° (T), during eleven of these passes and was on a descending orbit, with a satellite heading of 210° (T), during only one orbit (Rev. 529).

The origins of the Tongue of the Ocean and other deep-water channels within the Great Bahama Bank have not been totally resolved. Mullins, et al. (1978) lists three categories of theories describing the initial formation of these channels: constructional, erosional and tectonic (grabens). The presence of the deep-water TOTO channel most likely led to the formation of the tidal bar belts along its southern edge, which were quite visible on the Seasat SAR imagery.

In general, tidal bar belts form in regions of intensified current flows. Even though the tidal range between high and low water in the Caribbean is less than one meter, at the edge of the Bahama Banks, tidal currents can be quite strong. (Ball (1967) reported tidal current speeds between one and one and one-half meters per second (two to three knots) off Schooner Cay at the tip of the Exuma Sound. During a geologic survey along the southern edge of the TOTO, Palmer (1979) reported currents in excess of one and one-half meters per second in the tidal bar belt region, with ebb currents generally being stronger than flood currents.)

The magnitude of the tidal currents in the southern edge of the TOTO can also be influenced by wind and wave conditions. Winds blowing in the same direction as the current will increase the velocity, while wind blowing in the opposite direction to the tide will decrease the velocity. Wind driven waves and ocean swell can also affect tidal flow in this region. As waves propagate onto the Great Bahama Bank from the TOTO, bottom induced wave refraction will occur. Because of vertical constriction exerted on the waves moving onto the shelf, a current will be formed in the direction of the waves (Ball, 1967), i.e., perpendicular to the edge of the shelf. This wave driven current will either increase or decrease the tidal current depending upon its direction.

The combined tidal, wind and wave generated currents eventually eroded channels into the carbonaceous bank sediments. Once the channels started to form, the currents' flow patterns were concentrated into these channels; thus, the channels actively influenced their own formation (Ball, 1967).

As previously mentioned in Section 4.3, there are two distinct bottom features which were detected on Seasat SAR imagery of the TOTO region: the tidal bar belts in the southern portion of the TOTO and

the edge of the Great Bahama Bank which surrounds the TOTO (see Figures 9 and 11). All twelve Seasat SAR images of the TOTO were examined and the detectability of these two features were classified using one of the following categories:

Excellent      Feature very visible on the Seasat SAR image;

Good      Feature moderately visible on the Seasat SAR image;

Poor      Feature faintly visible on the Seasat SAR image; and

None      Feature not visible on Seasat SAR image.

Because the edge of the Great Bahama Banks, which surround the TOTO covers such a large area (approximatey 500 kilometers of edge), it was divided into four sections. These sections are indicated on Figure 46. The visibility of the bottom-related surface patterns for the four sections in Figure 46 and the tidal bar belts are pre-sented in Table 4 for the twelve Seasat passes. Table 5 summarizes these categories for each area.

From Table 5, it can be seen that the tidal bar belts in the southern TOTO were detected 92 percent of the time Seasat made an overpass of this area; the edge of the Great Bahama Bank was detected to some extent 100 percent of the time in section I, 83 percent of the time in section II and 50 percent of the time in sections III and IV. These results indicate that enough current (either tidally, wind or wave driven) existed to cause a current/bottom interaction resulting in the patterns detected on the Seasat SAR images over the tidal bar belts. The edge of the TOTO was not always indicated by a pattern on the imagery, indicating that less favorable conditions existed in these regions.

Weather conditions at the time of the Seasat orbits were obtained from the Bahama Meteorological Office in Nassau. Predictions of tide
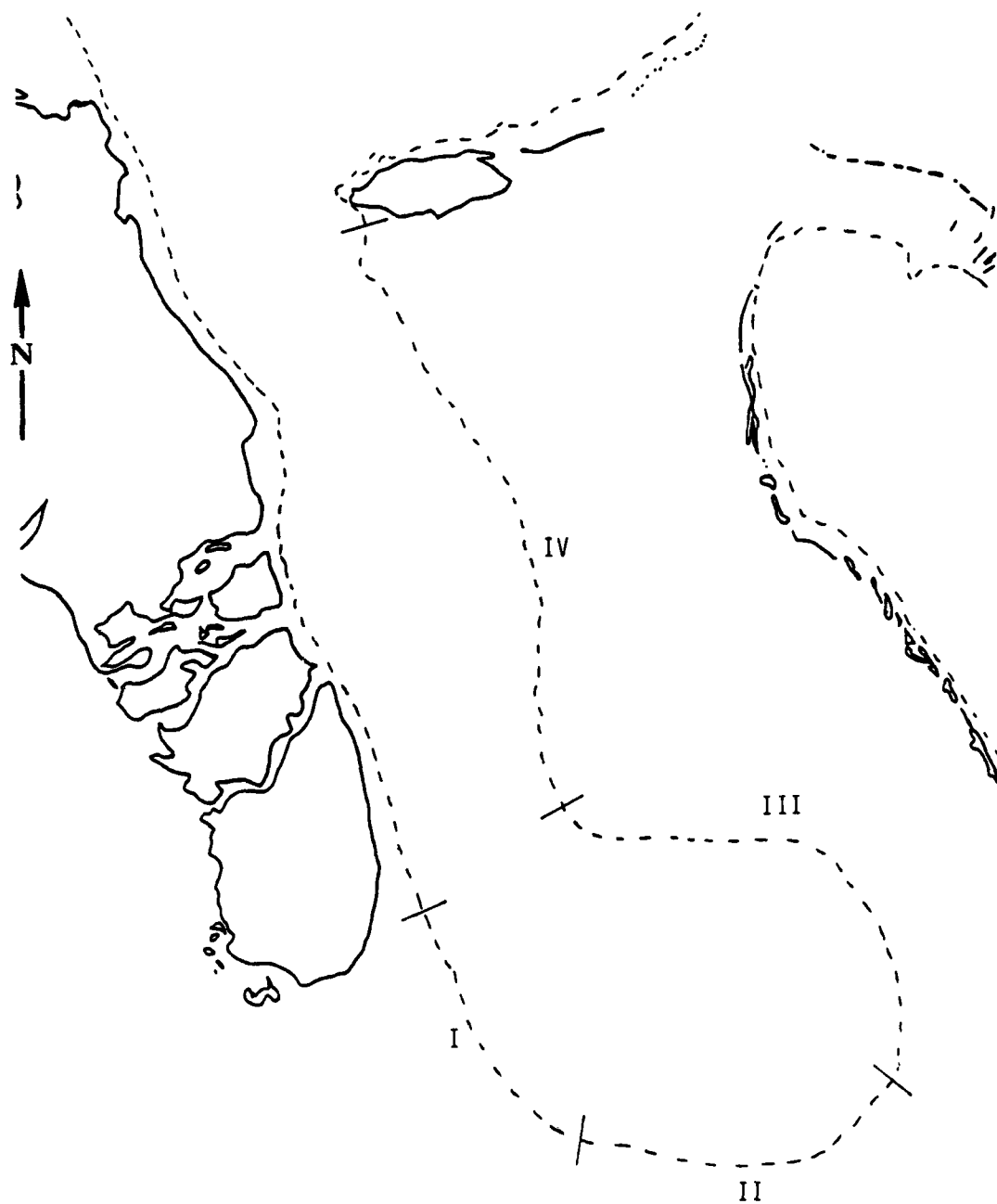
FIGURE 46. FOUR SUB-REGIONS OF THE EDGE OF THE GREAT BAHAMA
BANKS IN THE TONGUE OF THE OCEAN AREA

TABLE 4
DETECTABILITY OF BOTTOM-RELATED SURFACE PATTERNS ON
SEASAT SAR IMAGERY COLLECTED OVER THE
TONGUE OF THE OCEAN

| Seasat Revolution | Tidal Bar Belts[*] | Edge of Great Bahama Banks[*] | | | |
|---|---|---|---|---|---|
| | | I | II | III | IV |
| 450 | G | NC | E | G | G |
| 529 | P | NC | N | N | N |
| 694 | G | NC | E | N | E |
| 1024 | G | P | P | P | P |
| 1110 | G | P | P | P | P |
| 1153 | G | E | E | P | P |
| 1196 | N | P | N | N | N |
| 1239 | E | G | P | N | N |
| 1282 | P | G | P | N | N |
| 1325 | P | P | P | N | N |
| 1368 | E | E | E | P | N |
| 1411 | E | E | G | P | P |

[*]Detectability Categories:  
E – Feature Very Visible  
G – Feature Moderately Visible  
P – Feature Faintly Visible  
N – Feature Not Visible  
NC – Feature Outside Area of SAR Coverage

TABLE 5
SUMMARY OF DETECTABILITY CATEGORIES FOR TONGUE OF THE OCEAN SEASAT SAR IMAGES

| Detectability Category | Tidal Bar Belt | | Edge of Great Bahama Bank | | | | | | | |
| --- | --- | --- | --- | --- | --- | --- | --- | --- | --- | --- |
| | | | Section I | | Section II | | Section III | | Section IV | |
| | Number | Percent | Number | Percent | Number | Percent | Number | Percent | Number | Percent |
| E - Feature Very Visible on SAR Image | 3 | 25 | 3 | 33 | 4 | 33 | 0 | 0 | 1 | 8 |
| G - Feature Moderately Visible on SAR Image | 5 | 92 | 2 | 22 | 1 | 8 | 1 | 8 | 1 | 8 |
| P - Feature Faintly Visible on SAR Image | 3 | 25 | 4 | 45 | 5 | 42 | 5 | 42 | 4 | 33 |
| N - Feature not Visible on SAR Image | 1 | 8 | 0 | 0 | 2 | 17 | 6 | 50 | 6 | 50 |
| Total Number of Seasat Passes over Area | 12 | | 9 | | 12 | | 12 | | 12 | |
| Feature Detected on SAR Image (E, G, P Combined) | 11 | 92 | 9 | 100 | 10 | 83 | 6 | 50 | 6 | 50 |

stages and heights were obtained from tide tables (Kline, 1978) and tidal currents were estimated using the observations of Palmer (1979) and the linear model presented in Figure 47. The model presented in Figure 47 was constructed by assuming the semidiurnal tides in the Bahamas had a maximum current velocity of 1.5 m/s when they were flowing on or off the Great Bahama Banks (after Palmer, 1979). If the stage of the tides were known (as they were for the TOTO region), then a current velocity could be obtained from Figure 47 assuming the standing wave mode to be dominant in this region. The environmental conditions are summarized in Table 6.

Although not enough data exist for a rigorous statistical analysis, we can examine the data for trends by plotting the average of an environmental parameter versus each detection criteria. This information is presented in Table 7 and summarized in Figures 48-50 for wind speed, tidal height, and tidal velocity. From these figures, the following trends can be observed:

1. All the wind speeds (see Figure 48) for the TOTO region were between the minimum and maximum suggested in the previous section (greater than 1 m/s but less than 10 m/s). From these data, it appears that the bottom-related surface patterns are most visible when the wind is less than 3 m/s.

2. Tidal heights appear to be correlated to detectability of the surface patterns (see Figure 49), with greater visibility occurring at lower water levels.

3. Tidal current velocities (see Figure 50) are somewhat correlated to the detectability categories, with the greater visibility occurring at higher current velocities.

In addition, no apparent correlation exists between the stage of the tide (e.g., ebb or flow) and the detectability of the features on the Seasat SAR imagery.
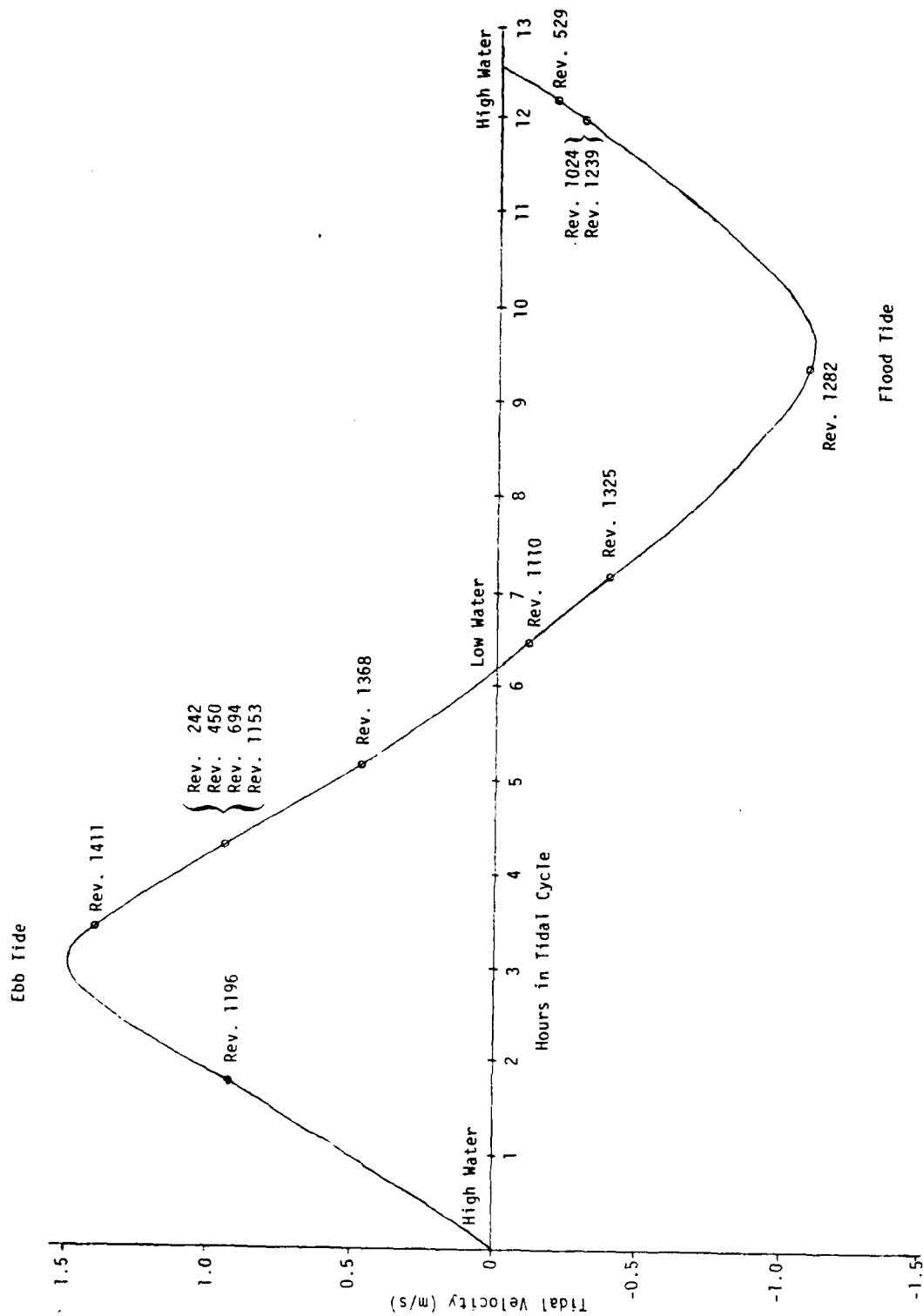
FIGURE 47. MODEL OF TIDAL CURRENT VELOCITIES AT EDGE OF TONGUE OF THE OCEAN

TABLE 6

SUMMARY OF THE ENVIRONMENTAL CONDITIONS FOR THE TONGUE OF THE OCEAN TEST SITE

| Seasat* Revolution | Wind Speed (m/s) | Wind Direction (°T) | Tidal Height (feet Above Mean Low Water) | Tide Direction | Estimated Tidal Current Velocity (m/s) |
|---|---|---|---|---|---|
| 450 | 2.0 | 150 | 1.6 | Ebb | 0.9 |
| 529 | 3.5 | 80 | 3.5 | Flood | 0.3 |
| 694 | 2.0 | 90 | 1.5 | Ebb | 0.9 |
| 1024 | 5.5 | 200 | 3.6 | Flood | 0.8 |
| 1110 | 4.0 | 210 | 1.1 | Flood | 0.1 |
| 1153 | 3.0 | 20 | 1.8 | Ebb | 0.9 |
| 1196 | 2.0 | 90 | 3.3 | Ebb | 0.9 |
| 1239 | 4.8 | 90 | 3.6 | Flood | 0.8 |
| 1282 | 3.5 | 95 | 2.4 | Flood | 1.3 |
| 1325 | 4.0 | 325 | 1.6 | Flood | 0.4 |
| 1368 | 2.5 | 70 | 1.3 | Ebb | 0.4 |
| 1411 | 2.5 | 360 | 2.4 | Ebb | 1.4 |

*For date and time of each revolution, and also satellite heading, see Table 2.

TABLE 7
SUMMARY OF AVERAGE WIND SPEED, TIDAL HEIGHT AND TIDAL CURRENT
VELOCITY FOR EACH DETECTION CATEGORY,
TONGUE OF THE OCEAN TEST SITE

| | Wind Speed (m/s) | Tidal Height (feet Above Mean Low Water) | Tidal Current Velocity (m/s) |
|---|---|---|---|
| **Tidal Bar Belt Region** | | | |
| None Category | 2.0 | 3.3 | 0.9 |
| Poor Category | 3.4 | 2.5 | 0.6 |
| Good Category | 3.3 | 1.9 | 0.7 |
| Excellent Category | 3.3 | 2.4 | 0.9 |
| **Great Bahama Bank** | | | |
| **Region I** | | | |
| None Category | --- | --- | --- |
| Poor Category | 3.9 | 2.4 | 0.6 |
| Good Category | 4.2 | 3.0 | 1.0 |
| Excellent Category | 2.7 | 1.8 | 0.9 |
| **Region II** | | | |
| None Category | 2.8 | 3.4 | 0.6 |
| Poor Category | 4.4 | 2.5 | 0.7 |
| Good Category | 2.5 | 2.4 | 1.4 |
| Excellent Category | 2.4 | 1.6 | 0.7 |
| **Region III** | | | |
| None Category | 3.3 | 2.7 | 0.8 |
| Poor Category | 3.5 | 1.0 | 0.7 |
| Good Category | 2.0 | 1.6 | 0.9 |
| Excellent Category | --- | --- | --- |
| **Region IV** | | | |
| None Category | 3.4 | 2.6 | 0.7 |
| Poor Category | 3.8 | 2.2 | 0.8 |
| Good Category | 2.0 | 1.6 | 0.9 |
| Excellent Category | 2.0 | 1.5 | 0.9 |
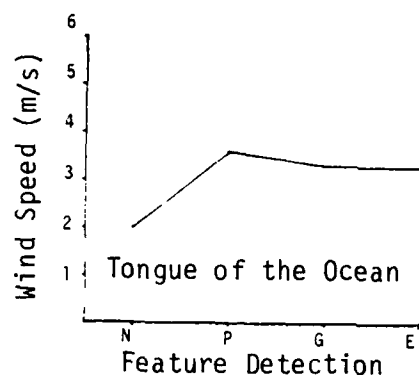
N - None
P - Poor
G - Good
E - Excellent
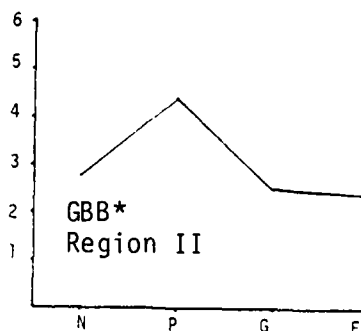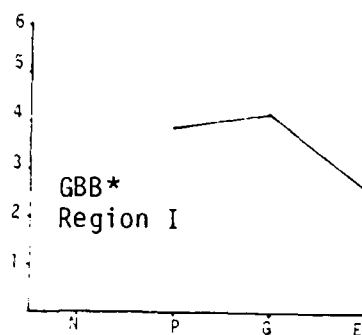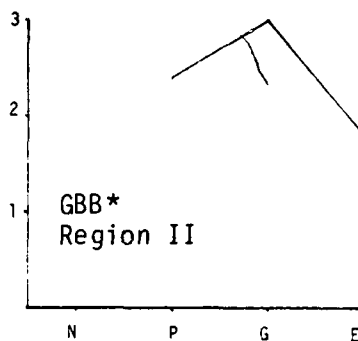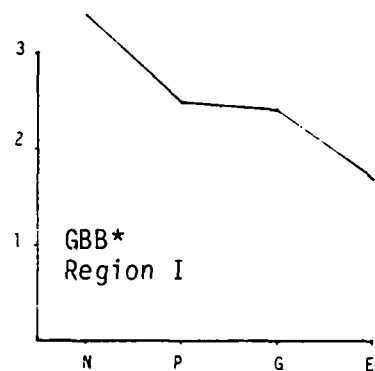
*Great Bahama Bank

FIGURE 48.   DETECTION OF BOTTOM FEATURES IN THE TONGUE OF THE
OCEAN REGION AS A FUNCTION OF WIND SPEED
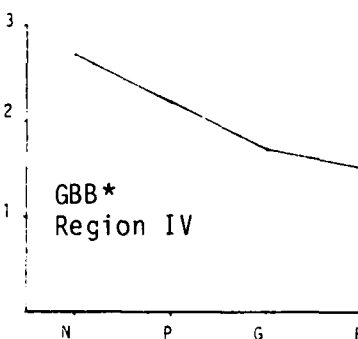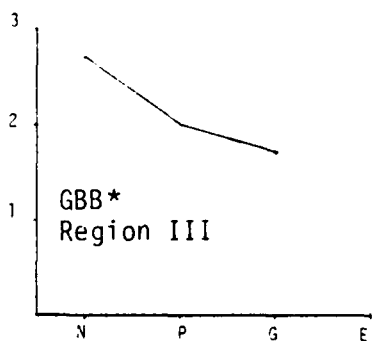
FIGURE 49. DETECTION OF BOTTOM FEATURES IN THE TONGUE OF THE
OCEAN REGION AS A FUNCTION OF TIDE HEIGHT
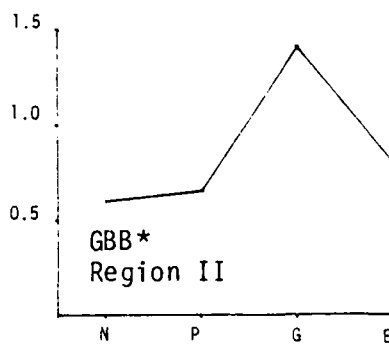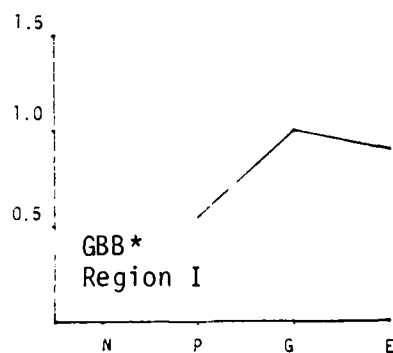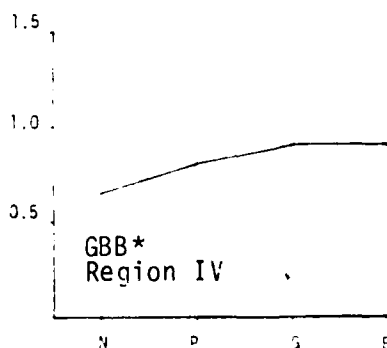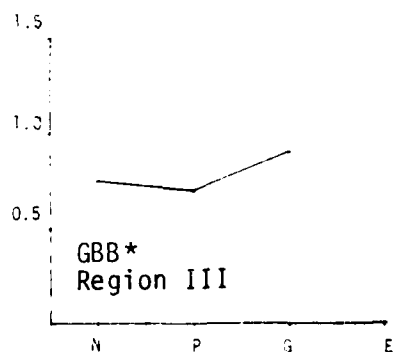
FIGURE 50.   DETECTION OF BOTTOM FEATURES IN THE TONGUE OF THE
OCEAN REGION AS A FUNCTION OF TIDAL CURRENT VELOCITY

A comparison of the observed (on Seasat imagery) position of the tidal bar belts and the edge of the Great Bahama Bank reveals that each of these features occurs in approximately the same position on the various Seasat SAR images. The appearance of these features, however, can change rather dramatically.

Figure 51 presents two examples of Seasat SAR images collected at the edge of the Great Bahama Bank, over a series of tidal bar belts in the southern end of the Tongue of the Ocean. The two images presented in Figure 51 were collected during Revolution 1411 (3 October 1978) and Revolution 1239 (21 September 1978). Comparison of the SAR images with the corresponding hydrographic chart reveals that the pattern located from B1 to E4 corresponds to the edge of the Great Bahama Bank, while the banded patterns (A2 to E5) correspond to the tidal bar belts in this area. The differences in the imagery in Figure 51 can be explained through the use of the hydrodynamic/ electromagnetic model developed by Shuchman (1982).

Examination of tide tables for the Bahamas (Kline, 1978) indicates at the time of Revolution 1411, the tide stage was four hours before low tide, indicating the presence of an ebb flow of water off the Great Bahama Bank into the TOTO. During Revolution 1239, the tide stage was one hour before high water, indicating the presence of a flood tide onto the Great Bahama Bank from the TOTO. Weather records from the Bahama Meteorological Office at Nassau showed a north wind with a velocity of 2.5 m/s was present during Revolution 1411 while an east wind of 4.8 m/s was present during Revolution 1239.

There are three environmental factors influencing the ocean surface roughness sensed by the SAR. These factors are: the current speed, depth of water, and the wind. In regions where the depth (and therefore the current speed) is changing rapidly, the roughness is influenced primarily by the rate of change of the current speed. A

(a) Rev. 1239

(b) Rev. 1411

(c) Hydrographic Chart
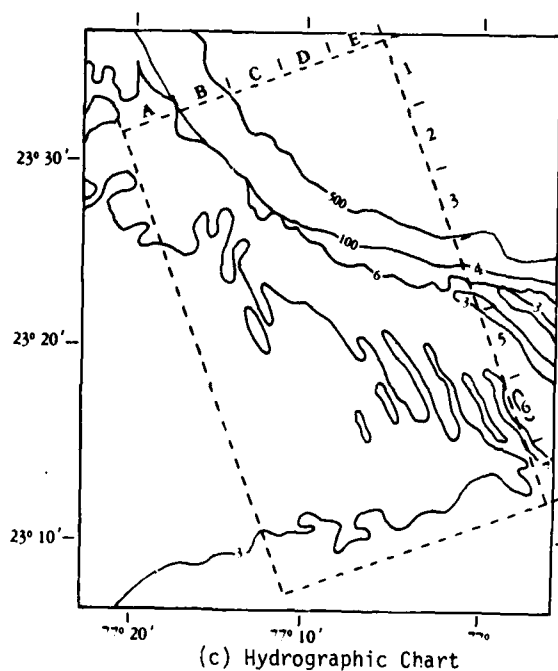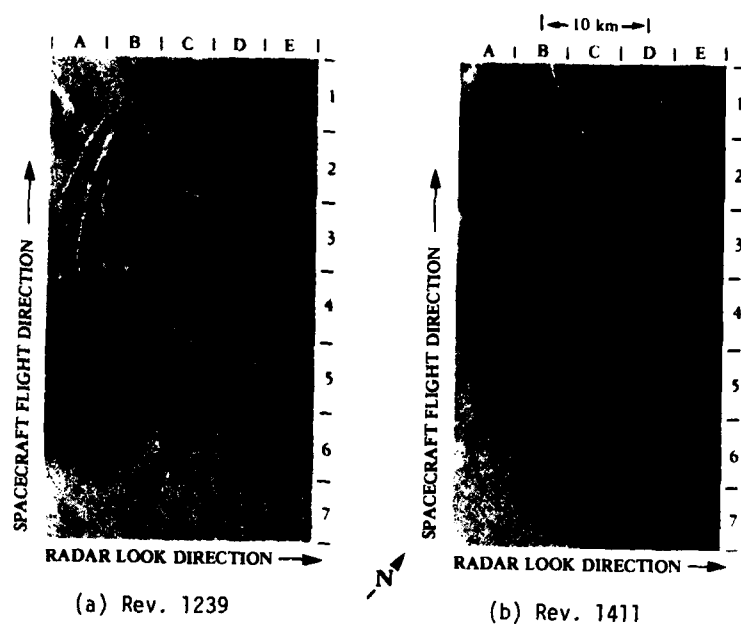
FIGURE 51.    SEASAT SAR IMAGERY AND HYDROGRAPHIC CHART OF THE TONGUE
OF THE OCEAN: (a) SEASAT REV. 1239 (21 Sept 1978), (b)
SEASAT REV. 1411 (8 Oct 1978), AND (c) HYDROGRAPHIC CHART
OF AREA.  (Seasat digitally processed imagery courtesy
of JPL.  Chart reproduced from DMA Chart Nos. 26300 and
27040.)

101

changing current tends to increase or decrease the amplitude of the small capillary and ultra-gravity waves on the surface and make the surface rougher or smoother, depending on the direction of the current relative to the waves. In areas where the depth and the current are nearly constant, the surface roughness is governed primarily by the wind. The wind can be thought of as a restoring force which tends to bring the wave height or surface roughness into an equilibrium value which depends on the wind speed. Thus, if current variations cause the wave height to be decreased, the wind, given sufficient time, will return the wave height to its original value. These general statements are illustrated for the two particular cases illustrated in Figure 51 in the following paragraphs.

The bottom topography for the southern edge of the TOTO maybe modeled and divided into seven regions as illustrated in Figure 52. The pattern of surface roughness variations depends on the current direction. For simplicity, in both of these cases the waves are assumed to be propagating in the same direction as the current. Essentially the same qualitative descriptions hold if the waves are propagating in the opposite direction to the current except that the phenomenon of wave blockage can occur if the current velocity changes from less than the group velocity of the waves to larger than this velocity. For a falling tide (Figure 52a) the following interactions occur:

Region 1: The depth is assumed to be uniform over a large enough area so that the wave height (surface roughness) has reached an equilibrium value for the existing wind speed and current conditions.

Region 2: Decreasing depth causes an increasing water current which in turn causes a progressive smoothing out of the surface roughness pattern (i.e., a decrease in the amplitude of the capillary and ultra-gravity waves).

a) Falling Tide:

| Radar Image Tone | Gray | Dark | Bright | Gray | Bright | Gray |
|---|---|---|---|---|---|---|

Surface Roughness

Current Magnitude

| Zone | 1 | 2 | 3 | 4 | 5 | 6 | 7 |
|---|---|---|---|---|---|---|---|

Bottom

b) Rising Tide:

| Radar Image Tone | Gray | Bright | Gray | Dark | Gray | Dark | Gray |
|---|---|---|---|---|---|---|---|

Surface Roughness

Current Magnitude

| Zone | 1 | 2 | 3 | 4 | 5 | 6 | 7 |
|---|---|---|---|---|---|---|---|
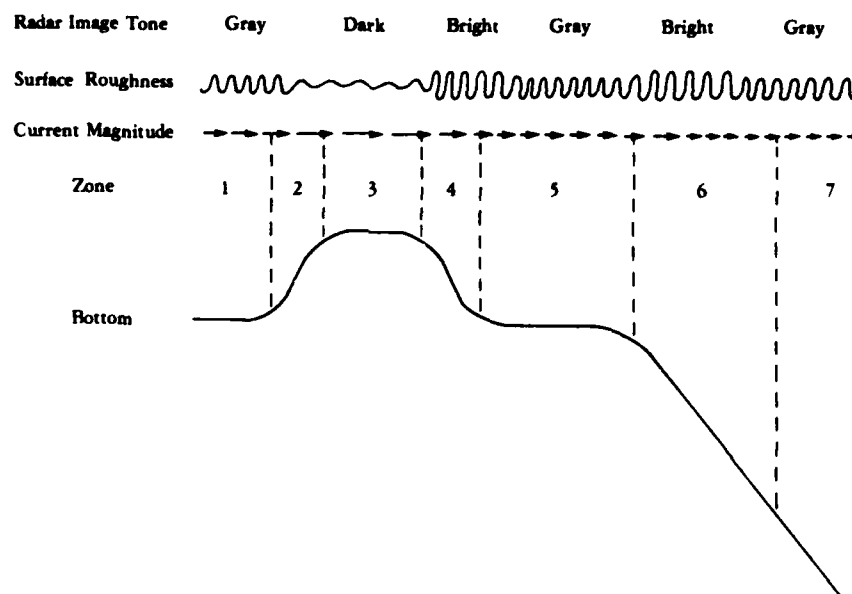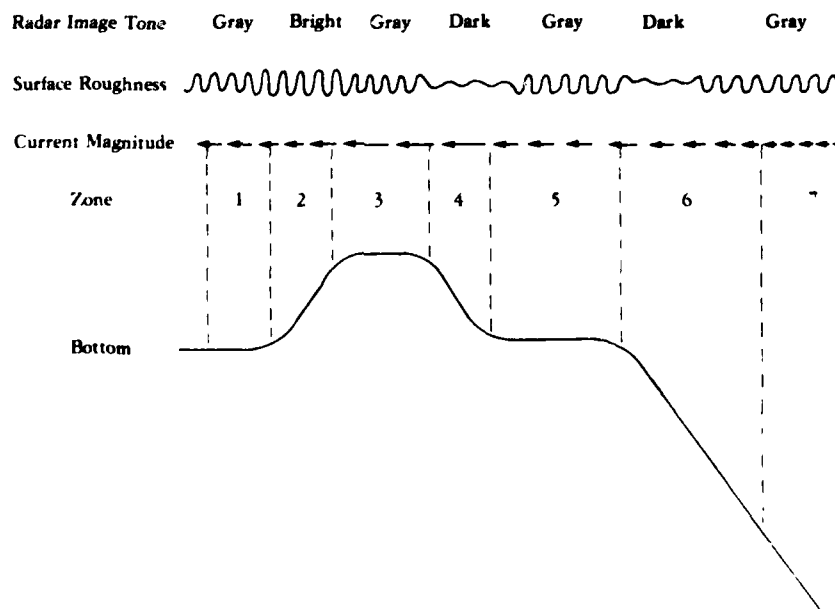
Bottom

FIGURE 52. SCHEMATIC DIAGRAM OF INTERACTIONS OF CURRENT, BOTTOM, AND CAPILLARY WAVES AND THE RESULTANT SAR IMAGE INTENSITY VARIATION FOR THE EDGE OF THE TONGUE OF THE OCEAN

103

Region 3:   The current remains constant while the wave height (sur-
face roughness) is brought back into equilibrium by the action of
the wind.

Region 4:   Increasing depth causes a decreasing current, thus a com-
pression of the surface, and a progressive roughening of the surface.

Region 5:   Depth and current remain constant while the wave height
readjusts into equilibrium with the wind.

Region 6:   Similar to region 4, i.e., a decreasing current causes an
increasing surface roughness.

Region 7:   Similar to region 5, i.e., a gradual return to equilibrium
with the given wind conditions.

The above model appears to adequately describe the patterns in Figure
51 for Revolution 1411, when an ebb tidal flow was present.  Note in
the SAR image collected over the southern portion of the TOTO, there
exists a series of ridges, each of which has the banded appearance
as described in regions 1 through 5 above.

For a rising (flood) tide (i.e., a current flowing onto the
bank), the following interactions occur, as illustrated in Figure
52b:

Region 7:   The depth is assumed to be uniform over a large enough
area so that the wave heights (i.e., surface roughness) has reached
an equilibrium with the existing wind speed and current conditions,
resulting in an area of uniform radar backscatter.

Region 6:   A decreasing water depth causes an increasing current
which in turn causes a smoothing out (damping) of the surface capil-
lary and ultra-gravity waves.

Region 5:   Gradual return to equilibrium.

Region 4:   Same as Region 6.

Region 3:  Gradual return to equilibrium.

Region 2:  An increasing water depth causes a decreasing current which in turn causes a compression of the surface waves and a progressive roughening of the surface with respect to the incident radar waves.

Region 1:  Gradual return to equilibrium.

This model appears to adequately describe the patterns present on Revolution 1239 during a flood tide.

Thus the surface patterns present on the two Seasat SAR images in Figure 51 are consistent with the hydrodynamic/electromagnetic model developed by Shuchman (1982) and illustrated in Figure 52. All Seasat SAR images collected over TOTO during ebb flows had patterns similar to those on Revolution 1411 imagery, while all those collected during flood conditions were similar to Revolution 1239 imagery.

Finally, the many Seasat SAR passes available over the Great Bahama Bank assisted in the elimination of a bottom feature being the cause of an anomalous surface pattern.  During the examination of the TOTO SAR imagery, numerous patterns, similar to those presented in Figure 53, were noted over the Great Bahama Banks.  Because of many sandy shoal areas on the Great Bahama Banks, they were considered to be a potential source for these anomalous patterns.  Another potential source for these patterns is the thunderstorms which are present in this area during this time of the year.

If the anomalous surface patterns were caused by a shoal area, then we would expect these patterns to be clustered around the same geographic location.  If, on the other hand, they were caused by thunderstorms, their locations would be more or less random.

The positions of these anomalous features from all twelve SAR passes from the TOTO region were plotted on the same map.  This map

FIGURE 53. EXAMPLES OF SURFACE PATTERNS CAUSED BY RAIN SQUALLS ON SEASAT SAR IMAGERY. (Rev. 1368. Optically processed imagery courtesy of JPL.)

106
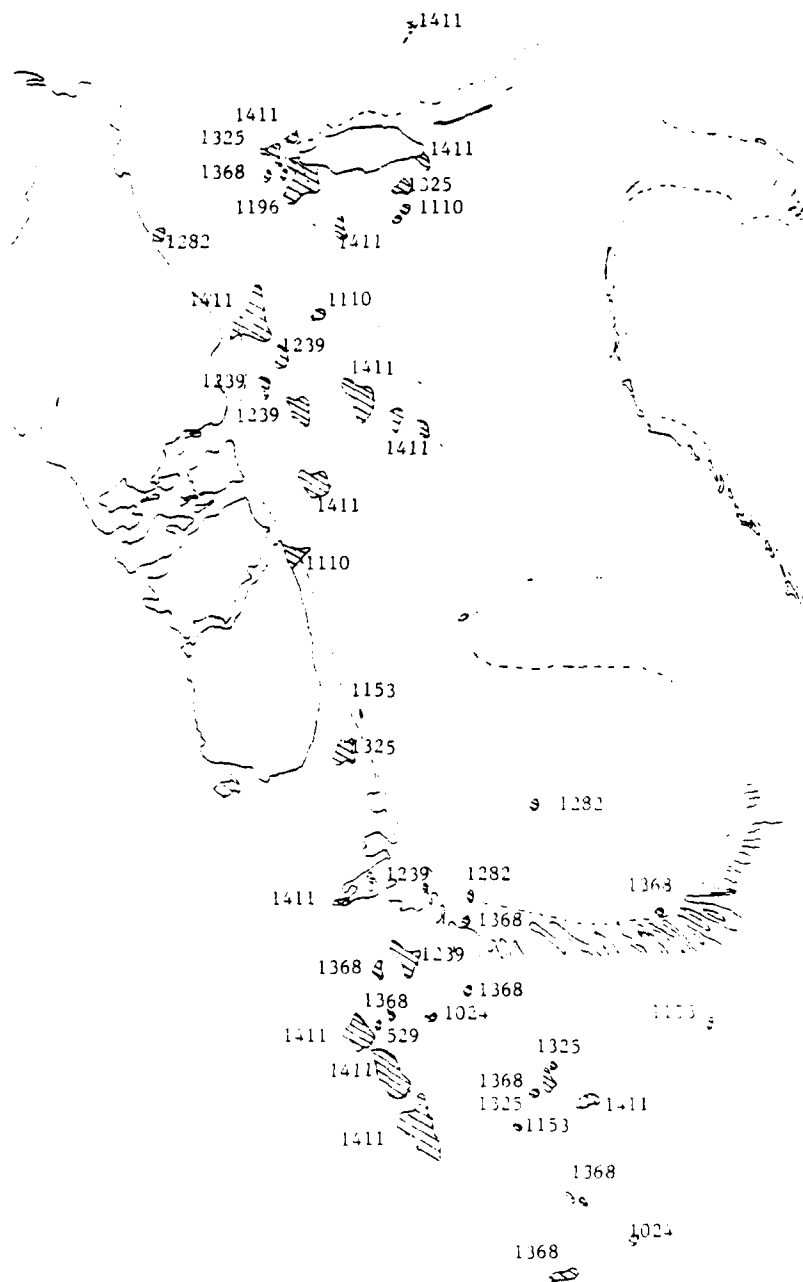
FIGURE 54.    LOCATIONS OF THUNDERSTORM SIGNATURES ON
              SEASAT SAR IMAGERY COLLECTED OVER TOTO
              REGION

is presented as Figure 54, which reveals that the patterns are randomly distributed and also occur in the center of the deep-water area of the TOTO. Therefore, these patterns are believed to be due to thunderstorms or other transient meteorological effects evidenced on the ocean surface. (For a further discussion on SAR detection of meteorological events, see Appendix A.)

## 5.3 JASIN TEST SITE

Data used in this portion of the study were collected during the Joint Air/Sea Interaction (JASIN) experiment (Allan and Guymer, 1980). The JASIN experiment was proposed in 1966 as part of the Global Atmospheric Research Project and was sponsored and organized by the Royal Society of the United Kingdom. The primary aims of the JASIN experiment were to "observe and distinguish between the physical processes causing mixing in the atmospheric and oceanic boundary layers and relate them to mean properties of the layers; and to examine and quantify aspects of the momentum and heat budgets in the atmospheric and oceanic boundary layers and fluxes across and between them" (Royal Society, 1979). To this end, fifty principal investigators from nine countries collaborated on an intensive experiment from mid-July to mid-September, 1978. Fourteen oceanographic research vessels were on site during this period.

Seasat, launched just prior to the JASIN experiment, offered investigators a unique opportunity to collect satellite data over a well instrumented test site. A Seasat SAR receiving station had been set up at Oakhangar, England for the European Space Agency and radar data were collected on twenty different occasions when Seasat passed over or near the JASIN study area. Fifteen of those passes form the basis for part of the present study (data from two passes were of too poor quality to process and imagery from three passes did not have accurate final annotations and no land nd therefore could not be accurately located). Surface data collected during the JASIN

experiment included measurements of wave frequency, direction and height, and wind speed and direction. In addition, numerous sub-surface measurements of temperature, salinity and current direction and velocity were obtained by instruments suspended from buoys.

Figure 25 shows the location of the oceanographic intensive array where many of the oceanographic measurements were obtained during the JASIN experiment. When Seasat made its passes over JASIN, it not only covered this test site, but also the areas adjacent to it. Therefore, extensive SAR coverage of the Northeast Atlantic during the late summer and early fall of 1978 exists.

Figure 55 was reproduced from the Institute of Oceanographic Sciences Chart Number C6567 (for a description of this chart, see Roberts, et al., 1980). In conjunction with the JASIN experiment, extensive hydrographic surveys of this portion of the Atlantic were made, resulting in a bathymetric chart which is unusually accurate for a deep-water area.

There are 17 distinct bottom topographic features present in this area (see Figure 55). These features are listed in Table 8, along with the shallowest contour interval charted for that feature, the estimated depth of the adjacent deep-water area, and the calculated slope for the feature.

In order to study the relationship between surface patterns on Seasat SAR imagery and these bottom features, the following procedure was used: the location of the ground coverage of the Seasat SAR was obtained by consulting the satellite data record (SDR) for each pass. A SDR contains a series of ground latitude and longitude coordinates for specific times during the Seasat pass. Most of the Seasat SAR images contained annotations of the time the data were collected. Therefore, the location of a particular surface pattern could be identified by noting the time when the pattern occurred during that orbit. First the ground coverage of each pass was marked on an over-lay placed on the chart. Second, the locations of all internal waves
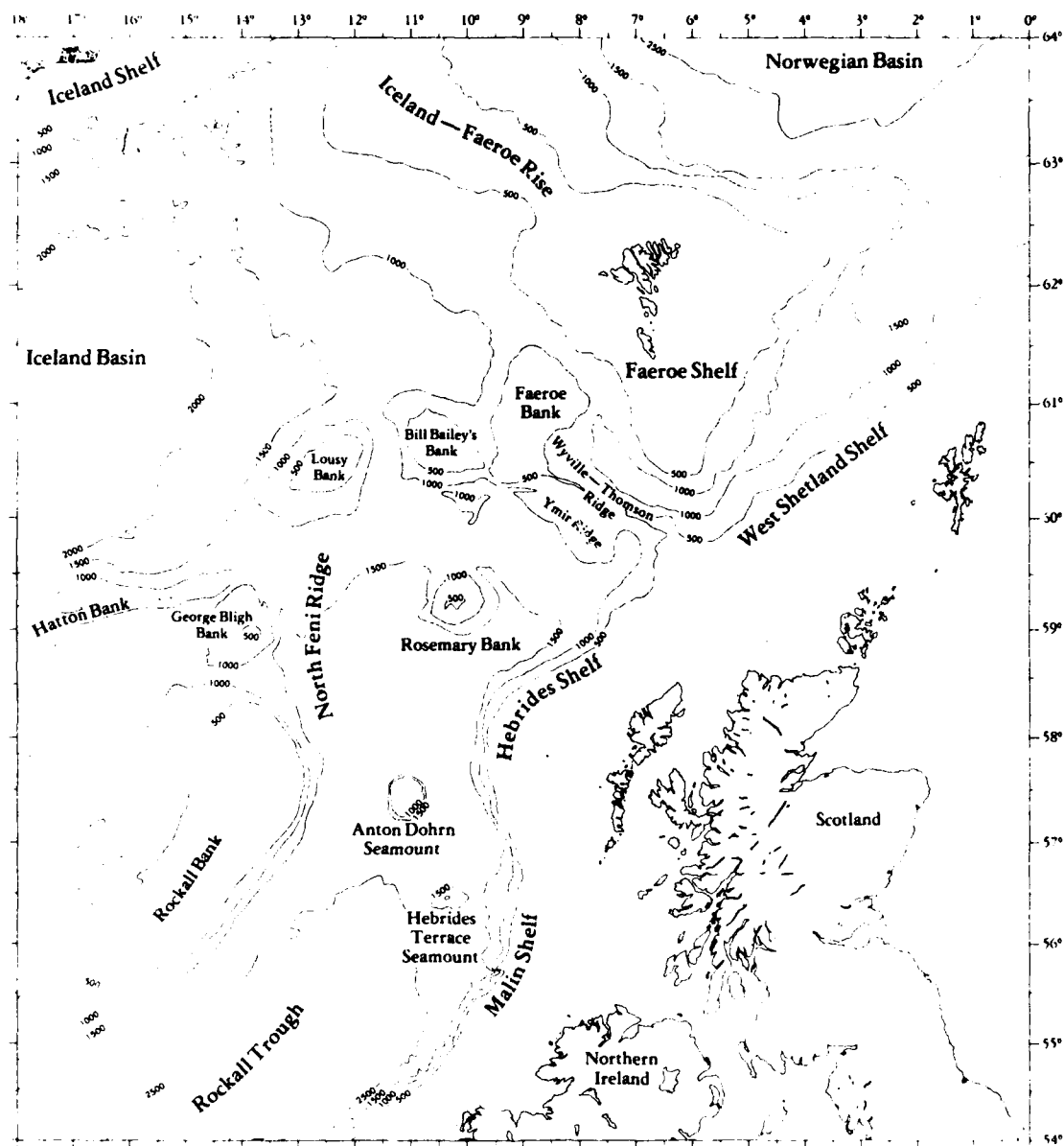
FIGURE 55. LOCATION OF MAJOR BOTTOM TOPOGRAPHIC FEATURES IN
NORTHEAST ATLANTIC

110

## TABLE 8
## BOTTOM TOPOGRAPHIC FEATURES IN THE NORTHEASTERN ATLANTIC

| Bottom Feature | Shallowest Point (m) | Depth of Adjacent DW* (m) | Local Slope (Degrees) |
|---|---|---|---|
| Iceland-Faeroe Rise | 300 | 1000 | 5 |
| Bill Bailey's Bank | 100 | 1200 | 13 |
| Lousy Bank | 300 | 1500 | 28 |
| Hatton Bank | 500 | 2000 | 18 |
| George Bligh Bank | 500 | 1100 | 11 |
| Faeroe Bank | 100 | 1000 | 8 |
| Faeroe Shelf | 300 | 1000 | 7 |
| Wyville-Thomson Ridge | 400 | 1200 | 17 |
| Ymir Ridge | 600 | 1500 | 31 |
| North Feni Ridge | 1200 | 2000 | 5 |
| Rosemary Bank | 500 | 2000 | 23 |
| Rockall Bank | 300 | 2300 | 20 |
| Anton Dohrn Seamount | 600 | 2100 | 28 |
| West Shetland Shelf | 300 | 1000 | 11 |
| Malin Shelf | 200 | 2000 | 31 |
| Hebrides Terrace Seamount | 1000 | 2400 | 27 |
| Hebrides Shelf | 200 | 1500 | 28 |

*Deep Water

and frontal boundaries (see Section 4.4) were noted and then these locations marked on the overlay. Finally, a surface pattern was said to be associated with a bottom feature if its location was within 10 kilometers of that feature, as will be discussed below.

The internal wave groups and frontal boundaries observed on the JASIN SAR imagery were very large features, often being over 100 km long and 30 to 50 km wide. The hydrodynamic interactions believed to be responsible for these features are very much different than those responsible for shallow-water patterns; therefore, the surface patterns occur over a much larger area with less exactness than the shallow-water patterns (i.e., they usually do not take on the same shape as the bottom feature).

Figure 56 shows the total SAR coverage of the northeast Atlantic obtained by the 15 passes. Each deep-water feature listed in Table 8 was covered during a minimum of two passes and a maximum of eight.

Table 9 presents the occurrence of internal wave and frontal boundary patterns on Seasat SAR imagery for each of the seventeen deep-water bottom features. Table 10 summarizes these occurrences for each Seasat revolution. Given in Table 10 are the Seasat revolution number, the total number of deep-water bottom features within the ground coverage of a pass, and the total number of times an internal wave or frontal boundary pattern occurred over or near (±10 km) a bottom feature.

Presented in Figure 57 are the locations of the internal wave features which appeared on the Seasat imagery. The length of the lines indicate the two-dimensional extent of each internal wave packet. The lines with the arrows indicate the direction the crests of the internal waves are traveling. If no direction could be determined, then an arrow was placed at both ends. Plotted on Figure 58 are the locations and extent of the frontal boundaries identified on the JASIN SAR imagery.
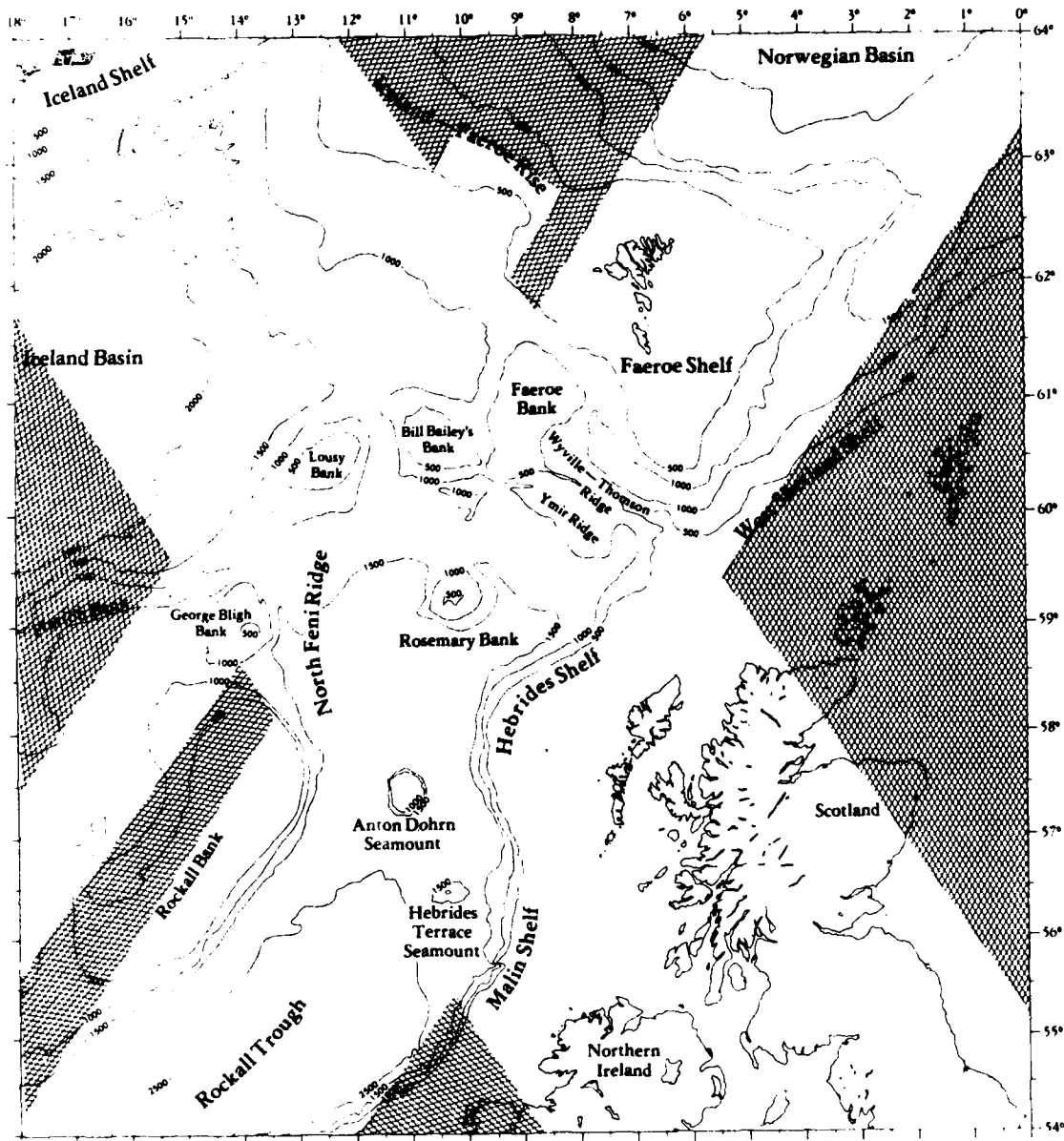
FIGURE 56. COVERAGE OF NORTHEAST ATLANTIC OCEAN BY THE SEASAT SAR
FROM OVERFLIGHTS MADE DURING THE JASIN EXPERIMENT.
(Depth in meters.)

TABLE 9
SUMMARY OF OCCURRENCES OF BOTTOM-RELATED SURFACE PATTERNS
ON SEASAT SAR IMAGERY

| Bottom Feature Covered by Seasat SAR | SAR Revolution Number | SAR Observed Pattern[*] | |
|---|---|---|---|
| | | Internal Wave | Frontal Boundary |
| Iceland-Faeroe Rise | 719 | X | |
| | 762 | X | X |
| | 958 | X | |
| | 1044 | X | X |
| | 1087 | X | |
| Bill Bailey's Bank | 719 | X | X |
| | 757 | | |
| | 1006 | | X |
| | 1044 | | |
| | 1049 | X | X |
| | 1087 | X | |
| Lousy Bank | 633 | X | X |
| | 791 | | X |
| | 834 | X | |
| | 958 | X | |
| | 1006 | | |
| | 1044 | X | X |
| | 1049 | X | X |
| | 1087 | X | |
| Hatton Bank | 547 | | |
| | 791 | | X |
| | 958 | | X |
| | 1044 | X | |
| George Bligh Bank | 547 | X | |
| | 791 | | X |
| | 958 | X | |
| | 1044 | X | |
| | 1087 | X | |
| Faeroe Bank | 556 | | X |
| | 719 | | X |
| | 757 | X | X |
| | 762 | X | X |

114

TABLE 9
SUMMARY OF OCCURRENCES OF BOTTOM-RELATED SURFACE PATTERNS
ON SEASAT SAR IMAGERY (Continued)

| Bottom Feature Covered by Seasat SAR | SAR Revolution Number | SAR Observed Pattern[*] | |
|---|---|---|---|
| | | Internal Wave | Frontal Boundary |
| Faeroe Shelf | 556 | | X |
| | 599 | X | X |
| | 642 | X | X |
| | 757 | | |
| | 762 | X | X |
| Wyville-Thomson Ridge | 556 | X | |
| | 599 | X | |
| | 642 | | X |
| | 719 | X | |
| | 757 | | |
| | 762 | X | X |
| Ymir Ridge | 556 | X | |
| | 599 | X | |
| | 642 | X | |
| | 719 | X | |
| | 757 | X | |
| | 1049 | X | |
| North Feni Ridge | 547 | X | X |
| | 556 | | X |
| | 633 | | |
| | 757 | | |
| | 791 | X | X |
| | 834 | | |
| | 1006 | X | X |
| | 1049 | | X |
| Rosemary Bank | 556 | X | |
| | 599 | X | |
| | 633 | X | X |
| | 757 | | |
| | 834 | X | |
| | 1006 | X | X |
| | 1049 | X | |

TABLE 9
SUMMARY OF OCCURRENCES OF BOTTOM-RELATED SURFACE PATTERNS
ON SEASAT SAR IMAGERY (Concluded)

| Bottom Feature Covered by Seasat SAR | SAR Revolution Number | SAR Observed Pattern* | |
|---|---|---|---|
| | | Internal Wave | Frontal Boundary |
| Rockall Bank | 547 | X | |
| | 556 | | X |
| | 757 | X | |
| | 791 | X | |
| | 958 | X | X |
| | 1044 | | |
| | 1087 | | X |
| Anton Dohrn Seamount | 547 | X | X |
| | 556 | X | |
| | 599 | X | |
| | 791 | X | |
| West Shetland Shelf | 642 | X | |
| | 762 | X | |
| Malin Shelf | 547 | | X |
| | 633 | X | |
| | 791 | X | |
| | 834 | | |
| Hebrides Terrace Seamount | 547 | X | |
| | 642 | X | |
| | 791 | | |
| Hebrides Shelf | 599 | | |
| | 633 | | |
| | 642 | | |
| | 719 | | |
| | 762 | X | |
| | 834 | | |
| | 1006 | | X |
| | 1049 | | |
| TOTAL | 92 | 58 | 35 |

--------
*An x indicates that surface pattern appeared over the position of the bottom feature during a particular Seasat revolution.
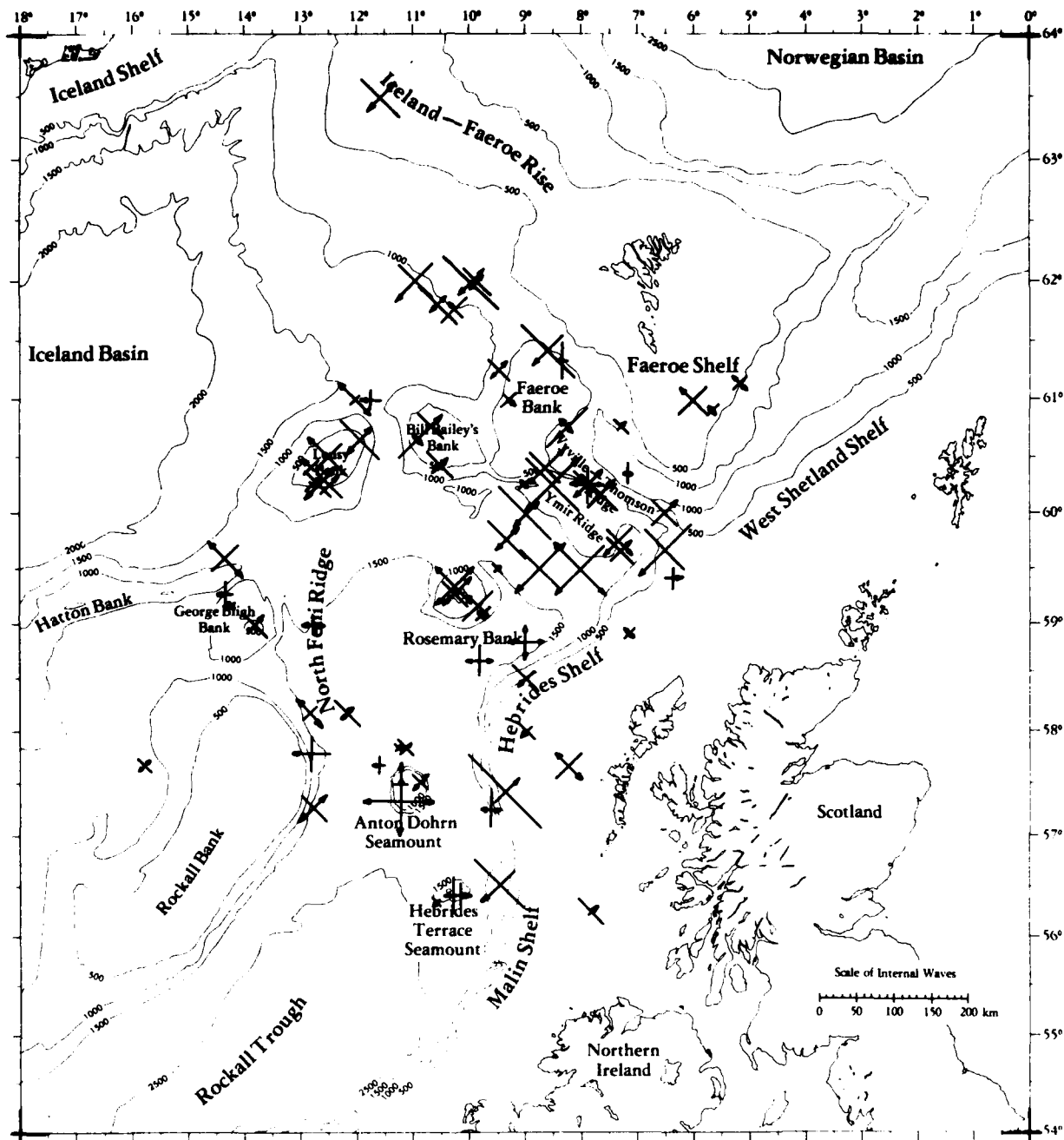
FIGURE 57. LOCATION OF INTERNAL WAVE-LIKE SIGNATURES IDENTIFIED ON SEASAT
SAR IMAGES COLLECTED OVER THE JASIN AREA

117

TABLE 10
SUMMARY OF DETECTIONS OF DEEP WATER TOPOGRAPHIC FEATURES
BY SEASAT SAR IMAGERY USING DATA COLLECTED
DURING THE JASIN STUDY

| Seasat Revolution | Total Number of Deep Water Bottom Features Covered | Total Number of Occurrences of Internal Waves Over Features | Total Number of Occurrences of Frontal Boundaries Over Features |
|---|---|---|---|
| 547 | 7 | 5 | 3 |
| 556 | 8 | 4 | 4 |
| 599 | 6 | 5 | 1 |
| 633 | 5 | 3 | 2 |
| 642 | 6 | 4 | 3 |
| 719 | 6 | 4 | 2 |
| 757 | 8 | 3 | 1 |
| 762 | 6 | 6 | 4 |
| 791 | 8 | 4 | 4 |
| 834 | 5 | 2 | 0 |
| 958 | 5 | 4 | 2 |
| 1006 | 5 | 2 | 4 |
| 1044 | 6 | 4 | 2 |
| 1049 | 6 | 4 | 2 |
| 1087 | 6 | 4 | 1 |
| Total | 89 | 58 | 35 |
| Percent | | 63 | 38 |
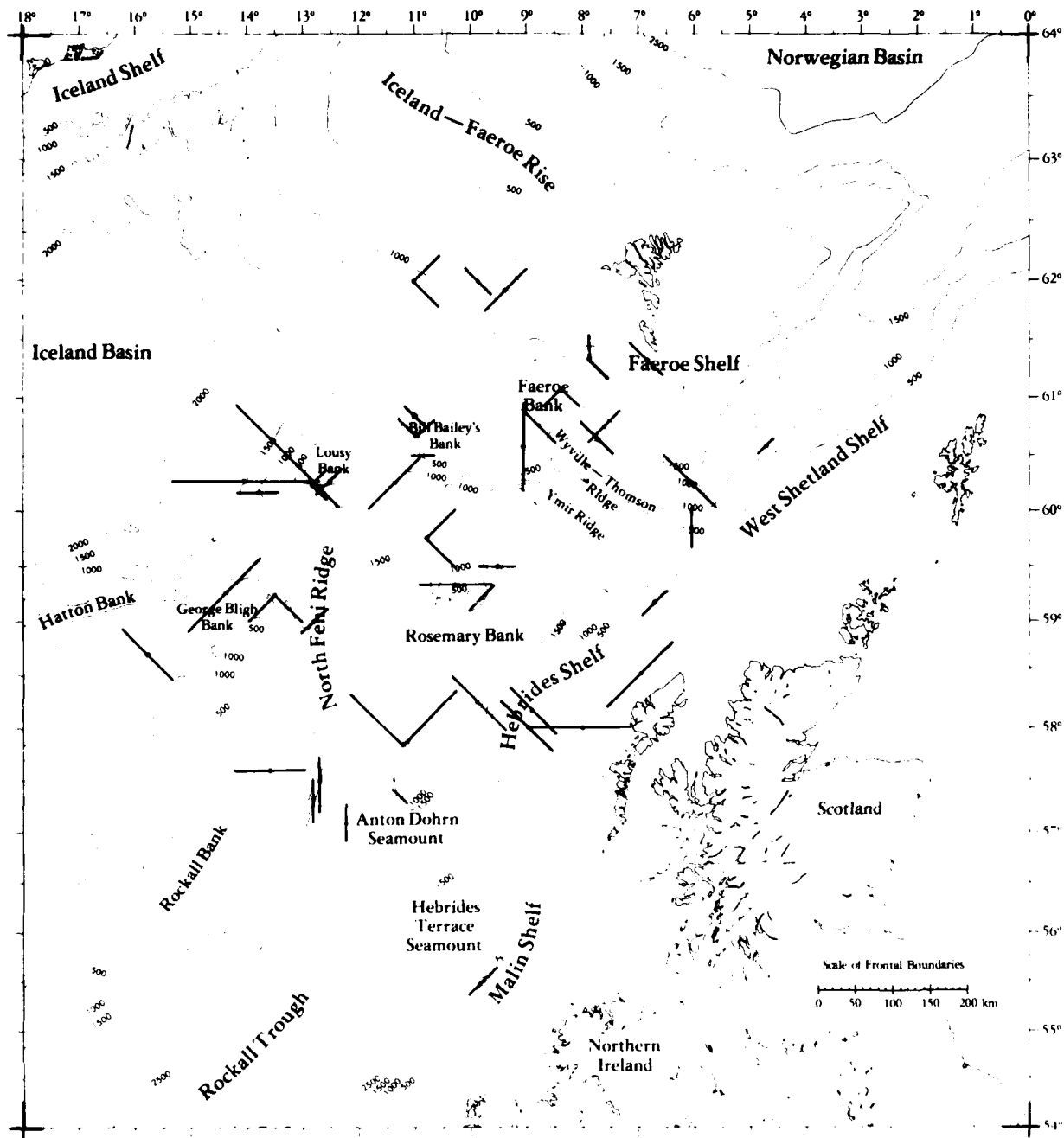
FIGURE 58. LOCATION OF FRONTAL BOUNDARIES IDENTIFIED ON SEASAT SAR IMAGES COLLECTED OVER THE JASIN AREA

From Table 10, we can see that 63 percent of the internal waves
and 38 percent of the frontal boundaries were associated with a bot-
tom feature.  An interesting result of the multi-temporal, deep-water
analysis was that at no time did an internal wave pattern occur over
a deep-water area without a corresponding bottom feature (i.e., the
Rockall Trough, Iceland Basin or Norwegian Basin).  These results
strongly suggest a correlation between the deep-water bottom features
and the internal waves and also indicate some relationship may exist
between the occurrence of frontal boundaries and deep-water features.
They also suggest that the dissipation of deep-water propagating in-
ternal wave pockets is sufficiently high to preclude their detection
through successive passes.

To gain a better understanding of the deep-water surface patterns
on the JASIN Seasat imagery, the ancillary environmental data were
examined, and correlated to the appearance or absence of internal
waves or frontal boundaries.

### 5.3.1  INTERNAL WAVE SIGNATURES

The surface environmental conditions present at the times of the
Seasat overpasses were compared to the occurrence of the internal
waves to determine if the absence of patterns could be explained by
the theory that adverse surface conditions (i.e., high winds and/or
waves) would mask the internal wave patterns.  The surface con-
ditions, collected during the JASIN experiment, are presented in
Table 11, along with the Seasat revolution number, dominant gravity
wave wavelength and direction of propagation, significant wave
height, and wind speed and direction.  These data were provided
courtesy of Dr. R. Stewart of the Scripps Institute of Oceanography.
For those cases where no surface measurement of dominant wave fre-
quency and direction existed, SAR derived values were substituted
(after Kasischke, 1980).

## TABLE 11
### SEA TRUTH AND SEASAT SATELLITE PARAMETERS FOR JASIN DATA

| Pass | STS* | Distance Between Sea Truth and SAR (m) | Wave Direction (°T) | Wavelength (m) | Wave Height (m) | Wind Speed (m/s) | Wind Direction (°T) |
|------|------|------|------|------|------|------|------|
| 547 | a | 10 | 263 | 170 | 1.6 | 4.5 | 015 |
| 556 | a | 65 | 280 | 151 | 1.5 | 3.6 | 030 |
| 559 | b/f | 145 | 20 | 71 | 1.1 | 6.9 | 014 |
| 663 | a | 58 | 220 | 89 | 1.1 | 7.9 | 150 |
| 642 | a | 210 | 200 | 169 | 2.7 | 10.9 | 160 |
| 719 | --- | --- | --- | --- | --- | 7.6 | --- |
| 757 | b | 10 | 240** | 256 | 4.9 | 15.2 | --- |
| 762 | d/f | 45 | 240 | 210 | 5.5 | 12.0 | 164 |
| 791 | b/f | 35 | 230 | 151 | 3.1 | 13.0 | 224 |
| 834 | a | 55 | 295 | 147 | 2.8 | 10.7 | 280 |
| 958 | c/b | 32 | 354 | 108 | 1.4 | 7.2 | --- |
| 1006 | a | 70 | 109 | 105 | 3.6 | 12.1 | 120 |
| 1044 | e/c | 30 | 264** | 244** | 5.7 | 11.5 | --- |
| 1049 | c/e | 30 | 264 | 244 | 5.0 | 6.3 | --- |
| 1087 | --- | --- | --- | --- | --- | 13.2 | --- |

\* Surface Truth Source
a. Atlantis II, pitch and roll buoy
b. Moored OIA, wave rider buoy
c. Discovery, pitch and roll buoy
d. John Murray, wave recorder
e. Discovery, wave recorder
f. John Murray, visual readings

\*\*Estimate

121

The Seasat revolutions were divided into two groups for this analysis. Group I contained all those revolutions where the internal wave detection rate was greater than 70 percent. Group II contained all revolutions where the internal wave detection rate was less than 70 percent.

The average wavelength, wave height, wind speed, and direction of wave travel with respect to radar look direction for each group are presented in Table 12. Also presented in Table 12 are the range of these values for each group. Table 12 shows that no strong patterns exists in the data, with the internal waves being detected over a wide variety of environmental conditions including high surface wind and look directions.

For detecting internal waves on SAR imagery, it has been suggested that internal waves with crest orientations perpendicular to the radar line of sight (i.e., range traveling) are detected more often than those whose crests are parallel (i.e., azimuth traveling) (Fu and Holt, 1982). Although cases exist where azimuth traveling internal waves have been imaged by SARs (see Vesecky and Stewart, 1982 or Figure 28, this report), these are thought to be the exception rather than the rule.

The orientations with respect to the radar line-of-sight of the crests of the internal waves on the JASIN SAR imagery were determined. Four orientation classifications were used:

1. $0°-30°$: The crests of the internal waves are parallel to the radar line-of-sight (i.e., azimuth traveling).

2. $30°-60°$: The crests of the internal waves are half-way between range and azimuth traveling.

3. $60°-90°$ The crests of the internal waves are perpendicular to the radar line-of-sight (i.e., range traveling)

4. $0°-90°$: The crests of the internal waves are oriented in all directions.

122

TABLE 12
COMPARISON OF INTERNAL WAVE DETECTION GROUPS TO
ENVIRONMENTAL PARAMETERS

| Environmental Condition | Group I (Internal Wave Detection Rate > 70%) | Group II (Internal Wave Detection Rate < 70%) |
|---|---|---|
| Wavelength | | |
| Average | 169 m | 175 m |
| Minimum | 71 m | 1ம்3 m |
| Maximum | 299 m | 256 M |
| | | |
| Wave Height | | |
| Average | 2.7 m | 3.4 m |
| Minimum | 1.1 m | 1.5 m |
| Maximum | 5.7 m | 5.0 m |
| | | |
| Wind Speed | | |
| Average | 8.9 m/s | 10.3 m/s |
| Minimum | 4.5 m/s | 3.6 m/s |
| Maximum | 13.2 m/s | 15.2 m/s |
| | | |
| Wave Direction with Respect to Radar Look Direction | | |
| Average | 60° | 47° |
| Minimum | 25° | 14° |
| Maximum | 84° | 85° |

Table 13 summarizes the distribution of the internal wave orientations for both the ascending passes and the descending passes. Also presented in Table 13 are the direction of orientation for the internal waves. A direction of NE-SW, for example, means the crest of the internal wave is oriented from the northeast to the southwest. Note from the data in Table 13, that 44 internal wave packets were observed during the eight ascending orbits and 44 internal wave packets were observed during the seven descending orbits.

If the orientation of the internal waves in the JASIN area were equally distributed in all directions, and the SAR had no bias in the manner it detects internal waves, then we would expect that an equal number of azimuth $(0°-30°)$ waves and range waves $(60°-90°)$ would be observed. From Table 13, we can see that well over 50 percent of the detected internal waves had a range orientation. However, we can also see that the majority of the waves were oriented in a northeast to southwest or southeast to northwest direction, indicating the waves were not equally distribute in all directions. It therefore appears more analysis is needed to interpret the meaning of the data presented in Table 13.

Throughout the analysis of the JASIN data, we have referred to a portion of the anomalous deep-water surface patterns on the SAR images as internal waves. Although we have yet to develop direct evidence that these surface patterns are internal waves, the circumstantial evidence for this being the case is strong.

The generation mechanisms and sources responsible for internal waves have been extensively researched during recent years (Wunch, 1976; Muller and Olbers, 1975; Bell, 1975; Baines, 1979). Even so, the knowledge of the physical processes for internal wave generation is still very limited because a determination of the sources and sinks of internal waves requires a continuous record of the wave spectra (Garrett and Munk, 1975 and 1979).

TABLE 13
ORIENTATION OF INTERNAL WAVES OBSERVED ON SEASAT SAR IMAGERY
COLLECTED OVER THE JASIN AREA

| Seasat Revolution | Internal Wave Orientation* | | | |
|---|---|---|---|---|
| | 0°-30° | 30°-60° | 60°-90° | 0°-90° |
| Descending Orbits | | | | |
| 556 | 1 | 1 | 3 | 0 |
| 599 | 4 | 3 | 2 | 1 |
| 642 | 5 | 3 | 2 | 1 |
| 757 | 0 | 1 | 5 | 0 |
| 958 | 1 | 0 | 3 | 0 |
| 1044 | 2 | 0 | 2 | 0 |
| 1087 | 0 | 4 | 0 | 0 |
| Subtotal | 13 | 12 | 17 | 2 |
| Ascending Orbits | | | | |
| 547 | 0 | 3 | 4 | 1 |
| 633 | 1 | 1 | 5 | 1 |
| 719 | 2 | 0 | 4 | 0 |
| 762 | 0 | 1 | 8 | 0 |
| 791 | 0 | 1 | 4 | 0 |
| 834 | 0 | 0 | 2 | 0 |
| 1006 | 0 | 0 | 1 | 0 |
| 1049 | 3 | 0 | 2 | 0 |
| Subtotal | 6 | 6 | 30 | 2 |
| Total Ascending and Descending | 19 | 18 | 47 | 4 |

| | N-S | E-W | NE-SW | SE-NW | All |
|---|---|---|---|---|---|
| Total by Direction of Orientation | 4 | 14 | 43 | 23 | 4 |

*A 0° orientation indicates the crests of the internal waves are aligned parallel to the radar line-of-sight; a 90° orientation indicates they are aligned perpendicular to the radar line-of-sight.

Several sources for the generation of internal waves have been identified, including surface atmospheric effects, internal (oceanic) effects and topographic effects (Thorpe, 1975). Surface atmospheric effects include traveling atmospheric pressure and stress, buoyancy flux, surface wave interactions and Ekman layer instability. Internal (oceanic) generation can be caused by decay of large scale circulations and breaking baroclinic instability (of which there is very little known). The generation of internal waves due to topographic features is similar to the generation of Lee waves by air flow over irregular surfaces. In the ocean, internal waves can be generated when a current (tidal or otherwise) flows over a deep-water feature such as a seamount, guyot, submarine ridge or the edge of a continental shelf (Wunch, 1975; Bell, 1975; Baines, 1973).

For the JASIN area, it is now suspected that tidal currents flowing over the bottom topographic features are forming internal waves along the thermocline. In many cases, the internal wave fields are felt to have sufficient energy to modulate the surface capillary wave structure, and hence allow the internal waves to be detected on SAR imagery.

## 5.3.2 FRONTAL BOUNDARIES

Even though they were not as prevalent on the JASIN Seasat SAR imagery as were internal waves, the case for frontal boundaries also being related to deep-water bottom features is strong.

A front has been described as a convergence zone between two ocean water masses or currents of different velocities. Hence, a frontal boundary is usually characterized by an altered surface roughness because of the formation of white caps, the bunching of the surface capillary waves due to water velocity differences or the alteration of capillary waves by surface slicks or foam fronts. Ocean fronts have often been detected on SAR imagery (see Appendix A).

126

There are four different types of fronts to consider: (1) major ocean currents; (2) mixing of water from estuaries and rivers; (3) coastal upwelling; and (4) deep-water upwelling. Fronts at the boundary of major ocean currents can extend over thousands of kilometers. These fronts are associated with the intrusion of either warm, salty water of tropical origin into higher latitudes (e.g., the Gulf Stream) or the intrusion of cold, less saline water into lower latitudes (e.g., the Labrador Current). These currents are generally in quasi-geostrophic balance.

Two smaller scale fronts, which are generally restricted to continental or near-continental regions, are those found at river or estuary mouths and coastal upwellings, and are the result of an offshore surface Ekman transport caused by alongshore wind stresses. These fronts are formed in continental seas and estuaries, occur around islands, banks, capes, and shoals, and are generally found in the boundary regions between shallow, wind and tidally mixed nearshore waters and stratified, deeper offshore waters. These fronts are more influenced by local acceleration, bottom stress and interfacial friction than by the Coriolis Force.

The JASIN area is sufficiently far away from the British Isles to rule out the latter two small scale fronts as those observed on the Seasat SAR imagery. Surface measurements of currents made during the JASIN experiment (Tarbell, et al., 1979) and during previous years (Bainbridge, 1980) indicate that no persistent large scale surface currents exist in this region. It is believed this area is dominated by tidal currents with velocities of less than 0.5 m/s at the surface (U.S. Naval Oceanographic Office, 1977). These tidal currents can also generate areas of deep-water upwelling.

To illustrate this mechanism for frontal boundary generation, we refer to the profiles of potential temperature, salinity and sigma theta presented in Figure 59 (after Bainbridge, 1980). These profiles were generated from data collected over the Iceland-Faeroe
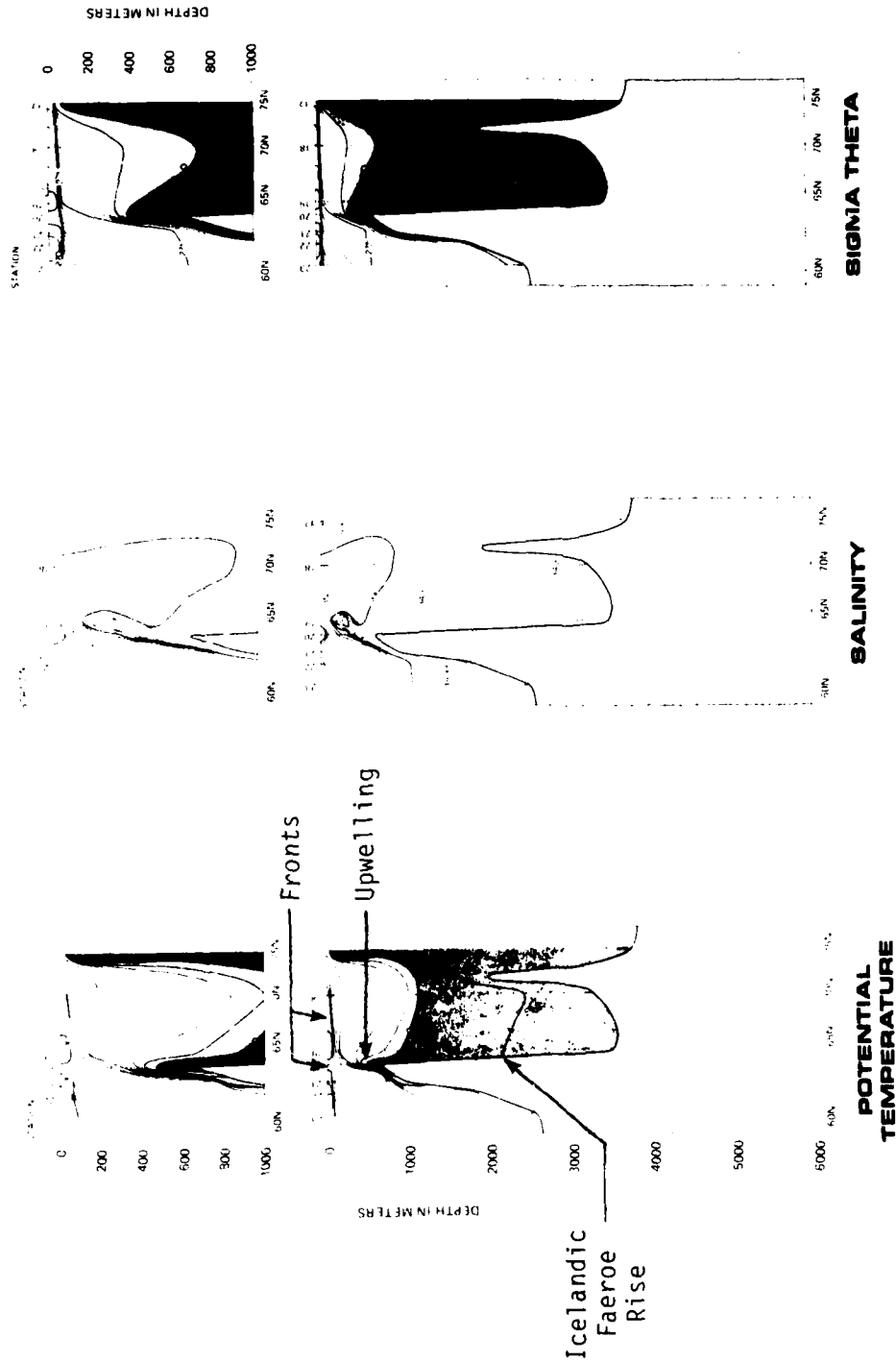
FIGURE 59. PROFILES OF POTENTIAL TEMPERATURE, SALINITY, AND SIGMA THETA FROM DATA COLLECTED OVER THE ICELANDIC-FAEROE RISE ILLUSTRATING DEEP WATER UPWELLING. (After Bainbridge, 1980)

Rise. A current (most likely tidal driven) forces the deep-water isopyncals up to the surface, resulting in a frontal boundary. This concept is graphically illustrated in Figure 60.

Although the oceanographic data from the JASIN experiment are not yet available, the suspected generation mechanism for fronts and internal waves is believed to be similar to the concept outlined in Figure 60.

### 5.3.3 SUMMARY OF DEEP-WATER MULTI-TEMPORAL ANALYSES

The conclusion to be drawn from this deep-water, multi-temporal analysis is that the appearance of internal waves and localized frontal boundaries in a deep-water area on SAR imagery most likely indicate the presence of a deep-water bottom feature in the same area. Unlike shallow-water sand banks and sand waves, whose shapes and locations are imaged accurately by a SAR (when they appear on SAR imagery), the internal waves do not give the exact location or shape of a deep-water feature. Since internal waves were present 63 percent of the time the Seasat ground coverage passed over a deep-water, bottom feature, it appears that this type of remote sensor might be used to determine the presence of such features, especially where multi-date imagery is available.

### 5.4 DISCUSSION

Through the use of three case studies, we have shown that multi-temporal analysis is an effective means for analyzing SAR data for information on bottom topographic features. During the examination of SAR data collected at different times over the same test site, we have begun to define the limitations of using SAR imagery to update hydrographic charts.

The frequency with which a SAR will successfully image a surface pattern related to a bottom feature depends on the test site. For
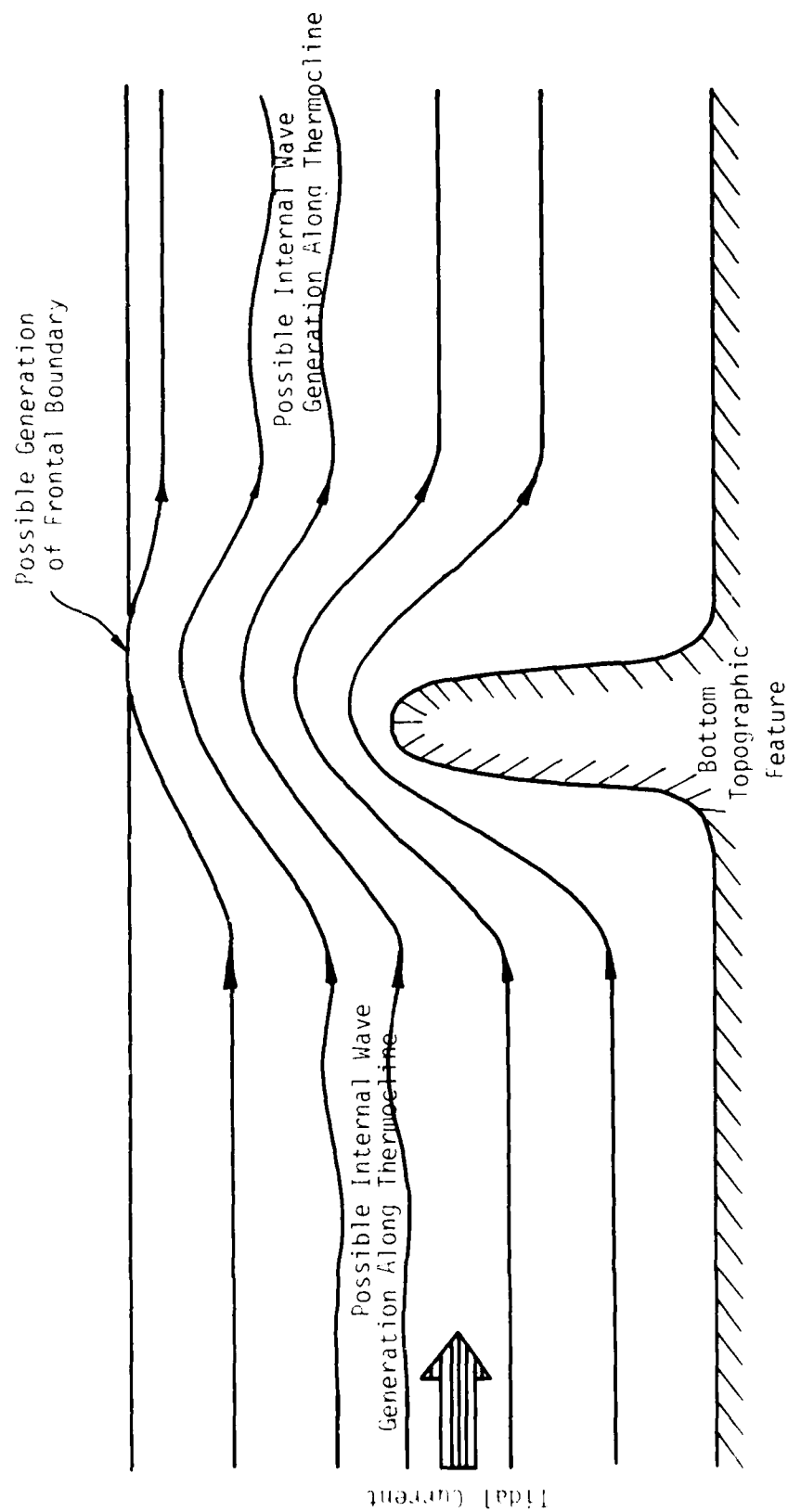
FIGURE 60. SCHEMATIC ILLUSTRATION OF FORMATION OF FRONTAL BOUNDARIES AND
INTERNAL WAVES DUE TO TIDAL CURRENTS FLOWING OVER A DEEP WATER
TOPOGRAPHIC FEATURE

the two major sand banks in the English Channel, the Seasat SAR imaged distinct surface patterns 50 percent of the time. The smaller sand banks and ridges in this area were imaged only 25 percent of the time. In the Tongue of the Ocean, distinct surface patterns occurred over 90 percent of the time on SAR imagery collected over the tidal bar belts in this area. The edge of the Great Bahama Bank was imaged between 50 and 80 percent of the time. In our deep-water study site (the northeast Atlantic JASIN site), on 63 percent of the occasions when SAR imagery was collected over deep-water bottom features such as a seamount, bank, or ridge, an internal wave pattern was present on the imagery. Frontal boundary signatures occurred almost 40 percent of the time SAR imagery was collected over a deep-water bottom feature.

The multi-temporal analyses demonstrated that the appearance or non-appearance of a bottom-related surface pattern is not a random event, but one which is based upon predictable environmental events. This point was illustrated through the use of an electromagnetic/ hydrodynamic model which used environmental parameters as inputs to predict the radar backscatter from an ocean surface. The data collected over the English Channel test site was used to verify this model.

In the shallow-water test sites studied, the appearance of surface patterns over the same bottom feature on SAR imagery collected from different dates was usually quite similar. These patterns occur in the same geographic location on successive dates and can be used to map the location of a bottom feature. For sand banks and ridges, SAR imagery often can be used to map the small scale structure of these features.

Although internal wave and frontal boundary patterns in deepwater areas indicate the presence of a bottom feature, they cannot be used at this time to indicate what that feature is or determine the exact

shape or location of the feature.  The chances of an internal wave pattern being present near the same feature on two successive dates is high, but the chances are low that these patterns will be in the same exact location or that they have the same shape and appearance.

The multi-temporal analyses have also led to a better understanding of the environmental conditions under which bottom related surface patterns will be detected by a SAR.  For the TOTO and English Channel test sites, it was determined that the bottom features were being imaged because of the hydrodynamic interaction between surface capillary waves and tidal currents flowing over the bottom features. It has been shown that tidal current velocities below a minimum value do not sufficiently alter the surface capillary waves to be detectable by a SAR (see Table 3 and Figure 42); therefore a minimum tidal current is necessary to view bottom features (i.e., sand ridges, banks and tidal bar belts).

Finally, during the TOTO study an example was presented where the multi-temporal analysis assisted in identifying a surface pattern as being caused by an atmospheric event rather than being bottom related.  The examples shown were the random surface patterns caused by localized rain squall activity present in the TOTO region.

6
MULTI-SENSOR ANALYSIS

This chapter contains a description of the methods used and the results obtained from a detailed comparison between Seasat, Landsat, and bathymetry data for the Nantucket Shoals area. The purposes of this study were to investigate the degree of correlation between the SAR image brightness and the water depth, and to determine the extent to which information from different sensors such as Seasat and Landsat are complementary or redundant for hydrographic applications. Photographic data from the Skylab mission were also visually compared with the Seasat and Landsat data, but were not registered or quantitatively evaluated.

6.1  TEST SITE AND DATA SET DESCRIPTIONS

The test site selected for this multi-sensor analysis was over the Nantucket Shoal, as shown in Figure 61. The Nantucket test area is a shoal region composed of long ridges trending generally northwest-southeast and rising to within 5 meters of the surface. The Nantucket Shoal test site is similar to the English Channel test site (Section 5.1) in that both have longitudinal and transverse sand waves. Shepard, et al. (1934) and Uchupi (1968) describe the Nantucket Shoal region as an area of glacial morainic ridging reworked by tidal currents to form a series of sand shoals (longitudinal) and sand waves (transverse). Figure 62 from Uchupi (1968) shows the distribution of sand shoals and sand waves on Nantucket Shoals and in Nantucket Sound. The shoals run many tens of kilometers in length, while the transverse sand wave crests are up to ten kilometers long and average 10 meters in height. A typical wavelength for these transverse sand waves is approximately 400 meters (Stewart and Jordan, 1956).
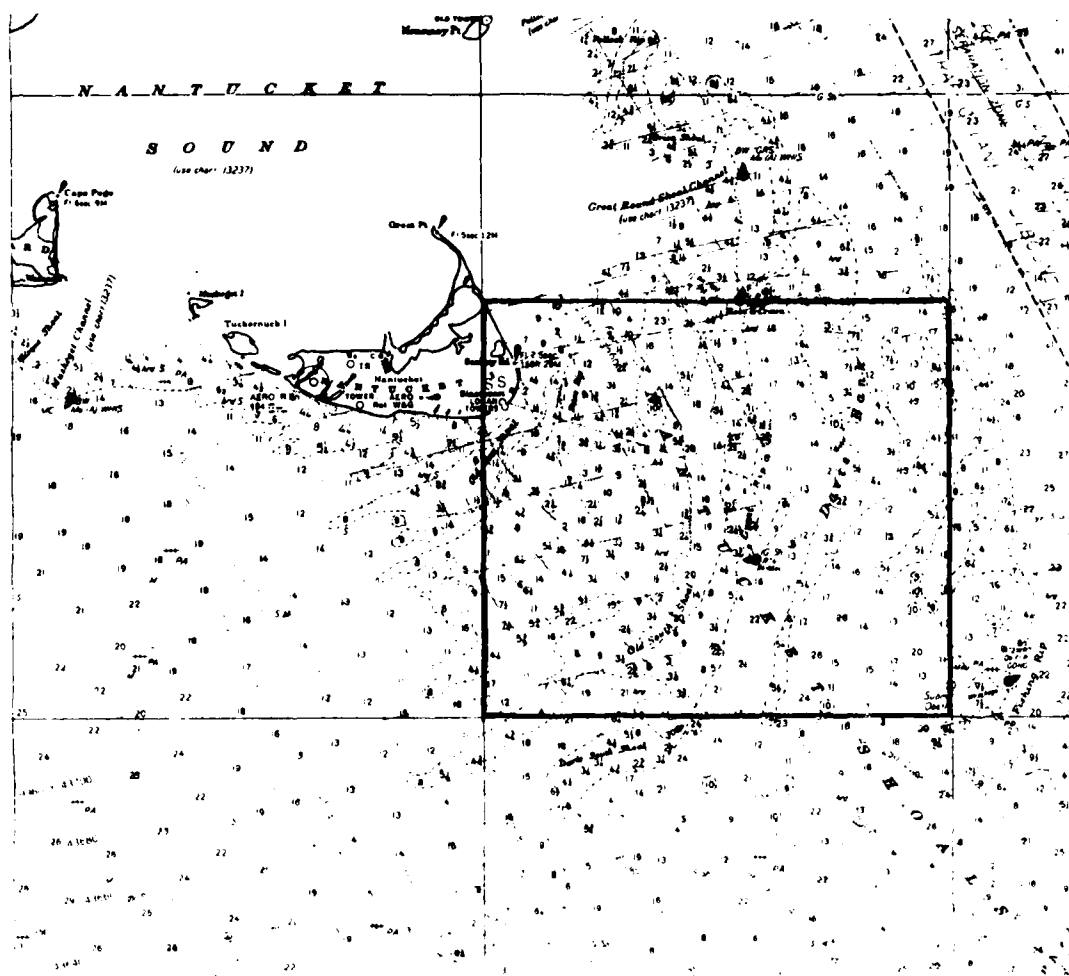
FIGURE 61.   PORTION OF NOAA CHART NO. 13200 SHOWING
LOCATION OF NANTUCKET SHOALS TEST SITE
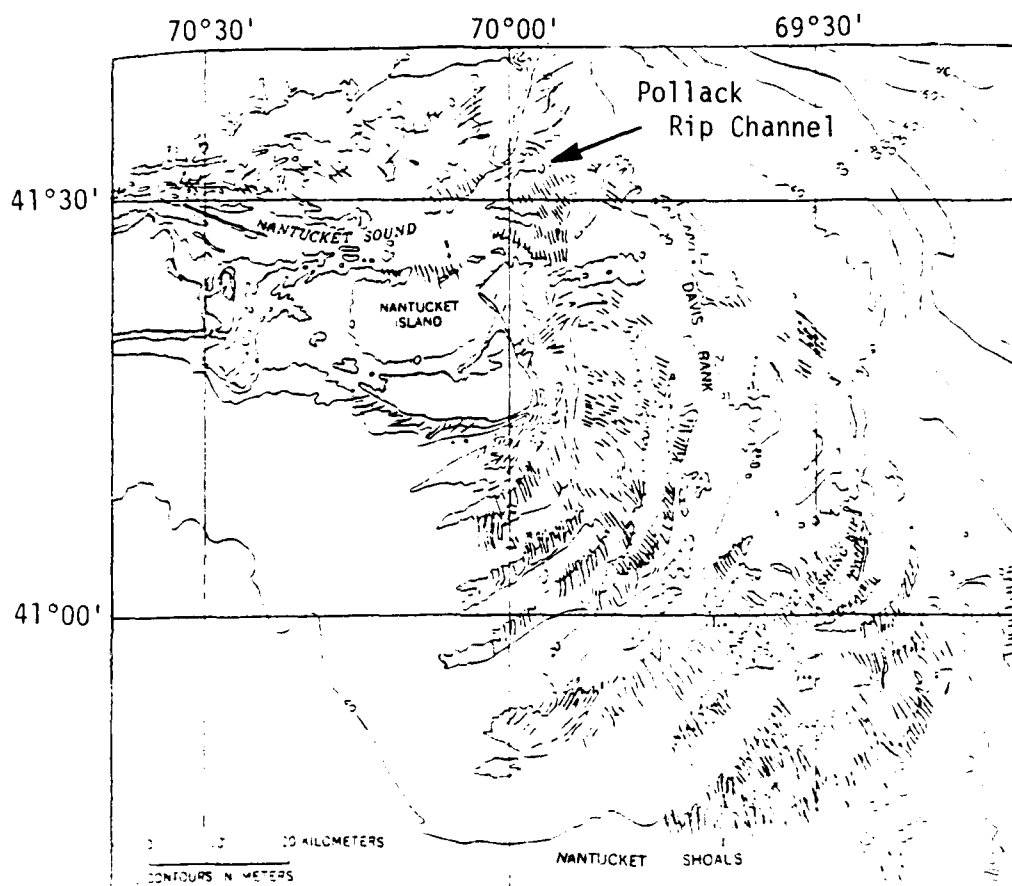
FIGURE 62.   DISTRIBUTION OF SAND SHOALS AND SAND WAVES ON NANTUCKET
SHOALS AND NANTUCKET SOUND.  (Curved lines indicate crests
of Sand Waves.  Based on soundings from U.S. Coast and
Geodetic Survey.) [From Uchupi, 1968]

The data used in this analysis came from five sources. Water depth data were obtained in the form of digitized depth soundings, collected by the National Ocean Survey and obtained from the NOAA Environmental Data and Information Service, and supplementary depth data were obtained from NOAA Chart No. 13237. Three types of remote sensor data were considered, including digitally processed Seasat data from Revolution 880 acquired on 27 August 1978, Landsat data for Scene I.D. No. 1724-14472 acquired on 17 July 1974, and Skylab S-190A photography taken on 12 September 1973. The Seasat data from Revolution 880 represent the only Seasat data collected over this area. Several Landsat images exist for this area; the particular data set used in this study was chosen because it shows the greatest amount of detail in the Nantucket Shoals area, and environmental conditions were similar to those during the Seasat over-pass.[*] Environmental conditions at the time of collection of these three data sets are summarized in Table 14. Coincidentally, the time of over-pass occurred within a few minutes of maximum ebb tide at Pollack Rip (see Figure 62) channel for all of the data sets. The tidal current is rotary in this area and thus varies throughout the test site. The values shown in Table 14 are at Davis Bank (see Figure 62), which was the location nearest the center of the test site at which tidal information was available. These data were obtained from several sources, including NOAA tide tables, U.S. Coast Guard observations, and daily weather maps.

## 6.2 DATA PREPARATION

In order to make a detailed comparison between the Seasat, Landsat, and bathymetry data on a point-by-point basis, a composite data set was generated from all of these sources. This data set consists of a six-channel image file in which the first channel contains the

---

*Selection of the Landsat data set depended heavily on a survey of the various images by Reed (1981), who also obtained the Skylab data used in this study.

TABLE 14

ENVIRONMENTAL CONDITIONS FOR NANTUCKET SHOALS REGION
DURING SEASAT, LANDSAT, AND SKYLAB OVERPASSES

| | Time (EST) | Current Speed (kts) | Current Direction (°T) | Wind Speed (kts) | Wind Direction (°T) |
|---|---|---|---|---|---|
| 27 Aug. 78 | 7:34 | 1.2 | 197 | 7 | 10° |
| 17 July 74 | 9:47 | 1.2 | 197 | 14 | 20° |
| 12 Sept. 73 | 12:30 | 1.5 | 200 | 4 | 248° |

137

bathymetry data, the cond channel contains the Seasat data
registered onto ' batnymetry data, and the third through sixth
channels contain the four Landsat bands similarly registered. The
generation of this composite data set is described in this section,
and the analysis of the data is described in Section 6.3.

### 6.2.1 GENERATION OF WATER DEPTH FILE

The digital water depth data obtained from the NOAA Environmental
Data and Information Service consists of a series of 40-character
records on magnetic tape, each record containing the latitude and
longitude of the measurement and the depth in feet, fathoms, or
meters. The units of the depth measurement are specified by a car-
tographic code, and some auxiliary information, such as the date of
the survey, is also contained in each record. Each file on the data
tape contains soundings for an area of one degree in latitude by one
degree in longitude. Typically, there are several hundred thousand
records in each file. Within each file, the soundings are arranged
in 10-minute by 10-minute segments. Thus, for example, all the data
for the area from 41°10'N to 41°20'N and 69°50'W to 70°W are con-
tained in records 86,000 to 90,000 of the NOAA/EDIS tape.

The first step in the generation of the water depth file was to
copy a subset of these data points for the area of interest into an
image file format. The particular format chosen for this purpose
consisted of a rectangular grid whose elements (pixels) are spaced
at regular intervals of latitude and longitude. The area selected
for this analysis lies between 41°N and 41°20'N latitude and 69°30'W
to 70°W in longitude, as indicated in Figure 61. The grid spacing
was selected as 0.02701 minutes in latitude and 0.03566 minutes in
longitude, corresponding to a 50 x 50-meter pixel size. This results
in an image file consisting of 740 records or lines, and 840 samples
or points per line.

Each sounding in the NOAA depth file was assigned to the nearest location on this grid. Multiple depths assigned to the same grid location were averaged together, and grid locations for which no depths were available were assigned a "null" value. This procedure resulted in the copying of 63,858 depth values from the NOAA tape into 59,188 pixel locations on the output image file. An additional 1103 depth values were read from NOAA Chart No. 13237 to fill in the larger gaps in the image, mainly near Nantucket Island. Thus, roughly one tenth of the 740 x 840 pixel locations in the file were assigned a depth value, implying an average spacing of about 3 pixels between the depth values.

In order to assign depths to the remaining pixel locations, a previously developed routine, resident on ERIM's Earth Resources Data Center computer, was exercised on the data set. This routine computes a two-dimensional polynomial fit to the data within each 20 x 20 pixel subset of the image file. A depth value is then computed at each pixel location in the scene by evaluating the polynomial expression at each point. In order to ensure continuity at the boundaries of each 20 x 20 pixel subset, the polynomial coefficients are interpolated between subsets. This routine degrades the resolution of the depth data somewhat, by attempting to fit a smooth surface through the data. However, for the purposes of this study, the results were judged to be adequate. The rms difference between the input depth values and the fitted values at the same locations was approximately 1 meter.

### 6.2.2  REGISTRATION OF SEASAT DATA

The next step in the preparation of the composite data set was to register the Seasat data onto the water depth file. Prior to this step, the Seasat data were radiometrically corrected, as described in Appendix C. The Seasat data were also smoothed by averaging each contiguous block of 3 x 3 pixels together into a single pixel. This

was done to improve the signal-to-noise ratio and to make the pixel size comparable to that of the water depth file.

The procedure for registering the Seasat data set uses a set of ground control points in combination with the known slant-to-ground range nonlinearity. The slant range for each point is converted into a ground range using the equations presented in Appendix C, and a linear regression or least-squares fit is obtained between the ground range and the earth coordinates, and between the azimuth sample number and the earth coordinates of the ground control points. This relationship is then used to resample the Seasat data onto the water depth file grid, using a nearest-neighbor method. The details of this procedure are described in the following paragraphs.

First, a set of ten identifiable features were located in the Seasat data by making line printer gray maps of the data. These points are listed in Table 15. The Seasat coordinates (i.e., the line and point numbers) for these points are denoted by L2 and P2. Next, the latitudes and longitudes of the features selected as ground control points were obtained from NOAA Chart No. 13237 (scale 1:80,000). These latitudes and longitudes were converted to equivalent line and point numbers (L1 and P1) in the hydrographic file using the equations

$$L1 = \frac{41°20'N - \text{latitude}}{0.02701} + 1.5 \tag{2}$$

and

$$P1 = \frac{70°00'W - \text{longitude}}{0.03566} + 1.5 . \tag{3}$$

The resulting pairs of coordinates for corresponding points in the hydrographic file and in the Seasat data were entered into the registration program.

In the registration program, the range coordinate for each control point is converted into a ground range before the least-squares fit is computed. In actuality, two conversions are required, since

140

TABLE 15
SEASAT GROUND CONTROL POINTS

| Latitude | Longitude | Line | Point | Description |
|---|---|---|---|---|
| 41° 17.4' | 70° 12.4' | 279 | 1567 | Eel Point (Nantucket Island) |
| 41° 17.6' | 70° 4.8' | 461 | 1484 | Coatue Point (Nantucket Island) |
| 41° 19.0' | 70° 2.0' | 546 | 1500 | Pocomo Head (Nantucket Island) |
| 41° 18.9' | 70° 2.8' | 526 | 1507 | Five-Fingered Point (Nantucket Island) |
| 41° 15.4' | 70° 3.5' | 464 | 1395 | Airport (Nantucket Island) |
| 41° 20.2' | 70° 17.2' | 198 | 1718 | East end of Muskaget Island |
| 41° 20.3' | 70° 18.7' | 167 | 1741 | West end of Muskaget Island |
| 41° 25.2' | 70° 27.0' | 37 | 2006 | Tip of Cape Page (Martha's Vineyard) |
| 41° 24.7' | 70° 27.2' | 26 | 1988 | Small Point on Martha's Vineyard |
| 41° 33.0' | 70° 0.9' | 754 | 1972 | Monomoy Island |

the coordinates for the JPL digitally-processed Seasat data have been
modified to correct for earth rotation effects.  The first conversion
is to remove this skew correction in order to obtain the slant range
coordinate.  This conversion may be written as

$$R = R_0 + \Delta R(L2 + S * P2) \tag{4}$$

where R is the slant range, $R_0$ is the minimum range, $\Delta R$ is the
range distance between lines, and S is the slope of an iso-range line
in the image (this is 1/16 for the Nantucket data set but may be
positive or negative depending on the geographic location of the
image).  The second conversion is the slant-to-ground range conver-
sion described in Appendix C.  The ground range X, resulting from
this conversion, is substituted for the line number and the least-
squares fit is obtained, resulting in the equations

$$X = 281584 - 21.55 * L1 + 45.31 * P1 \tag{5}$$

and

$$P_2 = 1514.0 - 0.9337 * L1 - 0.4123 * P1 \tag{6}$$

where X is the predicted ground range and $P_2$ is the predicted azi-
muth sample number.  For a given L1,P1, these equations can be
solved, and the slant-to-ground range equations can be inverted to
yield the corresponding coordinates (L2 and P2) for the Seasat data.
Comparing these predicted coordinates with the actual coordinates of
the 10 ground control points for the Seasat data, an rms difference
of 0.670 lines and 0.688 points was observed.  In physical coordi-
nates, this implies an rms error of

$$[(0.670)^2 + (0.688)^2]^{1/2} \times 48\ m = 46\ m.$$

When the least-squares fitting was done without the slant-to-ground
range conversion, the rms error for lines was 1.417, or about twice
as large as with the conversion.

Once the transformation from ground coordinates (L1,P1) to satellite coordinates (L2,P2) has been established, the actual registration of the data begins. This is done by stepping through the input (hydrographic) file one pixel at a time. At each location (L1,P1), the corresponding satellite coordinates (L2,P2) are calculated from the transformation equations. The satellite data from the pixel nearest to this location is then copied along with the hydrographic data onto the output file. This procedure is referred to as nearest-neighbor resampling, and is appropriate for the relatively continuous scene brightness distributions occurring in this area. The output of this process is a two-channel data file with the hydrographic data in Channel 1 and the Seasat data in Channel 2.

### 6.2.3 REGISTRATION OF LANDSAT DATA

The procedure for registering the Landsat data is similar to that for Seasat, except that no slant-to-ground range conversion is necessary. The same set of ground control points were located in the Landsat image, and their coordinates are listed in Table 16. These coordinates were entered into the registration program, where a least-squares fit was obtained directly between the Landsat coordinates (L2 and P2) and the depth file coordinates (L1 and P1). This results in the set of equations

$$L2 = 1684 + 0.6043 * L1 - 0.1300 * P1$$

and

$$P2 = 2208 + 0.2251 * L1 + 0.8386 * P1$$

where L2 is the predicted Landsat line number and P2 is the predicted point number. The rms difference between the predicted line and point numbers (L2 and P2) and the observed line and point numbers (L2 and P2) for the set of ground control points used was 0.804 lines and 0.989 points. In physical units, this amounts to an rms error of

TABLE 16
LANDSAT GROUND CONTROL POINTS

| Latitude | Longitude | Line | Point | Description |
|---|---|---|---|---|
| 41° 17.4' | 70° 12.4' | 1788 | 1959 | Eel Point (Nantucket Island) |
| 41° 17.6' | 70° 4.8' | 1755 | 2136 | Coatue Point (Nantucket Island) |
| 41° 19.0' | 70° 2.0' | 1715 | 2193 | Pocomo Head (Nantucket Island) |
| 41° 18.9' | 70° 2.8' | 1718 | 2173 | Five-Fingered Point (Nantucket Island) |
| 41° 15.4' | 70° 3.5' | 1801 | 2185 | Airport (Nantucket Island) |
| 41° 20.2' | 70° 17.2' | 1744 | 1821 | East end of Muskaget Island |
| 41° 20.3' | 70° 18.7' | 1745 | 1787 | West end of Muskaget Island |
| 41° 25.2' | 70° 27.0' | 1665 | 1551 | Tip of Cape Page (Martha's Vineyard) |
| 41° 24.7' | 70° 27.2' | 1680 | 1551 | Small Point on Martha's Vineyard |
| 41° 33.0' | 70° 0.9' | 1398 | 2099 | Monomoy Island |

$$[(0.804 \times 79 \text{ m})^2 + (0.989 \times 57 \text{ m})^2]^{1/2} = 84.9 \text{ m}.$$

This set of equations was used to control the nearest-neighbor re-sampling of the Landsat data onto the combined water depth/Seasat file generated previously. The result was a six-channel image file in which the first two channels are the same as the input file (i.e., the water depth and Seasat data) and channels 3-6 contain the four Landsat bands.

## 6.3  DATA ANALYSIS

This section discusses the analysis of the composite multi-sensor data set described in Section 6.2, and also discusses some additional observations which were made using photography from the 1973 Skylab mission. Comparisons among the data sets constituting the composite image file were carried out in two ways: first, image displays were generated in order to visually compare the data over the entire test site, and second, quantitative statistical correlations were made for selected areas within the test site.

### 6.3.1  VISUAL IMAGE COMPARISONS

Gray level images were made for each data set within the composite file, as shown in Figure 63. Note that only bands MSS5 (0.6-0.7 μm) and MSS6 (0.7-0.8 μm) are shown here. It has been demonstrated by Reed (1981) that the patterns appearing in the Landsat image for this area are due to surface reflection, and are essentially the same in all four bands. There is a general decrease in the atmospheric path radiance toward the infrared, so that the contrast of the features tends to be larger in the near-IR bands. However, this consideration is offset by a decreasing signal-to-noise ratio with increasing wavelength, so that the optimum image quality occurs for MSS5 or MSS6. Because of the small dynamic range of the MSS6 signals, further analysis of this data was done using band MSS5 only. Except for noise and digitization effects, however, the results should be essentially the same for all the MSS bands.
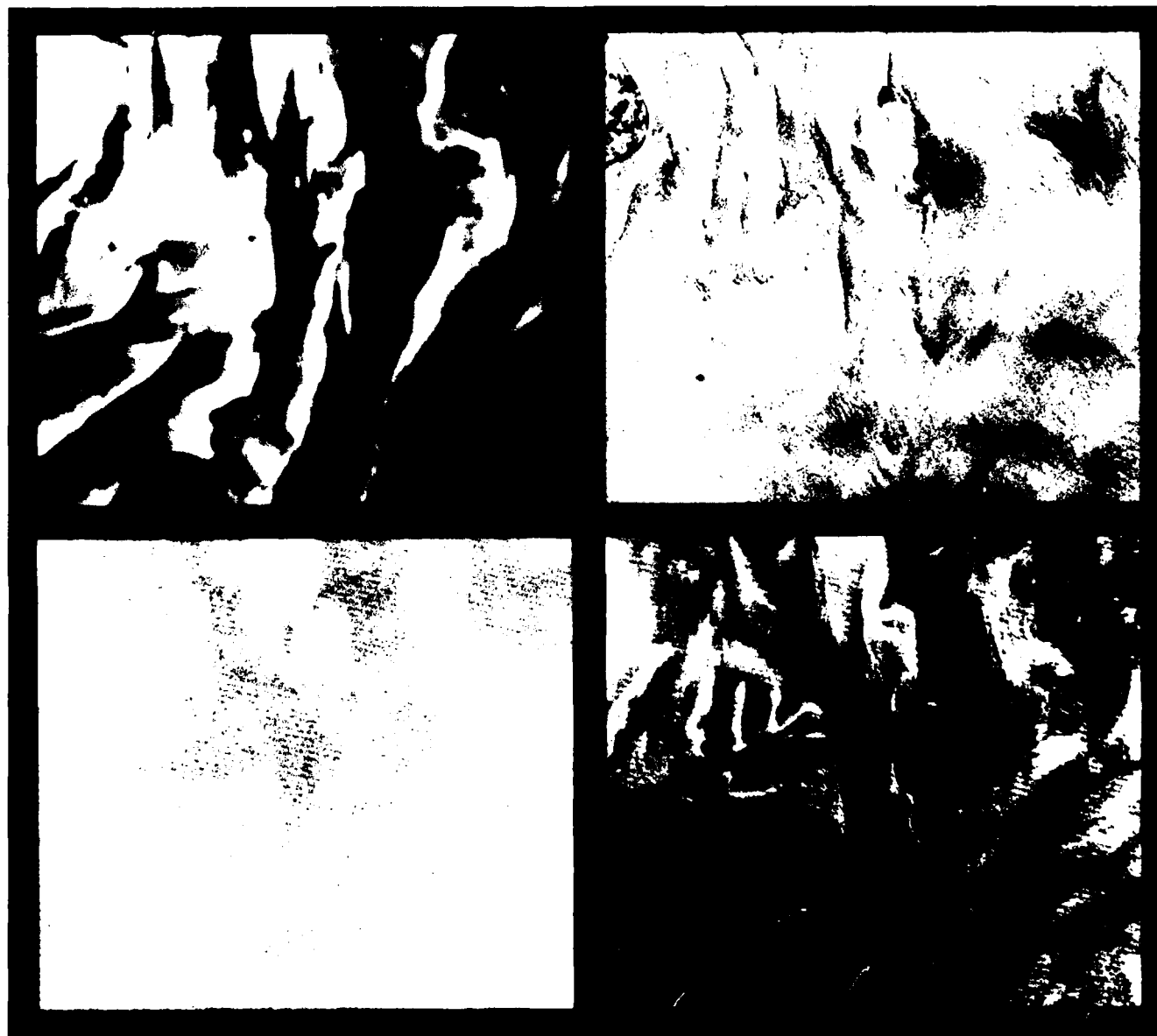
FIGURE 63.   IMAGES FOR REGISTERED WATER DEPTH FILE (TOP LEFT),
             SEASAT DATA (TOP RIGHT), LANDSAT MSS 5 (LOWER LEFT),
             AND LANDSAT MSS 6 (LOWER RIGHT)

Although this form of display does not permit quantitative comparisons, several observations can be made. First, the spatial resolution of the Seasat data appears to be superior to both the Landsat data and the NOAA depth data presented here. Many small features appear in the Seasat image, having scales on the order of hundreds of meters, which are not present in the depth image. Most of these features are also absent in the Landsat image, although some of the larger ones are visible. Evidence will be presented in the following section that these features correspond to transverse sand waves on the bottom. The depth information is not adequate to resolve these small features, and the interpolation process described in the previous sections further reduces the spatial resolution of these data, resulting in the "fuzzy" appearance of the depth image.

The second observation which can be made from these images regards the tonal variations in the Seasat and Landsat images. In most cases, the tonal variations in the Seasat images are bidirectional, i.e., consisting of brighter regions in juxtaposition with darker ones. In the Landsat image the tonal variations appear to be only in one direction, i.e., brighter than the background. This suggests that the Seasat signal may be related more closely to the slope of the bottom than to the water depth. This conjecture will also be pursued in the following section.

The final observation is that there is a good deal of consistency between the large-scale patterns in the Seasat data, the Landsat data, and the NOAA depth data. Most of the gross features are common to all three images, although their positions are slightly shifted in some cases. The frequency of co-occurrence of the major features and the amount of shift between them will be quantitatively investigated in the following section by examining one-dimensional plots of the data along selected lines.

As an example of an alternative type of display of the two-dimensional image data, perspective plots were generated from the Seasat, Landsat, and depth data for one area. Figure 64 shows these perspective plots for the data within the box indicated in Figure 65. These plots show the fall-off in the Seasat and Landsat signals at the edge of a bank-like bottom feature. Although helpful in visualizing the data, these plots are of limited value for extracting quantitative information.

### 6.3.2  QUANTITATIVE DATA COMPARISONS

Detailed comparisons were made between the data sets along the lines indicated in Figure 65. In order to reduce noise and to make the spatial resolution of the satellite data comparable to that of the water depth data, the Seasat and Landsat data were smoothed using either a 5 x 5 or a 10 x 10 pixel window. Figure 66 shows the raw Seasat data (top curve) and the smoothed data (lower curves) for line 80 of the composite file. Figure 67 shows the comparable Landsat data along the same line. In order to test the hypothesis that the Seasat data are related to the slope of the bottom, the linear slope $(dz/dx)$ and the logarithmic slope $(1/Z \, dz/dx)$ were also computed from the depth file. Figure 68 shows the depth $(Z)$ and these two slope values plotted versus distance $(x)$ along line 80.

The 10 x 10 smoothed Seasat data show distinct peaks at pixel numbers 30, 125, 323, and 510, corresponding to distances of 4.0, 6.2, 16.2, and 25.5 km along this line. The 10 x 10 smoothed Landsat data show similar peaks at pixel numbers 80, 125, 329, and 519. Comparing these plots with the depth data, these peaks seem to correspond to the depth minima at pixel numbers 72, 122, 328, and 525. This visual observation was tested by computing the local correlation function between the Seasat and depth data, and between the Landsat and depth data. The correlation function is obtained by calculating the correlation coefficient $(r)$ for a set of 41 points (i.e., a 2 km
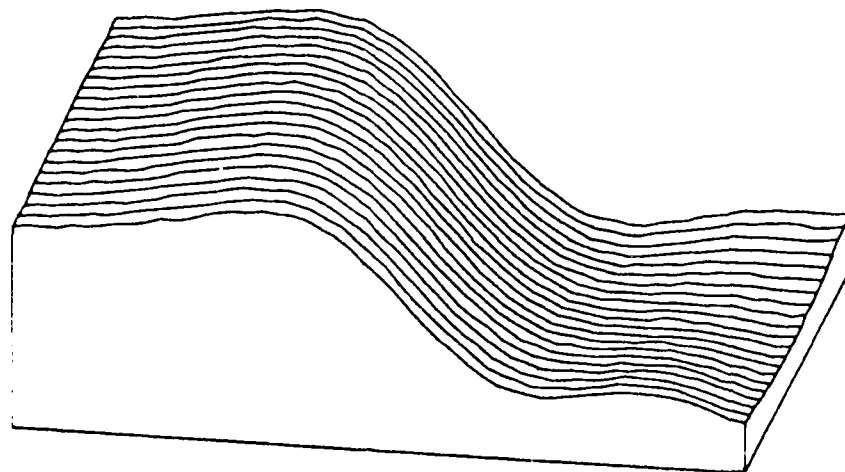
WATER DEPTH
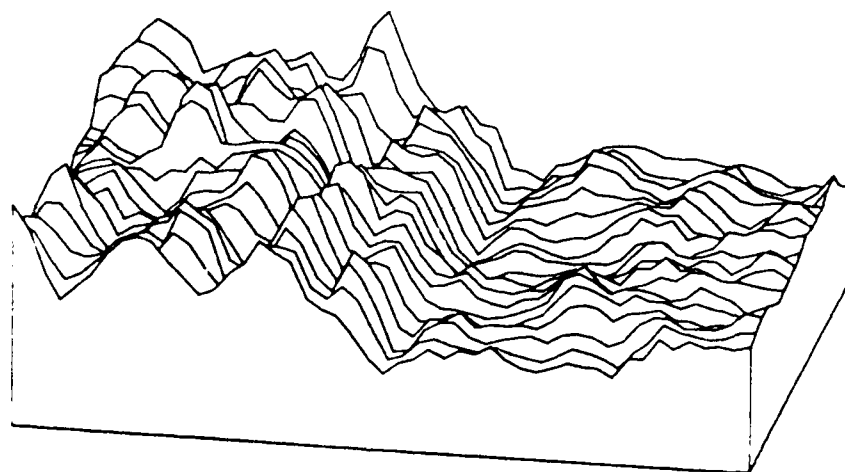
SEASAT
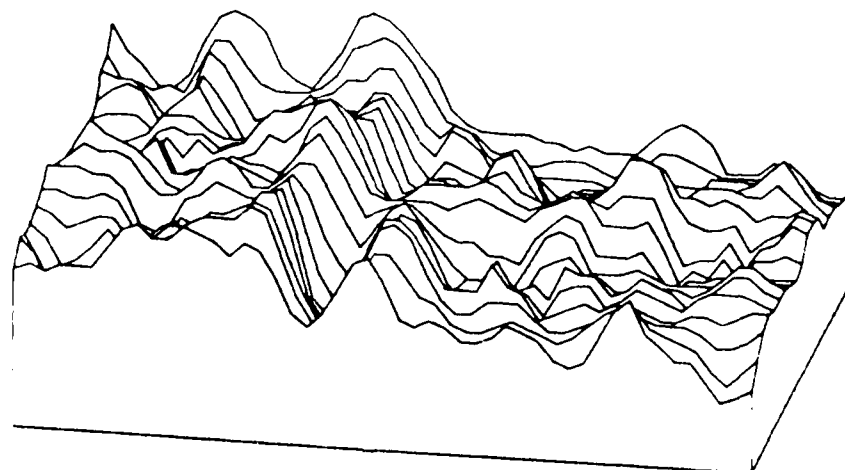
LANDSAT MSS 5

FIGURE 64.   PERSPECTIVE PLOTS OF WATER DEPTH, SEASAT, AND LANDSAT DATA
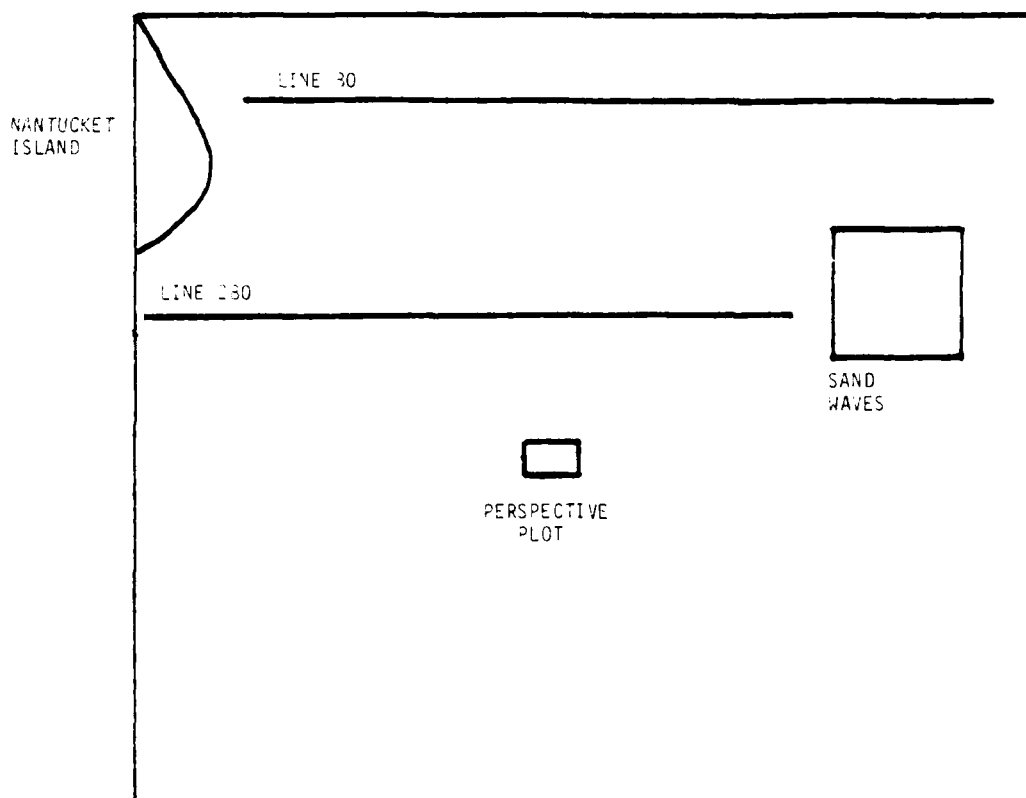
FIGURE 65.   LOCATION OF SUBAREAS (LINES 80 AND 280)
SELECTED FOR FURTHER ANALYSIS

FIGURE 66.   SEASAT DATA FOR LINE 40:   (a) RAW DATA,
(b) SMOOTHED 5X5, (c) SMOOTHED 10X10

(a)

(b)

(c)

FIGURE 67.　LANDSAT DATA FOR LINE 80:　(a) RAW DATA,
(b) SMOOTHED 5X5, (c) SMOOTHED 10X10

(a)

(b)

(c)
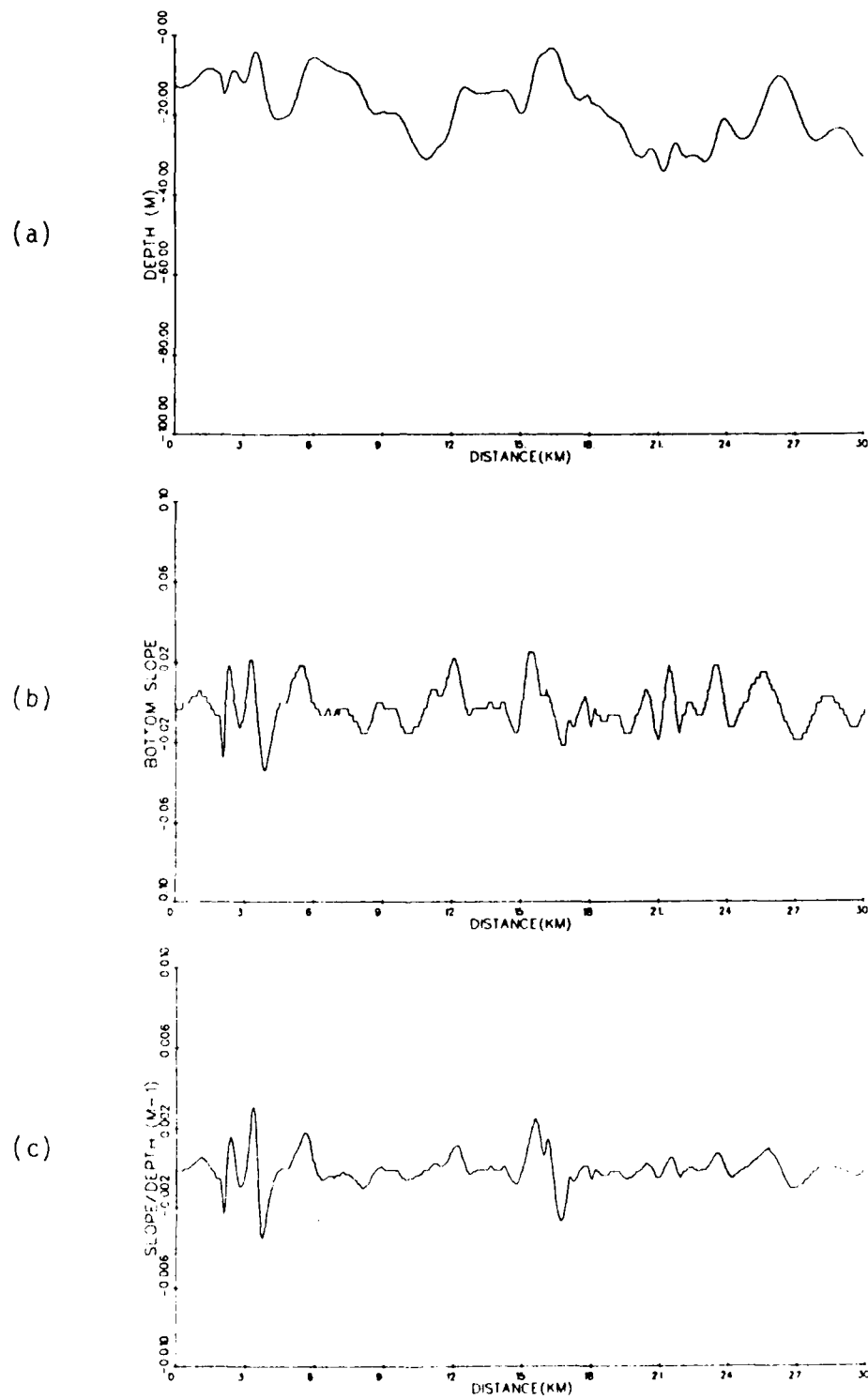
FIGURE 68. HYDROGRAPHIC DATA FOR LINE 80: (a) WATER DEPTH,
(b) BOTTOM SLOPE, (c) SLOPE DIVIDED BY DEPTH

interval) as a function of the relative shift between the data sets. An example of such a correlation function is shown in Figure 69, for the feature located at pixel 323 in the Seasat data. The results of this set of computations are summarized in Table 17 in terms of the maximum correlation (r) and the relative shift for which this maximum correlation occurred.

The same analysis was carried out for the data along line 280, which is shown in Figures 70-72. Five prominent features were selected and the correlation functions computed for those features. The results of this set of calculations are also shown in Table 17. Combining the results for these two lines, one obtains a mean shift of 4.7 pixels (235 meters) and an rms shift of 9.0 pixels (450 meters) between the Seasat image features and the corresponding bottom features. For the Landsat data, the mean shift is 4.4 pixels (220 meters) and the rms shift is 8.4 pixels (420 meters). The average correlation coefficient was 0.86 for Seasat and 0.87 for the Landsat data.

In order to determine whether there is a better correlation between the Seasat data and the bottom slope, or the slope divided by the depth, the same set of correlation functions was calculated for these variables. The results are summarized in Table 18. These studies appear to indicate that the Seasat data correlates better with the water depth than with the bottom slope or the slope divided by the depths, at least for line 80. For line 280, the rms shift is slightly smaller for the slope/depth case. A visual comparison of the plots also seems to indicate a better correlation with the depth for line 80 and with the slope/depth for line 280 (see Figures 73 and 74). The lack of consistency in these observations may indicate that there is more than one mechanism causing the backscatter variations. The current speed and direction is known to be highly variable throughout the scene due to flow around Nantucket Island and over

TABLE 17
SUMMARY OF CORRELATION STATISTICS FOR SEASAT AND
LANDSAT DATA VERSUS DEPTH

| Line, Point | Seasat vs. Depth | | Landsat vs. Depth | |
|---|---|---|---|---|
| | $r_{max}$ | Shift (pixels) | $r_{max}$ | Shift (pixels) |
| 80, 80 | 0.95 | +6 | 0.86 | +6 |
| 80, 125 | 0.80 | -4 | 0.83 | -2 |
| 80, 325 | 0.94 | -2 | 0.90 | -2 |
| 80, 520 | 0.93 | -7 | 0.80 | -9 |
| 280, 25 | 0.91 | -5 | 0.86 | -5 |
| 280, 145 | 0.88 | +4 | 0.95 | 0 |
| 280, 205 | 0.88 | -1 | 0.92 | +1 |
| 280, 260 | 0.61 | -12 | 0.91 | -9 |
| 280, 450 | 0.84 | -21 | 0.78 | -20 |
| All Points | 0.86 | -4.7 (mean) | 0.87 | -4.4 (mean) |
| | | 9.0 (rms) | | 8.4 (rms) |

## SEASAT VS. DEPTH - LINE 80, POINT 325
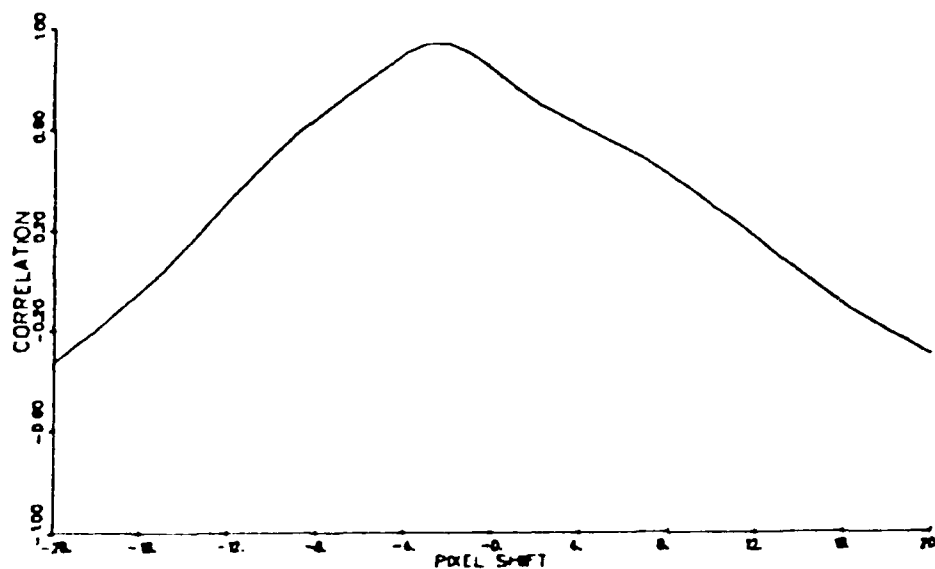


FIGURE 69. CORRELATION FUNCTION FOR SEASAT VS. DEPTH
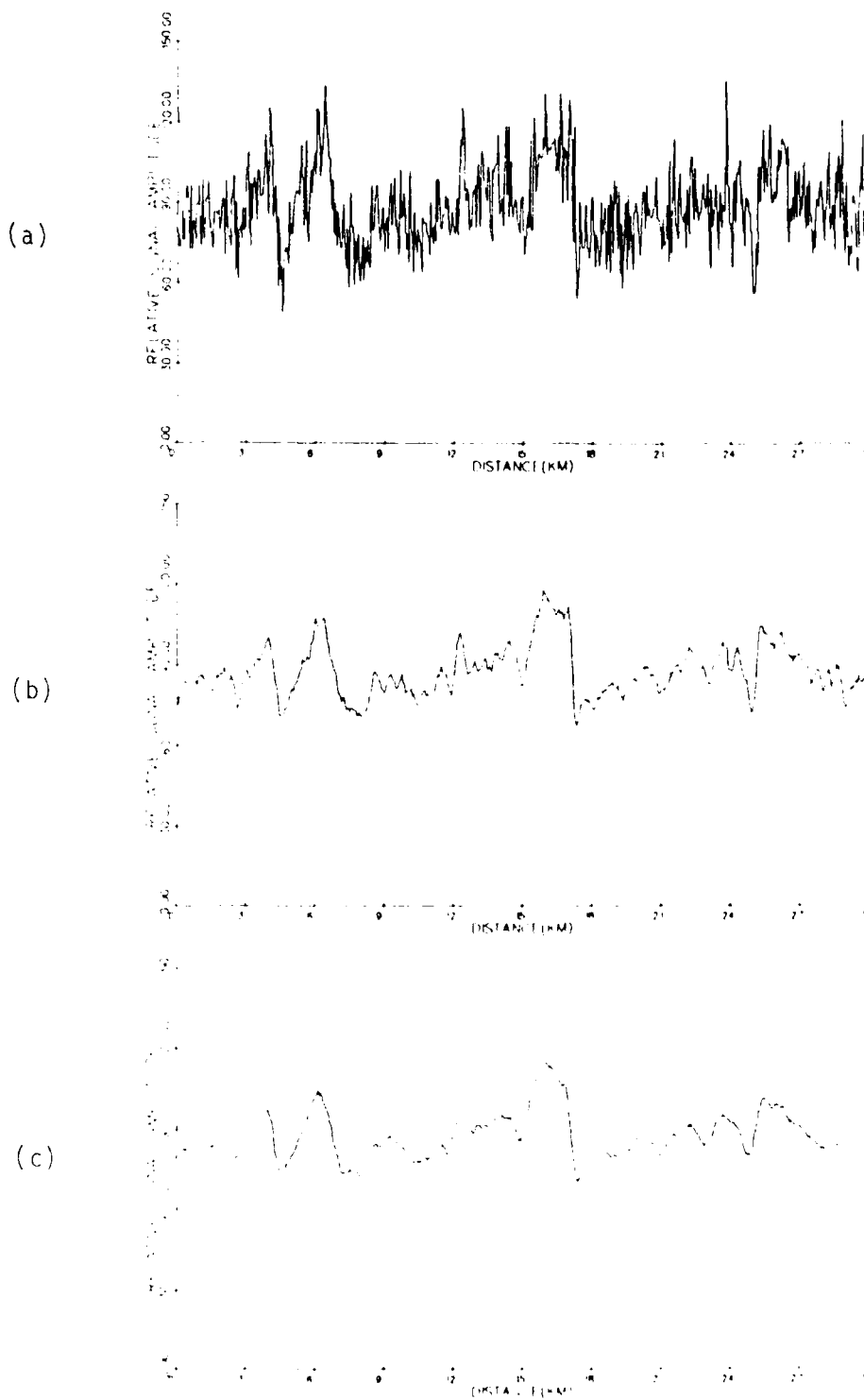DATA

(a)

(b)

(c)
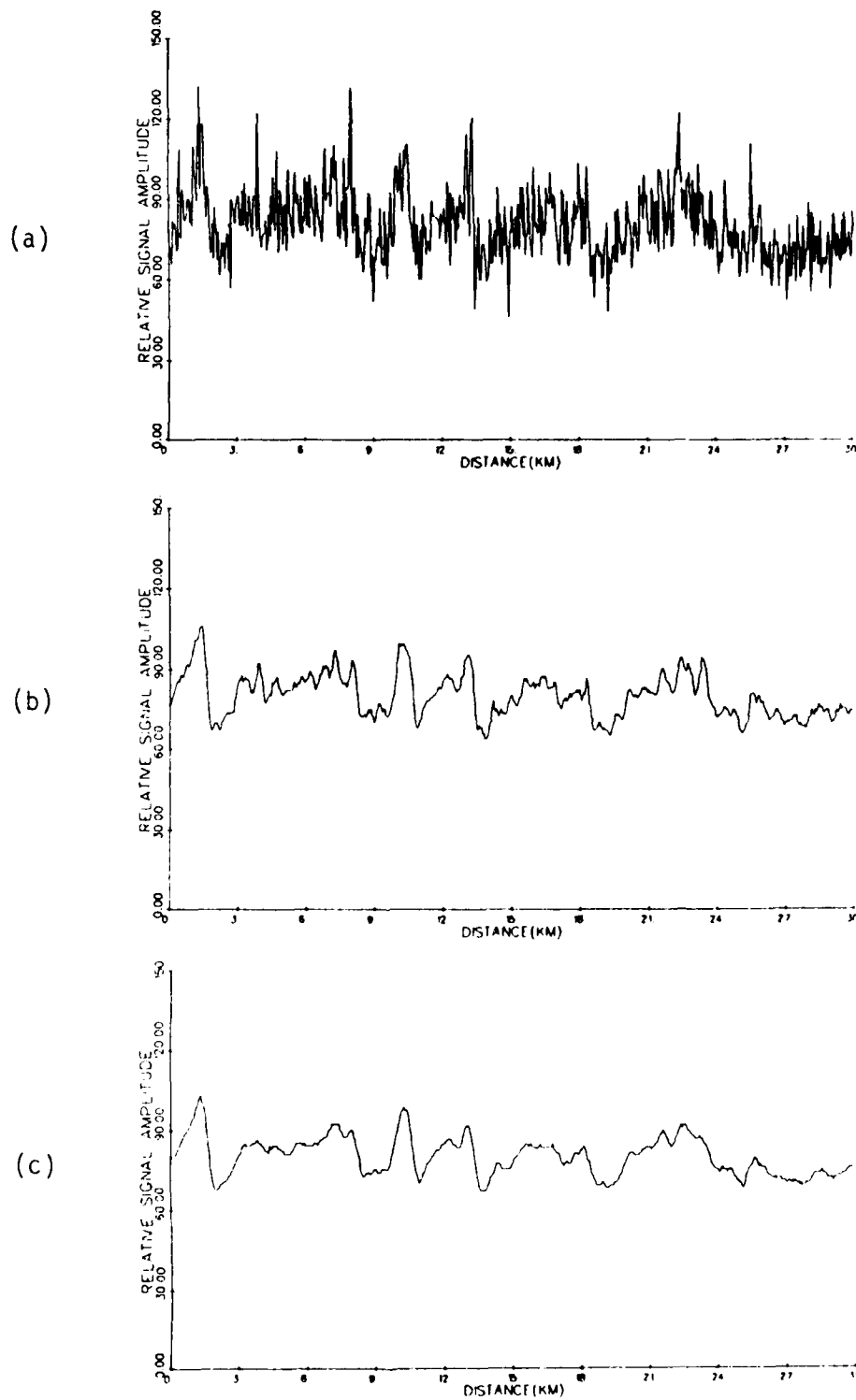
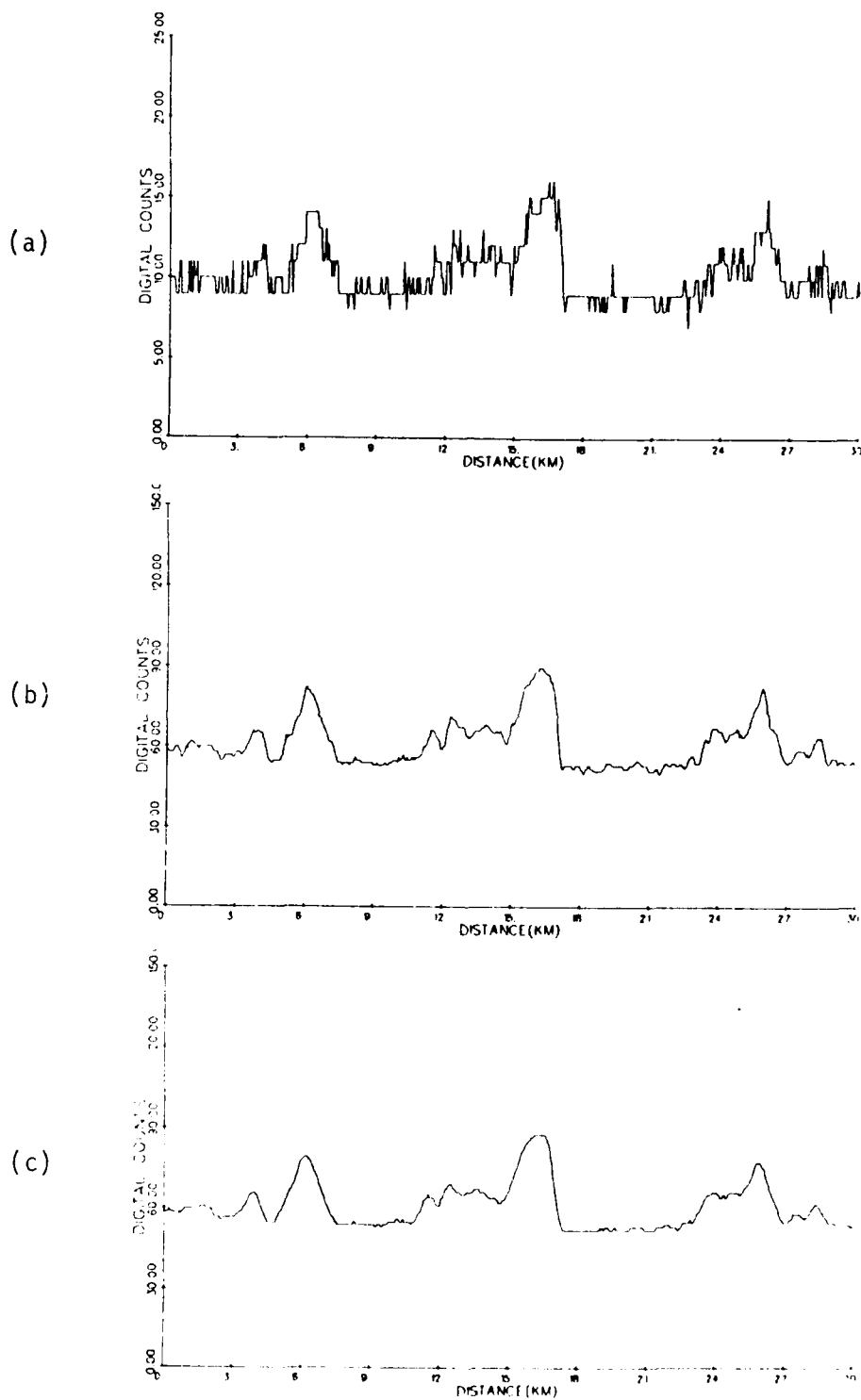FIGURE 70     SEASAT DATA FOR LINE 280:   (a) RAW DATA, (b) SMOOTHED 5X5, (c) SMOOTHED 10X10
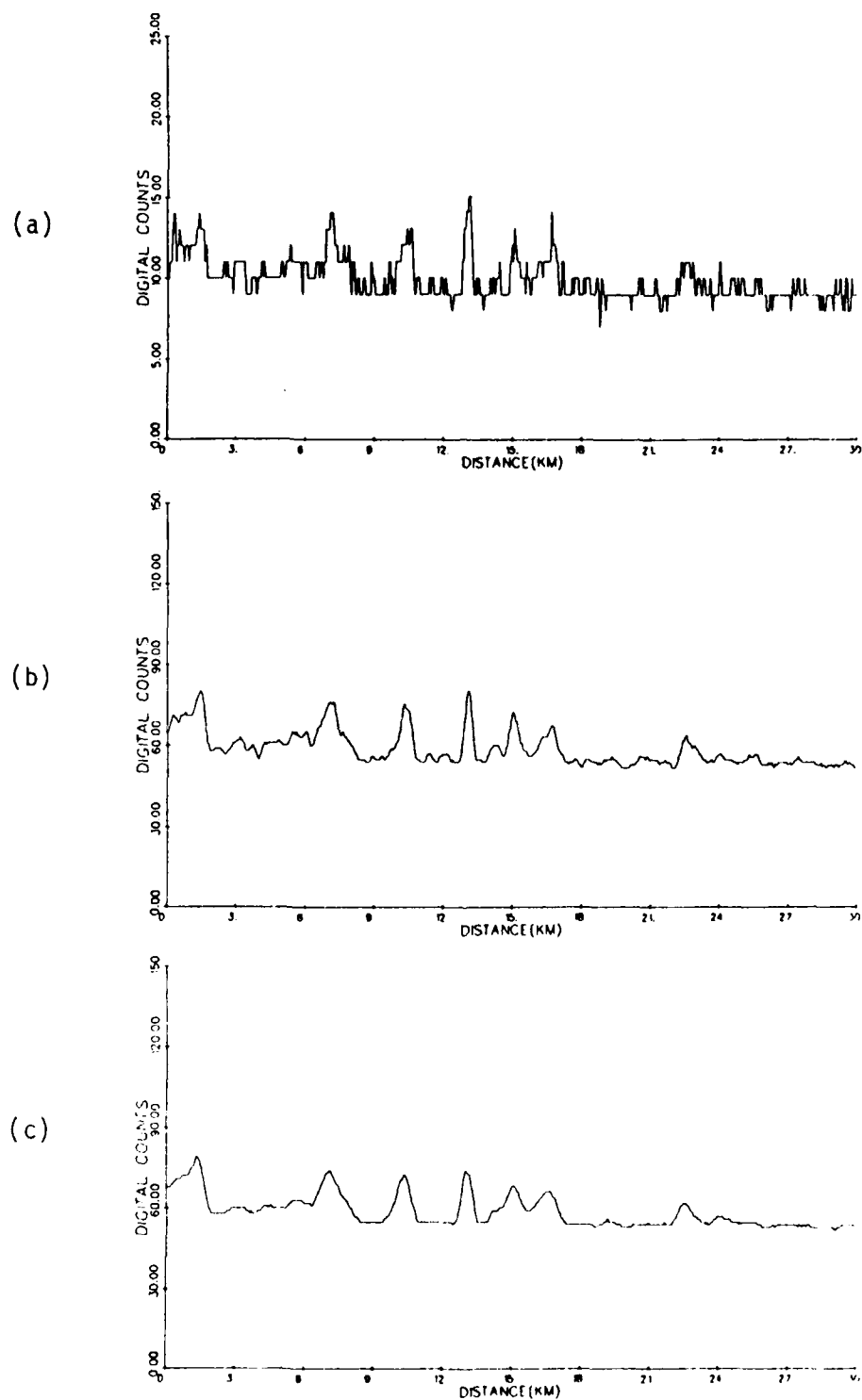
FIGURE 71　　LANDSAT DATA FOR LINE 280:　(a) RAW DATA,
　　　　　　　(b) SMOOTHED 5X5, (c) SMOOTHED 10X10

(a)

(b)

(c)
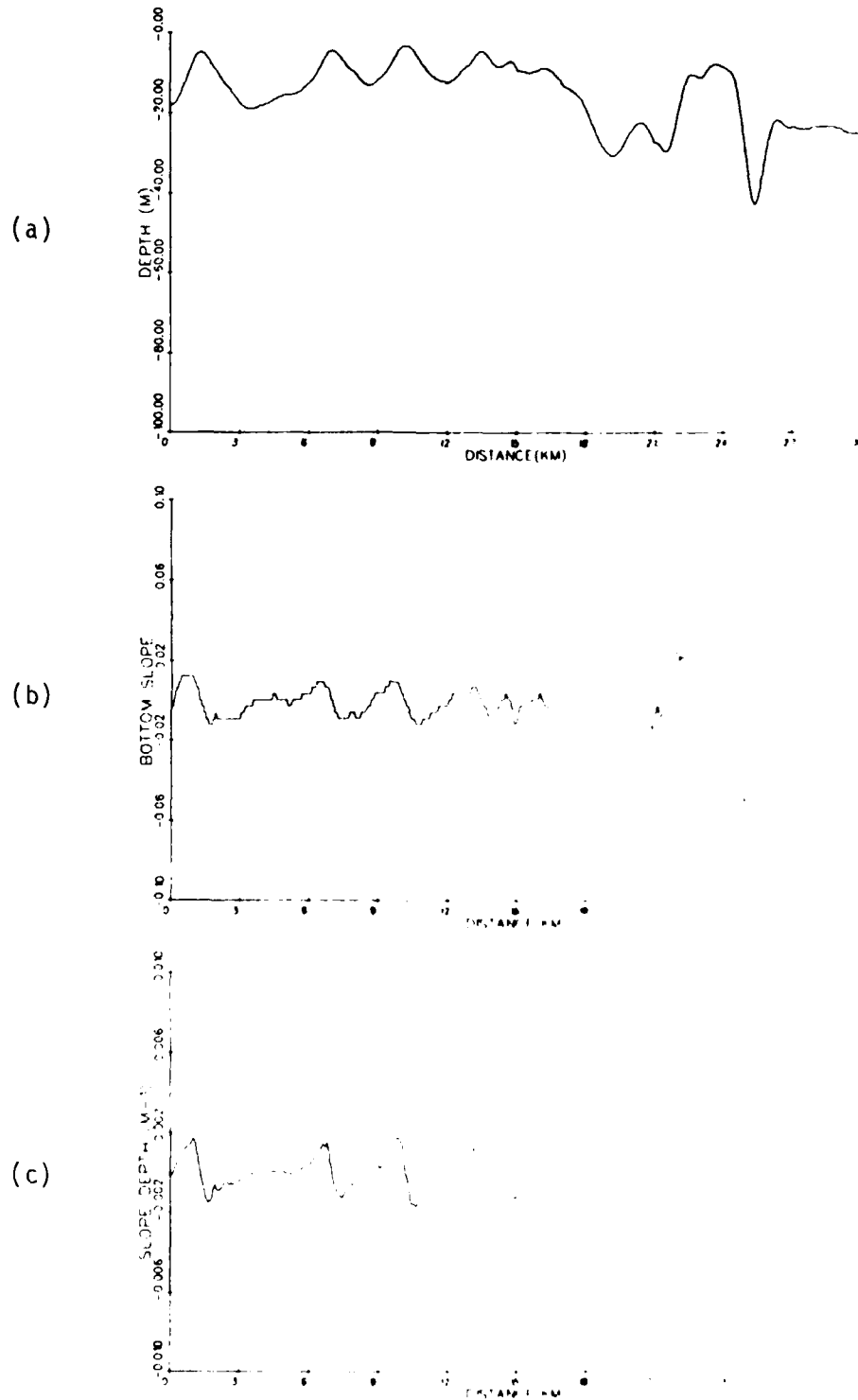
FIGURE 72. HYDROGRAPHIC DATA FOR LINE . . . . . W . . . . .
(b) BOTTOM SLOPE, (c) SLOPE D:V:R: . . . .

TABLE 18
SUMMARY OF CORRELATION STATISTICS FOR SEASAT DATA
VERSUS BOTTOM SLOPE AND SLOPE DIVIDED BY DEPTH

| Line, Point | Seasat vs. Slope | | Seasat vs. Slope/Depth | |
|---|---|---|---|---|
| | $r_{max}$ | Shift (pixels) | $r_{max}$ | Shift (pixels) |
| 80, 80 | 0.74 | +14 | 0.74 | +14 |
| 80, 125 | 0.92 | +13 | 0.92 | +13 |
| 80, 325 | 0.93 | +11 | 0.93 | +11 |
| 80, 520 | 0.66 | +7 | 0.66 | +7 |
| 80, 75 | 0.93 | +8 | 0.99 | +7 |
| 80, 145 | 0.67 | +20 | 0.53 | +19 |
| | 0.87 | +9 | 0.87 | +9 |
| 60 | 0.97 | -2 | 0.97 | -3 |
| | 0.75 | -11 | 0.67 | +10 |
| | 0.83 | +10.1 (mean) | 0.81 | +9.7 (mean) |
| | | 11.6 (rms) | | 11.2 (rms) |

160
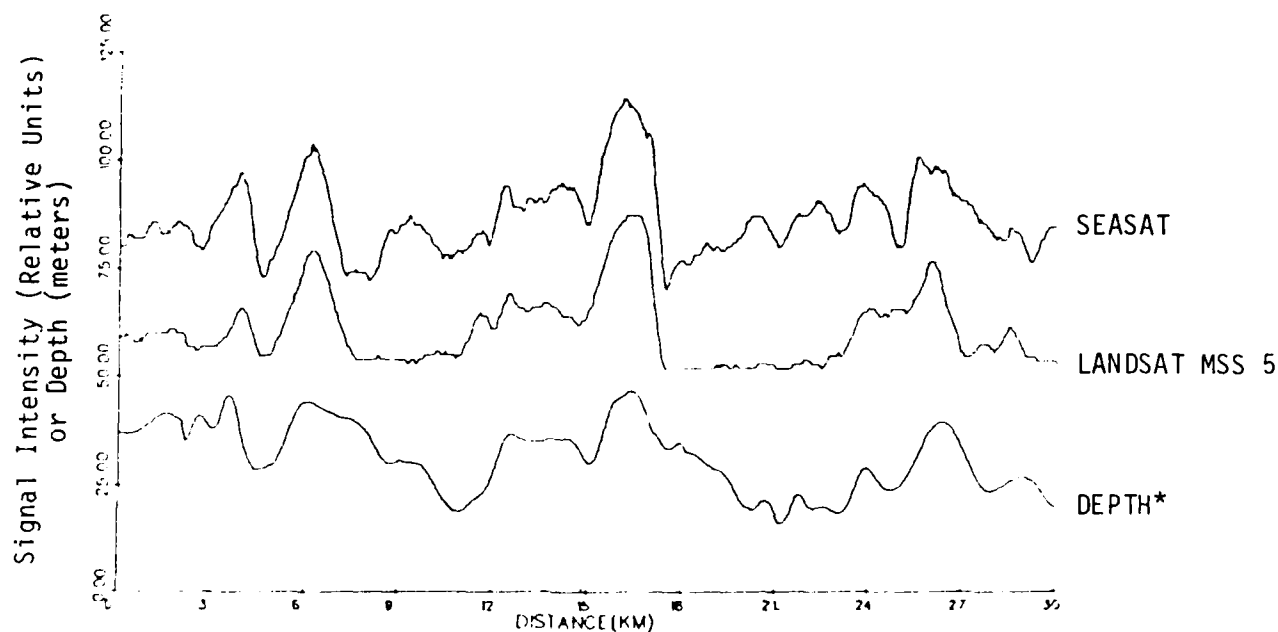
# *LINE 80*



FIGURE 73. COMPARISON OF SEASAT, LANDSAT, AND DEPTH DATA
ALONG LINE 80

* Depth value plotted as 50-z, where z is depth in meters.

# LINE 280
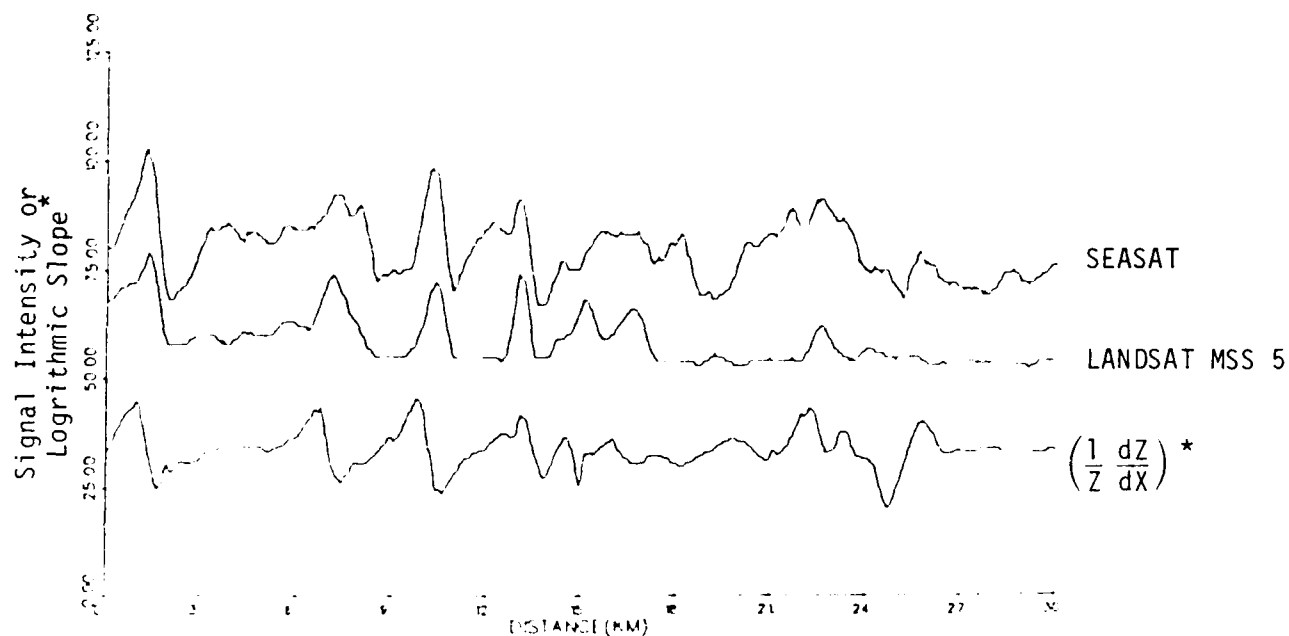


FIGURE 74.  COMPARISON OF SEASAT AND LANDSAT DATA WITH
LOGARITHMIC SHAPE $\left(\frac{1}{Z} \ \frac{dZ}{dX}\right)$ ALONG LINE 280

---

* Logrithmic slope value plotted as $35 + 6250 \left(\frac{1}{Z} \ \frac{dZ}{dX}\right)$, where Z and X are
in meters.

162

the complex bottom topography. Thus, wave breaking and tidal over-
falls (Stewart and Jordan, 1956) may occur in parts of the scene
while simple modulation of the Bragg waves may be the dominant back-
scatter mechanism in other areas (Shuchman, 1982).

The final investigation reported in this section deals with the
small-scale features which appear in the Seasat image and to a lesser
extent in the Landsat image, but not in the interpolated NOAA depth
data. Several pieces of evidence suggest that these features corre-
spond to transverse sand waves on the bottom. One is a study by
Uchupi (1968) indicating the existence of transverse sand waves in
this area with approximately the same orientation and spacing as the
SAR image features (see Figure 62). These features are oriented in
a direction normal to the mean tidal current, and are similar in
appearance to the sand waves in the English Channel (see Section
5.1).

To test this hypothesis, the raw depth data obtained from the
NOAA archives was re-examined in the area indicated by the box on
the right side of Figure 65. An alternate procedure was used in this
area to fill in the depth values while preserving the spatial resolu-
tion of the data. This procedure was to average the depth values
within a 3 x 3 pixel window, neglecting the pixels where no depth
sounding was present, and to enter this average value in the pixel
located at the center of the window. A gray map of the resulting
data set is shown in Figure 75. Gray maps of the corresponding
Seasat and Landsat data, also smoothed using a 3 x 3 window, are
shown in Figures 76 and 77. Two lines were selected from this area,
as indicated on these gray maps, and the data values along those
lines were extracted and plotted in Figures 78 and 79. Figure 78
shows four distinct peaks in the Seasat and Landsat data which cor-
respond quite closely to the minimum depths along this line. Three
similar occurrences are shown in Figure 79. These features have
approximately the same spacing and depth as the transverse sand waves

ERIM

LEGEND
------
..    0   TO  -6.0  DB
--  -6.0  TO  -6.5  DB
++  -6.5  TO  -7.0  DB
**  -7.0  TO  -7.5  DB
**  -7.5  TO  -8.0  DB
**  -8.0  TO  -10   DB

FIGURE 75.   HIGHER-RESOLUTION WATER DEPTH DATA FOR SAND WAVE TEST
AREA.   LINES INDICATE LOCATIONS OF PLOTS IN FIGURES 78
AND 79

164

ΣERIM

LEGEND
------

| | | | |
|--|--|--|--|
| .. | 0 | TO | -6.0 DB |
| -- | -6.0 | TO | -6.5 DB |
| ++ | -6.5 | TO | -7.0 DB |
| ** | -7.0 | TO | -7.5 DB |
| ** | -7.5 | TO | -8.0 DB |
| ®® | -8.0 | TO | -10 DB |

FIGURE 76. SEASAT DATA IN SAND WAVE TEST AREA

165

ΣERIM

LEGEND

| | | | | | |
|---|---|---|---|---|---|
| .. | 0 | TO | -6.0 | DB |
| -- | -6.0 | TO | -6.5 | DB |
| ++ | -6.5 | TO | -7.0 | DB |
| ** | -7.0 | TO | -7.5 | DB |
| ** | -7.5 | TO | -8.0 | DB |
| ** | -8.0 | TO | -10 | DB |
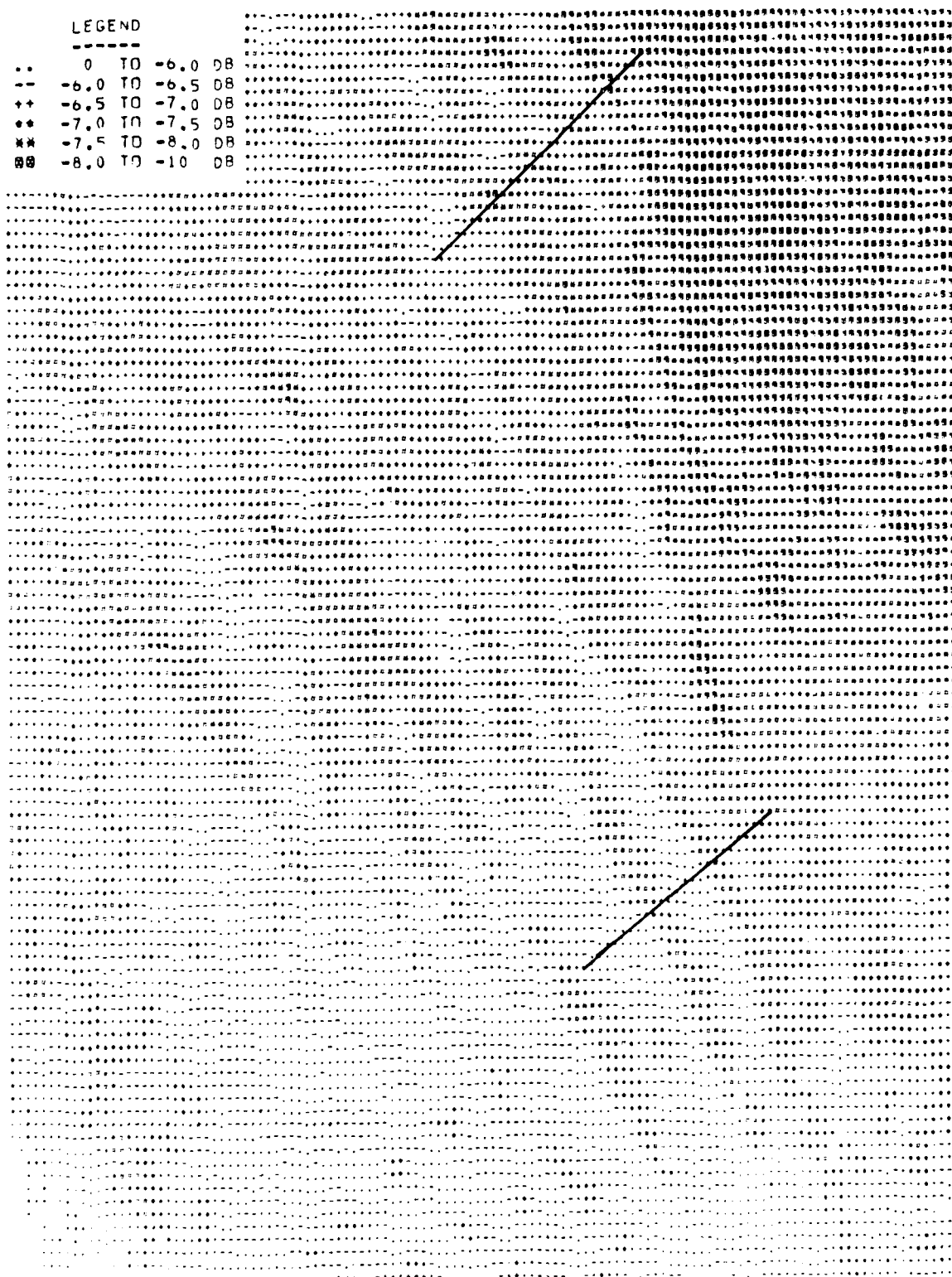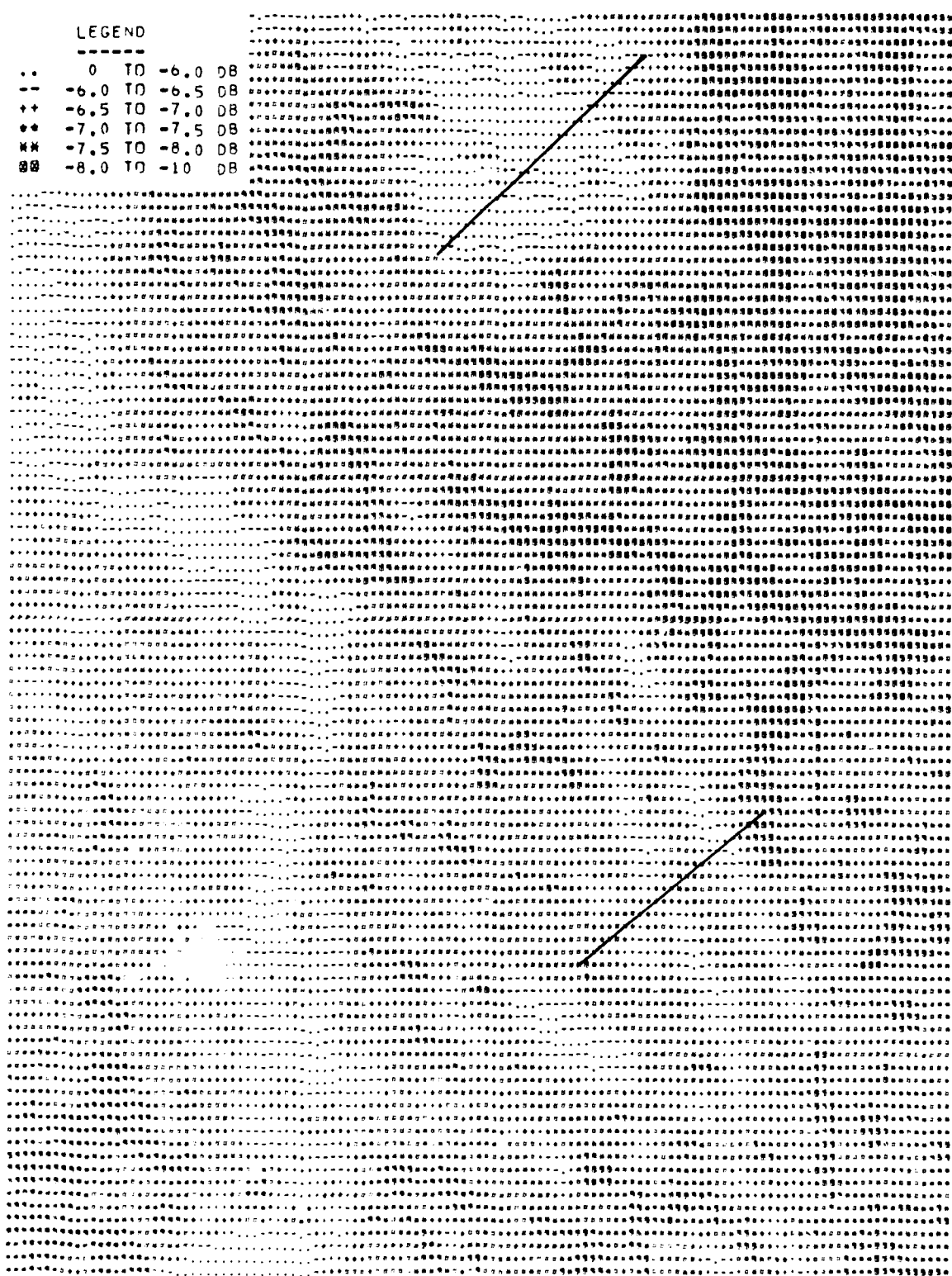
FIGURE 77. LANDSAT DATA IN SAND WAVE TEST AREA

166
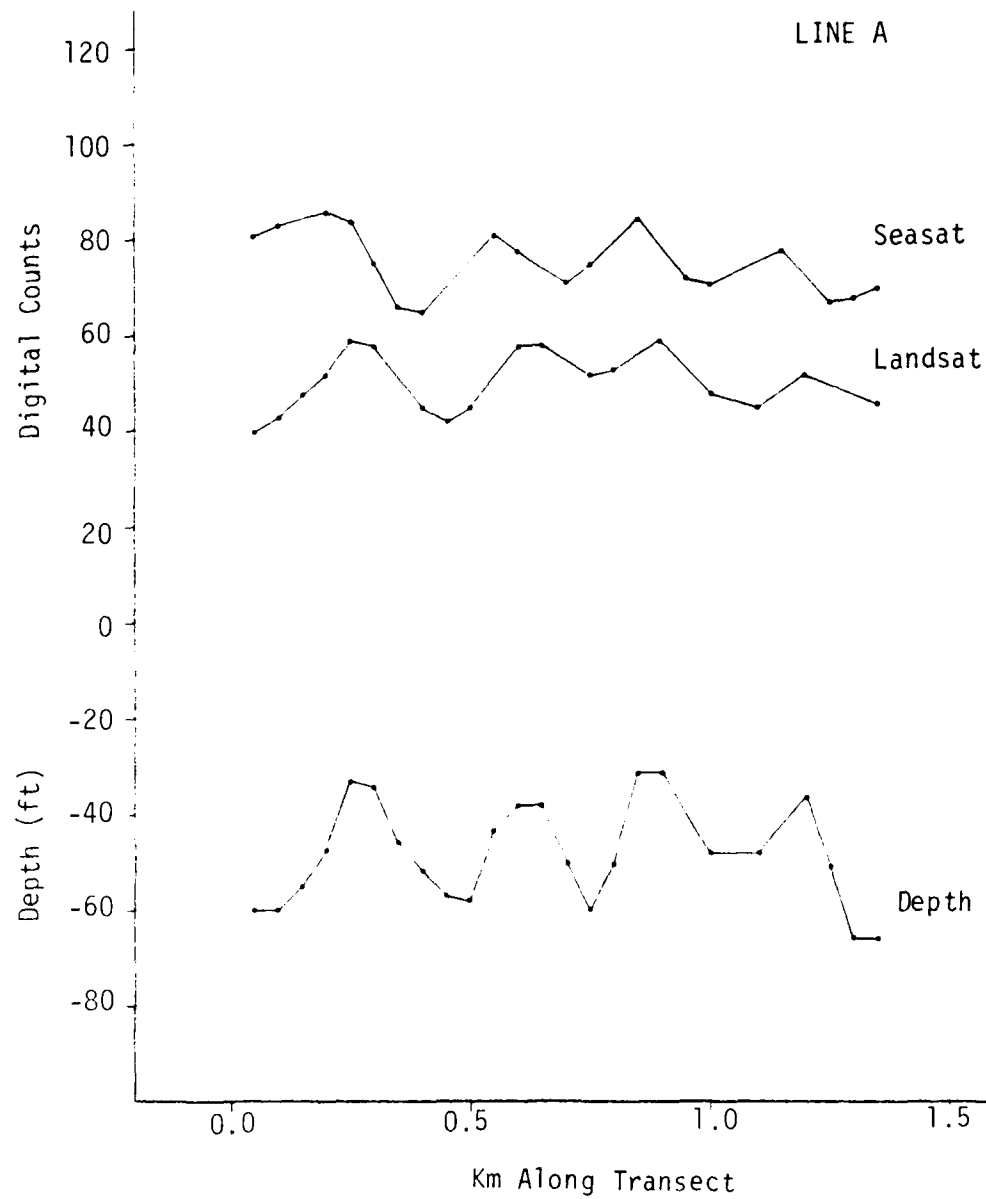
FIGURE 78.   PLOTS OF SEASAT, LANDSAT AND DEPTH
             DATA ALONG UPPER LINE IN FIGURE 75
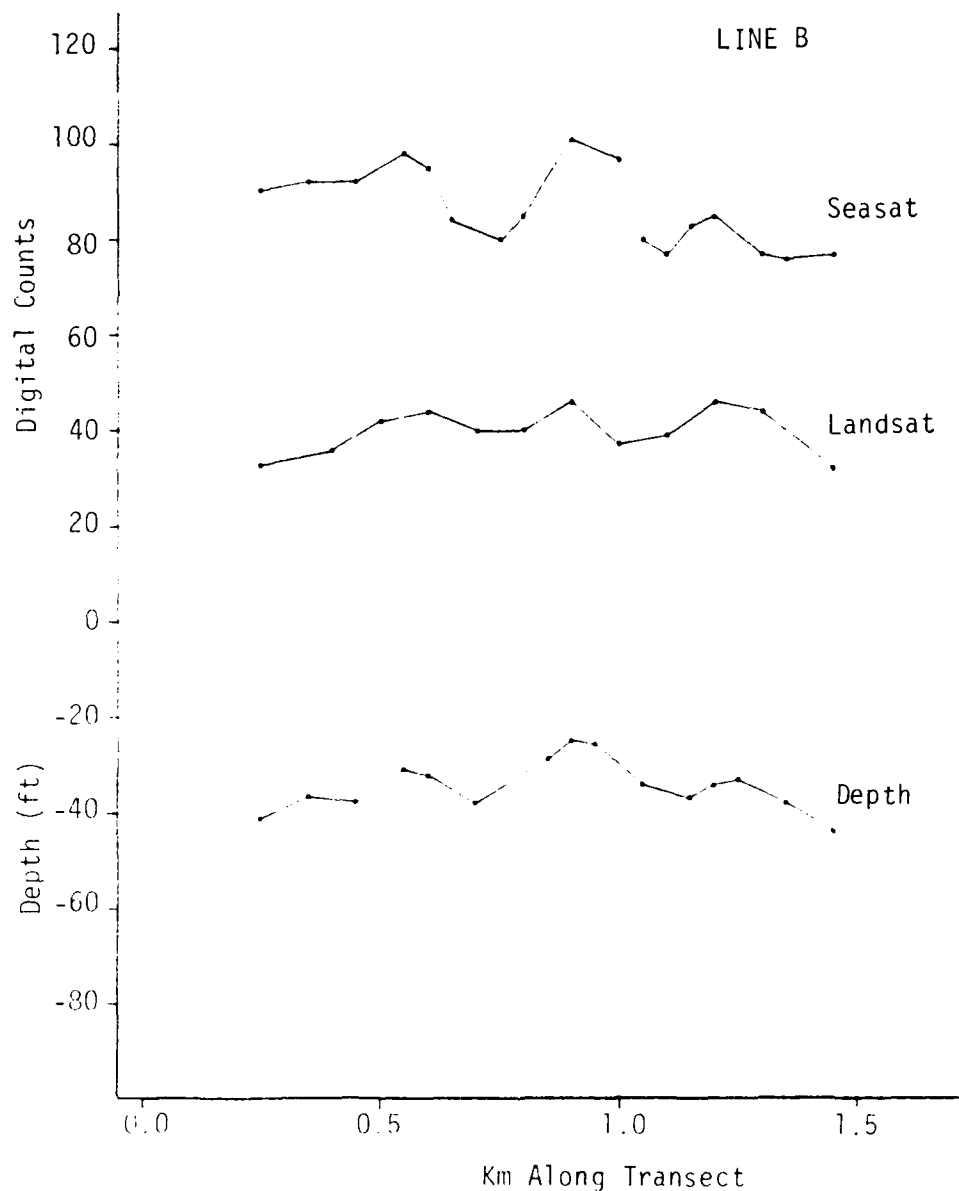
FIGURE 79. PLOTS OF SEASAT, LANDSAT AND DEPTH
DATA ALONG LOWER LINE IN FIGURE 75

reported by Uchupi (1968). Since this area is quite distant from the geometric ground control points used for registering the data, the relative location of these features may be in error and no firm conclusions can be drawn about the relative shifts between the image and bottom features. However, the apparent correspondence between the depths and the image features is strong evidence that those features are indeed related to transverse sand waves on the bottom.

### 6.3.3 SKYLAB OBSERVATIONS

The data presented in the preceding section shows that the information supplied by Seasat and Landsat over this area is essentially equivalent, although the Seasat data provide a higher spatial resolution. Data are presented in this section from one additional source, namely the photography from the Skylab-3 mission in 1973. Figure 80 shows two sequential frames taken over the Cape Cod area on 12 September 1973, using the S-190A multispectral camera (0.5-0.6 μm).

Many of the features observed on the Seasat and Landsat imagery appear in the Skylab photography as well. These features are much more distinct in the second frame of the sequence, where the viewing angle for the Nantucket Shoals region is closer to the specular direction for direct sunlight. This dependence on the look direction would tend to suggest that the primary mechanism for the appearance of these features, at least in the visible region of the spectrum, is a modulation of the surface slope. This same mechanism may contribute to the tonal variations in the Seasat imagery as well, although modulation of the small-scale Bragg waves is probably the most important factor in the SAR case (Shuchman, 1982).

In addition to indicating the probable mechanism for the appearance of bottom-related surface features in visible imagery, the strong look-angle dependence observed in the Skylab photography also
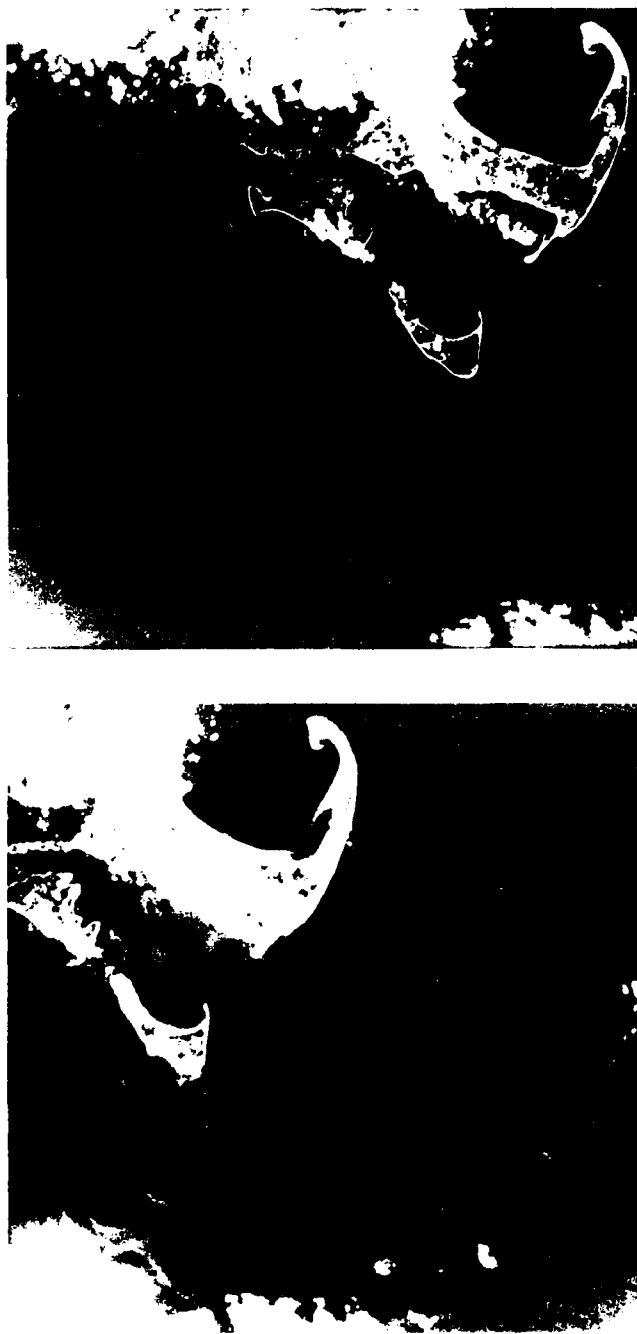
FIGURE 80.    SEQUENCE OF TWO SKYLAB S-190A PHOTOGRAPHS OVER THE CAPE COD
AREA.   NOTE THE MORE DISTINCT APPEARANCE OF BOTTOM-RELATED
FEATURES IN THE SECOND PHOTOGRAPH.

seems to imply that a favorable viewing geometry is required for imaging these features with visible sensors. Scanning systems such as Landsat view the scene along a fixed plane which moves with the platform. The Skylab data indicate that this plane must be within approximately 45° of the solar azimuth in order to image the features. For the Landsat frame used in this study, the viewing azimuth was approximately 100° while the solar azimuth was 120°.

## 6.4 SUMMARY AND CONCLUSIONS OF THE MULTI-SENSOR ANALYSIS

A multi-sensor study was carried out using Seasat, Landsat, and water depth data registered onto a common 50 x 50 meter geographic grid system. The area selected for this study was the Nantucket Shoals region, which shows numerous depth-related surface features on both the Seasat and Landsat images. The features visible on the Landsat imagery are apparently due to surface reflection, unlike some areas where an actual bottom-reflected signal is present.

The results of the comparison between the Seasat and Landsat data presented in this section indicate that for the particular data sets examined: (1) bottom features larger than about 0.5 km, such as longitudinal sand waves, are imaged equally well by both sensors, while (2) features smaller than about 0.5 km, such as transverse sand waves, are frequently resolved by Seasat but infrequently by Landsat. Imaging of bottom features by Landsat via the current/bottom interaction mechanism probably requires a favorable viewing geometry relative to the sun in addition to favorable current and wind conditions. Photographs taken by Skylab indicate that the contrast of these features varies strongly with the look direction, and that the solar azimuth must be within about 45° of the viewing azimuth in order to image the features with a sensor operating in the visible region of the spectrum.

Statistical comparisons indicate that a high correlation ($r = 0.8 - 0.9$) exists between the water depth and the Seasat and Landsat signals over distances on the order of a few kilometers if allowance is made for a horizontal shift between the remote sensor data and the water depth. The mean shift between the location of maximum signal and the minimum depth is on the order of 200 meters, and the rms shift is about twice this value. The observed shifts are quite similar for the Seasat and Landsat data, but are not consistent throughout the scene, as indicated by the large r.m.s. values as compared to the mean values.

Although this study concentrated on the spatial relationships (i.e., the relative position of features) among the data sets considered, it was also noted that the relationship between the peak signal and the water depth is not uniform throughout the scene, for either the Seasat or the Landsat data. This variability, as well as the inconsistency in the positioning of the features, is probably a result of differences in the current from point to point, and may also indicate that more than one scattering mechanism is responsible for the appearance of the bottom features (i.e., modulation of Bragg waves may be the dominant mechanism in some areas, whereas wave breaking may occur in others). The conclusion seems to be that the position of shallow water features can be determined within a half of a kilometer from the Seasat (or, in some cases, Landsat) data, but in order to position the features more accurately or to determine the depths quantitatively, a large scale-circulation model may have to be used to determine the variation in the currents within the test area.

7
CONCLUSIONS AND RECOMMENDATIONS

This study has demonstrated the utility of the Seasat spaceborne synthetic aperture radar (SAR) to detect submerged ocean features that are potentially hazardous to ship navigation. Three research activities were undertaken in this demonstration project. They included broad surveys, a multi-temporal study, and a multi-sensor analysis.

The broad survey studies (Chapter 4) continued to document the occurrence of surface patterns on SAR imagery that are related to a bottom topographic feature. The scope of these survey studies was expanded from the surveys performed in the previous effort (Kasischke, et al., 1980) in two significant areas: first, deep-water test sites were examined; and second, several false alarms were documented. For the survey studies, ERIM has examined approximately one-fourth to one-third of the available Seasat SAR imagery. It should be noted that the surveys to date identify anomalous SAR signatures, and then a hydrographic chart is consulted to determine if the SAR signature is related to a bottom feature. Thus, the present analysis does not address the question of how many submerged hazards the Seasat SAR did not successfully image.

To overcome this omission, the following analysis technique is suggested. First, plot the relative ground track of Seasat SAR imagery from all available passes over open water areas, and then determine what significant bottom features are within the coverage of those passes. Next, consult the SAR imagery to determine what surface patterns exist on the SAR imagery that can be correlated to a bottom feature. This will help develop an understanding of the unconditional probability of detection for a specific bottom feature on spaceborne SAR imagery. It is also recommended that other sources of SAR imagery be reviewed, such as those collected by aircraft and the Shuttle Imaging Radar (SIR-A).

A multi-temporal study (Chapter 5) was carried out for three geographical areas, including the English Channel, the Tongue of the Ocean, and the northeast Atlantic Ocean (the JASIN test area). Two significant observations resulted from this study. First, the unconditional probability of observing depth-related image features in these areas was evaluated simply by noting the number of images in which these features occurred out of the total number of images acquired. In the English Channel, very distinct depth-related features were observed in one out of four passes and recognizable features were observed in two out of four passes. In the other two cases, the features were very faint or nonexistent. The depth of these features was on the order of 10 meters. At the southern end of the Tongue of the Ocean, bottom features with depths on the order of 3 meters were observed in 11 out of 12 passes. In the northeast Atlantic, surface features were observed corresponding to bottom features such as banks, submarine ridges, seamounts, and edges of the continental shelf in 63 percent of the cases imaged. The depths of these features ranged from 200-600 meters, in a surrounding depth of 1000-2000 meters.

The second observation of the multi-temporal study was to begin to understand the prerequisite SAR system imaging geometry and environmental conditions for the observation of these features. This was done by compiling a set of ancillary environmental data for each overpass and correlating these conditions with the appearance of the features. These data were interpreted by formulating a set of hypotheses regarding the hydrodynamic and electromagnetic interactions responsible for the appearance of the features. In one instance, this process was carried through to the implementation of a quantitative computer model which gives reasonably good agreement with the observed backscatter variations.

The value of these results for the hydrographer is that they allow an estimate of the confidence with which the existence of a

potent??l navigation hazard can be confirmed or dismissed on the basis o one or more Seasat (or other SAR) images of the area in question. Additional precision in this estimate can be obtained if some knowledge of the environmental conditions is used in conjunction with the results of the more detailed studies mentioned above. It is therefore recommended that further studies of this type be carried out in order to characterize both the unconditional probabilities of detection of each type of bottom feature observed, and also to determine the dependence on environmental and SAR system parameters.

A multi-sensor study (Chapter 6) was also performed for the purpose of comparing the information obtainable from various remote sensors over the Nantucket Shoals area. The sensors considered in this study included the Seasat SAR, the Landsat multispectral scanner (MSS), and Skylab photography. This study concluded that for the particular area considered, the data from these sensors were essentially equivalent although differing in spatial resolution. This equivalence is in part due to the fact that each of these sensors was viewing essentially the same phenomenon, namely perturbations in the surface roughness due to hydrodynamic interactions with the bottom. It was further concluded that the observation of these features with a Landsat-type sensor is restricted to favorable viewing geometries, sun illumination, and cloud cover and may therefore be considered to be less reliable than SAR observations of these features.

It should be noted that in other cases, water depth information can be obtained from visible sensors through a different interaction mechanism, for example, by direct reflection of light from the ocean bottom. In these cases, information of a more complementary and less redundant nature may be obtained from visible and microwave sensors. It is therefore recommended that additional multi-sensor studies be carried out in areas where bottom reflection effects predominate over surface reflection effects in the Landsat imagery. A prime candidate for such a study would be the Tongue of the Ocean region where surface effects have been observed in Seasat imagery, and where bottom

r flection effects are expected to be larger than surface effects in the Landsat imagery due to the clarity of the water and the less favorable viewing geometry for observation of surface effects.

The emphasis in our research to date has been on the positional information available from SAR data. It is also possible that when the interaction mechanisms for the appearance of depth-related features in SAR imagery are better understood, quantitative relationships between the SAR signal and the water depth may be developed. In order to begin this development, it is recommended that a detailed comparison be made between the SAR signal anu the water depth in an area where accurate depths are available.

In summary, our recommendations for further research are as follows:

1. Survey all available SIR-A L-band and APD-10 X-band imagery, and complete the survey of existing Seasat L-band SAR imagery of deep- and shallow-water areas to document the spatial and temporal distribution of SAR surface signatures from all three data sets which may be related to bottom hypsographic features.

2. Fully document a subset of the cases studied above by compiling an ancillary data set of meteorological, tidal, current, sea state and wave information for the dates when the SAR imagery being examined was collected.

3. Make detailed quantitative comparisons between water depths and a radiometrically enhanced and geometrically corrected digital SAR data set for a suitable test site, in order to determine whether a statist cally significant relationship exists between radar backscatter and water depth.

4. Using the multiple Seasat SAR passes of the Tongue of the Ocean, combine this SAR data with Landsat MSS and other NASA

remote sensor data (if available) to see if the multiple data sets are complementary in providing bathymetric information in an area where bottom reflection effects predominate in the visible region of the spectrum.

5. Continue to provide a first order description of the hydrographic applications and limitations of using SAR data through the use of specific case studies and false alarm examples.

APPENDIX A

EXAMPLES OF SURFACE PATTERNS
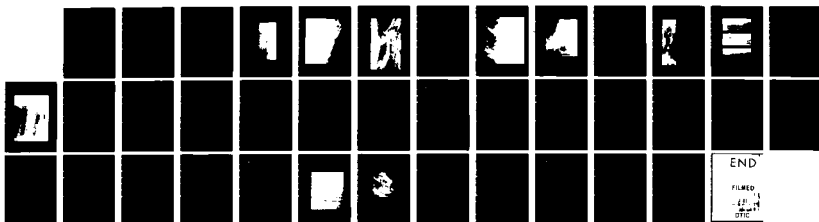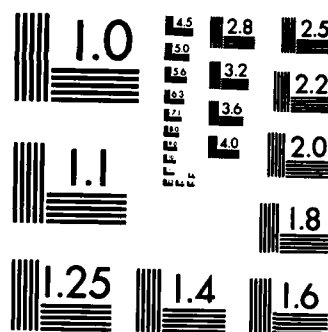
ON SAR IMAGERY

MICROCOPY RESOLUTION TEST CHART

NATIONAL BUREAU OF STANDARDS-1963-A

APPENDIX A
EXAMPLES OF SURFACE PATTERNS ON SAR IMAGERY

In order for SAR data to be effectively used in updating hydro-
graphic charts, the SAR image interpreter must be able to distinguish
between bottom-related SAR signatures and those caused by other
oceanic or meteorologic phenomena.  The image interpreter also needs
to have an understanding of the reliability of the SAR data in re-
spect to detecting submerged hazards.  In other words, how many times
will a SAR signature be considered to be bottom-related when it is
in actuality an oceanographic feature unrelated to bathymetry (i.e.,
determination of a "false-alarm" rate).

The Seasat SAR operates at a radar wavelength (23.5 cm) which
does not significantly penetrate the water surface (Hollinger, 1973).
Thus, the subsurface-related patterns recorded on SAR data are the
result of surface perturbations which are caused by a hydrodynamic
interaction between a variety of oceanic processes (currents, waves,
and tides,), climatic processes (wind and rain), bottom features
(topographic irregularities), man-made phenomena (ships and buoys),
and the surface gravity ocean wave field and particularly the Bragg
ocean waves.  The question arises as to whether the motion resulting
at the ocean surface from each of these oceanic processes generates
a unique signature observable with SAR.

Image examinations have revealed SAR's ability to observe a vari-
ety of microscale, macroscale, and mesoscale ocean features.  These
features include gravity waves, ocean and coastal currents, long-
period waves, internal waves, frontal boundaries, surface winds,
storms cells, surf zone conditions. oil slicks, kelp beds, ship wakes
and sea ice.  While we will present examples of many of these phenom-
ena in the following pages, a discussion of why they appear on SAR
imagery is beyond the scope of this report.  For this information,
the reader is referred to reports by Shuchman, et al. (1981a), Fu and
Holt (1982), or Beal, et al. (1981).

181

Presented in the next several pages are examples of SAR-observed signatures that are a result of oceanographic phenomena not directly controlled by the local bathymetry. Examples will be presented of deep-water gravity waves, coastal and ocean currents, cold and warm water masses, surface related wind patterns, meteorological rain squalls, ship wakes, oil slicks, and kelp beds. These types of surface phenomena generate unique SAR signatures which need to be recognized by SAR interpreters as non-bathymetry related SAR patterns.

A gravity wave field imaged by Seasat during Rev. 1049 (8 September 1978) is presented in Figure A1. The islands in this image [St. Kilda (bottom) and Boreray (center)] are located 25 kilometers west of the coast of Scotland. During this revolution, surface wave measurements made 250 kilometers away indicated the presence of a swell with a dominant wavelength of 244 meters, significant wave height $(H_{1/3})$ of 5.0 meters, and a direction of propagation of $84°(T)$. Fast Fourier transform analysis of the SAR data results in a dominant wavelength of 300 meters and direction of propagation of $80°(T)$ (Kasischke, et al., 1981). These waves are clearly visible on the SAR image and are observed to diffract as they pass the islands.

The presence of ocean and coastal currents is a necessary condition for the appearance of certain depth-related features in SAR imagery. However, ocean or coastal currents may also cause image features which are unrelated to depth. Figure A2 is a JPL-digitally processed SAR image from Rev. 974 collected on 3 September 1978 off the coast of Cape Hatteras, North Carolina. Comparisons of the reported position of the Gulf Stream with this image have led researchers to believe that the striated patterns (see letter C) in the right-hand side of the image are the Gulf Stream (Kasischke, et al., 1981). Figure A3 is an ERIM optically-processed image collected by Seasat during Rev. 150 (July 1978) over the mouth of the Columbia River in Oregon. The Columbia River has a velocity between 2-3 m/s and its discharge into the Pacific is clearly visible on the SAR image.
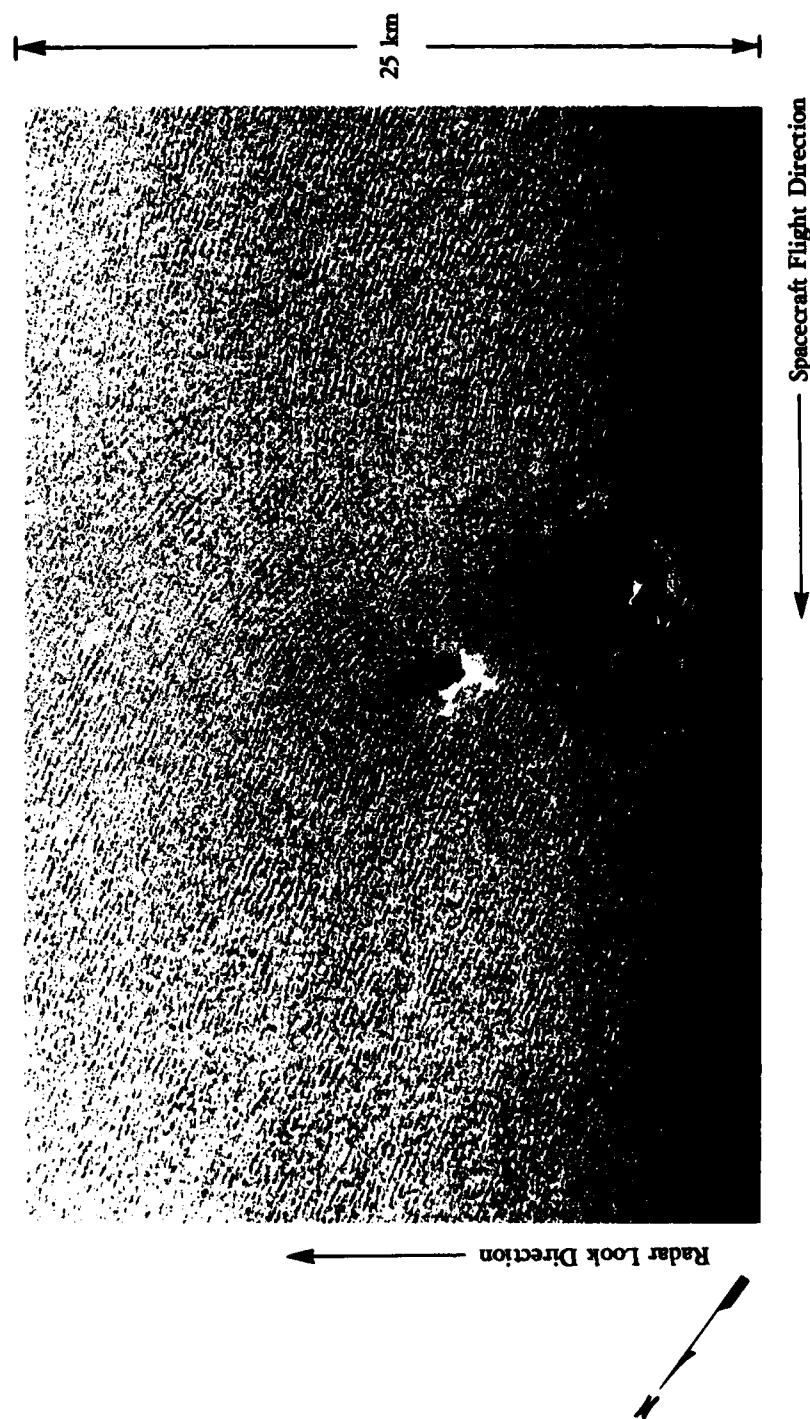
FIGURE A1.    SEASAT SAR IMAGERY COLLECTED DURING REV. 1049 ILLUSTRATING WAVE
DIFFRACTION AROUND AN ISLAND.    (ERIM Optically Processed Imagery.)
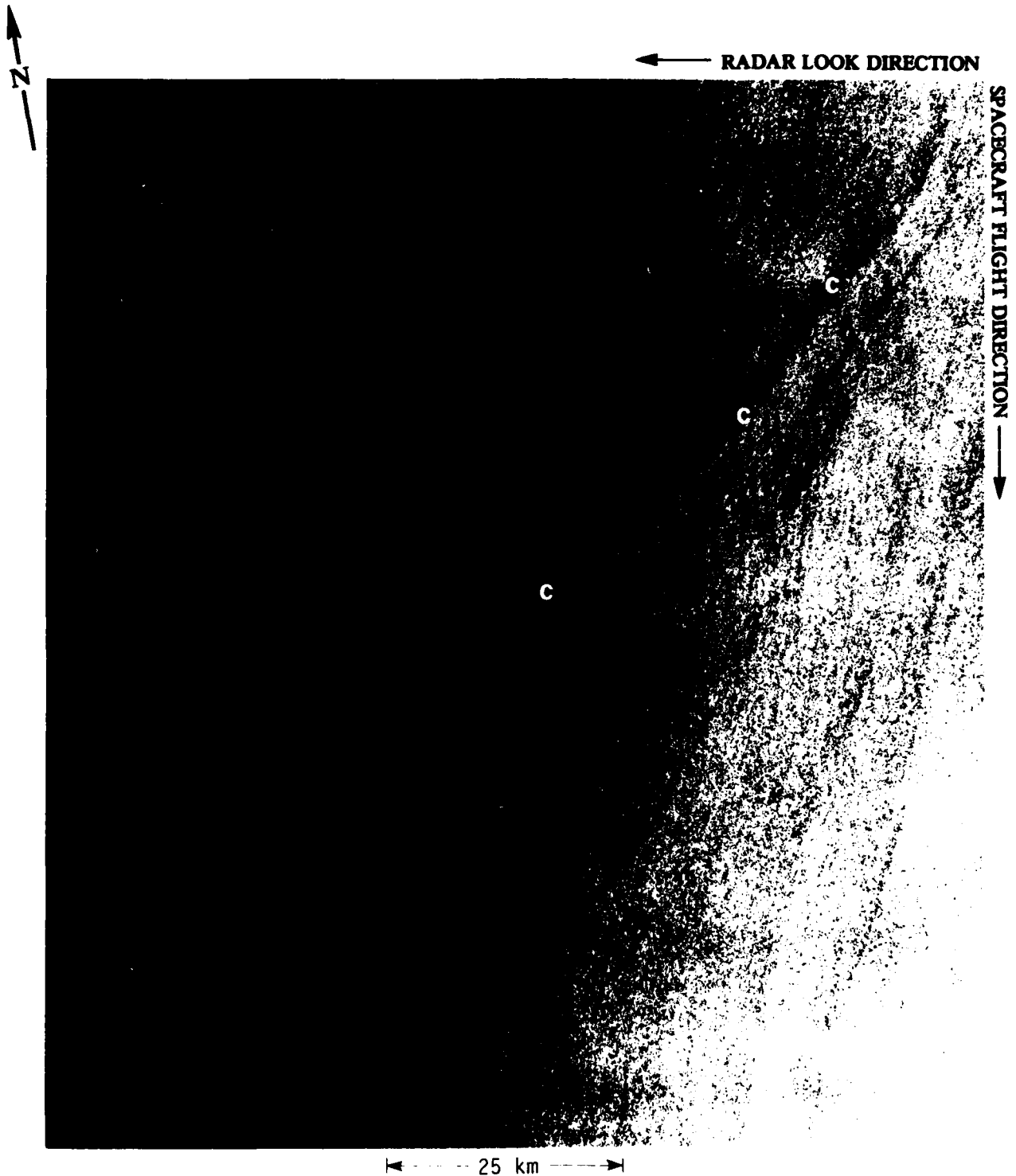
FIGURE A2.   NORTHERN EDGE OF THE GULF STREAM BOUNDARY (LETTER C) OBSERVED
             ON SEASAT REV. 974, 3 SEPTEMBER 1978.  (Image generated from
             JPL digitally processed data.)
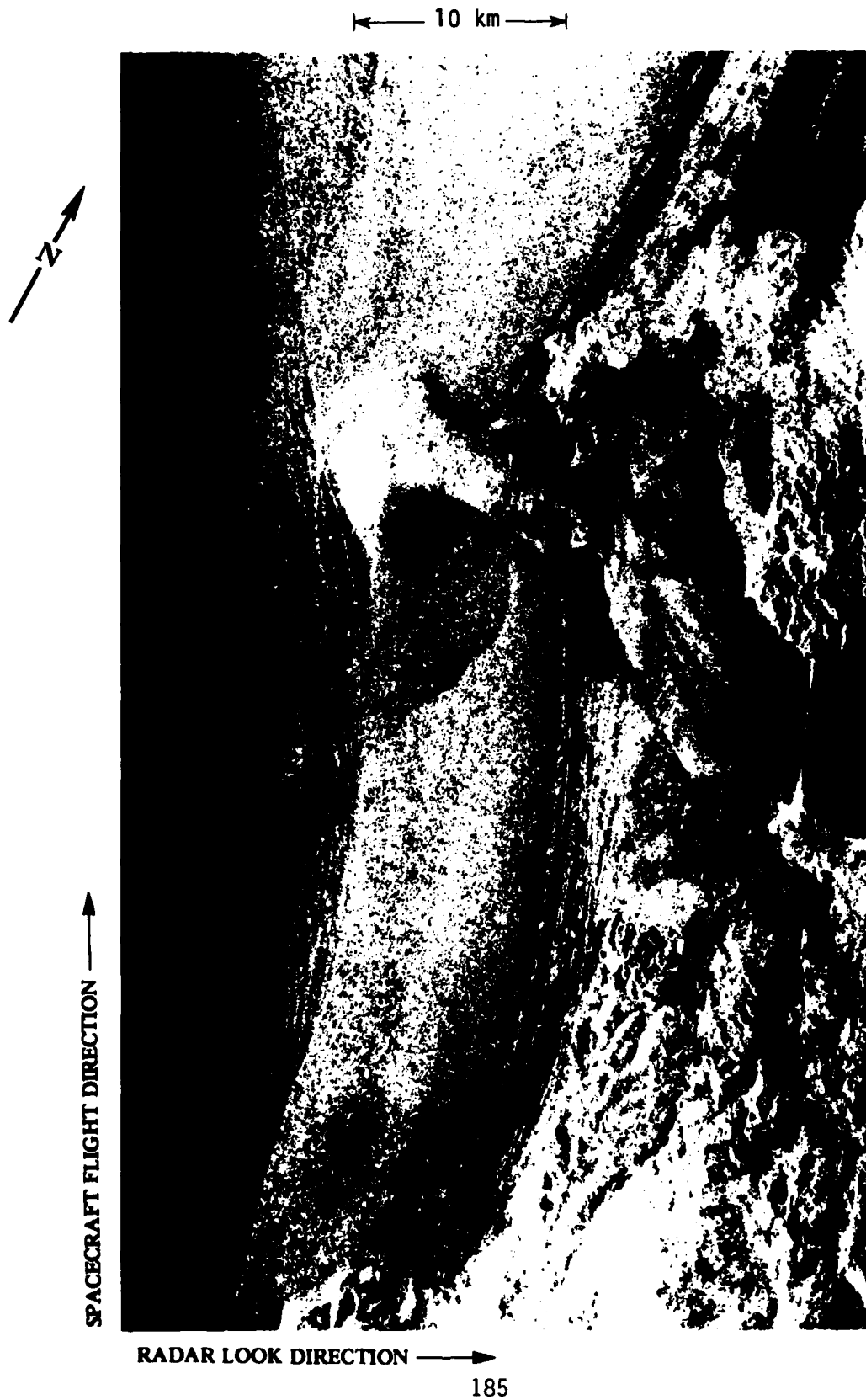
FIGURE A3.   SAR IMAGE OF COLUMBIA RIVER BAR.   (Rev. 150, ERIM Optically Processed Imagery.)

185

Figure A4 is a JPL-digitally processed SAR image collected during Rev. 880 (27 August, 1978) over Nantucket Island. Although this image has been extensively analyzed for bottom features (see Chapter 6 of this report), it also contains two examples of ocean frontal boundaries. Valenzuela (1981) determined that at the time Seasat made its overpass, a cold water mass originating from the Labrador current existed off Nantucket Island. This cold water mass had a temperature of approximately 13°C while the warmer surrounding shelf water had a temperature of approximately 15°C. The position of this cold water coincides with the dark central region of Figure A4 as is indicated by the letter A. The colder water is darker in this image because the stable atmospheric temperature (i.e., warmer air temperature than the water) profile causes less turbulence and hence a smoother surface. The boundary region between the warm and cold water body also exhibits a sinusoidal shape typical of frontal boundaries (see areas labeled "B" on Figure A4).

Wind speeds of less than 1-2 m/sec are usually not of sufficient strength to generate the capillary/ultra-gravity waves necessary to reflect radar energy from the water surface. Thus, low wind conditions will be represented by dark areas on the radar imagery. Figure A5 is a JPL-digitally processed image of Seasat data collected during Rev. 1339 (28 September 1978) representing an area located southeast of the entrance of Chesapeake Bay. Wind magnitude measurements over the area of dark return indicate wind speeds of less than 1 m/sec (Beal, et al., 1981). The long, straight features marked by an "A" in Figure A5, are believed to be surface manifestations of Eckman spirals (Mollo-Christensen, 1981).

Because of the dependence of radar backscatter from a water surface on wind speed, atmospheric disturbances such as rain squalls show up particularly well on SAR imagery of open-water areas. Figure 53 (presented in the main text) is a JPL-optically processed Seasat SAR image collected during Rev. 1368 (30 September 1978) over the

FIGURE A4.   OCEANIC FEATURES OBSERVED OFF OF NANTUCKET ISLAND,
MASSACHUSETTS ON SEASAT REV. 880, 27 AUGUST 1978.
(Image generated from JPL digitally processed data.)

187
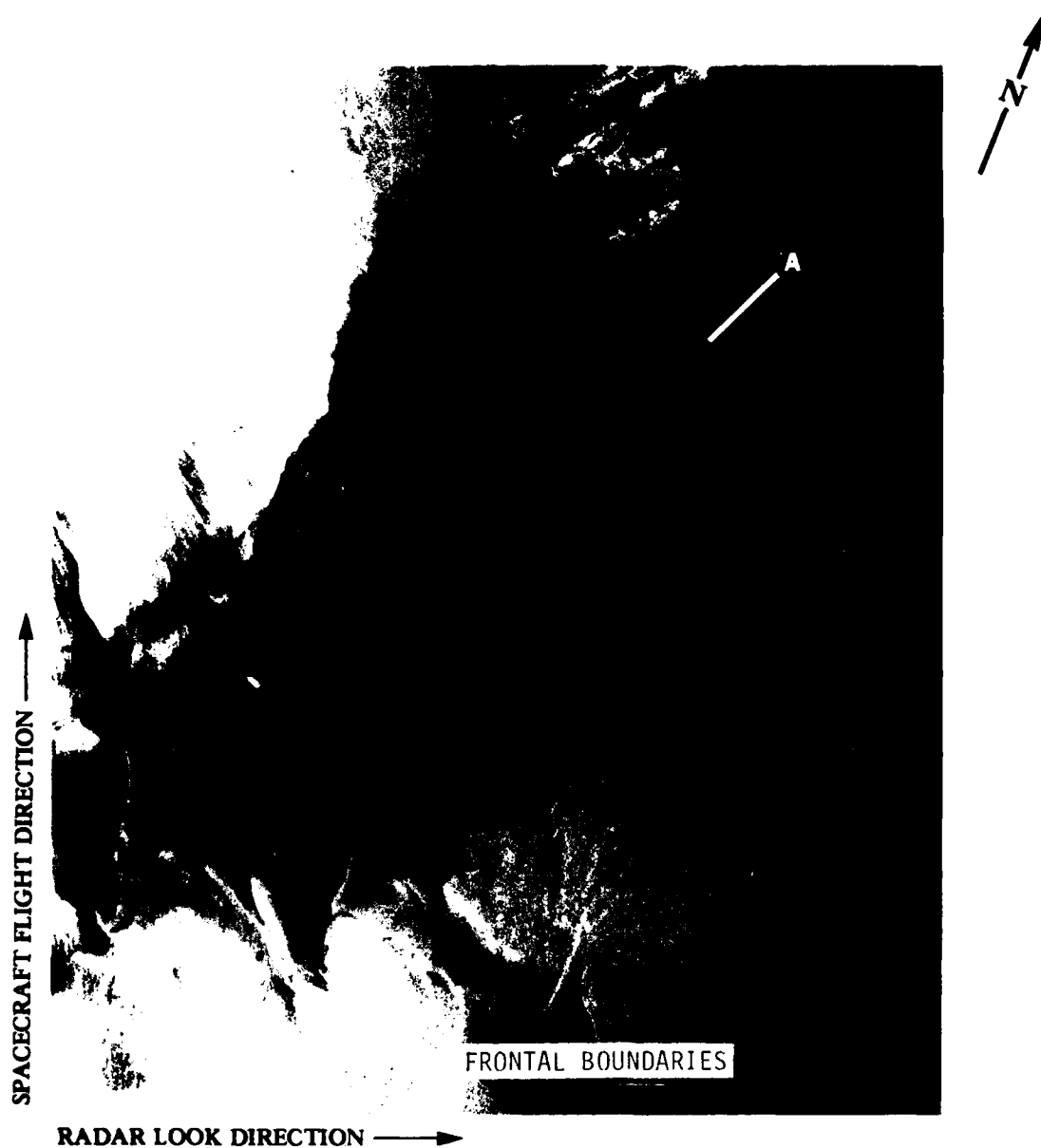
FIGURE A5. EXAMPLE OF WIND PATTERN AND EKMAN SPIRALS ON SEASAT
SAR IMAGERY. (Rev. 1334. Image generated from JPL
digitally processed data.)

southern edge of the Tongue of the Ocean. This area is believed to be dominated by localized rain-squalls (e.g., "A" on Figure 53), which have higher winds than the areas immediately adjacent to them (e.g., "B" on Figure 53). Characteristic to these rain squalls are areas of extremely heavy precipitation rates ("C" in Figure 53), which are characterized by their extremely low radar returns. These low radar returns are believed to be due to attenuation of the L-band microwave radiation by the heavy precipitation.

Rain squall patterns are quite common on Seasat SAR imagery. Figure A6 is a JPL-optically processed Seasat SAR image collected during Rev. 694 (14 August 1978) approximately 350 kilometers southeast of the coast of Georgia over the Atlantic Ocean. The patterns in this image are quite similar to those on Figure 53.

Figure A7 illustrates examples of ships and their wakes which were present on Seasat SAR imagery. The upper image on Figure A7 was collected during Rev. 651 (11 August 1978) off the coast of Florida while the middle image was collected during Rev. 617 (9 August 1978) off the coast of California. Ships which are large enough to produce wakes detectable on Seasat SAR imagery are usually large enough to be seen as point targets (i.e., bright point returns). The V-shaped, Kelvin wakes of ships are quite distinguishable, as can be seen in the upper image on Figure A7. However, quite often only one side of the Kelvin wakes is clearly visible on SAR image, as is illustrated by the Rev. 651 image. These one-sided Kelvin wakes are easily identified because they are usually associated with the bright return from the ship and also because they are very straight.

Figure A7 (lowest image) also presents a Seasat SAR image of an oil slick generated by a ship. This image was produced from Seasat SAR data collected during Rev. 737 (11 June 1978). Oil slicks are characterized on SAR imagery by extremely low return and are of limited areal extent.

FIGURE A6.    EXAMPLE OF RAIN SQUALL PATTERNS IN DEEP WATER AREA.    (Rev. 694.    Optically processed imagery courtesy of JPL.)

190
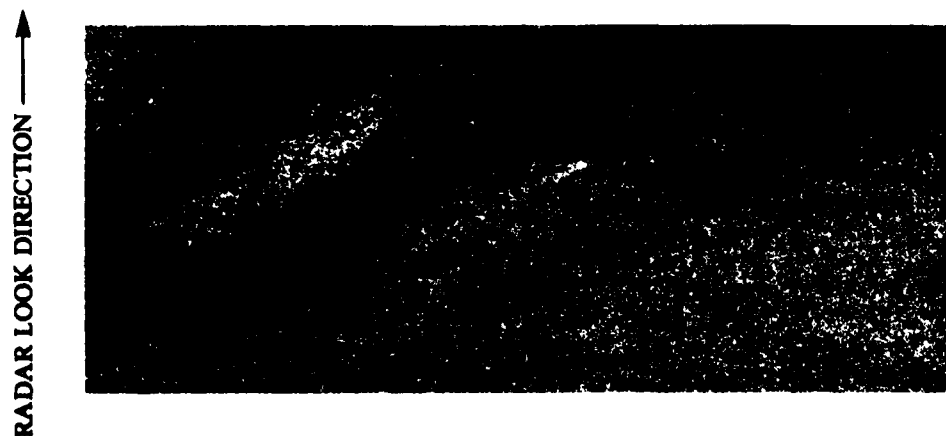
FIGURE A7. EXAMPLES OF SURFACE PATTERNS CAUSED BY SHIP WAKES AND OIL SLICKS

Figure A8 is an image generated from data collected by a UPD-4 X-band SAR system of kelp beds off Point Loma in San Diego. The UPD-4 is a high-resolution airborne side-looking reconnaissance SAR transmitting 3.2 cm wavelength energy. The UPD-4 SAR data are recorded on 9.5-inch film in four sub-swaths where each sub-swath is nominally 4.6 km (2.5 nmi) in width with an additional 0.46 km (0.25 nmi) overlap between adjacent channels. The nominal resolution of these data is 3 meters and the nominal incident angle was approximately 50°. The data presented in Figure A8 were collected on 17 August 1981. The area of bright return on this image corresponds to the position of a kelp bed. Kelp generally lays 1.5 to 2.0 cm in height above the ocean surface (Jensen, et al., 1980). Kelp therefore appears "rougher" than the surrounding water to an X-band (3.2 cm) SAR system. Jensen, et al. (1980) reported that on Seasat imagery, kelp beds appeared darker than the surrounding water. To the L-band SAR, the kelp beds appeared smoother than the surrounding water surface due to suppression of the small-scale surface waves.
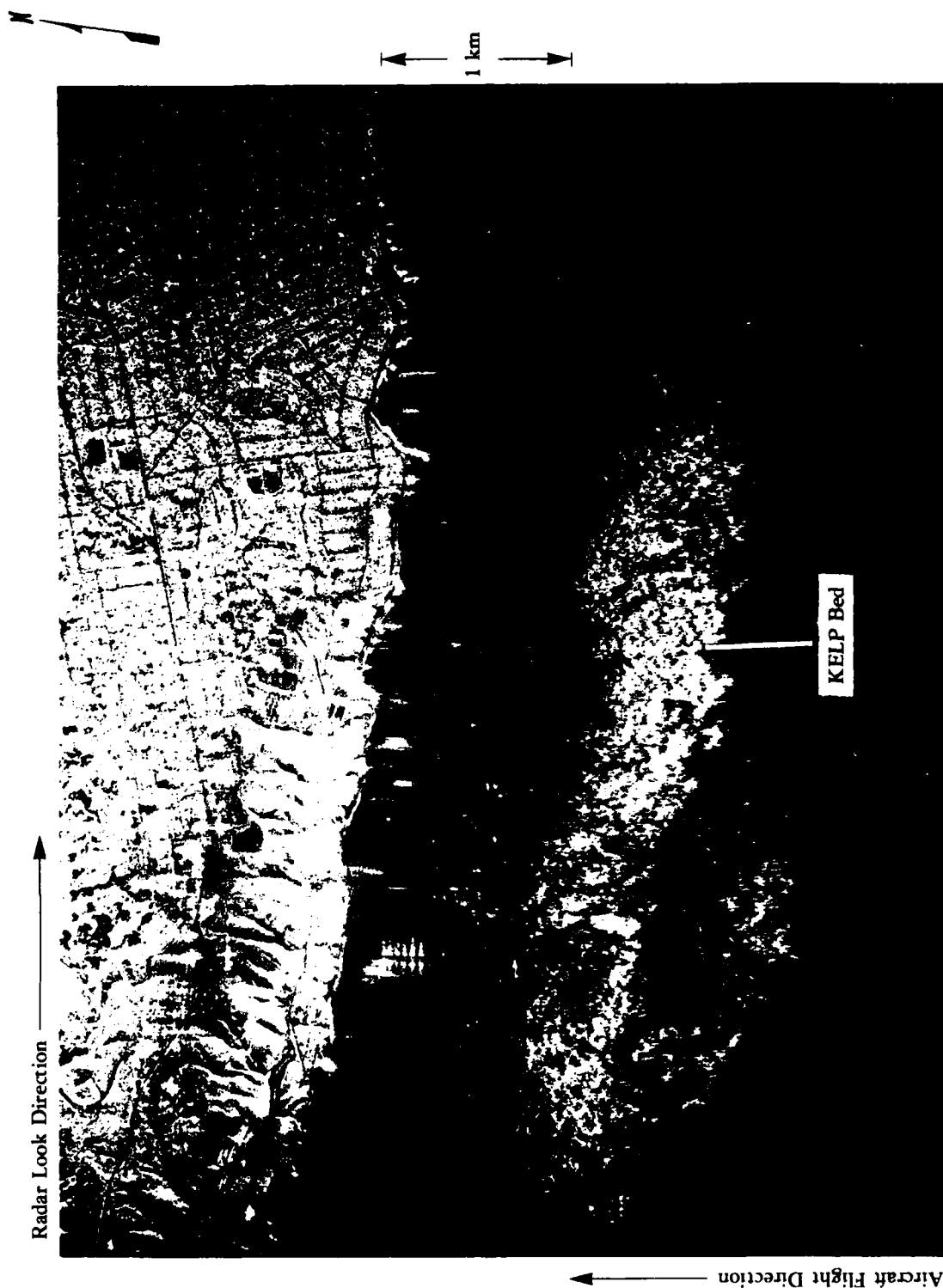
FIGURE A8. SAR IMAGE OF KELP BED OFF CALIFORNIA COAST (UPD-4 X-band SAR data).

APPENDIX B

SAR DETECTION OF NAVIGATION

BUOYS AND SHIPWRECKS

## APPENDIX B
## SAR DETECTION OF NAVIGATION BUOYS AND SHIPWRECKS

Seasat ∂AR imagery of the portion of the Southern Bight of the North Sea imaged during Rev. 762 (19 August 1978) was used in this investigation (see Figure 39). This area contains many navigation buoys and shipwrecks, and because these Seasat SAR data have been intensively studied in past investigations (see Kasischke, et al., 1980: Kenyon, 1981: Shuchman, 1982) and during the present one (see Section 5.1), sufficient ancillary data for the area, such as tidal current information, exists. For this study, Seasat SAR imagery digitally processed at JPL and geometrically and radiometrically corrected at ERIM (see Appendix C) was used.

Because of the great number of buoys and shipwrecks located in the section of the Southern Bight of the North Sea covered by Seasat, a sample of 32 buoys and 91 wrecks were selected from this area from DMA Chart No. 37140, "Thames River Estuary and Approaches." The locations of the buoys and wrecks, obtained from the DMA chart, were marked onto a clear-cell overlay which was then placed over the Seasat SAR image. This composite was examined to determine if any surface anomaly existed at or near the positions of the buoys and wrecks.

In their key to chart symbols, the DMA lists over 70 types of navigation buoys and 8 classes of shipwrecks (Department of Defense and Department of Commerce, 1979). For the purposes of this study, we have grouped all the buoys into one category and defined three categories of shipwrecks, as follows:

Buoys:   Any buoy or floating beacon used to mark navigation channels or hazards. Included in this category are ship- wrecks marked by buoys.

Shipwreck I:　Exposed shipwrecks which are defined as wrecks that show any portion of hull or superstructure above water.

Shipwreck II:　A submerged wreck whose depth is known and marked on the chart.

Shipwreck III:　A submerged wreck classified as dangerous to surface navigation. Exact water depth over the wreck is undetermined but known to be less than 20 meters (11 fathoms).

It is recognized that locating buoy positions via a navigation chart is not the most accurate method. Not only are buoys subject to movement by environmental forces such as waves and currents, but their positions can also be changed by the agencies responsible for their maintenance and upkeep. However, to obtain more accurate information would entail a time-consuming search of the records (if they exist), and for this study, the charted locations of buoys were assumed to be correct.

Three categories were used to classify the degree of detectability of the buoys and shipwrecks on the Seasat SAR image. These were:

None:　No detectable surface wake was present on the SAR image within 0.5 kilometers of the position of the buoy or wreck.

Possible:　A wake-like signature, sometimes quite faint, was present on the SAR image within 0.5 kilometers of the position of the buoy or wreck.

Probable:　A wake-like signature was present within 0.25 kilometers of the position of the buoy or wreck.

The wake-like signatures produced by buoys and shipwrecks are less distinctive than those produced by moving ships, as can be seen in Figures 21 and 22. This is due to several factors. First, the speeds of the currents in the English Channel are much less than

those of ships (one to two knots for the current versus ten knots or
more for ships).  Second, the cross-section of a shipwreck or buoy
is considerably less than that of ships of the types usually visible
on Seasat SAR images.  From Figure 21, we can clearly distinguish
the Kelvin (v-shaped) wake of the surface ship, along with the tur-
bulent wake behind the vessel.  Note how the ship has been displaced
from its wake.  This occurs because the ship's velocity causes a
shift in its signal histories, relative to the more stationary back-
ground on the SAR data.  Figure 22 illustrates a more subtle wake-
like signature formed near the reported position of a buoy.

Three pieces of ancillary data were obtained for each position.
These included water depth, current speed and current direction.
The water depth for each position was obtained from one of three DMA
charts:  No. 37140 ("Thames Estuary and Approaches"): No. 37122
("South Foreland to South Falls Head"), or No. 37125 ("Approaches to
Dunkerque").

The tidal current speed and direction were obtained from one of
two sources.  The first source was the tidal current tables on each
of the above three charts.  These tables list current speed and
directions for marked chart positions for each hour before and after
high tide.  The second source of information was the "Admiralty Tidal
Stream Atlas."  Specifically, the atlases used were:  NP249:  Thames
Estuary: NP 233:  Dover Strait: and NP 251:  North Sea-Southern por-
tion.  These atlases present hour-by-hour (relative to high tide)
tidal current charts for the specified area.  To obtain current speed
and direction values for most positions, it was necessary to inter-
polate between the data points given on the tables or charts.

Table B1 summarizes the detection categories for each buoy or
shipwreck type.  It is clear that the rate of detection is not high
for either the buoys or the shipwrecks in this area: only 16 percent
of the positions examined result in a positive detection (i.e., pos-
sible or probable).

199

$\sum$ERIM

TABLE B1
RATES OF DETECTION OF BUOYS AND SHIPWRECKS ON SEASAT
SAR IMAGERY (REV. 762, 19 AUGUST 1978)

| Buoy or Shipwreck | Detection Category | | | | | |
|---|---|---|---|---|---|---|
| | None | | Possible | | Probable | |
| Category | Number | Percent | Number | Percent | Number | Percent |
| Buoys (32) | 26 | 82 | 3 | 9 | 3 | 9 |
| Emerged Wrecks (3) | 2 | 67 | 0 | 0 | 1 | 33 |
| Submerged Wrecks I (81) | 68 | 84 | 11 | 14 | 2 | 2 |
| Submerged Wrecks II (7) | 7 | 100 | 0 | 0 | 0 | 0 |
| Total (123) | 103 | 84 | 14 | 11 | 6 | 5 |

Even with these low detection rates which could very well be a result of poor chart information trends can be observed in the data. Figure B1 plots the average current speed versus detection category for all positions combined and for the Buoy category and Shipwreck II category alone. From this figure, it can be seen that the average current speed is highest in the probable category and lowest in the none category. Figure B1 also shows a plot of average water depth versus detection categories for the Shipwreck II category. Here, the shallowest average water depth occurs for the probable category, and the deepest average water depth for the none category.

Although the Seasat SAR had a relatively low detection rate for shipwrecks and buoys in the English Channel, it is difficult to draw any definitive conclusion from the analysis of this data because it is unknown at this time what types of shipwrecks and classes of buoys are being examined. In order to do a more definitive analysis, it is necessary to know the exact position of the buoys and also what types of buoys are being used. The type of buoy will definitely influence the nature of both the SAR reflection from the buoy itself and the size of the wake the buoy is generating.

It is also necessary to more clearly determine the types and extents of the shipwrecks being examined. For example, a submerged shipwreck can be anything from the wreck of a fifty foot wooded vessel which is covered by sand to a 200 foot ship which is not covered. A clearer identification of the shipwrecks being examined should lead to a better understanding of SAR's ability to detect them.
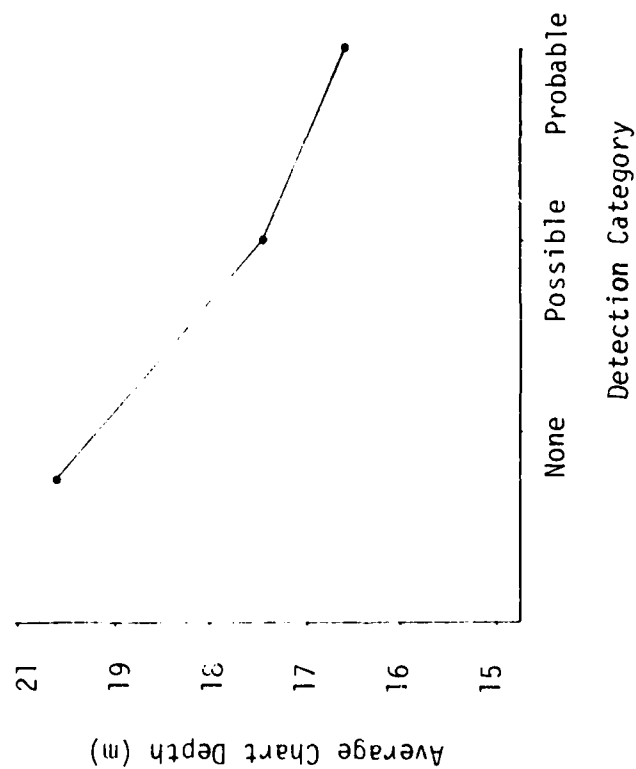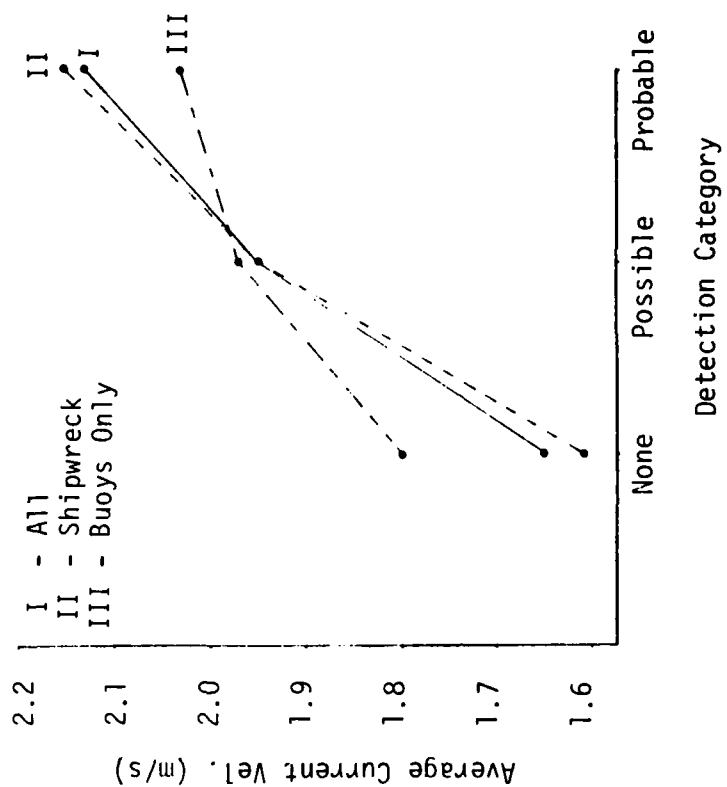
ΣERIM



FIGURE 81. PLOTS OF BUOY AND SHIPWRECK DETECTION CATEGORY VERSUS AVERAGE WATER DEPTH AND AVERAGE CURRENT VELOCITY.

202

APPENDIX C

RADIOMETRIC AND GEOMETRIC CORRECTIONS

OF DIGITAL SAR DATA

## APPENDIX C
## RADIOMETRIC AND GEOMETRIC CORRECTIONS OF DIGITAL SAR DATA

In order to perform a more detailed analyses than was possible with photographic imagery alone, digitally processed Seasat data were obtained for two areas: the English Channel (Revolution 762) and the Nantucket Shoals (Revolution 880). One of the principal advantages of using digital data is that corrections can be made for the radiometric and geometric distortions which are inherent in all SAR data. These distortions and the methods used for removing them are described in this appendix.

### C.1 RADIOMETRIC CORRECTIONS

The SAR image brightness at a given scene location is related to the physical characteristics of the surface (mainly the surface roughness and slope), but this relationship may vary from point to point due to system effects and to the inherent angular dependence of the radar cross section. The origin of these radiometric distortions is discussed in Section C.1.1, and their removal is described in Section C.1.2.

#### C.1.1 SOURCES OF RADIOMETRIC DISTORTIONS

The SAR image brightness is proportional to the power recorded per resolution cell. For a distributed scene with backscatter cross section $\sigma_o$ per unit area, the power received per resolution cell is given by

$$P_r = C \frac{G^2(\theta)\sigma_o}{R^3 \tan \theta} \qquad (C-1)$$

where R is the range, $\theta$ is the incidence angle, $G^2(\theta)$ is the two-way antenna gain, and C is the product of all the system parameters which are independent of R and $\theta$. For Seasat, the range of R and $\theta$

205

is sufficiently small that the primary variability in P for a given $\sigma_0$ is due to the antenna gain pattern $G^2(\theta)$. In order to reduce the variability in the recorded signal, the received signal was modified by a sensitivity time control (STC) before recording. However, because of timing errors, the STC did not completely cancel the effect of the antenna gain pattern and a strong range dependence remains in the recorded Seasat signal (Shuchman, et al., 1980).

Even if a perfect compensation could be made for the antenna gain, power loss $(R^3)$, and tan $\theta$ dependences, the recorded signal for a physically uniform scene would still depend on the incidence angle because of the inherent variability of $\sigma_0$ with $\theta$. The Bragg scattering model predicts that the cross-section varies approximately as $\cos^4 \theta$, neglecting the angular dependence of the Fresnel reflection coefficients, for a surface having a constant small-scale roughness and no large-scale slope. Variations in the large-scale slope modify this angular dependence somewhat (Valenzuela, 1978), especially in the Seasat range of incidence angles ($\theta \cong 20°$).

For the present application, it is desirable to display the image as a constant brightness for a constant surface roughness, rather than for a constant radar cross section. In view of the difficulty of calculating the angular dependence of the cross section and the system effects, an empirical procedure was used to normalize the image brightness. This procedure is described in the following section.

C.1.2 EMPIRICAL RADIOMETRIC CORRECTION

An empirical radiometric correction was made for both the Nantucket (Revolution 880) and English Channel (Revolution 762) digital data sets. For a detailed discussion of this technique, the reader is referred to Walker and Larson (1981). This correction was made by identifying areas having the same surface state at various range

locations in the image. The average signal was computed for each area and plotted versus range, and a smooth curve was fitted through these points. The multiplicative correction factor for range sample i was then obtained by dividing the maximum value on this curve by the value at range sample i: i.e.

$$C_i = \frac{S_{max}}{S_i}, \quad \text{for } i = 1 \ldots N \quad (C-2)$$

where $S_i$ is the value of the smoothed curves at range sample i and $S_{max}$ is the maximum value. The corrected data value for this range sample is then

$$V_i' = C_i V_i \quad (C-3)$$

where $V_i$ is the uncorrected data value. In applying this correction, the assumption was made that each sample in a given data record is at the same range. This is not exactly true, since a range offset is applied by JPL to correct for earth rotation effects (Wu, et al., 1981). However, the variation in range within a given data record is relatively small, and is not expected to introduce a significant error in the radiometric correction process.

Plots of the radiometric correction factors for the English Channel and Nantucket Shoals data sets are shown in Figures C1 and C2. These plots indicate the reciprocal of the correction factors defined above, i.e., $S_i/S_{max}$.

## C.2 GEOMETRIC CORRECTIONS

The location of each object within a SAR image is determined by its range distance and its Doppler history. Consequently, the relative positions of objects in the image may not correspond exactly to their actual positions on the surface of the earth. These distortions are discussed in the following section, and a first-order geometric correction scheme is described in Section C.2.2.
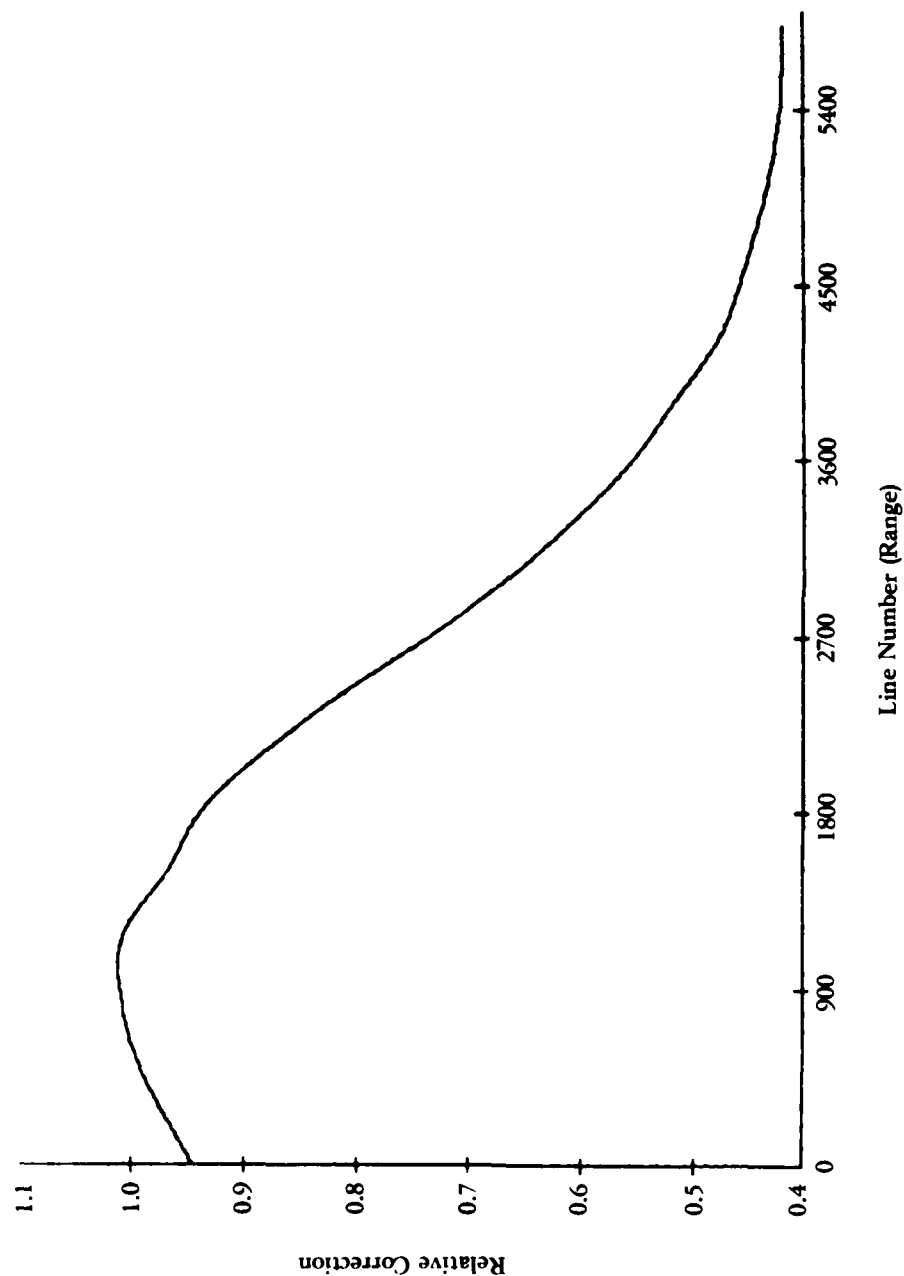
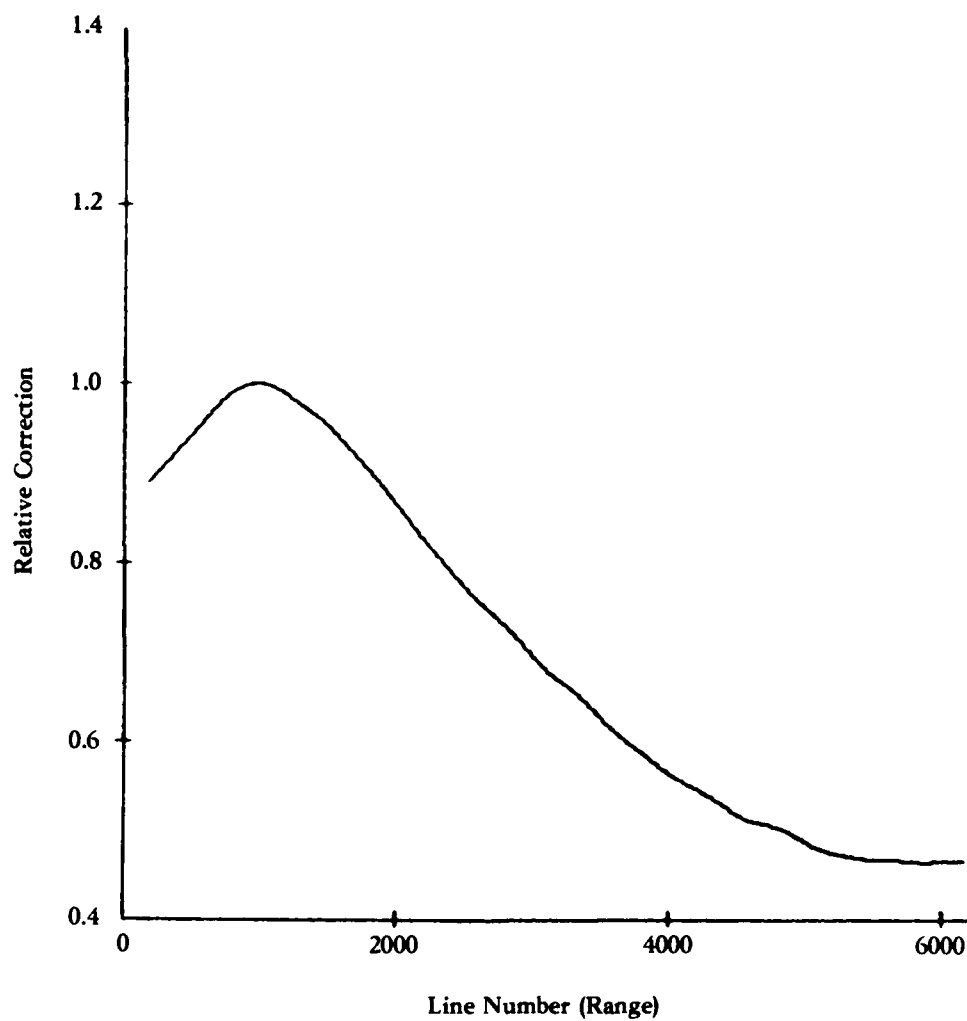FIGURE C1. EMPIRICAL RADIOMETRIC CORRECTION FACTORS FOR NANTUCKET SHOALS. (Seasat, Rev. 880, data set)

FIGURE C2. EMPIRICAL RADIOMETRIC CORRECTION FACTORS FOR ENGLISH CHANNEL SEASAT (REV. 762) DATA SET.

## C.2.1 SOURCES OF GEOMETRIC DISTORTIONS

There are many possible sources of geometric distortion in a SAR image, including variations in the elevation and radial velocity of objects in the scene and the slant/ground range nonlinearity. Elevation differences cause an apparent displacement in the across-track direction, while radial velocity variations cause a displacement of the object in the along-track direction. The effects of elevation and velocity variations may be neglected in Seasat images of the ocean surface, except for the systematic variation in radial velocity caused by the earth's rotation, which is corrected during the digital correlation (Wu, et al., 1981). The largest source of geometric distortion in Seasat images of the ocean is due to the slant/ground range nonlinearity. This distortion arises because the data are sampled in equal intervals of slant range. The ground range distance between samples thus varies throughout the image, being larger at near range and smaller at far range.

The relationship between the slant range and ground range is illustrated in Figure C3. The slant range (R) is the distance from the spacecraft to the target, while the ground range (X) is the arc length between the sub-satellite point and the target, i.e., the product of the angle $\alpha$ and the earth's radius ($R_e$). Using the law of cosines, the following relationship can be easily established:

$$\cos\left(\frac{X}{R_e}\right) = \frac{R_e^2 + (R_e + A)^2 - R^2}{2R_e(R_e + A)} \tag{C-4}$$

where A is the spacecraft altitude. Differentiating this equation with respect to X, the ground range distance between pixels is given by

$$\delta X = \frac{R_e}{R_e + A} \frac{\delta R}{\sin \theta} \tag{C-5}$$
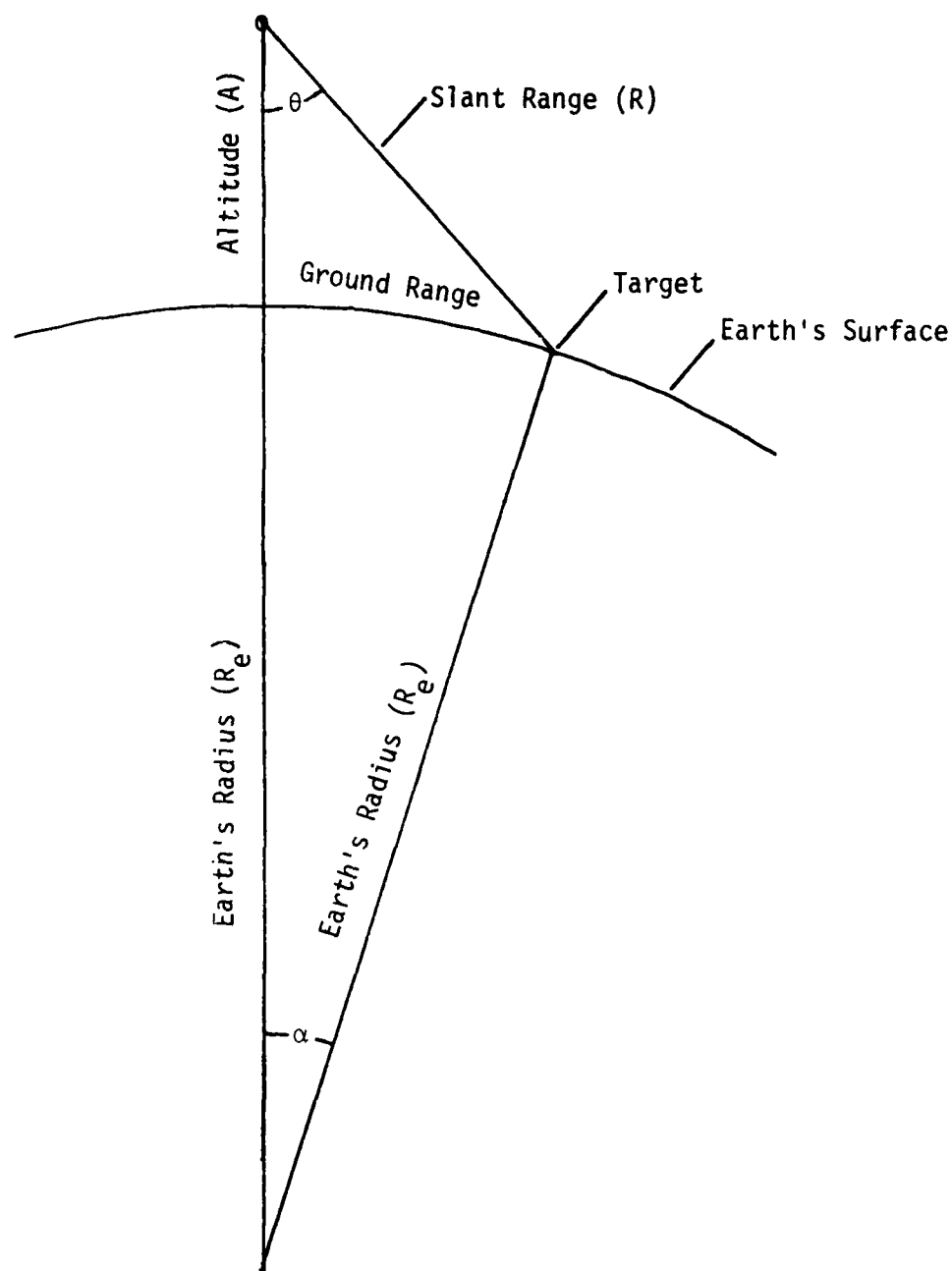
FIGURE C3.  SEASAT SAR VIEWING GEOMETRY.  (Equation in text
is obtained by applying the law of cosines to
the triangle with sides $R_e$, $R_e$ + A, and R.)

211

where δR is the range distance between pixels and θ is the incidence angle. For Seasat, the incidence angle ranges from approximately 19° to 25°. The range sampling rate of 45.53 MHz results in a pixel spacing of 6.59 meters in slant range. Thus, the pixel spacing in ground range varies from approximately 18 meters at near range to 14 meters at far range.

The pixel spacing in the along-track or azimuth direction is determined by the swath velocity (V) and the pulse repetition frequency (PRF). The use of four independent looks in processing the data results in a pixel spacing of

$$\delta y = \frac{4 \times V}{PRF} \tag{C-6}$$

which is typically on the order of 16 meters (for a swath velocity of 6700 m/sec and a PRF of 1647 Hz). Thus, the average aspect ratio of the uncorrected image is approximately correct but the image is significantly compressed at near range and expanded at far range, in the range direction. A method of correcting for this distortion is described in the following section.

It should be noted that the skew correction for earth rotation effects is done (at JPL) by applying an offset to the range coordinate which varies linearly with the along-track coordinate. Typically, the range coordinate is shifted by one pixel for every 16 azimuth samples, resulting in a step edge along the edge of the image. As a result of this correction, the pixels within a given data record are not at a constant range. This offset is ignored for the purpose of the first-order geometric correction described in the following section, but is taken into account in the registration procedure described in Chapter 5 of this report.

### C.2.2  SLANT/GROUND RANGE CORRECTION

In order to facilitate the interpretation of the imagery, a first-order slant/ground range correction was applied to the JPL-processed Seasat data. This correction is done using a nearest

neighbor resampling procedure in the range direction to make the aspect ratio equal to unity throughout the image. That is, the ground distance between range samples is made equal to the distance between azimuth samples as calculated from the swath velocity and the PRF. Since each data record is at approximately the same range in the JPL data, this procedure results in the repetition of some records at near range and the omission of some records at far range.

In slightly more detail, the procedure is as follows:

1. The first data record is read and copied. The ground range for this record is computed from the equation

$$X = R_e \cos^{-1}\left[\frac{R_e^2 + (R_e + A)^2 - R^2}{2R_e(R_e + A)}\right] \sqrt{\frac{R^2 - A^2}{1 + A/R_e}} , \quad (C\text{-}7)$$

where $X$ is the ground range, $R$ is the slant range, $R_e$ is the radius of the earth, and $A$ is the spacecraft altitude. The approximation used in this equation is obtained by assuming $\sin \alpha \cong \alpha$, where $\alpha$ is the angle indicated in Figure C3. The slant range for the first data record, the local earth radius, and the spacecraft altitude are obtained from the Auxiliary Data Listing for the data set under consideration.

2. This equation is inverted to yield the slant range

$$R_1 = \sqrt{A^2 + X_1^2(1 + A/R_e)} \quad (C\text{-}8)$$

corresponding to the ground range $X_1 = X_0 + \Delta X$, where $X$ is the ground range for the previous pixel and $\Delta X$ is the desired ground range between pixels, which is equal to

$$\Delta X = \frac{4 \times \text{swath velocity}}{\text{PRF}} , \quad (C\text{-}9)$$

3. The range record nearest to $R_1$ is read from the input tape and copied onto the output tape. If $R_1$ differs from the range for the previous record by less than 3.3 meters, the previous record is repeated. If $R_1$ is more than 9.9 meters away from the previous record, at least one record is skipped over and the next record is copied. The slant range corresponding to input record n is given by

$$R'_n = R_{min} + 6.585n \text{ meters },$$

for JPL-processed Seasat data, which is sampled at 45.53 MHz.

4. The process is repeated, beginning with step (2), until the last range record is encountered.

The above geometric correction procedure and the previously described radiometric correction procedure are used on both the Nantucket Shoals data set (Revolution 880) and the English Channel data set (Revolution 762). The geometrically and radiometrically corrected images for these two data sets are shown in Figures C4 and C5.
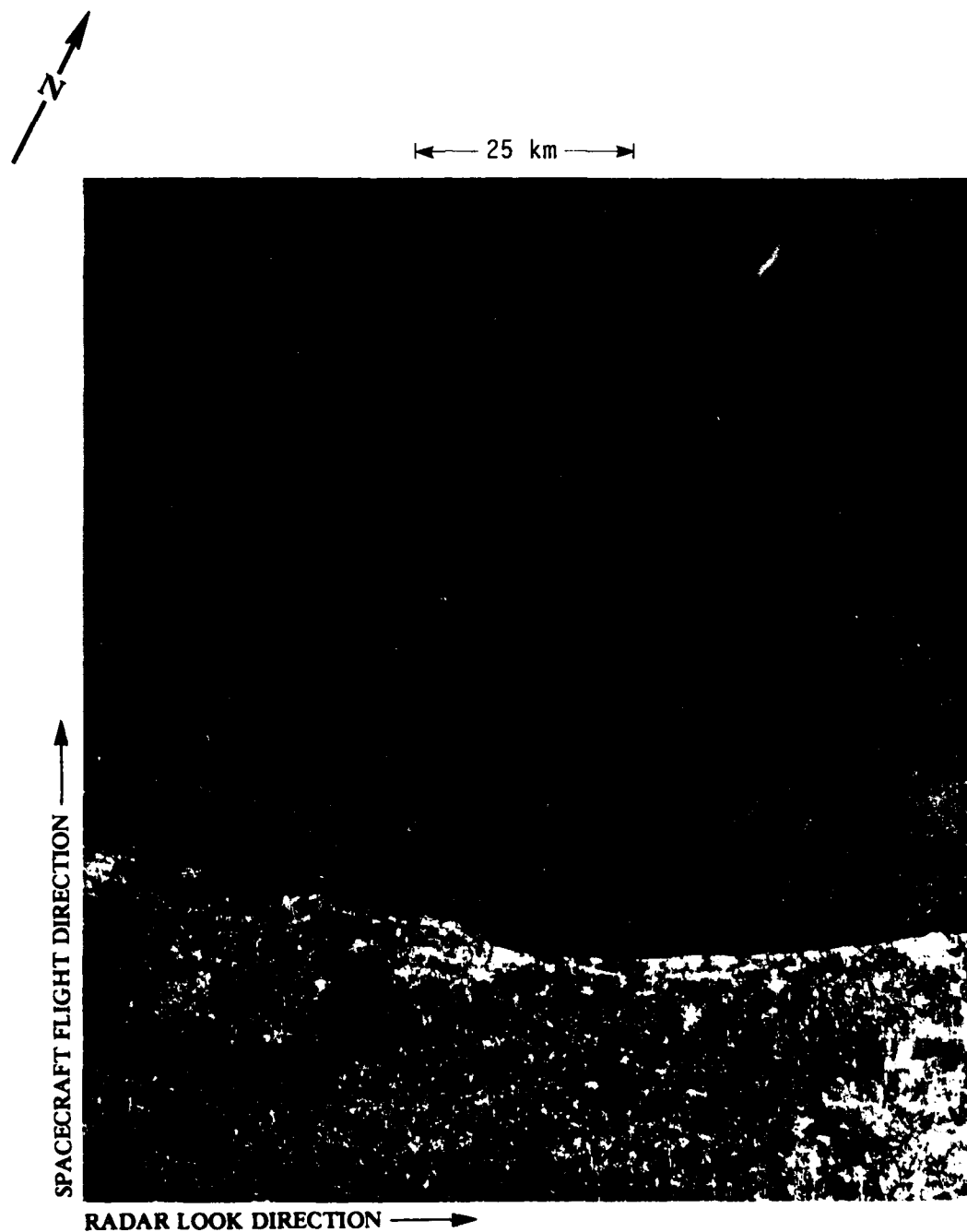
FIGURE C4.   RADIOMETRICALLY AND GEOMETRICALLY CORRECTED IMAGES
             FOR SEASAT DATA FROM REV. 762 OVER THE ENGLISH
             CHANNEL.

FIGURE C5.  RADIOMETRICALLY AND GEOMETRICALLY CORRECTED
IMAGE FOR SEASAT DATA FROM REV. 880 OVER
THE NANTUCKET SHOALS.

# REFERENCES

Allan, T.D. and T.H. Guymer, Seasat and JASIN, Int. J. Remote Sensing, 1, pp. 261-267, 1980.

Allan, J.R.L., Sand Waves: A Model of Origin and Internal Structure, Sedimentary Geology, 26, pp. 281-328, 1980.

Arthur, R.S., W.H. Munk, and J.D. Isaacs, Direct Construction of Wave Rays, Trans. Am. Geophys. Union, 33, 1952.

Ausherman, D.A., Digital Versus Optical Techniques in Synthetic Aperture Radar (SAR) Data Processing, Optical Eng., 19, pp. 157-167, 1980.

Bainbridge, A.E., Geosecs Atlantic Expedition - Volume 2: Sections and Profiles, U.S. Government Printing Office, Washington, D.C., 198 pp., 1980.

Baines, P.G., Observations of Stratified Flow Over Two-Dimensional Obstacles in Fluid of Finite Depth, Tellus, 31, pp. 351-371, 1979.

Ball, M. M., Carbonate Sand Bodies of Florida and the Bahamas, Journal of Sedimentary Petrology, 37, pp. 556-591, 1967.

Beal, R.C., P.S. DeLeonibus and I. Katz (eds.), Spaceborne Synthetic Aperture Radar for Oceanography, Johns Hopkins Univ. Press, Baltimore, MD, 215 pp., 1981.

Bell, T.H., Jr., Topographically Generated Internal Waves in the Open Ocean, J. Geophys. Res., 80, pp. 320-327, 1975.

Brown, W.M. and L. Porcello, An Introduction to Synthetic Aperture Radar, IEEE Spectrum, 6, pp. 52-66, 1969.

Caston, G.F., Wreck Marks: Indicators of Net Sand Transport, Marine Geology, 33, pp. 193-204, 1979.

DeLoor, G.P. and H.W. Brunsveld Van Hulten, Microwave Measurements Over the North Sea, Boundary-Layer Meteorol., 13, pp. 119-131, 1978.

Department of Defense and Department of Commerce, Chart No. 1: United States of America Nautical Chart Symbols and Abbreviations, 7th Edition, Washington, D.C., 36 pp., 1979.

Elachi, C., Radar Imaging of the Ocean Surface, Boundary-Layer. Meteorol., 13, pp. 165-179, 1978.

Fu, L. and B. Holt, Seasat Views Oceans and Sea Ice with Synthetic Aperture Radar, JPL Publication No. 81-120, 200 pp., 1982.

Garrett, C. and W. Munk, Space-Time Scales of Internal Waves: A Progress Report, J. Geophys. Res., 80, pp. 291-297, 1975.

Garrett, C. and W. Munk, Internal Waves in the Ocean, Ann. Rev. Fluid Mech., 11, pp. 339-369, 1979.

Hollinger, J.P., Microwave Properties of a Calm Sea, NRL Report 7110-2, 1973.

Harger, R.O., Synthetic Aperture Radar Systems, Academic Press, New York, NY, 240 pp., 1970.

Jensen, J.R., J.E. Estes and L. Tinney, Remote Sensing Techniques for Kelp Surveys, Phot. Eng. Rem. Sens., 46, pp. 743-755, 1980.

Jordan, R.L., The Seasat-A Synthetic Aperture Radar System, IEEE J. Oceanic Eng., OE-5, pp. 154-164, 1980.

Kasischke, E.S., Extraction of Gravity Wave Information from Synthetic Aperture Radar Data, Univ. of Mich. M.S. Thesis, 108 pp., 1980.

Kasischke, E.S., R.A. Shuchman and J.D. Lyden, Detection of Bathymetric Features Using SEASAT Synthetic Aperture Radar - A Feasibility Study, ERIM Final Report No. 135900-2-F$_2$, 77 pp., 1980.

Kasischke, E.S., R.A. Shuchman, G.A. Meadows, P.L. Jackson, Y. Tseng, J.D. Lyden, Further Seasat Coastal Ocean Wave Analysis, ERIM Final Report No. 138600-6-F, Ann Arbor, MI, 139 pp., 1981.

Kenyon, N.H., R.H. Belderson, A.H. Stride and M.A. Johnson, Offshore Tidal Sand Boules as Indicators of Net Sand Transport and as Potential Deposits, in Holocene Marine Sedimentation in the North Sea Basin, Selected Papers from the IAS Meeting, Texel, Netherlands, ed. by S.D. Nio, R.T.E. Schuttenhelm and T.C.E. Van Weering, IAS Spec. Pub. 5., Sept. 1979.

Kenyon, N.H., Bedforms of Shelf Seas Viewed with SEASAT Synthetic Aperture Radar, in Advances in Hydrographic Surveying, ed. M.J. Wright, Society for Underwater Technology, London, pp. 67-73, 1981.

Kline, H., Cruising Guide to the Bahamas, Miami, FL, 1978.

Kozma, A., E.N. Leith and N.G. Massey, Tilted Plane Optical Processor, Applied Optics, 11, pp. 1766-1777, 1972.

Lohmann, K.C., Marine Transgressions as a Factor in the Formation of Sandwave Complexes, Geologie En Mijnbouw, 55, pp. 18-40, 1976.

McLeish, W., D.J.P. Swift, R.B. Long, D. Ross and G. Merrill, Ocean Surface Patterns Above Seafloor Bedforms as Recorded by Radar, Southern Bight of North Sea, Mar. Geol., 43, pp. M1-M8, 1981.

Mollo-Christensen, E., Surface Signs of Internal Ocean Dynamics, in Spaceborne Synthetic Aperture Radar for Oceanography, ed. by R.C. Beal, P.S. Deleonibus and I. Katz, The Johns Hopkins Univ. Press, Baltimore, pp. 140-145, 1981.

Muller, P. and D.J. Olbers, On the Dynamics of Internal Waves in the Deep Ocean, J. Geophys. Res., 80, pp. 3848-3860, 1975.

Mullins, H.T., G.W. Lynts, A.C. Neumann, and M.M. Ball, Characteristics of Deep Bahama Channels in Relation to Hydrocarbon Potential, American Association of Petroleum Geologists Bulletin, 62, pp. 693-704, 1978.

National Ocean Survey, Tide Tables - High and Low Water Predictions, 1978 - East Coast of North and South America, including Greenland, Washington, D.C., 1978.

National Ocean Survey, Tide Tables - High and Low Water Predictions, 1978 - West Coast of North and South America, Washington, D.C., 1978a.

Palmer, M.S., Holocene Facies Geometry of the Leeward Bank Margin, Tongue of the Ocean, Bahamas, University of Miami, Master's Thesis, Coral Gables, FL, 1979.

Phillips, O.M., The Structure of Short Gravity Waves on the Ocean Surface, in Spaceborne Synthetic Aperture Radar for Oceanography, ed. by R.C. Beal, P.S. DeLeonibus, and I. Katz, Johns Hopkins Univ. Press, Baltimore, MD, pp. 24-31, 1981.

Raney, R.K. and R.A. Shuchman, SAR Mechanism for Imaging Waves, Proc. Fifth Canadian Symp. on Remote Sensing, Victoria, B.C., 1978.

Reed, C.L., Interpretation of Hydrographic Features in the Water Off Cape Cod, Univ. of Mich. M.S. Thesis, Ann Arbor, MI, 1981.

Rice, P.D., J.M. Hall, and N.D. Opdyke, Deep Drill 1972: A Paleomagnetic Study of the Bermuda Seamount, Cam. J. Earth Science, 17, pp. 232-243, 1980.

Roberts, D.G., P.M. Hunter, and A.S. Laughton, Bathymetry of the Northeast Atlantic: Continental Margin Around the British Isles, Deep-Sea Res., 26A, pp. 417-428, 1979.

Royal Society, Air-Sea Interaction Project: Summary of the 1978 Field Experiment, The Royal Society, London, England, 139 pp., 1979.

Shemdin, O.H., The Marineland Experiment: An Overview, Trans. Amer. Geophys. Union, 61, No. 38, pp. 625-626, 1980.

Shepard, F.P., J.M. Trefethen, and G.V. Cohee, Origin of Georges Bank, Bulletin of the Geological Society of America, 45, pp. 281-302, 1934.

Shuchman, R.A., Quantification of SAR Signatures of Shallow Water Ocean Topography, Univ. of Mich. PhD Dissertation, Ann Arbor, MI, 130 pp., 1982.

Shuchman, R.A. and R.T. Lowry, Vegetation Classification with Digital X-Band and L-Band Dual Polarized SAR Imagery, Proceedings of the Fourth Canadian Symposium on Remote Sensing, Quebec City, pp. 444-459, 1977.

Shuchman, R.A. and E.S. Kasischke, The Detection of Oceanic Bottom Topographic Features Using SEASAT Synthetic Aperture Radar Imagery, Proc. Thirteenth Int. Symp. Remote Sens. Environ., pp. 1277-1292, 1979.

Shuchman, R.A., E.S. Kasischke, A. Klooster and P.L. Jackson, SAR Coastal Ocean Wave Analysis - A Wave Refraction and Diffraction Study, ERIM Final Report No. 138600-2-F, Ann Arbor, MI, 78 pp., 1979.

Shuchman, R.A., K.H. Knorr, J.C. Dwyer, P.L. Jackson, A. Klooster and A.L. Maffett, Imaging Ocean Waves with SAR - A SAR Ocean Wave Algorithm Development, ERIM Interim Technical Report No. 124300-5-T, Ann Arbor, MI, 123 pp., 1979a.

Shuchman, R.A., A. Klooster, J.D. Lyden, and C. Liskow, Engineering Evaluation of ERIM Generated SAR Data, ERIM Informal Informational Note No. 151400-1-I, 85 pp., 1980.

Shuchman, R.A. and E.S. Kasischke, Refraction of Coastal Ocean Waves, in Spaceborne Synthetic Aperture Radar for Oceanography, ed. by R.C. Beal, P.S. DeLeonibus and I. Katz, Johns Hopkins Univ. Press, Baltimore, MD, pp. 128-135, 1981.

Shuchman, R.A., A.L. Maffett and A. Klooster, Static Modeling of a SAR Imaged Ocean Scene, IEEE J. Oceanic Eng., OE-6,, pp. 41-49, 1981.

Shuchman, R.A., E.S. Kasischke, G.A. Meadows, J.D. Lyden, D.R. Lyzenga, P.L. Jackson, A.L. Maffett, and A. Klooster, Jr., The Utility of SAR to Monitor Ocean Processes, ERIM Final Report 124300-11-F, 133 pp., 1981.

Shuchman, R.A., E.S. Kasischke, J.D. Lyden, A. Klooster, and W. Rosenthal, Analysis of MARSEN Synthetic Aperture Radar Wave Imagery, 1982 Int. Geoscience and Remote Sensing Symposium Digest (in press), 1982.

Stewart, H.B., Jr. and G.F. Jordan, Underwater Sand Ridges on Georges Shoal, in Marine Geology, Shepard Commemorative Volume, ed., Robert L. Miller, MacMillan Company, New York, 1956.

Tarbell, S., M.G. Briscoe, and R.A. Wellar, A Compilation of Moored Current Meter and Wind Recorder Data - Volume XVIII (JASIN 1978, Mooring, 651-653), Woods Hole Oceanographic Institute Technical Report No. WHOI-79-65, Woods Hole, MA, 200 pp., 1979.

Teleki, P.G., R.A. Shuchman, W.E. Brown, Jr., W. McLeish, D. Ross and M. Mattie, Ocean Wave Detection and Direction Measurements with Microwave Radars, Oceans '78, IEEE/MTS, pp. 639-648, 1978.

Thorpe, S.A., The Excitation, Dissipation, and Interaction of Internal Waves in the Deep Ocean, J. Geophys. Res., 80, pp. 328-338, 1975.

Uchupi, E., Atlantic Continental Shelf and Slope of the United States Physiography, Geological Survey Professional Paper 529-C, United States Printing Office, 1968.

U.S. Naval Oceanographic Office, Oceanographic Atlas of the North Atlantic Ocean - Section I - Tides and Currents, Washington, D.C., 1977.

Valenzuela, G.R., A Remote Sensing Experiment in the Nantucket Shoals, Proceedings of the IUCRM Symposium on Wave Dynamics and Radio Probing of the Ocean Surface (in press), 1981.

Valenzuela, G.R., Theories for the Interaction of Electromagnetic and Oceanic Waves -- A Review, Boundary Layer Meteorology, 13, pp. 61-85, 1978.

Vesecky, J.F. and R.H. Stewart, The Observation of Ocean Surface Phenomena Using Imagery from the Seasat Synthetic Aperture Radar - An Assessment, J. Geophys. Res., 87, pp. 3397-3430, 1982.

Walker, J.L. and R.W. Rawson, SAR Calibration Technology Review, ERIM Final Report No. 150400-7-F, 151 pp., 1981.

Wiegal, R.L., Oceanographical Engineering, Prentice-Hall, Englewood Cliffs, NJ, 1964.

Wright, J.W., Backscattering from Capillary Waves with Application to Sea Clutter, IEEE Trans. Antenna Propagat., AP-14, pp. 749-754, 1966.

Wright, J.W., W.J. Plant, W.C. Keller and W.L. Jones, Ocean Wave-Radar Modulation Transfer Functions from the West Coast Experiment, J. Geophys. Res., 85, pp. 4957-4966, 1980.

Wu, C., B. Barkan, B. Huneycutt, C. Leang, and S. Pang, An Introduction to the Interim Digital SAR Processor and the Associated Seasat SAR Imagery, JPL Publication 81-26, Pasadena, CA, 1981.

Wunch, C., Geographical Variability of the Internal Wave Field: A Search for Sources and Sinks, J. Phys. Ocean., 6, pp. 471-485, 1976.

4 - 8

DTI